

The Pennsylvania State University
The Graduate School

**CONTROL, ESTIMATION AND PLANNING FOR COORDINATED
TRANSPORT OF A SLUNG LOAD BY A TEAM OF AERIAL ROBOTS**

A Dissertation in
Aerospace Engineering
by
Junyi Geng

© 2020 Junyi Geng

Submitted in Partial Fulfillment
of the Requirements
for the Degree of

Doctor of Philosophy

December 2020

The dissertation of Junyi Geng was reviewed and approved by the following:

Jacob W. Langelaan
Professor of Aerospace Engineering
Dissertation Advisor
Chair of Committee

Joseph F. Horn
Professor of Aerospace Engineering

Eric N. Johnson
Professor of Aerospace Engineering

Minghui Zhu
Associate Professor of Electrical Engineering

Amy R. Pritchett
Professor of Aerospace Engineering
Head of Department of Aerospace Engineering

Abstract

This dissertation describes the development of a self-contained transportation system that uses multiple autonomous aerial robots to cooperatively transport a single slung load. The work described here is especially concerned with developing a transportation team that can adapt to the payload properties and is able to achieve energy efficiency. The capability to adapt to uncertainty in payload properties allows the system to transport payloads with little a priori information, while efficient transport will maximize global transportation performance.

This guiding problem requires advances in coordination, perception, estimation, control and planning. Of these, this dissertation has three foci: develop a comprehensive coordinated control strategy for minimizing the coupling of the payload and aerial vehicles while accounting for the payload dynamics; develop a payload inertial property estimation approach to enable transportation with little a priori payload information; develop a trajectory planning method that considers system power consumption.

This dissertation implements a hierarchical strategy that is scalable and allows human-in-the-loop in addition to fully autonomous operation. A key component of this approach is the computation of cable forces to enable desired payload behavior. This is shown to be a non-convex optimization problem, and a method to “convexify” cable force computation to enable fast computation is introduced and implemented. Next, the desired rotorcraft states for a given payload state is derived. A stability analysis based on singular perturbation shows that the closed-loop system can track the reference exponentially within an error bound.

Next, a method to estimate the payload’s inertial properties without the use of cable tension sensors is introduced. Here, cable tension is estimated using an indirect method based on rotorcraft states and acceleration. Using these estimated cable tensions and a sequence of maneuvers that enable observability of payload inertial properties, three estimation algorithms (least-squares, maximum likelihood, and a Kalman filter) are derived and implemented to estimate payload inertial properties.

Finally, a trajectory planning strategy is developed for the system to achieve near equal load distribution among the aerial vehicles for energy efficiency. The problem is simplified as planning for payload while considering other physical and geometric constraints. An optimal control problem is formulated that simultaneously plans payload trajectory and cable forces while satisfying path and force constraints and minimizing the variance in cable forces. Then, a feedback control law for tracking in the neighbor of the optimal trajectory is developed to equalize the cable tension load distribution.

Together these techniques compose a cooperative aerial transportation system which

has the ability to adapt to unknown payload properties and has the ability to optimize the power consumption. Components of this system are tested in simulation, indoor and outdoor flight experiments and demonstrate the effectiveness of the developed slung load transportation system.

Contents

List of Figures	ix
List of Tables	xii
List of Symbols	xiii
Acknowledgments	xvi
Chapter 1	
Introduction	1
1.1 Motivation	2
1.2 An Overview for the Cooperative Slung Load Aerial Transportation	5
1.3 The Integrated Multilift	8
1.3.1 A Comprehensive Coordinated Control Strategy	8
1.3.2 Estimation of Slung Load Properties	9
1.3.3 Trajectory Planning and Control Based on Load Distribution	10
1.4 Related Work	10
1.4.1 Configuration	11
1.4.2 Coordinated Control	12
1.4.3 Estimation and Sensor Fusion	13
1.4.4 Load Distribution Based Trajectory Planning	14
1.4.5 Cable-Driven Parallel Robot	15
1.4.6 State of the Art	16
1.5 Summary of Contributions	18
1.6 Reader's Guide	20
Chapter 2	
The Multilift Problem	21
2.1 System Description and Hierarchical Load-leading Control Architecture	22
2.2 Dynamics	24
2.2.1 Payload Dynamics	24
2.2.2 Rotorcraft Dynamics	25
2.3 Cable Force	26
2.4 Assumptions	27

2.5	Summary: The Multilift Problem	27
-----	--	----

Chapter 3

A Hierarchical Strategy Using Load-leading Control	29	
3.1	Cable Force Analysis	30
3.1.1	Cable Force Computation	30
3.1.2	Convexity Analysis	32
3.2	Kinematics Analysis for Desired Rotorcraft States	35
3.2.1	General Kinematics Derivation	35
3.2.2	Special Cases	37
3.2.2.1	Rigid Cable	37
3.2.2.2	Cable Modeled as Spring-damper	38
3.2.2.3	Rigid Formation	39
3.3	Control	39
3.3.1	Payload Trajectory Following Control	39
3.3.2	Rotorcraft Control	41
3.3.3	Stability Analysis of the Full System	43
3.4	Hardware Platform	43
3.4.1	Payload Side	44
3.4.2	Rotorcraft Side	44
3.4.3	Ground Side	45
3.4.4	External Sensor	46
3.4.5	Python State Machine	46
3.4.6	Information Flow	47
3.5	Flight Demonstration	48
3.5.1	Single Step Optimization Study	49
3.5.2	Cooperative Transport with a Circular Path Mission	50
3.5.3	Disturbance Rejection Test	55
3.5.4	Cooperative Transport with a Human-in-the-loop	57
3.5.5	Cooperative Transportation with Cable Internal Motion	59
3.5.6	Outdoor Lateral Trajectory Tracking	60
3.6	Summary	61

Chapter 4

Slung Load Inertial Property Estimation	66	
4.1	System Motion and Perception	67
4.1.1	Slung Load Motion and Sensing	67
4.1.1.1	Slung Load Motion	67
4.1.1.2	Sensing	68
4.1.2	Cable Force Estimation	70
4.1.2.1	Indirect Method for Cable Force Estimation	70
4.1.2.2	Cable Force Uncertainty Quantification	71
4.2	Estimation of Slung Load Parameters	73
4.2.1	Least-squares Method for Parameter Estimation	73

4.2.1.1	Batch Case	74
4.2.1.2	Sequential Case	74
4.2.1.3	Experimental Condition	75
4.2.2	Maximum Likelihood Estimation	75
4.2.3	Kalman Filter Method	77
4.2.4	Inertial Properties Estimation for Multilift	78
4.2.4.1	Estimation of Slung Load Mass	79
4.2.4.2	Estimation of Slung Load Center of Mass	80
4.2.4.3	Estimation of Slung Load Moments of Inertia	82
4.3	Hardware Experiment	82
4.3.1	Experiment Setup	82
4.3.1.1	Vicon Object Coordinate Frame	82
4.3.1.2	Initialization of Inertial Property Estimates	83
4.3.2	Experiment Implementation	83
4.3.3	Estimation of Slung Load Mass During Hover	83
4.3.4	Estimation of Slung Load Center of Mass (CM)	87
4.3.5	Estimation of Slung Load Moments of Inertia	90
4.4	Controller Compensation	92
4.4.1	Group 1: Single Channel Sinusoidal Movement	92
4.4.2	Group 2: Double Channel Sinusoidal Movement (“Figure 8” Pattern)	95
4.5	Summary	98

Chapter 5

	Trajectory Planning and Control Based on Load Distribution	100
5.1	Load Distribution Based Trajectory Planning and Control Problem . . .	101
5.1.1	Problem Simplification	102
5.1.2	Trajectory Planning Problem	103
5.1.3	Tracking Problem	104
5.2	Analysis and Methodology	105
5.2.1	Planning	106
5.2.1.1	Problem Analysis	106
5.2.1.2	Collocation	107
5.2.2	Tracking	108
5.3	Simulation	108
5.3.1	Setup	109
5.3.1.1	Multilift Parameter	109
5.3.1.2	Setup for Trajectory Planning	109
5.3.1.3	Tracking Controller Parameter	109
5.3.1.4	Wind Gust	110
5.3.2	Planning Results and Discussion	110
5.3.3	Tracking Results Under Wind Gust	113
5.4	Hardware Experiment	114
5.4.1	Experiment Setup	115
5.4.2	Results and Discussion	116

5.5	Towards Reinforcement Learning Based Trajectory Planning	119
5.5.1	Multilift Learning Problem	121
5.5.2	PPO Algorithm	122
5.5.3	Application of PPO to Multilift Trajectory Planning	123
5.5.4	Simulation	124
5.5.4.1	Setup	124
5.5.4.2	Preliminary Results and Discussion	124
5.6	Summary	130
Chapter 6		
Conclusion		132
6.1	Summary of Contributions	135
6.2	Recommendations for Future Work	137
6.2.1	Different Cone Angles for Each Cable	137
6.2.2	General Cable Model	138
6.2.3	General Dynamics Model	138
6.2.4	Complex Environment with Obstacles	139
6.2.5	Reinforcement Learning and Distributed System	139
6.2.6	Other Domains	140
6.2.7	System Redundancy	140
Appendix A		
Stability Proof		141
A.1	Proof of Prop. 1	141
A.2	Proof of Prop. 2	142
Appendix B		
Necessary Condition and Controller Parameters		143
B.1	Necessary Condition of the Planning Problem	143
B.2	Controller Parameters for Hardware Implementation	146
Bibliography		147

List of Figures

1.1	Sikorsky Twin-lift demonstration with CH-54B [1]	2
1.2	UH-60L Black Hawk with a CONEX cargo container [2]	3
1.3	Mi-26 lifting an airliner [3]	3
1.4	Ideal relative productivity at 100 nautical miles [4]	4
1.5	Schematic of cooperative slung load transportation by a team of aerial robots	4
1.6	A General Framework for Multilift	7
1.7	Two twin-lift configuration	12
1.8	Two cable-driven parallel robots	15
1.9	Slung load demonstration by AAU Bergen Industrial Twin helicopter and GTmax	17
1.10	The worldwide first load transportation task in real flight experiments using three helicopters [5]	17
1.11	Slung load transporation by three multirotors under wind distrubances [6]	18
2.1	Schematic of the coordinated transportation problem	22
2.2	Load-leading multilift system block diagram	23
3.1	Definition of cable cone angle and sector region	32
3.2	Geometrical interpretation of the constraints	34
3.3	Modify the equality constraints to inequality	34
3.4	Addition of affine constraints	35
3.5	Kinematics schematic	36
3.6	Block diagram of the payload trajectory following controller	40
3.7	Block diagram of rotorcraft controller	41
3.8	System poles (hover) [7]	43
3.9	Payload with control computer.	44
3.10	Diagram of state machine	47
3.11	Multilift system information flow	48
3.14	Payload yaw angle in pirouette	52
3.12	Payload with only translation	52
3.13	Payload with pirouette	52
3.15	Position of the robots for payload with only translation	53
3.16	Position of the robots for payload with pirouette	53

3.17	Sequence of images showing coordinated payload transport in the motion capture studio.	54
3.18	External disturbance	55
3.19	Payload position with impulse disturbances occurring at 5.5 s and at 9.2 s	56
3.20	Payload orientation with impulse disturbances occurring at 5.5 s and at 9.2 s	56
3.21	Position of the robots with impulse disturbances occurring at 5.5 s and at 9.2 s	57
3.22	Human operator “flying” the payload directly.	58
3.23	Payload velocity and yaw angle with human operator.	58
3.24	Formation changeing test	61
3.25	Test field near Penn State Arboretum	62
3.26	Outdoor lateral trajectory tracking	62
3.27	Test day wind condition [8]	62
3.28	Payload horizontal velocity tracking error, with wind shown as vector . .	63
3.29	Payload horizontal position	63
3.30	Position of the robots	64
4.1	Diagram of multilift with electronics attached on payload	69
4.2	Force analysis on one quadcopter	70
4.3	Payload excited motion	81
4.4	Converging curve for different masses (the label “std” in the lower plots denote 1σ bounds)	86
4.5	Cable force estimate z-component	87
4.6	Payload with 200g extra weight attached	88
4.7	Converging curve of z component of CM estimation (the label “std” in the lower plot denotes 1σ bound).	89
4.8	x and y component of CM estimation	90
4.9	Converging curve of x component of CM estimation (the label “std” in the lower plot denotes 1σ bound).	91
4.10	Roll moment and angular rate data	92
4.11	Payload configuration for controller compensation test	93
4.12	Payload trajectories for test group 1 with increasing frequency	94
4.13	Payload command cable force for test group 1 with increasing frequency .	94
4.14	Rotorcraft tracking error (in 2-norm) for test group 1 with increasing frequency	95
4.15	Payload trajectories for the compensated case in test group 2 with increasing frequency	96
4.16	Payload tracking behavior for test group 2 with increasing frequency . . .	97
4.17	Payload command cable force for test group 2 with increasing frequency .	97
4.18	Rotorcraft tracking error (in 2-norm) for test group 2 with increasing frequency	98
4.19	Absolute value of the payload Euler angle tracking error for test group 2 with increasing frequency	99

5.1	Multilift problem and symplification	102
5.2	Payload states with different arriving time	110
5.3	Cable tension	111
5.4	Cable sector angle	112
5.5	Tracking error of payload states under wind gust	113
5.6	Input tracking error	114
5.7	System behavior using the load distribution based trajectory planning and control	116
5.8	Payload tracking performance	117
5.9	Cable tension	117
5.10	Cable sector angle	118
5.11	Robots tracking performance	119
5.12	Energy comnsumpton performance of the rotorcraft	119
5.13	Payload States with only distance in reward function	125
5.14	Cable tension with only distance in reward function	126
5.15	Sector angle comparison with only distance in reward function	126
5.16	Payload States with velocity shaping involved into the reward function	127
5.17	Cable tension comparison with velocity shaping involved into the reward function	127
5.18	Sector angle comparison with velocity shaping involved into the reward function	128
5.19	Payload States with velocity shaping $\Delta t = 0.02s$	129
5.20	Multilift learning for trajectory planning based on load distribution	130

List of Tables

3.1	Parameter for payload and cables	45
3.2	Cable attachment geometry	45
3.3	IRIS quadcopter parameters	45
3.4	Comparison of non-convex and convex optimization	50
3.5	Solution difference between non-convex and convex optimization	50
3.6	Optimization Solver Performance Comparison	51
3.7	Tracking Performance Comparison	51
3.8	Optimization Solver Performance Comparison	59
3.9	Tracking Performance Comparison	60
4.1	Flight Tests Definition for Mass Estimation	84
4.2	Estimated payload mass	84
4.3	Comparison of Commanded and Estimated Vertical Component (f_z) of Cable force	86
4.4	Estimated error of ΔZ (cm)	89
4.5	Estimated error of ΔX (cm)	90
4.6	Payload estimated moments of inertia (g · m ²)	91
5.1	Maximum cable tension tracking error	113
5.2	Cost of load distribution	115
5.3	Comparison of energy consumption performance	118
5.4	Parameters for Multilift Learning	124

List of Symbols

g	Gravitational acceleration, $g = 9.81\text{ms}^{-2}$
$\mathcal{F}_e = \{\mathcal{O}_e, \mathbf{x}_e, \mathbf{y}_e, \mathbf{z}_e\}$	World fixed north-east-down frame
$\mathcal{F}_L = \{\mathcal{O}_L, \mathbf{x}_L, \mathbf{y}_L, \mathbf{z}_L\}$	Payload front-right-down body frame
$\mathcal{F}_{V_i} = \{\mathcal{O}_{V_i}, \mathbf{x}_{V_i}, \mathbf{y}_{V_i}, \mathbf{z}_{V_i}\}$	i^{th} rotorcraft front-right-down body frame
${}^e\square$	Variable expressed in frame \mathcal{F}_e
${}^L\square$	Variable expressed in frame \mathcal{F}_L
$V_i\square$	Variable expressed in frame \mathcal{F}_{V_i}
\square_d	Desired variable
\square^*	Optimal value
${}^b\mathbf{R}_a$	Rotation matrix from frame a to frame b
\mathbf{I}_n	$n \times n$ identity matrix
\mathbf{p}	Payload position vector
\mathbf{r}_i	Position vector of the i^{th} rotorcraft
\mathbf{r}_L, r_x	Payload center of mass location in frame \mathcal{F}_L and the first element
$\boldsymbol{\Omega}, \boldsymbol{\Omega}_i$	Orientation vector of the payload and the i^{th} rotorcraft
$\phi, \theta, \psi, \phi_i, \theta_i, \psi_i$	Roll, pitch and yaw angles of the payload and the i^{th} rotorcraft
$\boldsymbol{\omega}, \boldsymbol{\omega}_i, \boldsymbol{\omega}_{\mathbf{n}_i}, \omega_x$	Angular velocity of the payload, the i^{th} rotorcraft and the i^{th} cable; the first element of $\boldsymbol{\omega}$

$\mathbf{a}_o, \mathbf{a}_L, \mathbf{a}_{o_i}$	Payload linear acceleration on center of mass, \mathcal{O}_L and the linear acceleration of the i^{th} rotorcraft on the center of mass
$\boldsymbol{\alpha}, \alpha_x$	Payload angular acceleration vector and the first element
\mathbf{x}_L	Payload pose vector, including position and orientation
$\dot{\mathbf{x}}$	Payload velocity vector, including linear and angular velocity
$\ddot{\mathbf{x}}$	Payload acceleration vector, including linear and angular acceleration
\mathbf{x}_s	Payload state vector 12×1 , including position and orientation, velocity and angular velocity
$\mathbf{C}_i, \mathbf{W}_L$	Transformation matrix from $\dot{\mathbf{\Omega}}_i$ to $\boldsymbol{\omega}_i$ and from $\boldsymbol{\omega}$ to $\dot{\mathbf{\Omega}}$
\mathbf{g}_i	i^{th} cable attachment point position
\mathbf{G}, \mathbf{G}_i	Cable attachment geometry matrix and the block component from the i^{th} cable tether
$\tilde{\mathbf{G}}$	Null space matrix of \mathbf{G}
α_i, α	Cone angle of the i^{th} cable and a constant cone angle
β_i	Angle between the cable force projection on the payload body x-y plane and the positive direction of payload body x-axis of the i^{th} rotorcraft
ρ_i	Cable length of the i^{th} cable
k_c, c_c	Cable spring constant, damping constant
\mathbf{n}_i	Cable direction vector of the i^{th} cable
m_L, m_i	Payload mass and the mass of the i^{th} rotorcraft
$\mathbf{J}_{cm}, \mathbf{J}_i, J_{xx}$	Moments of inertia matrices of the payload and the i^{th} rotorcraft, the first diagonal element of \mathbf{J}_{cm}
$\mathbf{f}_{cable}, \mathbf{f}_{cable,i}$	Cable force vector and the block component from the i^{th} cable tether
\mathbf{f}_i, f_i	Cable force acting on the i^{th} rotorcraft and its magnitude, $\mathbf{f}_i = -\mathbf{f}_{cable,i}$
\mathbf{T}_i, T_i	Total trust generated by the i^{th} rotorcraft and its magnitude

τ_i	Total torque input generated by the i^{th} rotorcraft
$\mathbf{G}_g, \mathbf{G}_{g,i}$	Gravity force acting on the payload and the i^{th} rotorcraft
\mathbf{M}_g	Gravity moment acting on the payload
$\mathbf{f}_f, \mathbf{M}_f$	Total cable force and moment acting on the payload
$\mathbf{F}_p, \mathbf{M}_p, F_x, M_x$	Total external force and moment acting on the payload, and their first elements

Acknowledgments

The past six years at Penn State have been an unforgettable and invaluable experience to me. When I first started, I could barely speak fluent English, was afraid to talk to people, knew little about this country, and had never heard of the term “multilift”. It is unbelievable that over the following years I have actually been doing research about multilift and successfully flying my fleet of “little minions”. I witnessed how my multilift has been developing from the beginning of pieces of parts to the final agile roller coaster style maneuver. A great many people have contributed to its production. I own my gratitude to all those people without whom the work would not be possible.

This research was partially funded by the Government under Agreement No. W911W6-17-2-0003. The U.S. Government is authorized to reproduce and distribute reprints for Government purposes notwithstanding any copyright notation thereon. The views and conclusions contained in this document are those of the authors and should not be interpreted as representing the official policies, either expressed or implied, of the Aviation Development Directorate or the U.S Government. Thanks Penn State Vertical Lift Research Center of Excellence (VLRCOE) for providing me this amazing research opportunity.

First and foremost, my deepest gratitude to my advisor Dr. Jack Langelaan. I really didn’t know Jack when I first came to Penn State – only after a couple of years that I worked with him did I realized how amazingly fortunate I am to have an advisor who gave me the freedom to explore on my own as well as the guidance to proceed when my research faltered. Jack encouraged me to chase my own interest, use interdisciplinary knowledge to solve problems. I appreciate his insightful ideas, rich knowledge and skills in many areas. His advice, patience and support has enabled me to grow from a new graduate student to an independent researcher. More importantly, Jack is an extremely kind, caring and supportive advisor that I could not have asked for more. He is like a friend of mine and I can talk with him about many things. He always believes in me even though I am not always that confident about myself. I am forever grateful to him.

I would like to thank Dr. Joe Horn and Dr. Eric Johnson, the other two giants of the Penn State control and autonomy group in aerospace engineering for being on my doctoral committee and for a lot of guidance and help throughout my Ph.D. studies. Dr. Horn is a superman and I never understand how one can accomplish so many things at the same time. He was teaching me on 518 – aircraft stability and control, which has a continuously significant influence on my research style. His comments and guidance

in the VLRCOE review help me understand and enrich my ideas. Dr. Johnson is an extremely enthusiastic and knowledgeable person and I always feel my passion getting ignited after communicating with his group about their research. His suggestions on my comprehensive exam helped me think more and better shaped the rest of my research.

It is also my great honor to have Dr. Minghui Zhu on my committee. The work presented in this dissertation is very relevant to his research, and his student Guoxiang Zhao has provided valuable insights into my research. I look forward to working with him on the multi-agent system in the future.

I also would like to thank Dr. Puneet Singla for his continuous support and help after the optimal control class. His uncommonly detailed support and strong theoretical guidance provided vital help on my research, without whom I would have been stuck longer.

I am very grateful to the other members of the AVIA lab. My labmates have exchanged ideas with me and selflessly offered me advice. I deeply appreciate their friendship. I am especially grateful to Nathan Depenbusch, John Bird and William Holmes for helping me get started and develop my own research in the lab. Nate was like a lab captain who always ready to answer all kinds of my questions. He has helped create a very relaxed atmosphere in the lab, which makes every day's work an enjoyable experience. Will has helped me enormously in technical problems especially computer vision. He often shared the most effective way he found, without which I would have taken more detours. I had the longest overlap time with Bird. He gave me great assistance on both technical and spiritual issues. He is like a magician who can always help me overcome wired errors. The surprise he gave me on my birthday made me touched to tears, which made me feel the warmth of the lab family. He told me that pursuing a Ph.D. is like climbing a hill – be patient, and you will get there. With this in mind, I was more confident and progressing steadily towards my goal. Of my generation, I would like to thank Tomas Opazo, Tyler Rosenberger, Marc Volpe for helping me with the flight testing. Thanks Tomas for helping me designing the disturbance rejection test. Thanks Tyler for accompanying me in the flight test field no matter how heavy the scorching sun or cold wind was. I also would like to thank Nathan Kimmel, Duncan Nicholson, Jacob Reddington. They asked questions that made me examine my work more carefully. And thanks Zhenda Li for his enormous help on the reinforcement learning.

Outside of the AIVA lab, I have been extremely lucky to be surrounded by many great friends. Just to name a few: Shiyang Leng and Xuelu Li, my close friends for many years, who keep pulling me out from the stressful Ph.D. life, and I share a lot of happy moment with them. Yuelong Li and Pan Liu, two brilliant Ph.D. in EE and ME, I discussed a lot of interdisciplinary research with them, and we collaborated successfully in the end with papers published. All of my roommates during these years, Xuan Chen, Hongshen Liu, Xiao Zhang, Kejie Chen, Yuqi Zhou, Renmei Xu, I am very grateful for their company in this foreign country and the care when I was sick, which gave me the warmth of our small family. Everyone in the “Girls” group, Margalit Goldschmidt, Auriane Bottai, Mrunali Botre and the friends I met in the MIT Women in Aerospace Symposium – Cristina Riso, Flora Mech, Katherine Asztalos, I enjoyed the talking with

them to exchange my feelings and thoughts especially from the women's point of view. Boyu Wang, Guoxiang Zhao, Chao Gan and Le Shi, I miss the time we spent in the gym. Everyone in the "chifanma" and "Lion's Aero" groups, I am so happy that I spent so many Friday evenings and holidays with you.

None of this would have been possible without the love and patience of my parents: Yan Geng and Aiqin Hou. I have a very close relationship with them even if I only spend one hour video chatting with them every week. Throughout my academic studies, my parents have been there in every way possible. I never know how to pay them back. I would like to express my heart-felt gratitude to them.

Finally, the greatest thanks to my husband Daning for his love and support. I first met Daning in the university mathematical modeling competition, and then we experienced our wonderful college time together. Although we research on different speciality of aerospace engineering, he often came up with ideas that inspired me to develop effective solutions to my problems. For the past decade, he is not only my partner, my best friend, but also the person I admire most for his intelligence, concentration, persistence, and hard work. Without him, I would not have come to this country. Without him, I cannot imagine how I get out of the depression when I get stuck. I thank him for everything he has done for me. I am ever-blessed with him and our future.

Dedication

To my parents and Daning, for their unconditional love and support.

Chapter 1 |

Introduction

This dissertation describes the development of a self-contained transportation system that uses multiple autonomous aerial robots to cooperatively transport a single slung load, denoted *multilift*, Fig. 1.1. This research was motivated in part by the economic inefficiency that can occur because of the the “long tail” in payload size: extremely large payloads occur only infrequently, but would require design and fielding of very large rotorcraft for transport. The ability to use multiple smaller rotorcraft to cooperatively carry such large payloads would enable more efficient utilization of the fleet. The work described here is especially concerned with developing a transportation team that can adapt to unknown payload properties and is able to achieve energy efficiency. The capability to adapt to uncertainty in payload properties allows the system to transport payloads with little a priori information, while efficient transport will maximize global transportation performance.

This guiding problem requires advances in coordination, perception, estimation, control and planning. Of these, this dissertation has three foci: (1) coordinated control: developing a scalable approach to the problem of coordinating many robots; (2) parameter estimation: developing and implementing an algorithm that allows real-time estimation of payload inertial properties to improve system performance; (3) trajectory planning: developing and implementing a payload trajectory planner that is energy efficient.

The multilift problem is challenging. First, system complexity significantly increases as the number of aerial robots increases, leading to extreme difficulty for coordinated control along typical flight paths. Second, the complex coupling between the aerial robots and the slung load produces not only high system nonlinearity, but also imposes differing modeling and control requirements for the slung load and the aerial robots. The combination of system complexity and the difficulty of coordinated control leads a problem that cannot reliably be solved using the standard techniques for single robot.

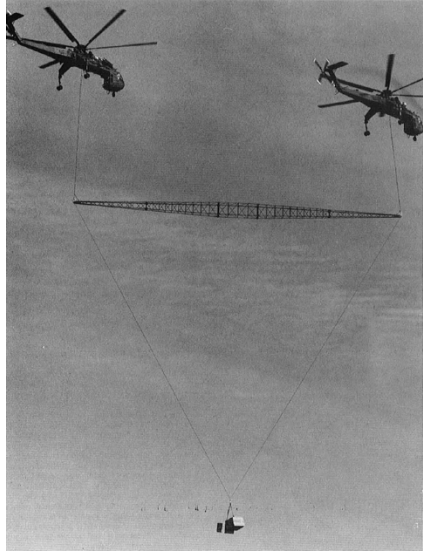


Figure 1.1. Sikorsky Twin-lift demonstration with CH-54B [1]

This dissertation examines the development of a self-contained multilift. It presents a framework for decomposing the complex multi robot problem into sub-problems so that the cooperative transportation can be solved in a hierarchical manner. An estimation strategy for slung load inertial properties is then developed to improve the system model accuracy. Finally, a load distribution based trajectory planning and control approach is developed to achieve power efficiency. Results of hardware tests using a team of four quadrotor robots and payload as the test bed are presented demonstrating the effectiveness of multilift system, slung load inertial property estimation and the load distribution based trajectory planning.

1.1 Motivation

The transport of externally slung loads has been a key capability of rotorcraft for several decades [9, 10]. This may occur because the payload is too large to fit into the helicopter's cargo bay or because the helicopter cannot land at the delivery site because of obstacles or other constraints or if the vehicle is being used as a ground-based crane. In some cases there are significant risks associated with cargo transport (for example, during combat) and payload transport by autonomous aircraft would be helpful in safeguarding human life. For example, the United State Marine Corps has demonstrated autonomous transport of a slung load using an unmanned Kaman K-MAX helicopter in Afghanistan from 2011 to 2014 [11]).

Traditionally, slung load transportation has been accomplished using a single rotorcraft with one or more cables attached to a payload, see Fig. 1.2. However, controllability is limited [12]. Further, only limited maximum payload capacity is achievable. Clearly, there are payloads that can only be carried by very large vehicles such as the Mi-26 helicopter [13], shown in Fig. 1.3. While larger and higher lifting capacity rotorcraft could be developed to solve this problem, it is often inefficient and not economic to develop very large vehicles for these “long tail” payload that are very large but may occur only infrequently. Moreover, Carter [4] showed earlier that as rotorcraft size increases, the gain in relative productivity becomes progressively smaller, Fig. 1.4. Therefore, when the rotorcraft get larger and larger at some point, the payload capacity stop increasing.



Figure 1.2. UH-60L Black Hawk with a CONEX cargo container [2]



Figure 1.3. Mi-26 lifting an air-liner [3]

Another way to increase payload capacity is transporting the slung load using a team of cooperating rotorcraft. This concept of multilift increases the utility of a fleet of smaller rotorcraft (developed to carry more common payloads) by enabling the transport of large, heavy payloads (the “long tail”) via coordinated transport so that the transportation can be much more economic and effective. Such systems have several advantages besides their payload capacity: mission redundancy, robustness and overall task efficiency may also be improved.

This dissertation describes the development of a self-contained transportation system which use multiple autonomous aerial robots to cooperatively transport a single slung

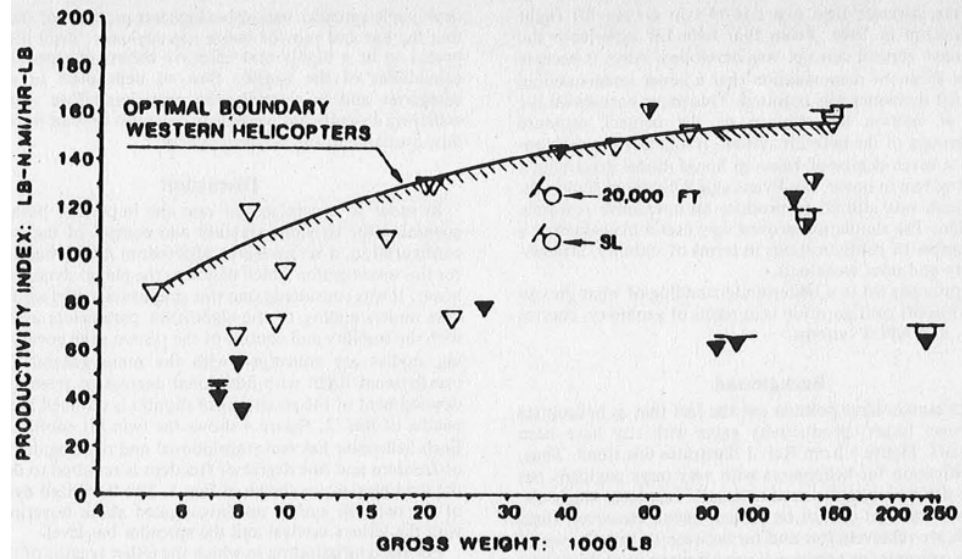


Figure 1.4. Ideal relative productivity at 100 nautical miles [4]

load, see Fig. 1.5. The work described here is especially concerned with developing a transportation team that can adapt to the payload properties and is able to achieve energy efficiency.

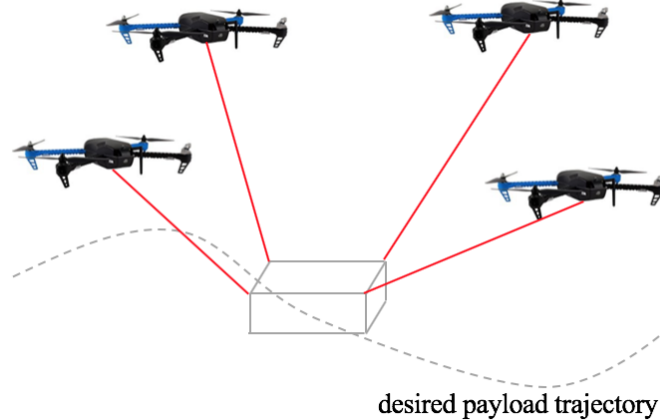


Figure 1.5. Schematic of cooperative slung load transportation by a team of aerial robots

Multilift problem is challenging. As the number of aerial robots increases, system complexity significantly increases, leading to extreme difficulty for coordinating control along typical flight paths. This complexity is inherent to the multilift problem. There is significant coupling between the rotorcraft and the slung load: rotorcraft dynamics determine cable tension and direction, which drives payload motion; payload motion

in turn affects tension of the cables, which results in forces acting upon the rotorcraft. Further, any tracking error in the rotorcraft (either real, such as those caused by external disturbances, or sensed, caused errors in sensors or state estimators) will result in unfavorable cable tension and payload motion. The complex coupling produces not only high system nonlinearity, but also imposes differing modeling and control requirements for the slung load and the aerial robots.

1.2 An Overview for the Cooperative Slung Load Aerial Transportation

In general, cooperative transport of a slung load involves three tasks:

1. The payload and the aerial vehicles must maintain controlled, collision-free flight. This requires a strategy to coordinately control the aerial vehicle and slung load motion and a way to know the payload states so that appropriate action can be taken by the aerial vehicles (*coordinated control*).
2. To have the capability to adapt to the payload properties, the multilift system should have the ability to obtain knowledge of the payload (states and properties). This requires a means to estimate the payload properties (*estimation*).
3. The system must be able to schedule the path to reach the destination. In the context of this work, “efficient transportation” means the system has the ability to optimize the power consumption. This requires a means to optimally plan trajectory for the system while consider the power consumption (*planning*).

These tasks are complicated due to the system complexity imposes by the increased number of aerial vehicles and the payload capacity (mass and dimension of the total sensing payload are constrained).

The task *coordinated control* could be accomplished by flying a formation of aerial vehicles without considering the external slung load. However, the coupling nature of the multilift suggests that unexpected and undesired payload motion will be hazardous to the aerial vehicles [7], which may cause unsafe flight and ultimately failure of the transportation task. Some coordinated control strategy of accounting for the payload dynamics while minimizing the coupling of the payload and aerial vehicles must be provided.

While it is a way of coordination, flying a formation may not be the ideal strategy: without the knowledge of payload properties or states, there is no guarantee that the system is able to feasibly transport the payload, especially in the unknown environment like in scenarios such as search and rescue when slung load properties may be unknown *a priori*. However, payload inertial properties such as mass, center of mass location and moments of inertia are important for achieving good transportation performance since they are directly related to the payload dynamics. When the payload is large or very heavy, specialized equipment may be required to measure mass properties (e.g. large scales) and some properties (such as the vertical position of the center of mass and moments of inertia) may be even more difficult to obtain [14]. There may also be cases where payload inertial properties cannot be determined in advance (for example, when picking up an injured hiker). Hence, it is necessary for the system to have the ability to estimate the payload inertial properties in real time so as to improve model accuracy and incorporate them into the control system to improve transportation performance.

Energy efficient multilift is appealing for the transportation mission that requires longer flight time. However, the power limitation of the individual aerial vehicle limits the global cooperative transportation performance based on the Liebig's barrel theory [15]: if one of the aerial vehicles runs out of energy or loses effectiveness during flight, cooperative transportation will breakdown due to the physical cable attachment and the highly coupled mechanism. In the case of a homogeneous fleet of rotorcraft carrying a payload, it is intuitively appealing to operate the vehicles at near-equal load (e.g. near-equal cable tension). In this way, all vehicles have similar control overhead and all vehicles operate at near-equal energy consumption, which will minimize total power consumption [16, 17]. Hence, if the system has the ability to plan trajectory to the destination while consider energy consumption, it can be called efficient transportation.

A general framework that describes the principle of multilift is introduced in Fig. 1.6. It comprises five parts: a trajectory planner; multiple stabilized aerial vehicles; several cable attachment; a payload, and state/parameter estimator. The trajectory planner uses knowledge of vehicle states and payload condition to compute a safe trajectory to the goal. This could be a trajectory for the payload or a set of feasible trajectories for the aerial vehicles depending on the coordinated control strategy. A stabilized aerial vehicle is one that can maintain a desired flight condition. One or more cables link each vehicle to the payload, affecting the motion of both the payload and the aerial vehicles. Finally, the estimator uses available sensing to compute the data required for payload pose and aerial vehicle control as well as the trajectory planning.

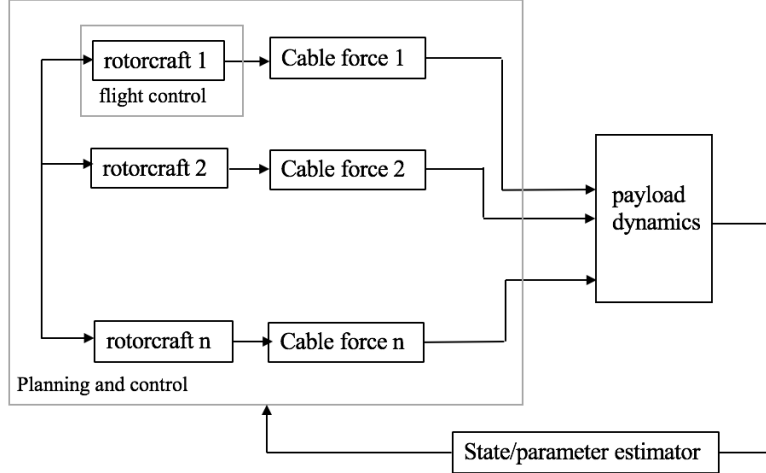


Figure 1.6. A General Framework for Multilift

Significant advances in coordination, sensing, perception, estimation, control and planning must be realized before cooperative aerial transportation of slung load can be successfully performed. Here, the concept of heirarchical control is used to decompose the problem to enable coordination. Sensing and perception include obtaining data about the aerial vehicles, payload, cable forces. Estimation is the process of extracting information about parameters of interest from measurements that are noisy but related to the parameters through complex mathematical models. For multilift that requires little a priori payload information, the parameters of interest include payload properties. Planning involves finding a safe dynamically feasible path to the destination. Energy consumption needs to be considered during planning for efficient aerial transportation. Finally, control involves both stabilizing the payload and the aerial vehicles and following the path computed by the planning algorithm.

The problem of coordinated control, estimation and planning are directly tied to enabling cooperative aerial transportation. Hence, the goals of this dissertation are: (1) to develop a comprehensive coordinated control strategy for the multilift system to minimize the coupling of the payload and aerial vehicles while accounting for the payload dynamics; (2) to develop an estimation approach for payload inertial properties to enable transportation with little a priori payload information; (3) to develop a trajectory planning method that considers system power consumption.

1.3 The Integrated Multilift

1.3.1 A Comprehensive Coordinated Control Strategy

The fundamental framework described is the development of a coordinated control strategy that decomposes the complex multi agent problem into several sub-tasks so that each of them can be solved in a hierarchical manner. This is the core ingredient that determines the solutions of other parts of the system, such as communication, state/parameter estimation, and motion planning. The multilift coordination problem is complex due to the number of active agents and the coupling between the aerial vehicles and payload. The combination of the system complexity and the difficulty of coordinated control leads to the multilift problem that cannot reliably be solved using the standard techniques for a single robot.

There are two main classes of coordinated control strategy for multilift: rotorcraft based (i.e. decentralized) and payload based (i.e. centralized). In the decentralized case, rotorcraft fly along defined trajectories while carrying an external payload. The slung load is then treated as an external force or disturbance that has either a known value or known bounds. Studies are performed usually for the rotorcraft based on the multilift formation and a quasi-static payload [6, 18], which neglects the payload dynamics. In the centralized case, efforts are mainly focused on payload dynamics and control, and rotorcraft perform as actuators driving the payload to the desired states [19–21].

In [19], the author proposed a solution based on the full dynamics of the system. An expression of flat output was given after showing the system is differentially flat. However, physical implementation of closed-loop control is complicated by the need for either measurement or estimation of higher-order derivatives. A direct relation between the motion of quadrotors and motion of payload was derived in [20] by describing the differential kinematics of a generic reconfigurable cable-driven parallel robots (CDPR). The method of using cable tension as independent variables however, leads to extra work computing the dynamics of cable direction during flight.

This dissertation presents an implementation of multilift using a scalable hierarchical approach developed in [22] based on a concept known as object-based task level control [23]. In this approach (here denoted load-leading control), the payload uses knowledge of its own state and its desired state to calculate required cable forces and transmits the corresponding desired states to the individual rotorcraft. The critical component of this implementation is the electronics unit attached to the payload so that the payload

can sense itself and lead the whole fleet. The load-leading implementation has several advantages: it is scalable, allowing the team of rotorcraft to grow as the payload weight increases; it is possible to bring a human into the loop at several levels; the implementation at each level does not have a significant effect on other parts of the control architecture.

1.3.2 Estimation of Slung Load Properties

A critical technology for enabling transportation with little a priori payload information is the design of an estimator which fuses the input of payload (external forces) and the payload response (inertial measurements) to determine the inertial properties, such as mass, center of mass and moments of inertia. Thanks to the load-leading framework, the payload states will be easily to obtain once the inertial property is available since the electronics unit attached on the payload provides states for a reference point.

Estimation of payload inertial property is difficult for several reasons. First, limited system payload capacity greatly restricts the weight and physical dimension of the sensors that can be carried, especially for small aerial vehicles discussed in this dissertation, complicating the problem of obtaining effective information that can directly measure the payload property or the cable force as excitation input. Second, due to the system complexity, adequate and efficient excitation of the system to isolate the interested parameters for accurate estimation is challenging since the six degrees of freedom of the payload may be coupled, and adequate excitation may be limited by available bandwidth of the rotorcraft. Third, additional challenge arise from the conflict between adequate excitation and ensuring that the system does not exceed actuation capabilities.

Earlier research has addressed payload inertial property estimation for a point mass payload, for a single-cable slung load [24] and for a payload rigidly gripped by a quadrotor [25]. However, in the case of multilift, the payload cannot be generally regarded as a point mass (it is after all assumed to be too large and heavy for a single vehicle to carry). The scenario for multilift with rigid payload is less-explored.

This dissertation describes a method to estimate payload inertial properties (mass, center of mass location and moments of inertia) in the context of the multilift system without introducing any cable tension load cells, so as to reduce the total weight and system cost. Hence, an additional challenge arises from the lack of a cable tension sensor. An indirect method on the aerial vehicles side is created to estimate the cable force. This is tackled by analyzing the robot motion given the knowledge of the flight status from the onboard sensors. Then, based on the payload dynamics analysis, sequence of flight tests are designed to excite different inertial properties to be observable using different

payload motion patterns. An array of estimation algorithms, including least-squares method, maximum likelihood and Kalman filter are derived for the estimation of various inertial properties with different dynamical characteristics.

1.3.3 Trajectory Planning and Control Based on Load Distribution

To first order, power required by a near hover low speed rotorcraft varies with $(\text{thrust})^{3/2}$. Balancing cable tension so that load is evenly distributed will therefore reduce total energy consumption of the multilift team [16]. Load distribution based trajectory planning consists of finding a safe, dynamically feasible path while minimizing the variance in cable tension. However, as the number of aerial vehicles increases, the dimension of the planning problem increases significantly, leading to challenge of finding feasible solutions which can achieve near equal load distribution while satisfy the payload and aerial vehicles dynamics. Furthermore, the high nonlinearity induced by the system coupling causes extra difficulty on the tracking control. Additional technique is needed to tackle this challenge.

Earlier research has addressed numeric optimization for cruise performance (i.e. steady level flight) of a four-vehicle multilift system [16] and load distribution control for a dual lift system [17]. Neither of these approaches can be applied directly to the problem of load-distributed trajectory planning for maneuvering flight of a multilift system (i.e. more than two cooperative vehicles).

This dissertation proposes a load distribution based trajectory planning for multilift. It first formulates an optimal control problem that simultaneously pre-plans a multilift slung load trajectory and cable forces while satisfying path and force constraints and minimizing the variance in cable tension. Direct collocation method is used to solve the formulated planning problem. Then, to tackle the tracking control given the planned trajectory, a feedback control law for tracking in the neighbor of the optimal trajectory is developed to equalize the cable tension load distribution during flight.

1.4 Related Work

There has been a significant amount of research relating to the problem of aerial transportation of slung load [26–28]. The previous section presented some references specifically related to the coordinated control strategy, parameter estimation and trajectory planning;

this section presents a more detailed discussion of research in the related fields of multilift configuration, coordinated control, estimation and sensor fusion, trajectory planning and the current state of the art.

1.4.1 Configuration

The overall configuration of the multilift system includes the number of vehicles, cable attachment points, and the use of additional structure to spread cables. Clearly the total lifting capacity of the vehicles must exceed the weight of the payload, cables, and any ancillary equipment (such as spreader bars).

Intuitively, the more vehicles, the more lifting power they can generate. However, adding too many aerial vehicles would increase the complexity of the system significantly since the system is highly coupled between each objects [29]. At the same time, the controllability of the payload might be lost by using too few vehicles. In [12], Murray showed only limited controllability of the payload is achievable with single attachment point. More generally, consider the mechanics of payloads suspended by n cables in the three dimensional world. In the context of cable-actuated platforms, the $n = 6$ case is addressed [30]. Hunt showed when $n = 5$, the line vectors and the gravity wrench axis must belong to the same linear complex, if the cables are in tension and the line vectors are linearly independent [31]. When $n = 4$, the line vector and the gravity wrench must belong to the same linear congruence under the similar assumptions on linear independence and cable tension. When $n = 3$, all the cable vectors and the gravity wrench must lie on the same regulus [32]. The cases of $n = 2$ and $n = 1$ are similar and special: the payload center of mass and the cables must lie on the same vertical plane for equilibrium in all these cases.

In [33], Mittal investigated stability and control characteristic of two twin-lift configuration, one with spreader bar and one without, Fig. 1.7. The results showed both systems can be made to perform well using feedback linearization. The pendant configuration simplifies the required equipment for slung load carriage, but additional power is required to ensure separation of the rotorcraft. The cables must be angled to maintain the safe separation, resulting in some loss of lift capability. The spreader bar configuration overcomes the separation issue. However, the added weight and drag of the spreader bar reduces the system's efficiency and operational flexibility.

Considering the payload controllability and the simplicity of the structure, this dissertation investigates a multilift configuration with four aerial vehicles without spreader bar.

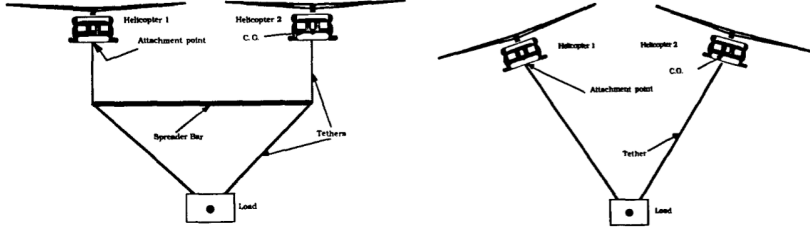


Figure 1.7. Two twin-lift configuration. One with spreader bar (left) and one without (right) [33]

1.4.2 Coordinated Control

A significant amount of prior research examining control techniques for coordinated aerial transport has been published.

In [34], a system consisting of a cable-suspended robot carried by a helicopter is presented. Oh proposed here a two time scale control method, which made it possible to control the helicopter and the cable robot independently. A robust controller was designed to control the motion of the cable robot, where the helicopter motion was unknown. The method provided an effective estimation on the bound of the helicopter motion so that the cable robot can be stabilized.

In [35], Mittal presents a control scheme that synthesized an input-output feedback linearization technique in conjunction with an adaptation algorithm for a twin-lift system. The proposed control scheme does not require any knowledge of the bound of uncertainties of system parameters and can adapt to unknown slung load properties.

Bisgaard designed a controller combining both feedforward and feedback control [29]. It can both prevent helicopter motion-induced swing and actively damp swing. The feedforward controller is based on input shaping and the feedback controller is based on delayed proportional feedback. Both the feedforward and feedback parts of the controller were designed to handle varying cable length and together with an adaptive slung load estimator they form an integrated control system.

However, all of these proposed control algorithms are mainly focusing on single or twin-lift system.

In the context of multilift, Bernard and Kondak proposed a two control loops approach for the load transportation system using small size unmanned helicopters: an outer loop to control the translation of each helicopter in compound, which only needs a simplified model based on interconnected mass points instead of a complex model of the helicopters and load, and an inner loop to control the orientation of helicopters, which can be

simplified by the use of force sensors in the ropes [36].

A novel nonlinear control design was developed in [37]. A concept of an “aerodynamic inverse” method was used, where the controls were calculated to track a desired trajectory using inversion of a simplified aerodynamic model and equations of motion. Simple PID loops were then designed for tracking. Simulation results showed that the aerodynamics inverse controller perform better than the standard linear dynamic inverse controller. Enciu enhanced that work in [37] by redesigning the dynamic inversion controller: cable tension measurements are no longer needed in the control system [7]. The controller also incorporated safe separation and payload/formation relative heading keeping control laws.

The approaches discussed above treated the slung load as external disturbances with known bound or know value or a point mass load, which neglected the payload motion and ended with a passive payload.

In 2014, Li developed a solution for multilift scalable at least up to a “reasonable” number of rotorcraft using a hierarchical approach [22] based on a concept known as Object Based Task Level Control [23]. A human can be brought into the loop at several levels. Implementation details at each level do not have significant effect on other parts of the control architecture if assuming adequate frequency separation is maintained between levels. However, that approach still required knowledge of payload inertial properties, and was not implemented in hardware until the work conducted in this dissertation.

1.4.3 Estimation and Sensor Fusion

Payload state and parameter estimation in the context of aerial transportation has been the subject of significant research.

A milestone work of slung load state estimation can be found in [29]. An adaptive slung load estimator based on an unscented Kalman filter implementation for a general helicopter based cargo transport slung load system was presented. In the work of full state estimation for helicopter slung load estimation [38, 39], two IMUs were used in this work, one mounted on the helicopter and one mounted on the load. Both of them were assumed to be close to the center of mass of their respective bodies. The position of a camera on the helicopter and the position of a marker on the load were also assumed to be known.

To the best of the author’s knowledge, the first work considered payload parameter estimation is Mellinger et al. [25]. A method based on batch and recursive least-squares was designed using commanded control input and acceleration data to estimate the

inertial parameters (mass, center of mass offset and moments of inertia) of a gripped robot+payload system. Significant improvement in tracking performance was shown with the inclusion of the estimated parameters.

Later, Reddi and Boje performed work on system identification for a twin-helicopter slung load transportation [40]. Parameter estimation using nonlinear least-squares method produced parameters that captured the plant dynamics to a high degree of accuracy. A set of parameters were estimated which completely define the plant dynamics for hover flight condition.

A problem of a quadrotor UAV transporting a point mass payload was discussed in [24]. The payload was connected to the quadrotor by a flexible cable modeled as serially-connected rigid links. A fixed gain geometric nonlinear PD controller followed by retrospective cost adaptive control were used to achieve desired performance and also compensate for the payload mass uncertainty.

For the case of an aerial manipulator with a two degree of freedom robotic arm [41], the unknown properties of the payload were estimated using the gradient method based on parametrization of the combined system, including a hexcopter and a robot arm.

None of these estimation methods described above addresses the problem of multilift slung load property estimation.

A more broad application was enabled in [42]. There, an approach to lift unknown objects by teams of aerial robots was proposed based on Bayesian filtering to estimate object parameters. It uses active sensing to select informative interactions coupled with a chance constrained deployment strategy to form feasible lifting configurations. However, the proposed strategy was still under theoretical study.

1.4.4 Load Distribution Based Trajectory Planning

Although significant work has been done in modeling the multilift dynamics [29, 43], developing control strategies [5, 6, 18, 37, 44] to make multilift flight feasible, and creating estimation method for slung load states or parameters [25, 38, 39, 45], comparatively little work has been done in control strategies or planning method that ensure equal load distribution.

In the decentralized multilift, path generation is usually performed for the rotorcraft based on the multilift formation and a quasi-static payload. In the centralized case, the trajectory of rotorcraft can be computed either based on a differentially flat output by specifying the payload trajectory of the load up to the sixth derivative in position and up to the fourth derivative in orientation [19] or based on the payload feedback by



(a)

(b)

Figure 1.8. a): Cable-driven parallel robot from the Max Planck Institute for Biological Cybernetics (MPI) in Tübingen [49]. b): Cable-driven parallel robot constructed at company B&R Automation Brno in partnership with Brno University of Technology [50].

computing the cable force in real time, then command the rotorcraft using the direct kinematic relation between payload and rotorcraft [20, 22].

Enciu [16] performed a numeric optimization for maximizing the cruise performance of a multilift system with four rotorcraft focusing on the control side instead of trajectory planning. Relative distance between the formation rotorcraft, airspeed and cable length were shown to have influence on the optimization results.

In [17] and [46], Berrios et al. investigated the load distribution control concept for a dual lift system to equalize the cable tension between the two cables. A swing angle feedback controller was designed which increased the damping ratio of the external payload's swinging motion. Flight tests showed that a system with load distribution control can reduce the tracking error significantly.

However, neither of these approaches can be applied to the problem of load-distributed trajectory planning for maneuvering flight of a multilift system (i.e. more than two cooperative vehicles).

1.4.5 Cable-Driven Parallel Robot

Cable-driven parallel robot (CDPR) consists of a mobile platform linked to a fixed base through flexible cables actuated by winches [47], Fig. 1.8. Origins of CDPR lie in the late 1980s when the first concepts of cranes, parallel kinematic manipulators, and cable-driven robotic devices were combined in the United States and in Japan [48]. The research on cable robots led to a number of challenging scientific questions in the field of kinematics, statics, dynamics, control, and design. Numbers of contributions in this field was rapidly growing.

The cooperative slung load transportation problem is similar to the problem of

controlling CDPR in three dimensions, where in the former the payload pose is affected by robot positions and in the latter pose control is accomplished by varying the lengths of multiple cable attachments. Recently, studies on reconfigurable cable-driven parallel robots (RCDPRs) becomes popular [51, 52]. RCDPRs are a special category of CDPR in which the actuators (in the slung load transportation problem, vehicles, more in general winches) pulling the cables posses some degrees of freedom to move in space [20]. Thus the work on workspace analysis [53], control [47, 54], and tension distribution [47, 55, 56] of CDPR is directly relevant to the cooperative slung load transportation.

In [53], it has been shown that for a CDPR it is extremely unlikely that more than six cables will ever be under tension simultaneously and this behaviour can be expected to be even more evident using quadrotors. Lemaury the first time introduced a dual-space feedforward control scheme with a joint space controller [47, 54], which can be applied to a redundantly actuated CDPR. An adaptive version of this controller was then proposed to improve the tracking performances. In [47, 55, 56], the cable tension problem was solved, which also mathematically proved that the cable tension can be computed by adding the null space solution to the least-square solution. A direct relation between the motion of the quadrotors and the motion of the payload was derived in [20]. For the first time, the differential kinematics of a generic RCDPR was described.

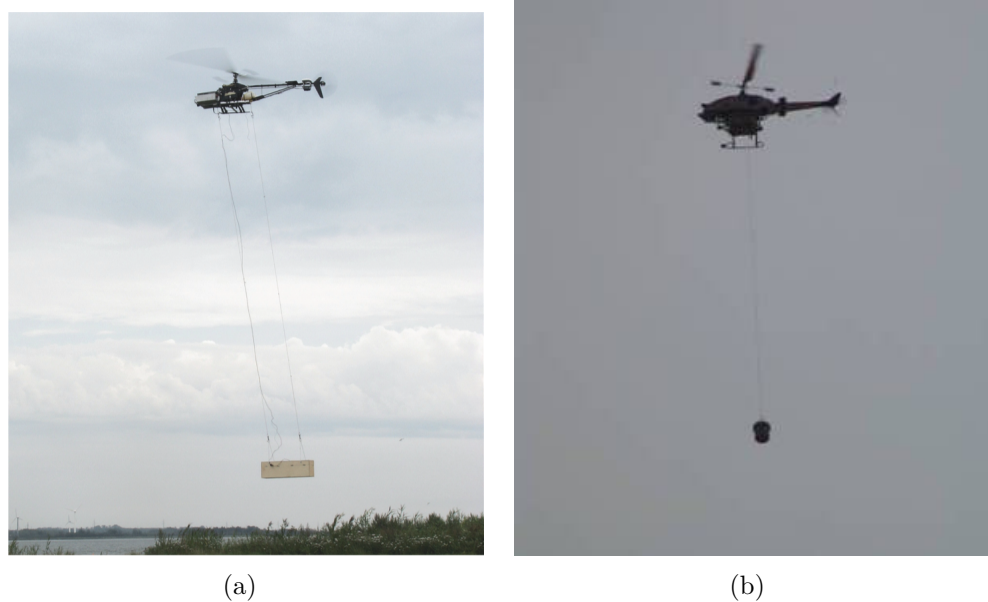
1.4.6 State of the Art

Although the complexity of system dynamics and difficulties in coordinated control limited the flight testing for the coordinated aerial transportation system, there have been several successful hardware demonstrations of twin lift and multilift.

In 1968, Sikorsky was funded for studies of the techniques for two coupled helicopters carrying a slung load. A successful demonstration of twin-lift system using two CH-54B helicopters was performed in 1970 [57].

For small size UAVs, a group at Aalborg University did research on modeling, control and estimation of slung load systems [29]. The work was verified using AAU Bergen Industrial Twin helicopter and the Georgia Tech GTMax. The AAU Bergen helicopter was developed during the course of this research. The Georgia Tech GTMax was used for testing part of the swing damping controller branch and the payload state estimation [39], see Fig. 1.9.

Regarding coupled autonomous slung load transportation using two or more full or small size helicopters, Bernard and Kondak demonstrated the worldwide first load transportation task in real flight experiments using three helicopters in Berlin, 2007 [5, 58],



(a)

(b)

Figure 1.9. a): AAU Bergen Industrial Twin flying with the dual cable demonstration slung load [29]. b): GTmax equipped with slung load [39].

see Fig. 1.10.



Figure 1.10. The worldwide first load transportation task in real flight experiments using three helicopters [5]

In 2010, researchers at UPenn's GRASP lab developed robot configurations that ensure static equilibrium of the payload at a desired pose while respecting constraints on the tension. A team of three quadrotors were used for demonstrations in an indoor

motion capture studio. [18, 25, 44].

Recently, researchers studied the cooperative control for multirotors transporting an unknown suspended point mass load under environmental disturbances [6]. Field flight experiments trials on an outdoor multirotor platform validated the proposed Lyapunov based control algorithm, see Fig. 1.11.



Figure 1.11. Slung load transporation by three multirotors under wind distrubances [6]

1.5 Summary of Contributions

This dissertation describes the development of an integrated multilift system that enables cooperative transport of a slung load by a team of small rotorcraft. The main contributions of this dissertation are summarized below:

- **A Comprehensive Hierarchical Load-leading Control Strategy**

A hierarchical load-leading control strategy for the multilift system is developed. The strategy employs a load-leading approach, where the payload pose control, cable force computation, and aerial vehicle kinematics commanding are achieved in a hierarchical manner. The cable force optimization problem is shown to be non-convex, and the constraints that make the problem convex are introduced and compared with the non-convex problem. A general derivation of desired rotorcraft states based on kinematics of the multilift problem is presented. This general case is then constrained to present results for the special cases of rigid connector, a spring/damper cable, and a rigid rotorcraft formation.

- **Estimator Design for Slung Load Inertial Properties**

A method to estimate payload inertial properties (mass, center of mass location and moments of inertia) in the context of the multilift without any tension load cells is developed. An indirect method on the aerial vehicle side is used to estimate the cable force by analyzing the robot motion given the knowledge of flight status. An analysis of payload motion in response to cable forces provides insight into the excitation and resulting motion required to estimate inertial properties. Three estimation methods: recursive least-squares, maximum likelihood, and Kalman filter are derived and implemented for the estimation of various inertial properties with different dynamics characteristics.

- **Trajectory Planning and Control Approach Based on Load Distribution**

A trajectory planning approach that simultaneously pre-plans the slung load trajectory and cable forces while satisfying path and force constraints and minimizing the variance in cable tension is developed. The load distribution based planning problem is formulated as an optimal control problem which is solved by the direct collocation method. Then, a feedback control law is designed for tracking in the neighbor of the optimal trajectory to equalize the cable tension load distribution during flight.

- **Hardware Testbeds for Both Indoor and Outdoor Performance Verification**

Hardware testbeds are designed for both indoor and outdoor scenarios. Flight demonstrations are presented for all three contributions addressed above. This implementation uses small single board computers carried onboard the payload and the rotorcraft to host all algorithms. Flight demonstrations conducted in an indoor motion capture studio are presented to show trajectory following, human-in-the-loop control of the payload, rejection of an impulse disturbance, and formation changes. An outdoor flight demonstration using RTK GPS shows payload control and trajectory following in the presence of light winds.

The estimation strategy has been validated in an indoor motion capture studio. The inertial properties, including payload mass, center of mass and moments of inertia are well estimated. Furthermore, trajectory tracking tests comparing uncompensated (i.e. nominal) center of mass and compensated (estimated) center of mass shows the benefit of system performance. Incorporating the estimated payload parameters into the compensated controller significantly improves the tracking performance for the aerial robots.

Indoor flight tests also shows that the load distribution based approach has a superior performance on the energy consumption over the conventional unequalized approach. The aerial robots ended up with less variance in cable tension, less total power and near-equal energy consumption.

1.6 Reader's Guide

The remainder of this dissertation is organized as follows:

Chapter 2: The Multilift Problem discusses the architecture of the hierarchical load-leading approach. It then develops the dynamics model for both the payload and the aerial vehicles.

Chapter 3: A Hierarchical Strategy Using Load-leading Control develops the load-leading control approaches at each level. The cable force optimization problem and convexity analysis are presented. It then derives the desired rotorcraft states via kinematics analysis. Next, it designs the controllers for both payload and rotorcraft trajectory tracking. Finally, it describes the hardware platform and presents the flight demonstrations.

Chapter 4: Slung Load Inertial Property Estimation analyses the sensing requirements for payload inertial property estimation. It then discusses the method for cable force estimation. Next, estimator design based on different approaches is shown. Subsequently, it presents the experimental results validating the proposed estimation strategy. Finally, controller compensation tests for the compensated and uncompensated cases are conducted and compared.

Chapter 5: Trajectory Planning and Control Based on Load Distribution formulates the load distribution based planning and tracking problem into a optimal control manner. It then analyses the problem and proposes methodology including the direct collocation and the neighboring feedback control for planning and tracking. Next, simulation results that includes wind gust are presented. Finally, it provides the indoor hardware flight tests results to validate the proposed approach.

Chapter 6: Conclusion summarizes the research results and discusses the potential areas for future work.

Chapter 2 |

The Multilift Problem

This chapter defines the multilift problem introduced in the previous chapter. It has three purposes: (a) presents a detailed system description and overview of the hierarchical load-leading control architecture and defines the sub-level problems for multilift; (b) develops equations for major components of the system.; (c) lists the assumptions considered in this dissertation. The sub-level problems are then analyzed and solved in Chapter 3, 4 and 5.

There are three major parts in the hierarchical load-leading control strategy: trajectory generation, load-leading control, state/parameter estimation. Load-leading control consists of another three parts: payload trajectory following, cable force computation, and rotorcraft control. All of these sub-level problems need to be solved before a successful smart and efficient multilift can be conducted.

The major physical components (payload, rotorcraft, and cables) are ultimately connected via the equations describing system dynamics and the cable forces that are required for the payload to follow its desired trajectory. The cable force computation algorithm is thus arguably at the heart of successful multilift.

Section 2.1 presents the system description and the hierarchical load-leading architecture. Section 2.2 develops the dynamics for both payload and rotorcraft. Section 2.3 computes the total cable force acting on the payload. Section 2.4 lists all the assumptions considered in this dissertation. Finally, Section 2.5 provides a summary.

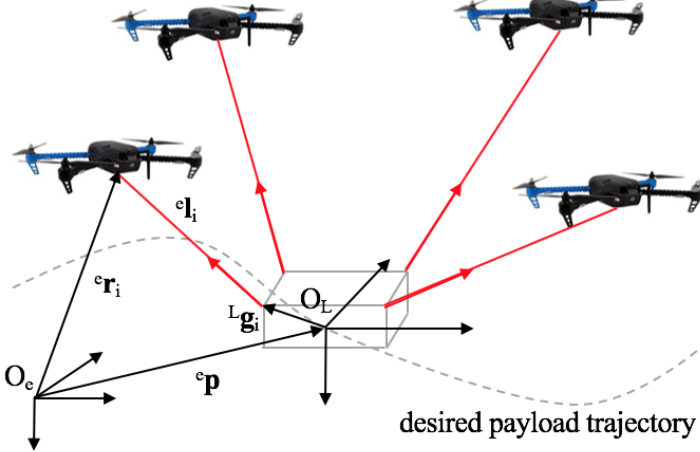


Figure 2.1. Schematic of the coordinated transportation problem

2.1 System Description and Hierarchical Load-leading Control Architecture

As discussed in Chapter 1, the scenario considered here is transporting a slung load by a team of autonomous aerial robots. This dissertation focuses on a team of four aerial robots considering about the payload controllability and system simplicity. However, the methods described here are scalable to larger numbers of vehicles.

Referring to Fig. 2.1, the payload is located at ${}^e\mathbf{p}$ in a world fixed north-east-down frame $\mathcal{F}_e = \{\mathcal{O}_e, \mathcal{X}_e, \mathcal{Y}_e, \mathcal{Z}_e\}$. The pose of the payload is described by the vector $\mathbf{x}_L = [{}^e\mathbf{p}^T, \boldsymbol{\Omega}^T]^T \in SE(3)$ that represents position ${}^e\mathbf{p} \in \mathbb{R}^3$ and orientation $\boldsymbol{\Omega} \in SO(3)$ of a payload in body frame $\mathcal{F}_L = \{\mathcal{O}_L, \mathcal{X}_L, \mathcal{Y}_L, \mathcal{Z}_L\}$. Notice that the frame \mathcal{F}_L may not be centered at the payload center of mass, especially for the unknown payload. It could be the payload geometry center, or any other convenient reference point on the payload. The rotation matrix from \mathcal{F}_e to \mathcal{F}_L ${}^e\mathbf{R}_L$ is a function of 3-2-1 euler angles $\boldsymbol{\Omega} = [\phi, \theta, \psi]^T$. Denote the velocity and acceleration of the payload as $\dot{\mathbf{x}} = [{}^e\dot{\mathbf{p}}^T, \boldsymbol{\omega}^T]^T$ and $\ddot{\mathbf{x}} = [{}^e\ddot{\mathbf{p}}^T, \dot{\boldsymbol{\omega}}^T]^T$, where $\boldsymbol{\omega}$ and $\dot{\boldsymbol{\omega}}$ are the angular velocity and acceleration of the payload. Note that $\boldsymbol{\omega} \neq \dot{\boldsymbol{\Omega}}$. A team of m rotorcraft located at ${}^e\mathbf{r}_i$, $i = 1, \dots, m$ in the frame \mathcal{F}_e with attitude $\boldsymbol{\Omega}_i = [\phi_i, \theta_i, \psi_i]^T$ are connected to the payload with individual cables attached to the payload at connection points ${}^L\mathbf{g}_i$ in frame \mathcal{F}_L .

This dissertation implements a scalable hierarchical approach [22] (here denoted load-leading control) based on a concept known as object-based task level control [23]. It

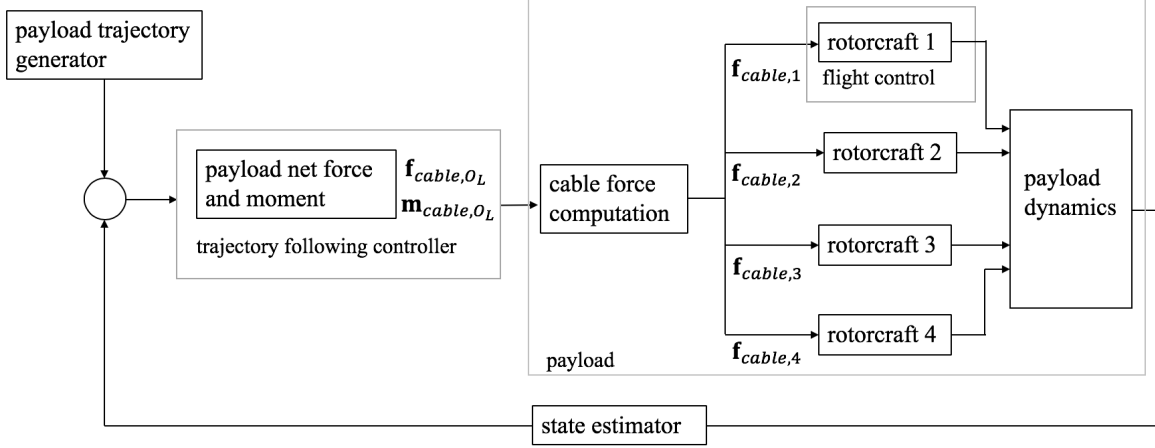


Figure 2.2. Load-leading multilift system block diagram

decomposes the complex multilift problem into several sub-problems in a hierarchical manner. Importantly, each level does not have a significant effect on other parts of the control architecture. The critical idea is that the payload is the team leader and uses knowledge of its own state and its desired state to calculate required cable forces and transmits the corresponding desired states to the individual rotorcraft.

A block diagram of this four-vehicle team is shown in Fig. 2.2. Based on the hierarchical approach, the multilift problem consists of three major parts: trajectory generation, load-leading control, state/parameter estimation. The load-leading control includes three parts: payload trajectory following, cable force computation, and rotorcraft control.

The “Trajectory Generator” block provides the desired trajectory of the payload. This can be pre-computed or come from a human operator. Note that this trajectory needs to be dynamically and kinematically feasible: each rotorcraft is assumed to be able to provide required thrust to generate desired cable force; the flight controller equipped with each rotorcraft is assumed to be able to maintain desired rotorcraft states. For energy efficient flight, the generated trajectory considers the load distribution among cables while satisfying path and force constraints.

Upon receiving the desired payload states \mathbf{x}_{des} , the trajectory following controller computes the desired net force and moment acting on the payload to “steer” the payload from its current state to the desired states. A controller needs to be designed for payload trajectory following so that the payload pose can be controlled.

Individual cable forces for each tether $\mathbf{f}_{cable,i}$ are computed based on the net force and moment and the geometry of the cable attachments on the payload. This step is critical

since it affects the operation safety of the rotorcraft and the controllability and stability of the payload [59]. When $m > 3$ the system is underdetermined. A means to compute the cable force to satisfy the net force and moment on the payload while considering other constraints such as vehicle separation and controllability is needed.

Given the desired cable force vectors, the desired state of each cable attachment on the rotorcraft can be computed based on these cable force vectors and physical properties of the cables. Then, the desired rotorcraft states will be commanded to the flight controller onboard each rotorcraft to ensure that the required cable tension and direction can be maintained. Hence, a way to compute desired rotorcraft states based on the desired cable force vectors and a reliable rotorcraft control mechanism to maintain stable flight are required.

All rotorcraft and the payload use a state estimator incorporating sensor data from navigation system such as GPS/INS or (in the case of indoor flight) Vicon/INS to provide state data that is fed back to each respective controller. For the load-leading strategy, the payload states are directly tied to the inertial property. An estimation approach is needed for obtaining payload inertial parameters.

The multilift major components: payload, rotorcraft, cables are tied to all levels including coordinated control, estimation and trajectory planning. The dynamic models of payload and rotorcraft are developed in Section 2.2. The total cable force acting on the payload is derived in Section 2.3.

2.2 Dynamics

The dynamics of both the payload and the rotorcraft will be introduced in this section.

2.2.1 Payload Dynamics

Several physical parameters need to be known before deriving the payload dynamics. The total mass m_L , the inertia matrix ${}^L\mathbf{J}_{cm}$ in \mathcal{F}_L (denote the diagonal elements of \mathbf{J}_{cm} as J_{xx}, J_{yy}, J_{zz}), and the payload center of mass position relative to \mathcal{O}_L , ${}^e\mathbf{r}_L = \begin{bmatrix} r_x & r_y & r_z \end{bmatrix}^T$ all have effect on the payload dynamics. The dynamics of the multilift slung load can be described by the well known Newton-Euler or Euler-Lagrangian approaches. Hence, the payload dynamics are

$$\mathbf{M}_L \ddot{\mathbf{x}} + \mathbf{C}_L \dot{\mathbf{x}} = {}^e\mathbf{W}_t \quad (2.1)$$

where ${}^e\mathbf{W}_t$ is the wrench (force and moment) exerted on the payload about \mathcal{O}_L . Notice that ${}^e\mathbf{W}_t$ includes the gravity wrench ${}^e\mathbf{W}_g$ with $g = 9.81\text{ms}^{-2}$ and the wrench generated by cable force ${}^e\mathbf{W}_f$ (Aerodynamic drag forces is neglected for the low speed or the steady situation). \mathbf{M}_L , $\mathbf{C}_L\dot{\mathbf{x}}$ and ${}^e\mathbf{W}_g$ are defined as

$$\mathbf{M}_L = \begin{bmatrix} m_L \mathbf{I}_3 & -m_L [{}^e\mathbf{r}_L]^\times \\ m_L [{}^e\mathbf{r}_L]^\times & {}^e\mathbf{J}_{cm} - m_L [{}^e\mathbf{r}_L]^\times [{}^e\mathbf{r}_L]^\times \end{bmatrix} \quad (2.2)$$

$$\mathbf{C}_L\dot{\mathbf{x}} = \begin{bmatrix} m_L [\boldsymbol{\omega}]^\times [\boldsymbol{\omega}]^\times {}^e\mathbf{r}_L \\ \boldsymbol{\omega} \times ({}^e\mathbf{J}_{cm} - m_L [{}^e\mathbf{r}_L]^\times [{}^e\mathbf{r}_L]^\times) \boldsymbol{\omega} \end{bmatrix} \quad (2.3)$$

$${}^e\mathbf{W}_g = \begin{bmatrix} 0 & 0 & m_L g & m_L r_y g & -m_L r_x g & 0 \end{bmatrix}^T \quad (2.4)$$

$${}^e\mathbf{J}_{cm} = {}^e\mathbf{R}_L {}^L\mathbf{J}_{cm} {}^L\mathbf{R}_e \quad (2.5)$$

where \mathbf{I}_3 is the 3×3 identity matrix. For the scenario when the payload center of mass location is known, the frame \mathcal{F}_L can be placed at the payload center of mass, which means ${}^e\mathbf{r}_L = \mathbf{0}$.

2.2.2 Rotorcraft Dynamics

For each rotorcraft, consider a front-right-down body frame $\mathcal{F}_{V_i} = \{\mathcal{O}_{V_i}, \mathcal{X}_{V_i}, \mathcal{Y}_{V_i}, \mathcal{Z}_{V_i}\}$ attached to the center of mass of the vehicle. By applying Newton's law, the dynamics of the i^{th} rotorcraft depending on its mass m_i and the inertia matrix ${}^{V_i}\mathbf{J}_i$ in frame \mathcal{F}_{V_i} can be expressed as

$$m_i {}^e\ddot{\mathbf{r}}_i = -T_i {}^e\mathbf{R}_{V_i} \mathcal{Z}_{V_i} + m_i g \mathcal{Z}_e + {}^e\mathbf{f}_i + {}^e\mathbf{f}_{Aero,i} \quad (2.6)$$

$${}^{V_i}\mathbf{J}_i \boldsymbol{\omega}_i = {}^{V_i}\tau_i - \boldsymbol{\omega}_i \times {}^{V_i}\mathbf{J}_i \boldsymbol{\omega}_i \quad (2.7)$$

where ${}^e\mathbf{R}_{V_i}$ is the rotation matrix from \mathcal{F}_{V_i} to \mathcal{F}_e . $\boldsymbol{\omega}_i$ is the angular velocity of the rotorcraft in \mathcal{F}_{V_i} . $T_i \in \mathbb{R}$ is the generated total thrust input with respect to \mathcal{F}_{V_i} . $\boldsymbol{\tau}_i \in \mathbb{R}^3$ is the total torque input generated by the rotorcraft. \mathbf{f}_i is the cable force connecting the i^{th} rotorcraft to the payload. $\mathbf{f}_{Aero,i}$ is the external aerodynamic force acting on the rotorcraft, which becomes significant when airspeed is high (due to high flight speed or high wind speed). Additional sensors such as a pitot tube may then be needed to obtain aerodynamic forces. During low speed/low wind flight (e.g. indoor flight), $\mathbf{f}_{Aero,i}$ can be

neglected. Also, $\boldsymbol{\omega}_i = \mathbf{C}_i \dot{\boldsymbol{\Omega}}_i$ where

$$\mathbf{C}_i = \begin{bmatrix} 1 & 0 & -\sin \theta_i \\ 0 & \cos \phi_i & \cos \theta_i \sin \phi_i \\ 0 & -\sin \phi_i & \cos \theta_i \cos \phi_i \end{bmatrix} \quad (2.8)$$

2.3 Cable Force

The i^{th} cable is attached to the payload at point ${}^L\mathbf{g}_i$. The wrench induced on the \mathcal{O}_L of the payload by this cable is:

$${}^L\mathbf{W}_f = \begin{bmatrix} {}^L\mathbf{f}_{cable,\mathcal{O}_L,i} \\ {}^L\mathbf{m}_{cable,\mathcal{O}_L,i} \end{bmatrix} = \begin{bmatrix} {}^L\mathbf{f}_{cable,i} \\ {}^L\mathbf{g}_i \times {}^L\mathbf{f}_{cable,i} \end{bmatrix} \quad (2.9)$$

$$= \begin{bmatrix} \mathbf{I}_3 \\ \mathbf{S}_i \end{bmatrix} {}^L\mathbf{f}_{cable,i} = \mathbf{G}_i {}^L\mathbf{f}_{cable,i} \quad (2.10)$$

where \mathbf{S}_i is the skew matrix of ${}^L\mathbf{g}_i$. Define \mathbf{G}_i as the geometry matrix for the i^{th} cable. The total force and moment acting at the payload \mathcal{O}_L will be the summation from each tether:

$$\begin{bmatrix} {}^L\mathbf{f}_{cable,\mathcal{O}_L} \\ {}^L\mathbf{m}_{cable,\mathcal{O}_L} \end{bmatrix} = \begin{bmatrix} \mathbf{G}_1 & \mathbf{G}_2 & \mathbf{G}_3 & \mathbf{G}_4 \end{bmatrix} \begin{bmatrix} {}^L\mathbf{f}_{cable,1} \\ {}^L\mathbf{f}_{cable,2} \\ {}^L\mathbf{f}_{cable,3} \\ {}^L\mathbf{f}_{cable,4} \end{bmatrix} \quad (2.11)$$

$$= \mathbf{G}_{6 \times 12} {}^L\mathbf{f}_{cable_{12 \times 1}} \quad (2.12)$$

Hence, for a given desired wrench (which depends on trajectory following control, see Chapter 3) acting upon payload \mathcal{O}_L with known geometry, there are 12 unknowns and 6 equations in (2.11) since both the payload and rotorcraft can move in the space. The system described in (2.11) is therefore underdetermined. There are infinite number of solutions for the set of cable forces.

In fact, a six degree of freedom payload will require at least three cables to provide control over all degrees of freedom. Although two cables will provide six components of cable force and thus generate a square matrix \mathbf{G} , a unique solution for ${}^L\mathbf{f}_{cable}$ does not exist since \mathbf{G} is not full rank. Physically, this condition will leave the payload free to rotate about the axis connecting the two attachment points. With more than three

cables as the system described in (2.11), the system is underdetermined, giving an infinite number of solutions. This property can provide some redundancy for the system so that the cable forces can be computed to satisfy the desired net force and moment of the payload while simultaneously satisfying other constraints. A cable force computation method will be discussed in Chapter 3.

2.4 Assumptions

Major assumptions considered in this dissertation are listed as follows:

- **Flat Earth**

Payload translational motion is assumed to be small compared with the radius of the Earth. The inertial reference frame is therefore assumed to be attached to the Earth and is assumed to be locally flat.

- **Massless Cables**

The cables are assumed to be massless when deriving the cable model and estimating the cable forces.

- **Cable Attachment on Rotorcraft**

For the small rotorcraft scenario discussed in this dissertation, the cables are assumed to be attached at the center of mass on the rotorcraft when computing the desired rotorcraft states and performing all the flight experiments

- **Attachment Joints**

Cable attachment points on both payload and the rotorcraft are assumed to be frictionless joints.

- **Aerodynamics Drag Forces**

For low speed or steady situation, aerodynamics drag forces acting on the payload, cables and rotorcraft is neglected.

2.5 Summary: The Multilift Problem

To operate the cooperative transportation of slung load by a team of autonomous aerial robots, the aerial vehicles and payload must maintain coordinated fight and navigate

to the destination. This requires a well designed coordinated control strategy, a way to obtain payload property for enabling transportation with little a priori payload information and an efficient trajectory planning approach for saving energy.

The complex and highly coupled multilift problem can be decomposed into several sub-level problems. Each level does not have a significant effect on other parts of the control architecture. The critical idea is that the payload is the team leader and uses knowledge of its own state and its desired state to lead the whole transportation team. All of the sub-level problems: trajectory planning, load-leading control and estimation must be solved before a successful multilift can be conducted. The load-leading control as the core level consists of another three parts: payload trajectory following, cable force computation, and rotorcraft control.

The payload, rotorcraft and cables are the major components and they are tied to all system levels. The equations describing the dynamics of payload and rotorcraft are important for controller design, estimation and planning.

The equation describing the total cable forces acting on the payload is shown to be underdetermined, giving an infinite number of solutions. This means that the cable forces can be computed to satisfy the desired net force and moment of the payload while simultaneously satisfying other constraints. A solution for cable force optimization is given in Chapter 3. All of the sub-level problems will be analyzed and solved in the following Chapter 3, 4 and 5.

Chapter 3 |

A Hierarchical Strategy Using Load-leading Control

This chapter describes in detail the hierarchical load-leading control for multilift problem. This is the core ingredient that determines the solutions of other parts of the system, such as communication, state/parameter estimation, and motion planning. Three parts make up the load-leading control strategy: payload trajectory following, cable force computation and rotorcraft control. It is complicated by three factors: the underdetermined cable force relation gives an infinite number of solutions; the nonlinear coupling between slung load and the rotorcraft imposes difficulty on controller design to stabilize the system; the lack of defined hardware solution to enable load-leading (Typical multilift solution usually uses a passive payload). This chapter presents: (a) a cable force analysis and computation method; (b) a kinematics analysis for computing desired rotorcraft states; (c) control algorithms for both payload trajectory tracking and rotorcraft control; (d) a platform design for hardware implementation; (e) indoor and outdoor flight demonstration.

To focus on developing the hierarchical load-leading control strategy, the payload studied in this chapter has known properties with fixed mass, center of mass and moments of inertia. Therefore, the payload body frame \mathcal{O}_L can be placed at center of mass with ${}^e\mathbf{r}_L = \mathbf{0}$ in (2.1). The trajectory designed for testing is generated by polynomials between given waypoints.

In Section 3.1, the cable force computation uses a least-norm solution to satisfy the net force and moment acting on the payload and uses the null space solution to satisfy constraints on the system such as vehicle separation and controllability. The cable force optimization problem is shown to be non-convex, and the constraints that make the problem convex are introduced and compared with the non-convex problem.

A general derivation of desired rotorcraft states based on kinematics of the multilift

problem is presented in Section 3.2. This general case is then constrained to present results for the special cases of rigid connector, a spring/damper cable, and a rigid rotorcraft formation.

Controller design for both payload trajectory tracking and rotorcraft control are presented using the standard PID control approach. However, the dynamics time scale are different for the payload and rotorcraft, additional analysis for stability is needed. This is addressed in Section 3.3.

Section 3.4 describes the design of the test platform for hardware implementation to achieve load-leading, including the payload, rotorcraft, ground side, external sensor and a Python state machine. This implementation uses small single board computers carried onboard the payload and the rotorcraft to host all algorithms presented in this dissertation.

In Section 3.5, flight demonstrations conducted in an indoor motion capture studio are presented to show trajectory following, human-in-the-loop control of the payload, rejection of an impulse disturbance, and formation changes. An outdoor flight demonstration shows payload control and trajectory following in the presence of light (7 km/h) winds.

Section 3.6 summarises this chapter. For the general scenario when payload is unknown, the inertial property estimation is discussed in Chapter 4. Trajectory planning based on load distribution is presented in Chapter 5 to achieve energy efficiency.

3.1 Cable Force Analysis

Cable forces directly bridge the payload and rotorcraft. They are critical since operation safety of the rotorcraft and the controllability and stability of the payload are affected by the cable forces [59]. Computing a group of feasible cable forces is challenging since the relation is underdetermined with an infinite number of solutions. Formulating the cable force computation as an optimization problem is a typical approach [47, 56]. However, the convexity needs to be addressed for real-time implementation.

3.1.1 Cable Force Computation

As stated in Chapter 2, (2.11) is underdetermined, giving an infinite number of solutions. Given a particular cable attachment geometry matrix \mathbf{G} , the least-norm solution ${}^L\mathbf{f}_{cable}^{LN}$

minimizes the total cable force and can be computed in closed form:

$${}^L\mathbf{f}_{cable}^{LN} = \mathbf{G}^T(\mathbf{G}\mathbf{G}^T)^{-1} \begin{bmatrix} {}^L\mathbf{f}_{cable,\mathcal{O}_L} \\ {}^L\mathbf{m}_{cable,\mathcal{O}_L} \end{bmatrix} \quad (3.1)$$

\mathbf{G} is constant in the payload body frame so that $\mathbf{G}^T(\mathbf{G}\mathbf{G}^T)^{-1}$ can be pre-computed.

The least-norm solution ensures that the desired net force and moment acting on the payload reference point can be satisfied. Cable force combinations that exist in the null space of \mathbf{G} are used to satisfy other constraints and considerations, such as rotorcraft separation and controllability of the system. The net cable force will thus be:

$${}^L\mathbf{f}_{cable} = {}^L\mathbf{f}_{cable}^{LN} + {}^L\mathbf{f}_{cable}^{null} \quad (3.2)$$

where

$${}^L\mathbf{f}_{cable}^{null} = \tilde{\mathbf{G}}\mathbf{c} \quad (3.3)$$

Here $\mathbf{G} {}^L\mathbf{f}_{cable}^{null} = \mathbf{0}$. $\tilde{\mathbf{G}}$ is the matrix whose columns are the basis of the null space of \mathbf{G} . \mathbf{c} is the coefficient of $\tilde{\mathbf{G}}$, which will be solved by the following optimization problem.

At each time step, an optimization problem is being solved:

$$\begin{aligned} \min_{\mathbf{c}} \quad & \| {}^L\mathbf{f}_{cable} = {}^L\mathbf{f}_{cable}^{LN} + \tilde{\mathbf{G}}\mathbf{c} \| \\ \text{subject to} \quad & g({}^L\mathbf{f}_{cable}) \leq \mathbf{0} \\ & \| {}^L\mathbf{f}_{cable,i} \| \leq \| \mathbf{f} \|_{max} \\ & h({}^L\mathbf{f}_{cable}) = \mathbf{0} \end{aligned} \quad (3.4)$$

where the inequality constraints $g({}^L\mathbf{f}_{cable}) \leq \mathbf{0}$ ensure that the cable force vectors remain in the same quadrant within a fixed sector region $\Delta\beta$ (see Fig. 3.1) in \mathcal{F}_L (so that cables will not cross and ensure vehicle separation); the equality constrains $h({}^L\mathbf{f}_{cable}) = \mathbf{0}$ are to maintain the cone angle α_i between each cable and the vertical axis of \mathcal{F}_L (to maintain system controllability and also ensure vehicle separation). The desired cone angle can be determined before flight or in real time during flight. It also depends on parameters such as vehicle separation or payload controllability [59].

Here, the Sequential Least Squares Programming implemented by Python interface function “fmin_slsqp” is used to solve the optimization problem. The optimized ${}^L\mathbf{f}_{cable}$ will be transformed to \mathcal{F}_e for the convenience of kinematics analysis for desired rotorcraft

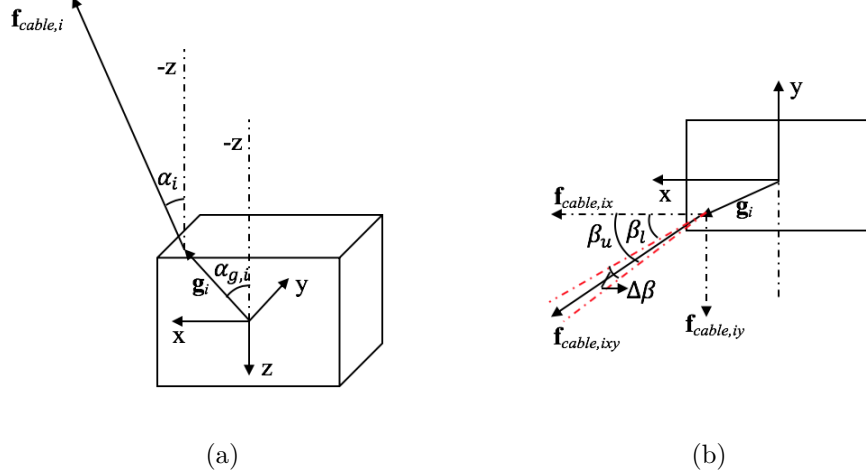


Figure 3.1. Definition of cable cone angle and sector region

states (Section 3.2).

3.1.2 Convexity Analysis

Convex optimization problems are fast to solve and result in globally-optimal solutions [60]. Here, the optimization problem of (3.4) will be analyzed for convexity and modified to make it convex. First, write the constraints of (3.4) explicitly. Denote \mathbf{e}_i as a 1×12 row vector with the i^{th} component as 1 and all other components as 0, and denote $\mathbf{1}_j$ as a 3×12 matrix with the j^{th} 3×3 blocks as identity matrices (there are four 3×3 identity matrices in total).

Therefore the inequality constraints $g({}^L\mathbf{f}_{\text{cable}}) \leq 0$ will be

$$\mathbf{e}_1 {}^L\mathbf{f}_{\text{cable}} > 0, \quad \mathbf{e}_2 {}^L\mathbf{f}_{\text{cable}} < 0 \quad (3.5)$$

$$\mathbf{e}_3 {}^L\mathbf{f}_{\text{cable}} < 0, \quad \| \mathbf{1}_1 {}^L\mathbf{f}_{\text{cable}} \| \leq \| \mathbf{f} \|_{\max}$$

$$\mathbf{e}_4 {}^L\mathbf{f}_{\text{cable}} > 0, \quad \mathbf{e}_5 {}^L\mathbf{f}_{\text{cable}} > 0$$

$$\mathbf{e}_6 {}^L\mathbf{f}_{\text{cable}} < 0, \quad \| \mathbf{1}_2 {}^L\mathbf{f}_{\text{cable}} \| \leq \| \mathbf{f} \|_{\max}$$

$$\mathbf{e}_7 {}^L\mathbf{f}_{\text{cable}} < 0, \quad \mathbf{e}_8 {}^L\mathbf{f}_{\text{cable}} > 0$$

$$\mathbf{e}_9 {}^L\mathbf{f}_{\text{cable}} < 0, \quad \| \mathbf{1}_3 {}^L\mathbf{f}_{\text{cable}} \| \leq \| \mathbf{f} \|_{\max}$$

$$\mathbf{e}_{10} {}^L\mathbf{f}_{\text{cable}} < 0, \quad \mathbf{e}_{11} {}^L\mathbf{f}_{\text{cable}} < 0$$

$$\mathbf{e}_{12} {}^L\mathbf{f}_{\text{cable}} < 0, \quad \| \mathbf{1}_4 {}^L\mathbf{f}_{\text{cable}} \| \leq \| \mathbf{f} \|_{\max}$$

$$-\mathbf{e}_2 {}^L\mathbf{f}_{\text{cable}} - \gamma_1 \mathbf{e}_1 {}^L\mathbf{f}_{\text{cable}} > 0, \quad \mathbf{e}_2 {}^L\mathbf{f}_{\text{cable}} + \gamma_2 \mathbf{e}_1 {}^L\mathbf{f}_{\text{cable}} > 0 \quad (3.6)$$

$$\mathbf{e}_5 {}^L\mathbf{f}_{\text{cable}} - \gamma_1 \mathbf{e}_4 {}^L\mathbf{f}_{\text{cable}} > 0, \quad -\mathbf{e}_5 {}^L\mathbf{f}_{\text{cable}} + \gamma_2 \mathbf{e}_4 {}^L\mathbf{f}_{\text{cable}} > 0$$

$$\begin{aligned} \mathbf{e}_8 {}^L \mathbf{f}_{cable} + \gamma_1 \mathbf{e}_7 {}^L \mathbf{f}_{cable} &> 0, & -\mathbf{e}_8 {}^L \mathbf{f}_{cable} - \gamma_2 \mathbf{e}_7 {}^L \mathbf{f}_{cable} &> 0 \\ -\mathbf{e}_{11} {}^L \mathbf{f}_{cable} + \gamma_1 \mathbf{e}_{10} {}^L \mathbf{f}_{cable} &> 0, & \mathbf{e}_{11} {}^L \mathbf{f}_{cable} - \gamma_2 \mathbf{e}_{10} {}^L \mathbf{f}_{cable} &> 0 \end{aligned}$$

where $\gamma_1 = \tan(\beta - \frac{\Delta\beta}{2})$, $\gamma_2 = \tan(\beta + \frac{\Delta\beta}{2})$, and β is the sphere angle of the cable in \mathcal{F}_L , see Fig. 3.1. Notice that the constraints group (3.5) ensures that the cable force vectors remain in the same quadrant of \mathcal{F}_L with cable tension less than the sustainable maximum. The constraints in group (3.6) limit the cable force within a fixed sector region $\Delta\beta$ in \mathcal{F}_L .

The equality constraints are to maintain the desired cone angle:

$$\begin{aligned} \frac{\mathbf{e}_3 {}^L \mathbf{f}_{cable}}{\|\mathbf{1}_1 {}^L \mathbf{f}_{cable}\|} &= C \\ \frac{\mathbf{e}_6 {}^L \mathbf{f}_{cable}}{\|\mathbf{1}_2 {}^L \mathbf{f}_{cable}\|} &= C \\ \frac{\mathbf{e}_9 {}^L \mathbf{f}_{cable}}{\|\mathbf{1}_3 {}^L \mathbf{f}_{cable}\|} &= C \\ \frac{\mathbf{e}_{12} {}^L \mathbf{f}_{cable}}{\|\mathbf{1}_4 {}^L \mathbf{f}_{cable}\|} &= C \end{aligned} \tag{3.7}$$

The objective function of (3.4) is quadratic. All the inequality constraints are either affine or quadratic (i.e. convex). However, the equality constraints are not affine: they are in second order cone form. Therefore the optimization problem (3.4) is not convex.

Regarding the geometrical interpretation of the cable force constraints, the equality and inequality constraints for a single rotorcraft are illustrated in Fig. 3.2. This formulation only allows the rotorcraft to move along the arc/edge of a cone, which is clearly non-convex.

The problem can be made convex by changing the equality constraints to inequality constraints (e.g. $\frac{\mathbf{e}_3 {}^L \mathbf{f}_{cable}}{\|\mathbf{1}_1 {}^L \mathbf{f}_{cable}\|} \geq C$), as illustrated in Fig. 3.3. However, this modification removes the ability to guarantee vehicle separation for small payloads, which cannot be accepted. Note that for some very large payloads vehicle separation may still be guaranteed with this inequality constraint.

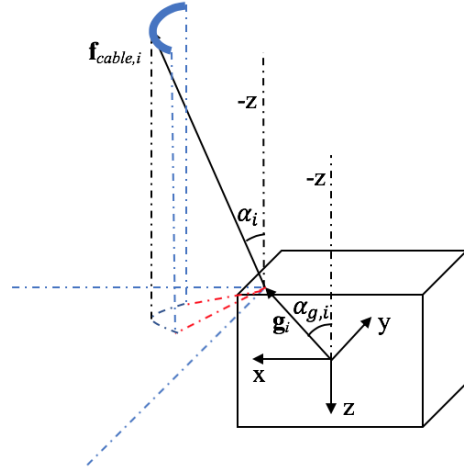


Figure 3.2. Geometrical interpretation of the constraints

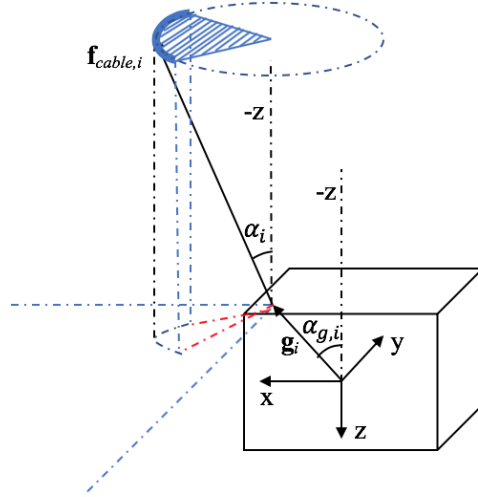


Figure 3.3. Modify the equality constraints to inequality

Guaranteed vehicle separation can be restored while retaining convexity by adding an affine constraint (shown in Fig. 3.4). The “extra plane” is defined by specifying cable length, cone angle, and sector angle.

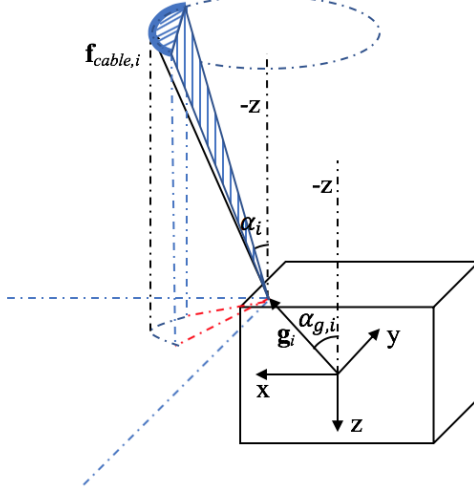


Figure 3.4. Addition of affine constraints

Note that if one defines $\Delta\beta$ as a small angle, then the arc in the initial optimization formulation (3.4) can be approximated as an affine equality by the small angle approximation. The original optimization problem can thus be regarded as “approximately convex” for appropriate limits.

3.2 Kinematics Analysis for Desired Rotorcraft States

As a payload leading transportation team, it is important to find the desired rotorcraft states by knowing the payload states and the cable force. The goal of this section is to find the kinematic model that relates \mathbf{x}_L , $\dot{\mathbf{x}}$ and $\ddot{\mathbf{x}}$ to \mathbf{r}_i , $\dot{\mathbf{r}}_i$ and $\ddot{\mathbf{r}}_i$, $i = 1, \dots, m$.

3.2.1 General Kinematics Derivation

Let us consider the i^{th} rotorcraft tether. Referring to Fig. 3.5, from the geometry of the attachment,

$${}^e\mathbf{r}_i = {}^e\mathbf{p} + {}^e\mathbf{g}_i + {}^e\mathbf{l}_i \quad (3.8)$$

where ${}^e\mathbf{g}_i = {}^e\mathbf{R}_L {}^L\mathbf{g}_i$, ${}^e\mathbf{l}_i \in \mathbb{R}^3$ is the vector from A_i to V_i expressed in \mathcal{F}_e . It is a product of the cable force direction unit vector ${}^e\mathbf{n}_i$ and the scalar of cable length ρ_i , ${}^e\mathbf{l}_i = \rho_i {}^e\mathbf{n}_i$. Also, it is assumed that all cables are in tension. The cable direction can

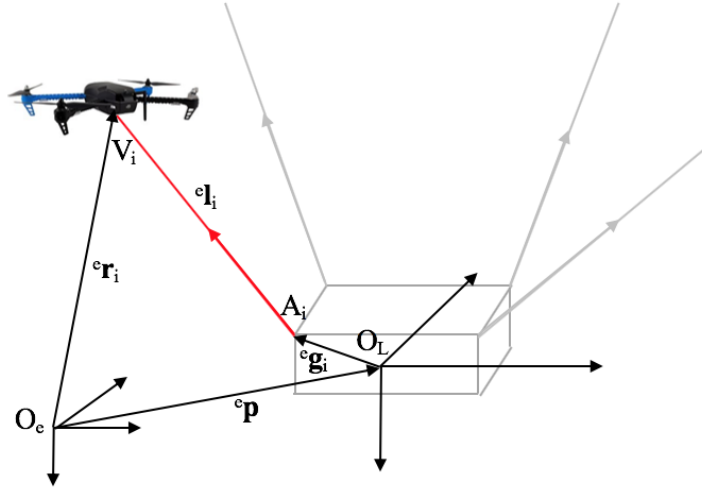


Figure 3.5. Kinematics schematic

thus be expressed as

$$\begin{aligned} {}^e\mathbf{n}_i &= \frac{{}^e\mathbf{f}_{cable,i}}{\|{}^e\mathbf{f}_{cable,i}\|} \\ {}^e\dot{\mathbf{n}}_i &= \boldsymbol{\omega}_{n_i} \times {}^e\mathbf{n}_i \end{aligned} \quad (3.9)$$

with $\boldsymbol{\omega}_{n_i}$ being the angular velocity of the i^{th} cable.

The corresponding velocity of the rotorcraft \mathbf{r}_i can be obtained by differentiating (3.8). Notice that \mathcal{F}_L is not a inertial frame. Hence,

$${}^e\dot{\mathbf{r}}_i = {}^e\dot{\mathbf{p}} + \boldsymbol{\omega} \times {}^e\mathbf{g}_i + {}^e\dot{\mathbf{n}}_i \rho_i + \dot{\rho}_i {}^e\mathbf{n}_i \quad (3.10)$$

where $\dot{\rho}_i$ is the cable length change rate.

Physically, the term $(\boldsymbol{\omega} \times {}^e\mathbf{g}_i + {}^e\dot{\mathbf{n}}_i \rho_i)$ is the velocity along the tangent line of vector $\mathbf{O}_L \mathbf{V}_i$ due to rotation. $\dot{\rho}_i {}^e\mathbf{n}_i$ is the velocity along the cable due to the cable length change.

Using the same procedure, the desired acceleration of the rotorcraft can be derived by differentiating (3.10).

$$\begin{aligned} {}^e\ddot{\mathbf{r}}_i &= {}^e\ddot{\mathbf{p}} + \dot{\boldsymbol{\omega}} \times {}^e\mathbf{g}_i + \boldsymbol{\omega} \times (\boldsymbol{\omega} \times {}^e\mathbf{g}_i) + \ddot{\rho}_i {}^e\mathbf{n}_i + \rho_i {}^e\ddot{\mathbf{n}}_i + 2\dot{\rho}_i {}^e\dot{\mathbf{n}}_i \\ &= {}^e\ddot{\mathbf{p}} + \dot{\boldsymbol{\omega}} \times {}^e\mathbf{g}_i + \boldsymbol{\omega} \times (\boldsymbol{\omega} \times {}^e\mathbf{g}_i) + \ddot{\rho}_i {}^e\mathbf{n}_i + \dot{\boldsymbol{\omega}}_{n_i} \times {}^e\mathbf{l}_i \end{aligned}$$

$$+ \boldsymbol{\omega}_{n_i} \times (\boldsymbol{\omega}_{n_i} \times {}^e\mathbf{l}_i) + 2\dot{\rho}_i {}^e\dot{\mathbf{n}}_i \quad (3.11)$$

where

$${}^e\ddot{\mathbf{n}}_i = \dot{\boldsymbol{\omega}}_{n_i} \times {}^e\mathbf{n}_i + \boldsymbol{\omega}_{n_i} \times (\boldsymbol{\omega}_{n_i} \times {}^e\mathbf{n}_i) \quad (3.12)$$

The physical meaning of the term $(\dot{\boldsymbol{\omega}} \times {}^e\mathbf{g}_i + \boldsymbol{\omega}_{n_i} \times {}^e\mathbf{l}_i)$ is the tangent acceleration orthogonal to the vector $\mathbf{O}_L\mathbf{V}_i$. $(\boldsymbol{\omega} \times (\boldsymbol{\omega} \times {}^e\mathbf{g}_i) + \boldsymbol{\omega}_{n_i} \times (\boldsymbol{\omega}_{n_i} \times {}^e\mathbf{l}_i))$ is the centripetal acceleration along the vector $\mathbf{O}_L\mathbf{V}_i$. $2\dot{\rho}_i {}^e\dot{\mathbf{n}}_i$ is the Coriolis force.

3.2.2 Special Cases

3.2.2.1 Rigid Cable

In the case of a rigid (i.e. inextensible) cable, $\dot{\rho}_i = 0$. Therefore, (3.10) and (3.11) become:

$${}^e\dot{\mathbf{r}}_i = {}^e\dot{\mathbf{p}} + \boldsymbol{\omega} \times {}^e\mathbf{g}_i + {}^e\dot{\mathbf{n}}_i \rho_i \quad (3.13)$$

$${}^e\ddot{\mathbf{r}}_i = {}^e\ddot{\mathbf{p}} + \dot{\boldsymbol{\omega}} \times {}^e\mathbf{g}_i + \boldsymbol{\omega} \times (\boldsymbol{\omega} \times {}^e\mathbf{g}_i) + \dot{\boldsymbol{\omega}}_{n_i} \times {}^e\mathbf{l}_i + \boldsymbol{\omega}_{n_i} \times (\boldsymbol{\omega}_{n_i} \times {}^e\mathbf{l}_i) \quad (3.14)$$

The rigid cable case is described in [20]. It has been shown that for the cable suspended payload with fully movable anchors (rotorcraft) and fixed cable length, the kinematic mapping from payload velocity $\dot{\mathbf{x}}$ and acceleration $\ddot{\mathbf{x}}$ to anchors linear velocities $\dot{\chi}$ and acceleration $\ddot{\chi}$ is:

$$\dot{\chi}_{\mathcal{R}} = NJ_{\mathcal{R}}\dot{\mathbf{x}} \quad (3.15)$$

$$\begin{aligned} \ddot{\chi}_{\mathcal{R}} &= NJ_{\mathcal{R}}\ddot{\mathbf{x}} + N\dot{N}^T(\dot{\xi} - \dot{\chi}) \\ \dot{\chi}_{\mathcal{K}} &= \dot{N}\boldsymbol{\rho} + J_{\mathcal{K}}\dot{\mathbf{x}} \end{aligned} \quad (3.16)$$

$$\ddot{\chi}_{\mathcal{K}} = \ddot{N}\boldsymbol{\rho} + J_{\mathcal{K}}\ddot{\mathbf{x}} - N\dot{N}^T(\dot{\xi} - \dot{\chi})$$

where $\boldsymbol{\rho} \in \mathbb{R}^m$ is the vector of cable lengths, $\boldsymbol{\xi} \in \mathbb{R}^m$ is the vector of stacked $\mathbf{O}_e\mathbf{V}_i = {}^e\mathbf{p} + {}^e\mathbf{g}_i$; $N \in \mathbb{R}^{3m \times m}$ is the block diagonal matrix of cable direction, $\cdot_{\mathcal{R}}$ indicates a vector on $\mathcal{R}(N)$, the range space of N ; $\cdot_{\mathcal{K}}$ indicates a vector on $\mathcal{K}(N)$, the null space of N ; $\dot{\chi} = \dot{\chi}_{\mathcal{R}} + \dot{\chi}_{\mathcal{K}}$, $\ddot{\chi} = \ddot{\chi}_{\mathcal{R}} + \ddot{\chi}_{\mathcal{K}}$, and

$$J_{\mathcal{R}} = N^T \begin{bmatrix} \mathbf{I}_3 & -[{}^e\mathbf{g}_1]_{\times} \\ \vdots & \vdots \\ \mathbf{I}_3 & [{}^e\mathbf{g}_m]_{\times} \end{bmatrix} \quad (3.17)$$

$$J_{\mathcal{K}} = (\mathbf{I}_{3m} - NN^T) \begin{bmatrix} \mathbf{I}_3 & [{}^e\mathbf{g}_1]_\times \\ \vdots & \vdots \\ \mathbf{I}_3 & [{}^e\mathbf{g}_m]_\times \end{bmatrix}$$

Hence,

$$\dot{\chi} = NJ_{\mathcal{R}}\dot{\mathbf{x}} + \dot{N}\boldsymbol{\rho} + J_{\mathcal{K}}\dot{\mathbf{x}} = \begin{bmatrix} \mathbf{I}_3 & [{}^e\mathbf{g}_1]_\times \\ \vdots & \vdots \\ \mathbf{I}_3 & [{}^e\mathbf{g}_m]_\times \end{bmatrix} \begin{bmatrix} {}^e\dot{\mathbf{p}} \\ \boldsymbol{\omega} \end{bmatrix} + \dot{N}\boldsymbol{\rho}$$

Therefore, ${}^e\dot{\mathbf{r}}_i = {}^e\dot{\mathbf{p}} + \boldsymbol{\omega} \times {}^e\mathbf{g}_i + {}^e\dot{\mathbf{n}}_i\rho_i$, which is consistent with (3.13).

Similarly,

$$\ddot{\chi} = NJ_{\mathcal{R}}\ddot{\mathbf{x}} + \ddot{N}\boldsymbol{\rho} + J_{\mathcal{K}}\ddot{\mathbf{x}} = NN^T\ddot{\xi} + \ddot{N}\boldsymbol{\rho} + (\mathbf{I}_{3m} - NN^T)\ddot{\xi} = \ddot{\xi} + \ddot{N}\boldsymbol{\rho}$$

Examining each component, it is consistent with (3.14) that ${}^e\ddot{\mathbf{r}}_i = {}^e\ddot{\mathbf{p}} + \dot{\boldsymbol{\omega}} \times {}^e\mathbf{g}_i + \boldsymbol{\omega} \times (\boldsymbol{\omega} \times {}^e\mathbf{g}_i) + \dot{\boldsymbol{\omega}}_{n_i} \times {}^e\mathbf{l}_i + \boldsymbol{\omega}_{n_i} \times (\boldsymbol{\omega}_{n_i} \times {}^e\mathbf{l}_i)$.

3.2.2.2 Cable Modeled as Spring-damper

If the cable is modeled as a spring-damper system, the tension magnitude in the i^{th} cable is

$$\|\mathbf{f}_{cable,i}\| = k_c\Delta\rho_i + c_c\dot{\rho}_i \quad (3.18)$$

where $\Delta\rho_i$ is the cable stretch, k_c is the cable spring constant, $\dot{\rho}_i$ is the cable length changing rate, and c_c is the damping constant of the cable. Therefore,

$${}^e\mathbf{l}_i = (\rho_{i,0} + \Delta\rho_i) {}^e\mathbf{n}_i \quad (3.19)$$

where $\rho_{i,0}$ is the unstretched cable length.

In fact, for the massless cable with slow rotation, the state of the cable stretch $\mathbf{x}_c = [\Delta\rho_i \ \Delta\dot{\rho}_i]^T$ (note that $\dot{\rho}_i = \Delta\dot{\rho}_i$) satisfies the well-known spring-damper governing equation

$$\dot{\mathbf{x}}_c = \mathbf{a}_i\mathbf{x}_c + \mathbf{b}_iu_i \quad (3.20)$$

where $u_i = \|\mathbf{f}_{cable,i}\|$, with

$$\mathbf{a}_i = \begin{bmatrix} 0 & 1 \\ -\frac{k_c}{m_i} & -\frac{c_c}{m_i} \end{bmatrix}, \quad \mathbf{b}_i = \begin{bmatrix} 0 \\ \frac{1}{m_i} \end{bmatrix} \quad (3.21)$$

For the general case with non-negligible cable mass or the cable rotation, the cable stretch $\Delta\rho_i$ dynamics can be derived from an approach similar to (3.10), (3.11) by using (3.9), (3.12).

Hence, $\Delta\rho_i$ and $\dot{\rho}_i$ can be obtained in real time by numerical integration. Notice that when $k_c \rightarrow \infty$, $\Delta\rho_i = 0$, it degenerates to the rigid cable case.

3.2.2.3 Rigid Formation

When the multilift formation is rigid, or the direction of the cable is fixed in the payload frame \mathcal{F}_L , $\boldsymbol{\omega} = \boldsymbol{\omega}_{n_i}$, ${}^e\dot{\mathbf{n}}_i = \boldsymbol{\omega} \times {}^e\mathbf{n}_i$, ${}^e\ddot{\mathbf{n}}_i = \dot{\boldsymbol{\omega}} \times {}^e\mathbf{n}_i + \boldsymbol{\omega} \times (\boldsymbol{\omega} \times {}^e\mathbf{n}_i)$. Therefore, (3.10) and (3.11) become:

$$\begin{aligned} {}^e\dot{\mathbf{r}}_i &= {}^e\dot{\mathbf{p}} + \boldsymbol{\omega} \times ({}^e\mathbf{g}_i + {}^e\mathbf{l}_i) + \dot{\rho}_i {}^e\mathbf{n}_i \\ &= {}^e\dot{\mathbf{p}} + \boldsymbol{\omega} \times \mathbf{O}_L \mathbf{V}_i + \dot{\rho}_i {}^e\mathbf{n}_i \end{aligned} \quad (3.22)$$

$$\begin{aligned} {}^e\ddot{\mathbf{r}}_i &= {}^e\ddot{\mathbf{p}} + \dot{\boldsymbol{\omega}} \times ({}^e\mathbf{g}_i + {}^e\mathbf{l}_i) + \boldsymbol{\omega} \times (\boldsymbol{\omega} \times ({}^e\mathbf{g}_i + {}^e\mathbf{l}_i)) + \ddot{\rho}_i {}^e\mathbf{n}_i + 2\boldsymbol{\omega} \times {}^e\mathbf{l}_i \\ &= {}^e\ddot{\mathbf{p}} + \dot{\boldsymbol{\omega}} \times \mathbf{O}_L \mathbf{V}_i + \boldsymbol{\omega} \times (\boldsymbol{\omega} \times \mathbf{O}_L \mathbf{V}_i) + \ddot{\rho}_i {}^e\mathbf{n}_i + 2\boldsymbol{\omega} \times {}^e\dot{\mathbf{l}}_i \end{aligned} \quad (3.23)$$

Further, if both rigid body and rigid formation are assumed, the kinematic model becomes:

$${}^e\dot{\mathbf{r}}_i = {}^e\dot{\mathbf{p}} + \boldsymbol{\omega} \times \mathbf{O}_L \mathbf{V}_i \quad (3.24)$$

$${}^e\ddot{\mathbf{r}}_i = {}^e\ddot{\mathbf{p}} + \dot{\boldsymbol{\omega}} \times \mathbf{O}_L \mathbf{V}_i + \boldsymbol{\omega} \times (\boldsymbol{\omega} \times \mathbf{O}_L \mathbf{V}_i) \quad (3.25)$$

3.3 Control

3.3.1 Payload Trajectory Following Control

Assume that the desired payload trajectory is given which consists of a series of waypoints in frame \mathcal{F}_e and corresponding timestamp. This could come from a trajectory planner before flight or from a human pilot during real-time flight. Each waypoint includes the desired position, orientation, velocity and angular rate of payload (waypoint states). Between two waypoints, the trajectory is generated starting from a 3rd order polynomial as the linear and angular feedforward acceleration $\ddot{\mathbf{x}}_d = [{}^e\ddot{\mathbf{p}}_d^T \quad \dot{\boldsymbol{\omega}}_d^T]^T$. 4th and 5th order polynomials are then used to generate the payload linear and angular velocity and position $\dot{\mathbf{x}}_d = [{}^e\dot{\mathbf{p}}_d^T \quad \boldsymbol{\omega}_d^T]^T$, $\mathbf{x}_{L,d} = [{}^e\mathbf{p}_d^T \quad \boldsymbol{\Omega}_d^T]^T$. This allows zero acceleration at

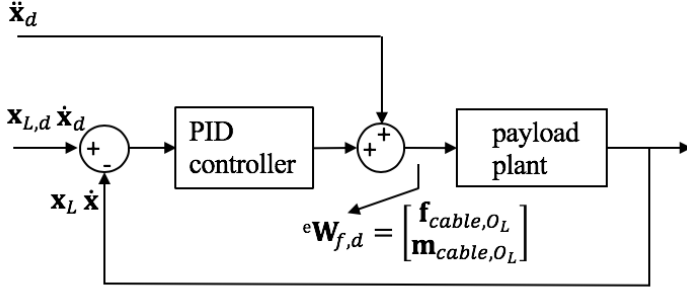


Figure 3.6. Block diagram of the payload trajectory following controller

both the start and endpoints, defines waypoint states, ensures smooth trajectories, and provides a convenient way to ensure that acceleration constraints are satisfied.

The purpose of the trajectory following controller is to compute the desired net force and moment acting upon the payload center of gravity (CG) (equivalently, the desired acceleration and angular acceleration of the CG). Trajectory following control is accomplished using a combination of feedforward of desired acceleration and feedback of state error (see Fig. 3.6). Proportional-integrator-derivative (PID) control is used for feedback. At time t , the PID controller for payload trajectory following is of the following form:

$$\ddot{\mathbf{y}} = \ddot{\mathbf{x}}_d + \mathbf{K}_p(\mathbf{x}_{L,d} - \mathbf{x}_L) + \mathbf{K}_i \int_0^t (\mathbf{x}_{L,d} - \mathbf{x}_L) d\tau + \mathbf{K}_d(\dot{\mathbf{x}}_d - \dot{\mathbf{x}}) \quad (3.26)$$

$$= \ddot{\mathbf{x}}_d + \mathbf{K}_p \mathbf{e} + \mathbf{K}_i \int_0^t \mathbf{e} d\tau + \mathbf{K}_d \mathbf{e}_v \quad (3.27)$$

where \mathbf{K}_p , \mathbf{K}_i , \mathbf{K}_d are diagonal matrices of positive gains. Errors are defined as $\mathbf{e} = \mathbf{x}_{L,d} - \mathbf{x}_L = [\mathbf{e}_p \ \mathbf{e}_\Omega]^T$, $\mathbf{e}_v = \dot{\mathbf{x}}_d - \dot{\mathbf{x}} = [\mathbf{e}_\dot{p} \ \mathbf{e}_\omega]^T$. The desired wrench induced by the cables ${}^e\mathbf{W}_{f,d}$ will then be computed through the payload dynamics (2.1):

$${}^e\mathbf{W}_{f,d} = \mathbf{M}_L \ddot{\mathbf{y}} + \mathbf{C}_L \dot{\mathbf{x}} - {}^e\mathbf{W}_g \quad (3.28)$$

The desired wrench ${}^e\mathbf{W}_{f,d}$ are computed in frame \mathcal{F}_e . For convenience of the cable force computation, the forces and moments vector will be transformed to frame \mathcal{F}_L by

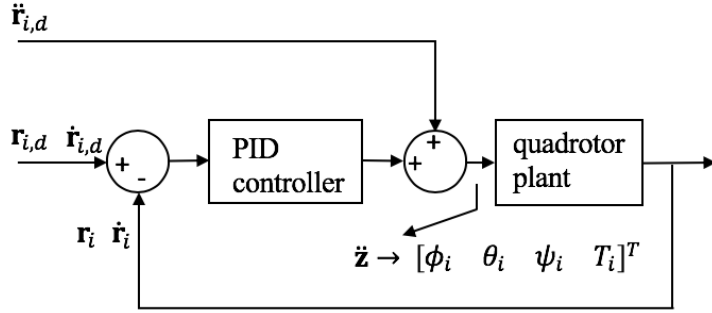


Figure 3.7. Block diagram of rotorcraft controller

multiplying a direction cosine matrix ${}^L\mathbf{R}_e$. The net cable force can then be computed based on the cable force analysis (Section 3.1).

Proposition 1: Define a *reduced system* that assumes each rotorcraft is able to maintain perfect desired states so that the desired cable forces (3.2) and external wrench (3.28) are achieved. Then there exist gain parameters \mathbf{K}_p , \mathbf{K}_i , \mathbf{K}_d such that the reduced system exponentially tracks the reference trajectory.

Proof. See Appendix A.1. □

3.3.2 Rotorcraft Control

Given the desired payload trajectory and the computed cable force on each tether, the corresponding desired trajectory for each rotorcraft ${}^e\mathbf{r}_{i,d}$, ${}^e\dot{\mathbf{r}}_{i,d}$, ${}^e\ddot{\mathbf{r}}_{i,d}$ can be obtained from the kinematics analysis, see Section 3.2.

Rotorcraft control ensures that the desired vehicle states and cable tension can be maintained. For the quadcopters, the desired vehicle attitude and throttle computed from slower outer loop position tracking controller can be used as setpoint for the faster inner loop control.

A block diagram of the rotorcraft outer loop controller is shown in Fig. 3.7. Here, the quadrotor plant includes the inner loop controller. A PID controller that follows the desired states command from the payload is used for the outer loop. Desired acceleration for the rotorcraft can be obtained by:

$$\ddot{\mathbf{z}} = {}^e\ddot{\mathbf{r}}_{i,d} + \mathbf{K}_{i,p}({}^e\mathbf{r}_{i,d} - {}^e\mathbf{r}_i) + \mathbf{K}_{i,i} \int_0^t ({}^e\mathbf{r}_{i,d} - {}^e\mathbf{r}_i) d\tau + \mathbf{K}_{i,d}({}^e\dot{\mathbf{r}}_{i,d} - {}^e\dot{\mathbf{r}}_i) \quad (3.29)$$

To compute the setpoint attitude and throttle for each quadcopter, apply the rotorcraft

translational motion dynamics (2.6) of the quadrotor. The desired thrust and Euler roll and pitch angles are of the following form [61]:

$$T_i = \frac{m_i g + f_{i3} - m \ddot{z}_3}{\cos \phi_i \cos \theta_i} \quad (3.30)$$

$$\begin{bmatrix} \sin \theta_i \\ \sin \phi_i \end{bmatrix} = T_i \mathbf{Q}^{-1} (-m_i \begin{bmatrix} \ddot{z}_1 \\ \ddot{z}_2 \end{bmatrix} + \begin{bmatrix} f_{i1} \\ f_{i2} \end{bmatrix}) \quad (3.31)$$

where

$$\mathbf{Q} = \begin{bmatrix} \cos \phi_i \cos \psi_i & \sin \psi_i \\ \cos \phi_i \sin \psi_i & -\cos \psi_i \end{bmatrix}$$

$\mathbf{z} = [z_1 \ z_2 \ z_3]^T$, ${}^e\mathbf{f}_{cable,i} = [f_{i1} \ f_{i2} \ f_{i3}]^T$. $\mathbf{K}_{i,p}$, $\mathbf{K}_{i,i}$, $\mathbf{K}_{i,d}$ are diagonal matrices of positive gains. Notice that the desired thrust and attitude of the rotorcraft (3.30)(3.31) takes the computed cable force ${}^e\mathbf{f}_{cable,i}$ into account, which would control the cable force commanded from the payload. (3.30) ensures local exponential stability of $({}^e\mathbf{r}_{i,d} - {}^e\mathbf{r}_i)_3 = e_{x_{i3}}$, the 3rd component of the vector (analogous meaning for $(\cdot)_{1:2}$), as long as the singularity $\cos \phi_i \cos \theta_i = 0$ is avoided [61]. The rotorcraft thrust/vertical position dynamics can thus be expressed as

$$\ddot{e}_{x_{i3}} = -k_{i,p} e_{x_{i3}} - k_{i,i} \int_0^t e_{x_{i3}} d\tau - k_{i,d} \dot{e}_{x_{i3}} \quad (3.32)$$

where $k_{i,p}$, $k_{i,i}$, $k_{i,d}$ are from the corresponding 3rd diagonal components of $\mathbf{K}_{i,p}$, $\mathbf{K}_{i,i}$, $\mathbf{K}_{i,d}$. (3.31) shows that (e_{x_1}, e_{x_2}) will be locally exponentially stable if the attitude controller (defined later) can track the pitch and roll commands. For the yaw angle, a constant heading angle ψ_i is commanded at each time step. Because of the characteristic of quadrotors, the 6 degree of freedom motion of payload can be achieved with only translational motion of the quadrotors.

Then the faster inner loop attitude regulation control can be designed by differentiating the rotorcraft rotational dynamics (2.7) with the torque input as

$$\boldsymbol{\tau}_i = \mathbf{J}_i (k_p \mathbf{C}_i^{-1} (\boldsymbol{\Omega}_{i,d} - \boldsymbol{\Omega}_i) - k_d \boldsymbol{\omega}_i) \quad (3.33)$$

with which the rotorcraft closed-loop dynamics can be expressed as:

$$\ddot{\mathbf{e}}_{\Omega_i} + (k_d + \mathbf{C}_i \mathbf{J}_i^{-1} \boldsymbol{\omega}_i \times \mathbf{J}_i \boldsymbol{\omega}_i - \dot{\mathbf{C}}_i \mathbf{C}_i^{-1}) \dot{\mathbf{e}}_{\Omega_i} + k_p \mathbf{e}_{\Omega_i} = 0 \quad (3.34)$$

where $\boldsymbol{\Omega}_{i,d}$ are the desired Euler angles, k_p , k_d are positive gains and \mathbf{C}_i is defined in (2.8).

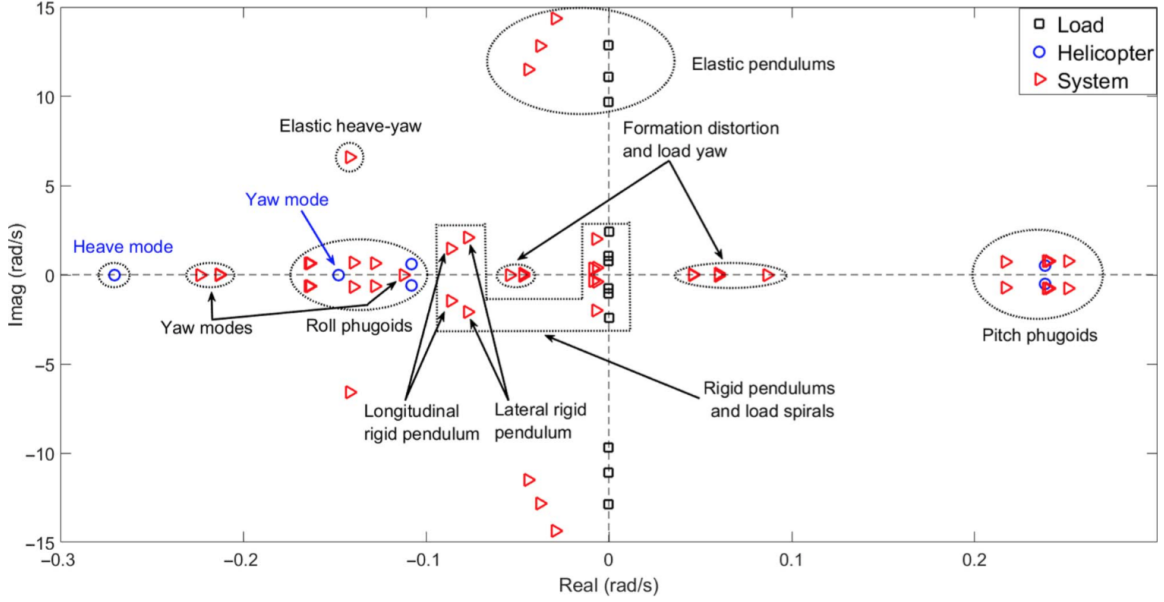


Figure 3.8. System poles (hover) [7]

Proofs of stability and convergence are presented in [61–63]. The rotorcraft’s orientation as well as position will therefore track the reference exponentially.

3.3.3 Stability Analysis of the Full System

The reduced system as well as the fast rotorcraft dynamics have been shown to be exponentially stable. The stability of the full model of the system which includes the rotorcraft dynamic will be analyzed.

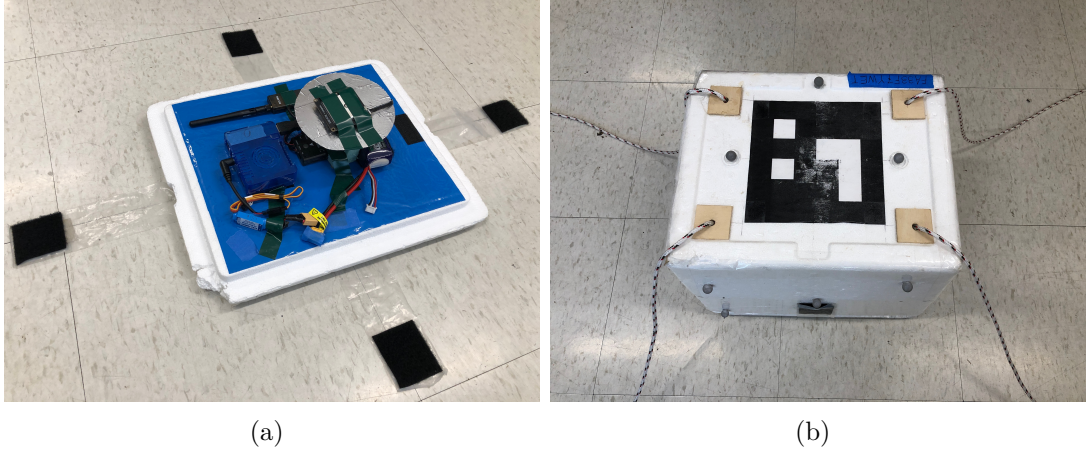
The method used here is *singular perturbation* [64] based on the knowledge that the single rotorcraft has a much faster dynamics comparing to the reduced model with the isolated payload [7, p.8], see Fig. 3.8. A similar analysis approach is shown in [65].

Proposition 2: Consider the full model of the multilift system and the optimized cable force $\mathbf{f}_{cable,i}$, along with ψ_i and (T_i, τ_i) specified by (3.30),(3.33). Then there exists $\bar{\epsilon}$ such that $\forall \epsilon < \bar{\epsilon}$, the closed-loop system can track the reference $\mathbf{x}_{L,d}, \dot{\mathbf{x}}_d, \ddot{\mathbf{x}}_d$ exponentially.

Proof. See Appendix A.2. □

3.4 Hardware Platform

This section describes the details of the design of testbed for hardware implementation. The critical component is the electronics unit attached to the payload so that the payload



(a)

(b)

Figure 3.9. Payload with control computer.

can sense itself and lead the whole fleet [66].

3.4.1 Payload Side

The payload is a foam box equipped with an ODroid-XU4, Pixhawk mini autopilot module, GPS+compass and corresponding power supply, as shown in Fig. 3.9.

The heart of the onboard computer ODroid-XU4 is a Samsung Exynos-A15 and quad-core ARM Cortex-A7 CPUs plus the ARM Mali-T628 MP6 GPU¹. A WiFi adapter mounted on one of the USB ports of the ODroid performs is used for communication. A Linux system with ROS (Robot Operating System) [67] installed operates on the ODroid. The ODroid computer runs a Python State Machine to manage the mission and host the payload trajectory controller and the cable force computation. Then the computed desired states are sent to each rotorcraft via WiFi.

Four cable cords are attached to the payload. Here, utility cords are used which can be regarded as almost rigid with a large spring constant. The parameters for the cables and payload as well as the attachment geometry are shown in Table. 3.1 and Table. 3.2.

3.4.2 Rotorcraft Side

Four 3DR IRIS quadcopters are the executors following the payload commands. The low-level interface is a Pixhawk 1 autopilot with firmware px4 1.6.0², which provides access to the servo motors, barometric altimeter, and accelerometer, gyroscope, and

¹Hardkernel Co., Ltd. <http://www.hardkernel.com>

²3DR Robotics, Inc. <http://3drrobotics.com/>

Table 3.1. Parameter for payload and cables

Parameter	Value	Parameter	Value
Cable length	2.1 m	Payload weight	0.815 kg
Payload length	0.3525 m	Payload J_{xx}	0.0170 kg · m ²
Payload width	0.298 m	Payload J_{yy}	0.0287 kg · m ²
Payload height	0.325 m	Payload J_{zz}	0.0106 kg · m ²
T_{max}	4.5 N	Sector region $\Delta\beta$	30 deg
Cone angle α	37.0 deg	Sector center β_c	35.2 deg

Table 3.2. Cable attachment geometry

Attachment #	g_x (m)	g_y (m)	g_z (m)
1	0.115	-0.090	-0.203
2	0.115	0.090	-0.203
3	-0.115	0.090	-0.203
4	-0.115	-0.090	-0.203

magnetometer suite. Each IRIS is also equipped with an ODroid-XU4 that acts as mission computer, communicating with the payload over ROS via WiFi. It also runs the high level control and connects to the low-level interface through serial mavros³. The IRIS ODroid provides a continuous command signal to the pixhawk so that the quadcopter can fly the OFFBOARD mode. High level control works to control the outer loop trajectory tracking of the quadcopter Fig. 3.7, then computes the required throttle and attitude for the inner loop to correct the vehicle. IRIS parameters are listed in Table. 3.3.

3.4.3 Ground Side

An XBox video gamepad connected to the ground laptop performs as the human interface. The gamepad is used to trigger the different system flight states and can be used for flight abort commands. During indoor flight this laptop is used to receive data from the Vicon system and distribute this data into the ROS space in real time for use by the

³Mavros Pacakge Summary. <http://wiki.ros.org/mavros>

Table 3.3. IRIS quadcopter parameters

Parameter	Value	Parameter	Value
Weight with battery	1.282 kg	Payload capacity	0.2 kg
ODroid pack weight	0.115 kg	Motor-to-motor	0.55 m
Brushless DC motor	950 kV	Propeller size	9.5 inch

payload and rotorcraft.

3.4.4 External Sensor

For the indoor flight, the capture space volume of the Vicon system is roughly $6\text{m} \times 6\text{m} \times 4\text{m}$. Real-time position and orientation are provided in an earth-fixed frame (Vicon frame) at 100 Hz for each rotorcraft and the payload ⁴. A 12-state Kalman Filter running on the payload ODroid filters the Vicon raw data and provides the payload states, including position, orientation, velocity and angular rate. On each IRIS ODroid, a coordinate transformer turns the raw VICON position/orientation data into the autopilot onboard estimator frame.

For the outdoor scenario, the autopilot with the GPS+compass group connected communicates with the onboard ODroid providing real-time state information for both the payload and the quadcopers. Here, the drotek RTK M8P GPS ⁵ is selected for both the payload and the quadcopters to achieve higher accuracy positioning.

3.4.5 Python State Machine

As mentioned in Section 3.4.1, a Python State Machine running on the payload ODroid conducts the payload trajectory control and the cable force computation. A Python based ROS library Smach⁶ is used as the framework. Five basic states constitute the state machine: GROUND, TAKE_OFF, HOVER, FOLLOW_TRAJ and LANDING. A gamepad performs as the human-interactive which can be used to trigger the TAKEOFF, FOLLOW_TRAJ and LANDING states.

As Fig. 3.10 shows, the system starts from the GROUND state, where the payload and all of the quadrotors are sitting on the ground. When the ready switch is triggered, the four quadcopters fly to the take off position, where the cables stretch to the equilibrium length so that the payload is still static but just about leaving the ground. The system will transit to HOVER state if all of the quadcopters fly within the error tolerance bounds with respect to the take off position. The take off position will also make the cables satisfy the requirement of cone angle and separation of quadcopters. In the TAKEOFF state, there is no payload feedback. A series of pre-planned waypoints are directly commanded to the quadrotors.

⁴Vicon Motion Systems, Ltd. <https://www.vicon.com>

⁵drotek ELECTRONICS. <https://drotek.com/docs/>

⁶Smach Package Summary. <http://wiki.ros.org/Smach>

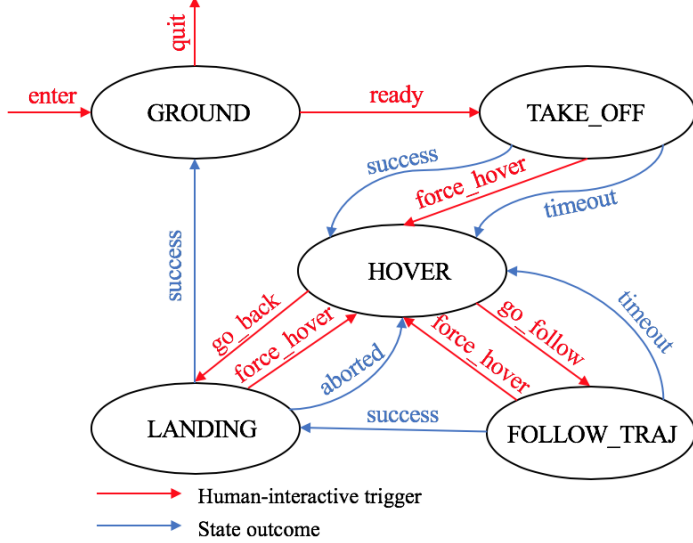


Figure 3.10. Diagram of state machine

The system can transit to FOLLOW_TRAJ or LANDING state depending on the human-interactive command. In FOLLOW_TRAJ state, the payload tracks the pre-planned trajectory and commands desired states to each quadrotor. The main algorithm for payload trajectory controller and cable force computation keep running until the payload achieves the desired states within error tolerance or jumps to HOVER if timeout.

During LANDING, all of the quadcopters start landing from the landing position, where the payload has already touched ground while the cables are still at equilibrium length, similar to the take off position. The system will return to the GROUND state if the landing is successful or jump to HOVER if aborted. Notice that there is also no payload feedback in the LANDING state. As with the TAKEOFF state, a series of pre-planned waypoints are directly commanded to the quadrotors.

For safety, human-interaction has highest trigger priority. Pressing a “Force-hover”, “Fail-safe” or “Disarm” button on the gamepad causes transition to the respective state. The safety states can be triggered at any time. Here, “Fail-safe” will trigger the “AUTO-LAND” mode in pixhawk. “Disarm” will kill all of the quadcopters.

3.4.6 Information Flow

The information flow of multilift system is shown in Fig. 3.11. The payload commands computed desired position, velocity and acceleration to each rotorcraft so that the motion of rotorcraft can steer the payload to the desired states. Here, the payload states are position, orientation, velocity and body rates. The ground station with a gamepad

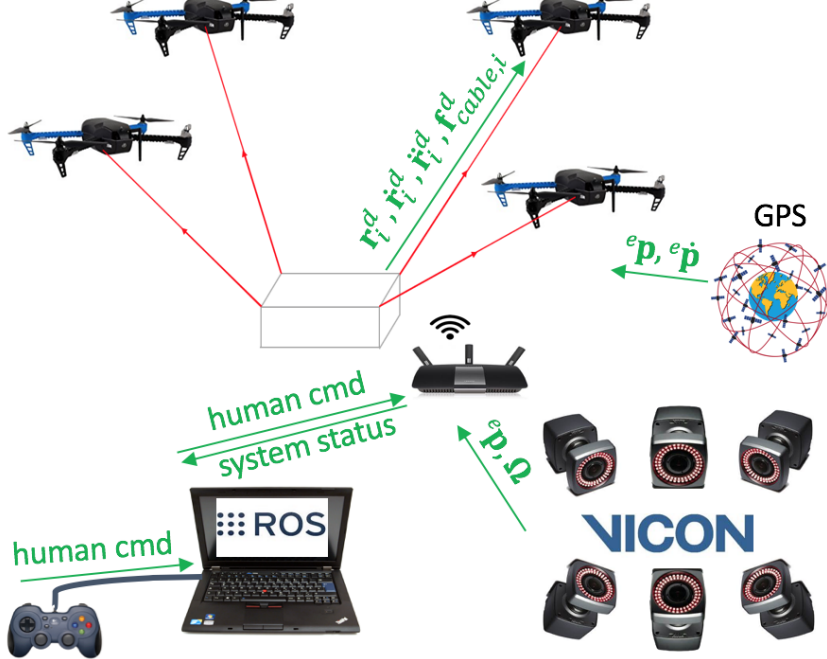


Figure 3.11. Multilift system information flow

connected casts the human-interactive command to the payload. The navigation system (Vicon or GPS) provides position and velocity information for the payload and rotorcraft.

All of the IRIS ODroids, the payload ODroid and the ground laptop run in the same ROS space under the same WiFi network. The operator can remotely log into the onboard computer of any rotorcraft or of payload from the ground laptop to launch the mission or monitor the performance of each individual object.

3.5 Flight Demonstration

Flight tests based on the developed hardware platform consisting of four quadcopters are performed to demonstrate the utility of this approach. Indoor flight tests are conducted to show the system performance for complex trajectory following, rejection of impulse disturbances, human-in-the-loop control and formation change. An outdoor flight test showing trajectory tracking is also presented to demonstrate system performance in the presence of winds.

3.5.1 Single Step Optimization Study

Before the hardware flight demonstration, a study of the single step optimization problem that solves for the cable force is performed to provide more understanding of the physical problem.

Consider a situation when the whole multilift system hovers above the ground at a fixed altitude. The total force and moment acting on the payload should be zero based on the Newton's second law. Therefore, the wrench acting on the payload generated by the cables exists only to balance payload weight. By knowing the payload geometry, see Table. 3.2, the least-norm solution and the null space of the geometry matrix $\tilde{\mathbf{G}}$ can be obtained.

The original non-convex optimization problem and the “convexified” problem are compared. For the hover case, it is easy to generate an accurate initial guess of \mathbf{c} in (3.4). In hover, the least-norm solution will have cable forces with z -component equal to one quarter of the payload weight. One of the valid null-space solutions will have only x and y components generated symmetrically around the payload according to the cone and geometry constraints. Then, the initial guess for \mathbf{c} is computed based on the Moore-Penrose inverse of the $\tilde{\mathbf{G}}$. With a 37° cone angle and 30° sector angle, different initial condition for \mathbf{c} are tried on both convex and non-convex problems, that is, $\mathbf{c}_1 = [-1.6530 \ -1.6552 \ 0.0611 \ -1.1303 \ 0.0795 \ -1.5215]^T$ (accurate), $\mathbf{c}_2 = [0.0 \ 0.0 \ 0.0 \ 0.0 \ 0.0]^T$ (only least-norm solution), $\mathbf{c}_3 = [0.9778 \ 2.0694 \ 1.4538 \ -0.6069 \ 0.5877 \ -1.5746]^T$. The optimized objective function value f^* at the solution \mathbf{c}^* are shown in Table. 3.4.

It can be seen the non-convex formulation can work well given a good initial guess. For some initial conditions the nonlinear solver failed to find a feasible solution. However, the convex formulation can always find the unique solution without reliance on the initial guess. This clearly shows the advantage of the convex formulation: it is robust to the initial condition and guarantees the existence of a stable solution. Notice that there is a slight difference between the solution of the two cases: recall that the convex version of the problem is generated by adding an extra constraint. The solution of the convex case lies on the secant line of a circle while that of the non-convex case lies on the arc. Further, compare the two cases under different sector angle $\Delta\beta$, i.e., $\Delta\beta = 10^\circ, 30^\circ, 50^\circ$ with accurate initial guess, see Table. 3.5. Only the $\Delta^L \mathbf{f}_{cable,1}$ is shown since the solution is geometrically symmetric around the payload. It can be seen as the sector angle becomes smaller, the difference between the convex and non-convex solution gets smaller. This is consistent with the small angle approximation.

Table 3.4. Comparison of non-convex and convex optimization

initial condition	non-convex f^*	convex f^*
\mathbf{c}_1	5.0055	4.9444
\mathbf{c}_2	fail with scipy “fmin_slsq”	4.9444
\mathbf{c}_3	fail with Matlab “fmincon”	4.9444

Table 3.5. Solution difference between non-convex and convex optimization

$\Delta\beta$	10°	30°	50°
$\Delta^L \mathbf{f}_{cable,1}$	$[-0.0047 \ 0.0033 \ 0]^T$	$[-0.042 \ 0.0295 \ 0]^T$	$[-0.1154 \ 0.0812 \ 0]^T$
Δf^*	0.0069	0.0611	0.1646

3.5.2 Cooperative Transport with a Circular Path Mission

To test the system performance under complex trajectories, a circular path mission is performed indoors in the Vicon motion capture studio. In this experiment, the system is tasked with lifting the payload, following a circular path, and then descending. A fixed 37° cable cone angle is used. Two groups of flight tests are performed: one with a fixed payload attitude, the other with a payload pirouette (i.e. the payload heading is controlled to keep the “nose” pointing to the center of the circle).

In the first flight test, the trajectory planner generated a smooth circular path:

$${}^e\mathbf{p}(t) = \begin{bmatrix} A \cos(2\pi ft) + x(t_0) - A \\ A \sin(2\pi ft) + y(t_0) \\ z(t_0) \end{bmatrix} \quad (3.35)$$

where $A = 0.8\text{m}$ is the circle radius, $1/f = 30\text{s}$ is the period of motion, ${}^e\mathbf{p}(t_0) = [x(t_0) \ y(t_0) \ z(t_0)]$ is the payload position at the start point. The desired payload roll/pitch/yaw attitude is set to zero, the desired velocity and angular rate can be obtained from taking the derivative of the path. The multilift system starts with vertical lift-off to an altitude above ground 0.6m in 3s. The payload then moves with only translational motion along the circular path starting and terminating at the same point. Finally, the system descends to touch down.

In the second flight test, a continuous changing yaw angle is planned based on the payload pirouette period, which guarantees that the payload can return to the start point with the same attitude after one period’s pirouette movement. The desired payload roll and pitch angles are set to zero.

For each flight test, non-convex and convex formulations for the cable force compu-

Table 3.6. Optimization Solver Performance Comparison

	translation average iteration	solving time (s)	pirouette average iteration	solving time (s)
non-convex	3.000	0.0043	3.022	0.00415
convex	2.000	0.00285	2.000	0.00280

Table 3.7. Tracking Performance Comparison

average position tracking error (m)	translation	pirouette
non-convex	0.07412	0.08222
convex	0.05814	0.07858

tation optimization problem are compared. Table. 3.6 shows the comparison results of the optimization solver performance. The average position tracking error for the two cases are compared in Table. 3.7. The convex formulation clearly shows better computation performance with less solving time at every time step. This is a meaningful improvement especially for the real-time flight. Tracking performance resulting from the convex formulation is also better than that from the non-convex formulation. This appears to be due to the fact that the convex formulation can always find a unique and feasible solution without relying on the initial guess, while the non-convex formulation uses the most recent result as the initial guess or the solution of current time stamp if it fails to find optimal solution in a limited amount of steps. The non-convex formulation thus brings in more approximation which causes bigger payload position tracking error. Hence, the system performance results from the convex formulation will be shown in the following.

Fig. 3.12 and Fig. 3.13 shows payload position in the 2D view. It can be seen in both cases, the payload can follow the commanded trajectory. The payload position remains within in a few centimeters of commanded position throughout the flight. However, in the second case when payload moves with pirouette, tracking error is somewhat larger compared with the case with only translation. This could be due to the inaccurate payload moments of inertia measurement which leads to the error in net moment computation as well as the cable force. A good measurement mechanism or estimation method could improve this behavior. Fig. 3.14 shows the payload yaw angle when moving in pirouette. The multilift system is able to orient the payload throughout the 360° yaw motion.

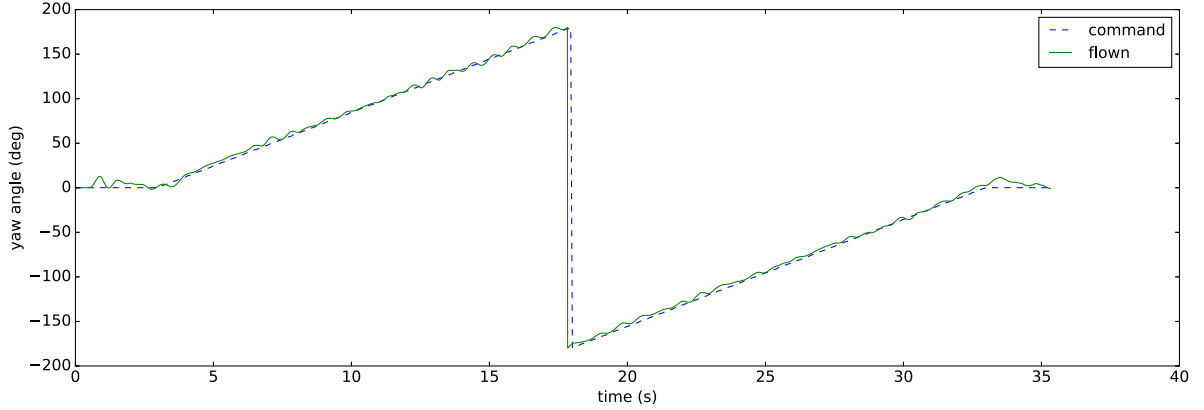


Figure 3.14. Payload yaw angle in pirouette

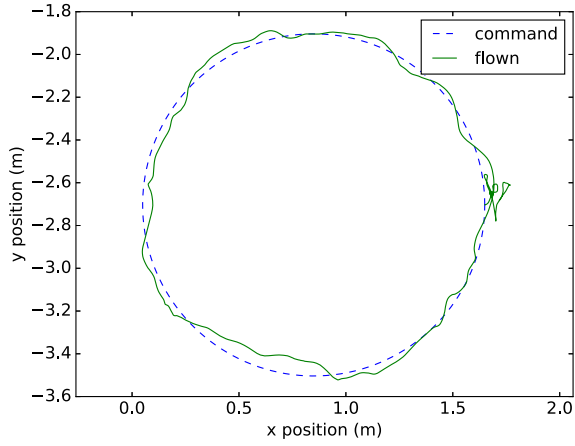


Figure 3.12. Payload with only translation

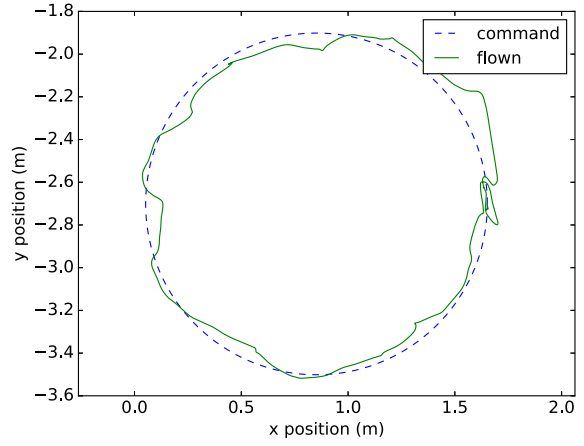


Figure 3.13. Payload with pirouette

In Fig. 3.15 and Fig. 3.16, position of the robots are shown for two group of flight test. It can be seen the robots track their commanded states quite well. Notice that in the second case, the payload can move with pirouette while the robots move with only translation. Fig. 3.17 depicts a sequence of images from the pirouette flight. The whole system starts from initial condition on the ground before takeoff, Fig. 3.17(a); flies to take off position, Fig. 3.17(b); lifts to the start point Fig. 3.17(c); circular flight with payload pirouette, Fig. 3.17(d)3.17(e)3.17(f); moves back to the start point with the same attitude, Fig. 3.17(g); returns the payload to the initial position before landing Fig. 3.17(h).

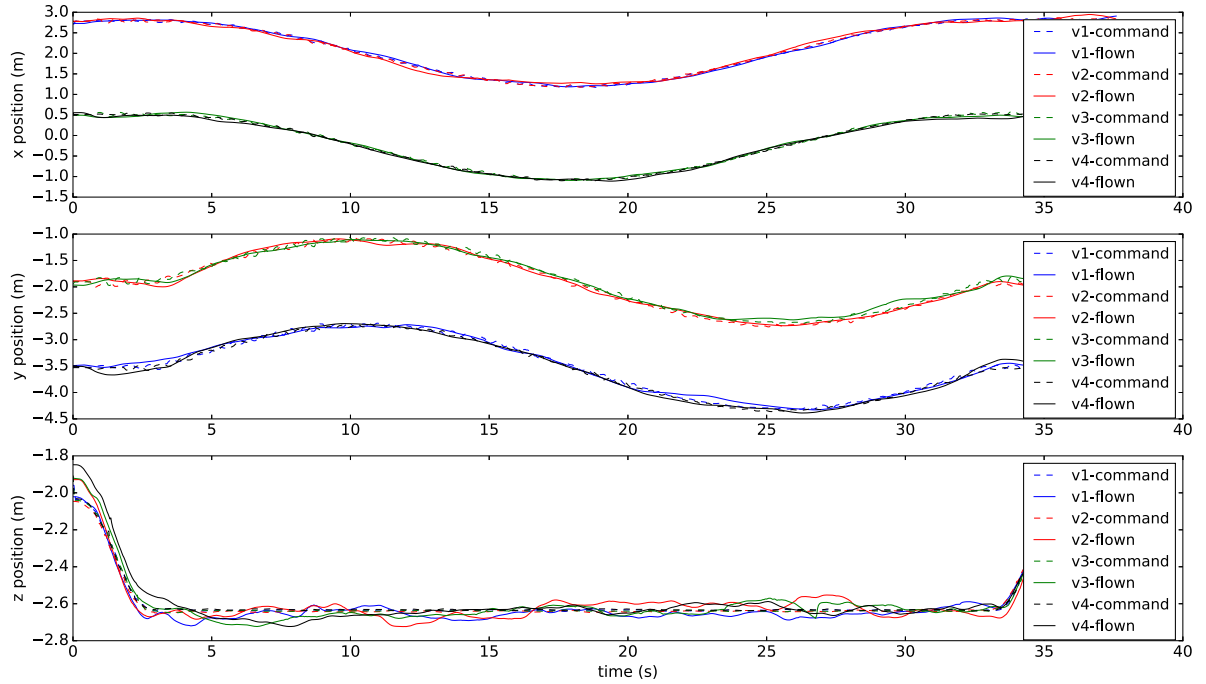


Figure 3.15. Position of the robots for payload with only translation

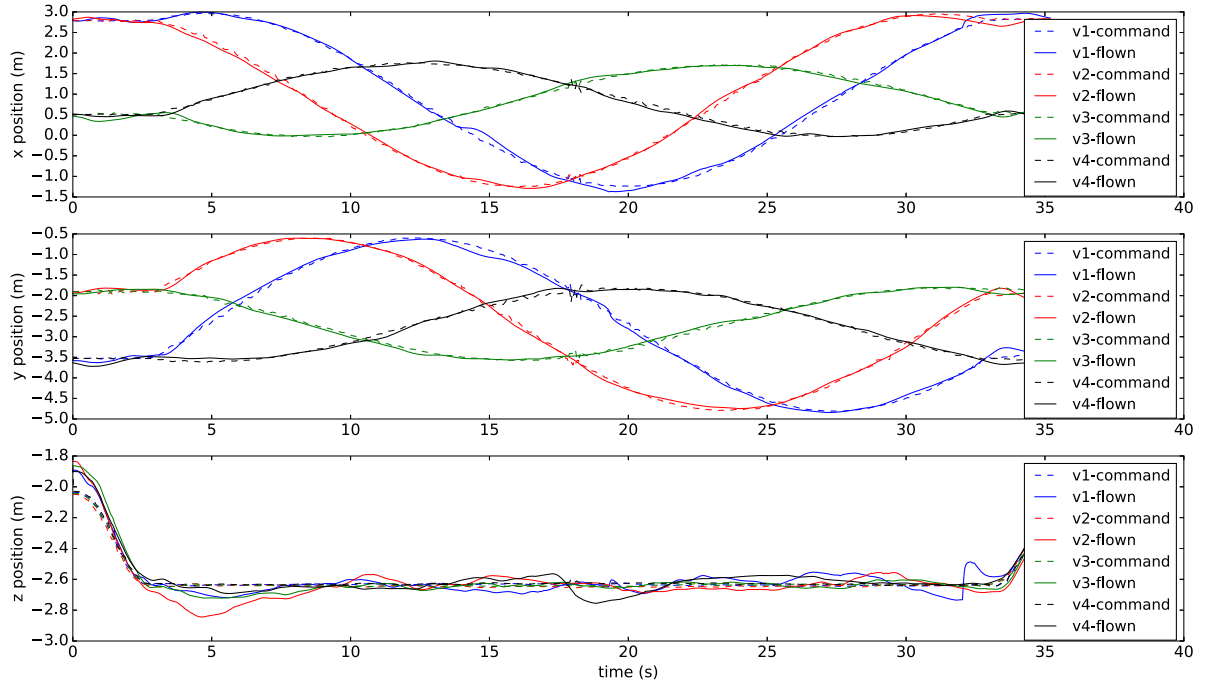


Figure 3.16. Position of the robots for payload with pirouette

The circular path mission demonstrates the effectiveness of the developed slung load leading cooperative transportation team, with good tracking of both payload position

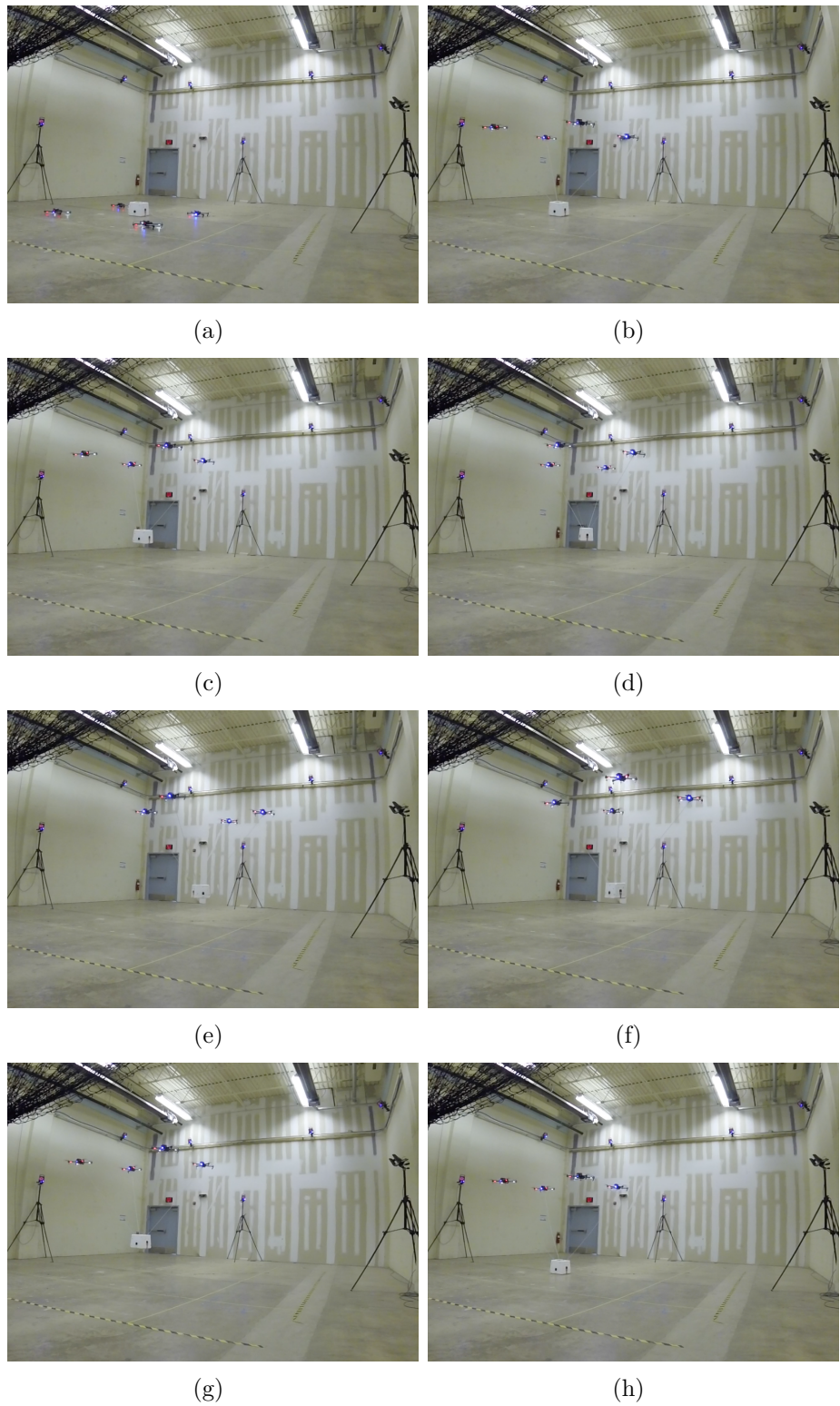


Figure 3.17. Sequence of images showing coordinated payload transport in the motion capture studio.

and heading. In particular, the system behavior resulting from the convex formulation of the cable force computation optimization problem shows clear advantage on both computational and tracking performance.

3.5.3 Disturbance Rejection Test

A disturbance rejection test is performed indoors to test the system robustness to external impulse disturbance. In this experiment, the system is tasked with lifting the payload and then hovering. During the hover phase, an external impulse disturbance was added to the payload (i.e. the payload was given a push using a stick), Fig. 3.18.



Figure 3.18. External disturbance

Fig. 3.19 and Fig. 3.20 show payload position and orientation in inertial frame during the disturbance rejection test. External disturbances were added to the payload from the negative y direction at time 5.5s and 9.2s during the hover phase, which caused a 0.23m and 0.37m disturbance in y direction, respectively, and roughly 0.15m distance in the z direction in the 2nd disturbance. Compare with the payload size, it can be regarded as a large disturbance. The payload is able to return to hover within 2s. This can be clearly observed from both the position and orientation response.

Positions of the four quadrotors is shown in Fig. 3.21. Notice that at timestamp 5.5s and 9.2s, in order to keep hovering at the planned position, the payload commanded a relatively large position change to the quadrotors to correct the disturbance.

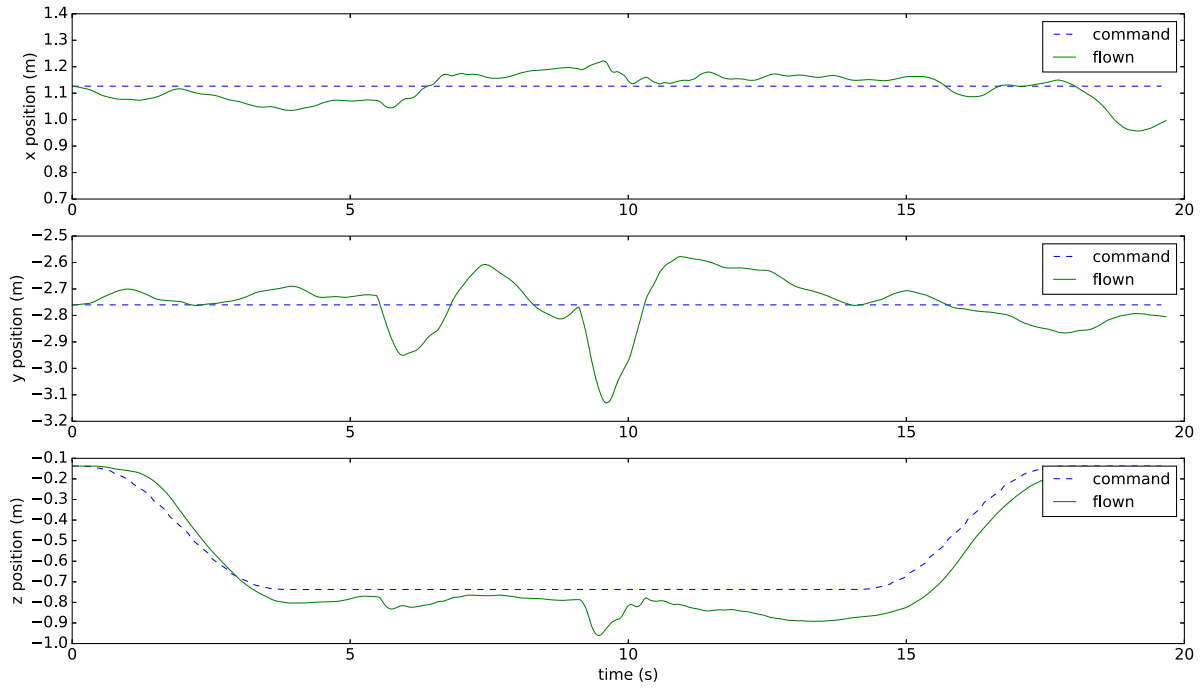


Figure 3.19. Payload position with impulse disturbances occurring at 5.5 s and at 9.2 s

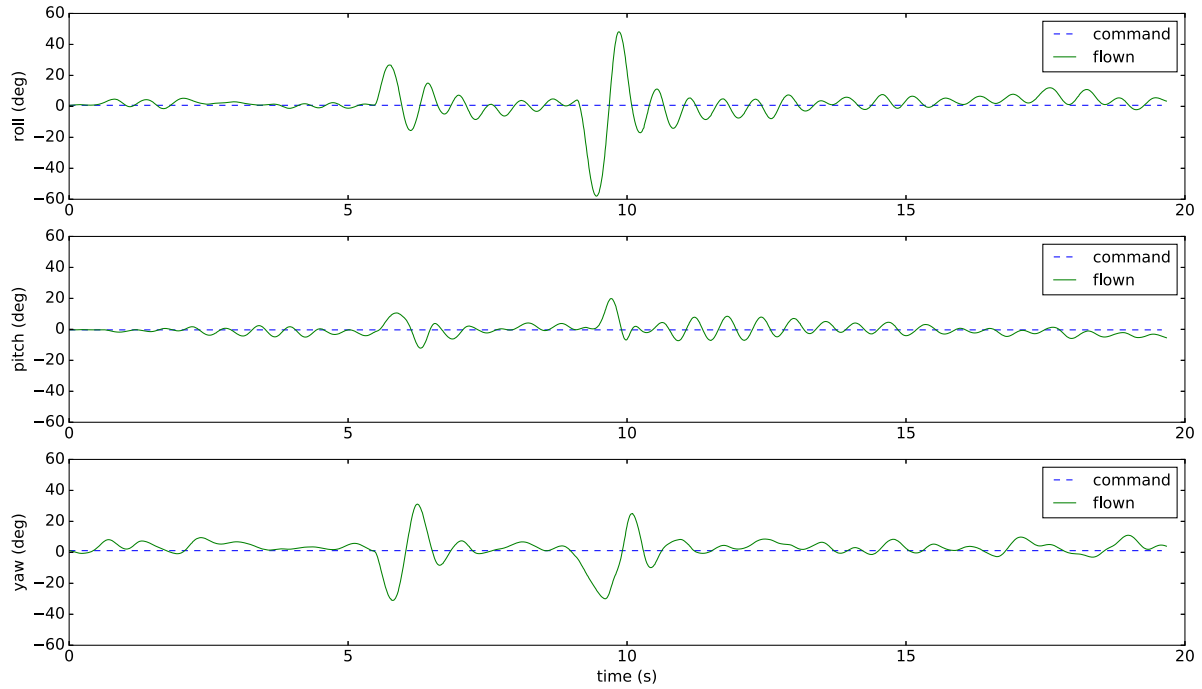


Figure 3.20. Payload orientation with impulse disturbances occurring at 5.5 s and at 9.2 s

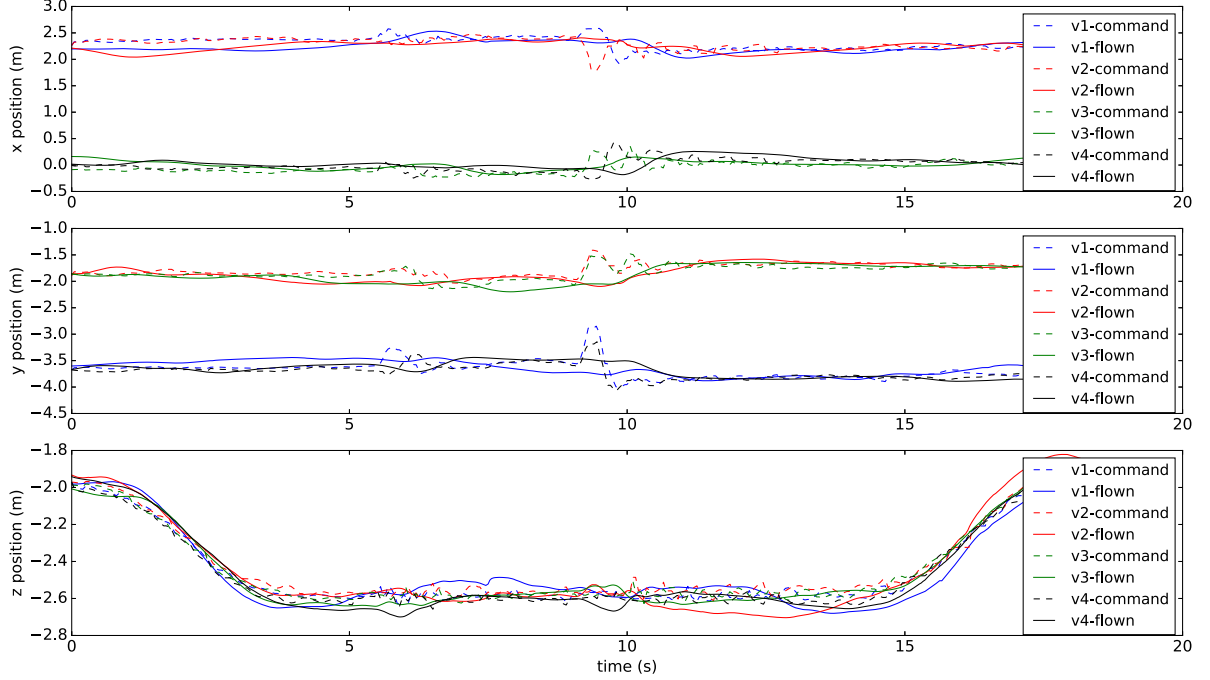


Figure 3.21. Position of the robots with impulse disturbances occurring at 5.5 s and at 9.2 s

The system is able to return to hover phase quickly even under large disturbance. Section 3.5.6 describes results of a flight test conducted outdoors showing ability to handle light winds.

3.5.4 Cooperative Transport with a Human-in-the-loop

A human operator is tasked to pilot the payload online during the FOLLOW_TRAJ state to show that human can be brought into the loop. Instead of tracking a pre-planned waypoints mission, the payload receives mission from the pilot. Specifically, the pilot gives velocities and yaw angle commands directly to the payload using a gamepad, Fig. 3.22. If no pilot command is given, the system should keep the current state and hover. In the end, the pilot decides when to land the system.

Fig. 3.23 shows payload velocity and yaw angle in inertial frame, with the blue dashed line indicating the pilot command obtained through the gamepad. At approximately 3s, the pilot commanded vertical velocity. At approximately 7s, the pilot sent a yaw motion command to the payload. The payload responded with a 40 degree rotation in the horizontal plane as commanded with 1s lag. Later at 14s, 21.5s and 24.2s, pilot commanded lateral velocities in x direction. At 15.5s, 17.5s and 26s, pilot commanded lateral velocities in y direction. It can be seen the payload behaved as commanded with



Figure 3.22. Human operator “flying” the payload directly.

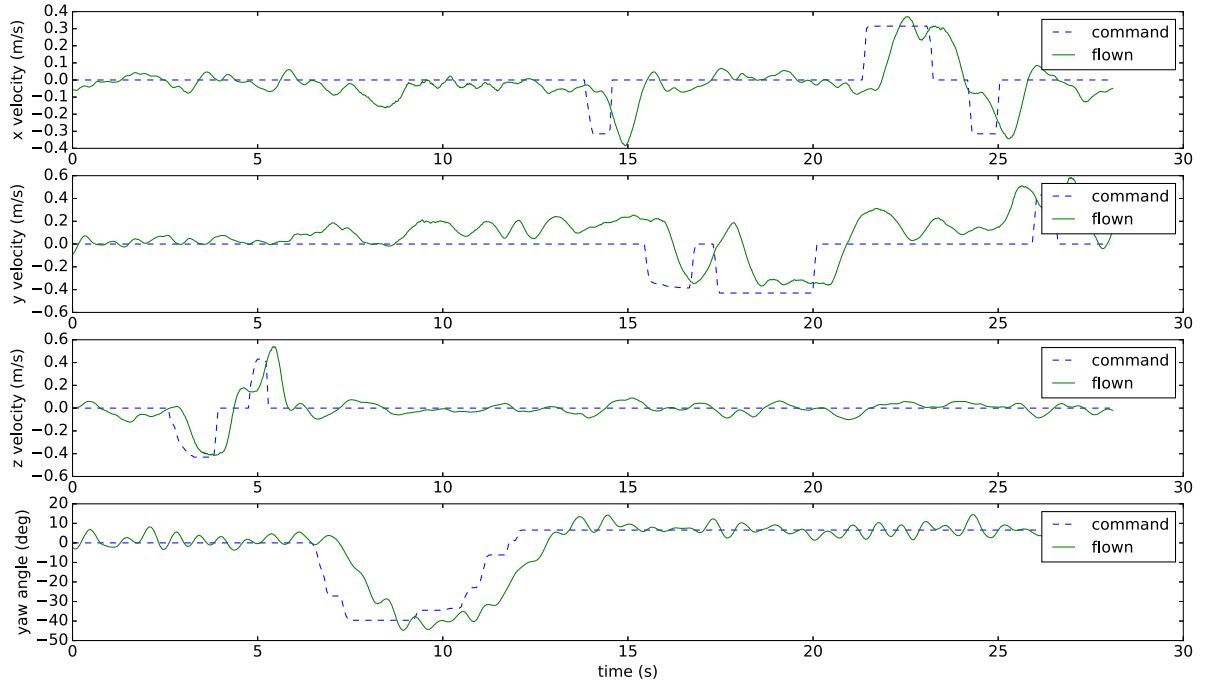


Figure 3.23. Payload velocity and yaw angle with human operator.

some of lag. This could be due to communication latency. Also note that no tuning of controller gains was undertaken.

This flight test demonstrates that human can be brought into the loop at several levels. In this test, the human operator not only handled the high level state machine, but also flew the payload in the FOLLOW_TRAJ phase, like flying a normal quadrotor. In other words, under load-leading control the whole multilift system can be operated as

Table 3.8. Optimization Solver Performance Comparison

average solver performance	iteration	solving time (s)
non-convex	4.16	0.0040
convex	2.00	0.0027

one single drone via payload commands.

3.5.5 Cooperative Transportation with Cable Internal Motion

The ability to change formation of the rotorcraft team adds significant operational flexibility in two ways: first, it permits operation in restricted spaces; second, changing cable cone angles allows changes in controllability of the payload [22].

In this experiment, the system is tasked with manipulating the payload through a sequence of maneuvers that include formation changes during flight. This results in changing constraints in the cable force optimization problem, and shows that the optimization problem can still be solved in real time as the formation changes.

The trajectory generator generated a smooth pre-computed trajectory for the payload and the cone trajectory for the multilift system, including take-off, hover, translation, formation change, translation, and landing. As the cone angles change, the equality constraints (3.7) in problem (3.4) will be change accordingly. Here, the formation cone angle is limited between 34° and 40° to account for both vehicle separation and the lifting capability. The implementation is obtained according to the analysis in Section 3.2. For the i^{th} cable,

$$\begin{aligned}\dot{e\mathbf{n}}_i &= \boldsymbol{\omega}_{n_i} \times e\mathbf{n}_i \\ \ddot{e\mathbf{n}}_i &= \dot{\boldsymbol{\omega}}_{n_i} \times e\mathbf{n}_i + \boldsymbol{\omega}_{n_i} \times (\boldsymbol{\omega}_{n_i} \times e\mathbf{n}_i) \\ \boldsymbol{\omega}_{n_i} &= \alpha_\omega (e\mathbf{n}_i \times \mathcal{Z}_e)\end{aligned}$$

where α_ω is a scalar defining the speed (positive α_ω denotes an expanding, or “blooming” cone; negative α_ω denotes a shrinking, or “withering” cone). It is chosen manually as $\alpha_\omega = \pm 2.0$ in this task.

Both non-convex and convex formulations for the cable force computation optimization problem are compared. Table. 3.8 shows a comparison of the solver performance while tracking performance is compared in Table. 3.9. Again the convex formation shows clear advantage in both computation and tracking performance.

Fig. 3.24(a) shows the cone angle of four cables. It can be seen that all the cable cones

Table 3.9. Tracking Performance Comparison

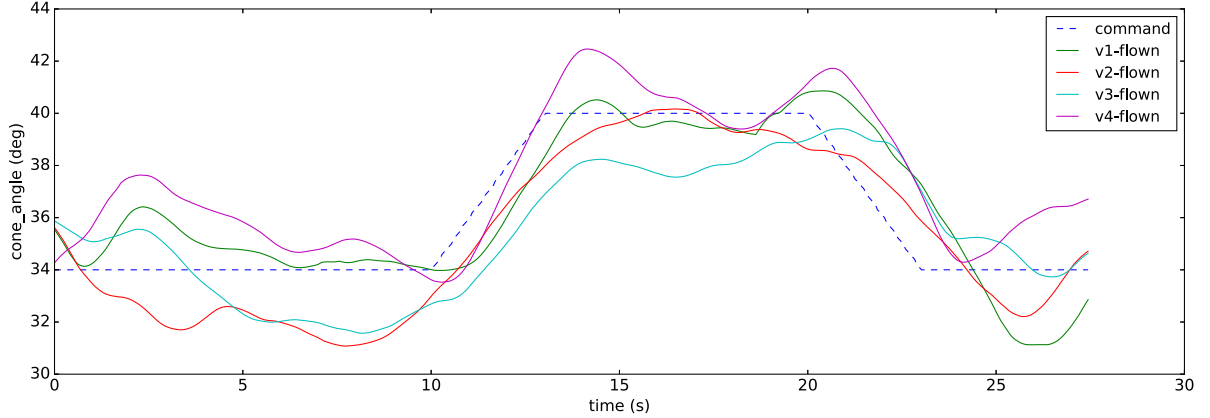
average tracking error	position (m)
non-convex	0.0791
convex	0.0599

are able to track the commanded cone angle. The formation of the multilift system opens like a blooming flower during the lateral translation then closes like a withering flower before descending. The tracking error of the payload when following such a trajectory stays within a few centimeters, shows in Fig. 3.24(b). Notice that in the blooming and shrinking phase, the formation opens up and closes down without moving the payload. The flight test demonstrates cable force computer has the ability to solve a changing constraints optimization problem in real time onboard.

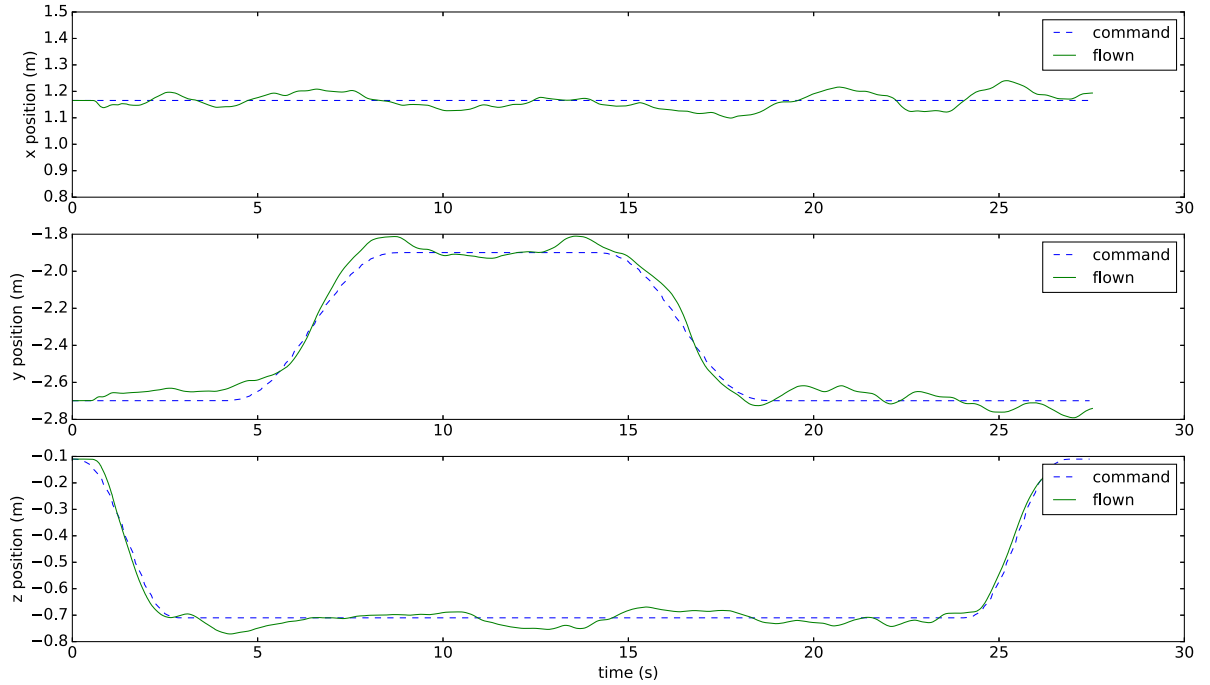
3.5.6 Outdoor Lateral Trajectory Tracking

An outdoor flight test was performed to show the system performance in more realistic operational conditions. The flight test was conducted in an open field near the Penn State Arboretum, Fig. 3.25, Fig. 3.26. At the time of the test skies were mostly cloudy and a light breeze (7 km/h) was blowing from the south-south-west Fig. 3.27 [8]. The system configuration differed from indoor testing in two ways: position and velocity information was obtained using Drotek M8P RTK GPS modules and longer cables (3.2 m vs. 1.8 m) were used.

In this experiment, the system is tasked with lifting the payload and tracking a lateral path at a ground speed ≤ 0.3 m/s (note that this is significantly less than the wind speed of 1.94 m/s) then translating back and descending to land. Fig. 3.28 shows the payload horizontal velocity tracking error in the world fixed north-east-down frame \mathcal{F}_e (the data sample frequency is 20Hz), with the wind vector indicated. The system is at low altitude (1.5 m above ground) so that only the horizontal wind is considered. Velocity error remains small, with mean error (0.0106, 0.0010) m/s in the north and east directions, respectively and standard deviation (0.1005, 0.0925) m/s in the north and east directions, respectively. Fig. 3.29 shows the corresponding payload horizontal position tracking performance in the payload inertial frame \mathcal{F}_{pe} (forward-right-down frame centered at the payload initial position). Steady hover is shown for several seconds before translation begins. The payload tracks the planned trajectory with error less than 0.3m in the x-direction. Slightly larger tracking error shows in the y-direction due to the larger wind velocity component. Considering the RTK GPS positioning error (≤ 0.1 m),



(a) Cone angle of four cables



(b) Payload position

Figure 3.24. Formation changeing test

this is a fairly good performance. The position of the robots are shown in Fig. 3.30 with the tracking error less than 0.25m.

3.6 Summary

This chapter presented the hierarchical load-leading control strategy for payload with known inertial properties. Here, “slung load leading” refers to a leader-follower control



Figure 3.25. Test field near Penn State Arboretum



Figure 3.26. Outdoor lateral trajectory tracking

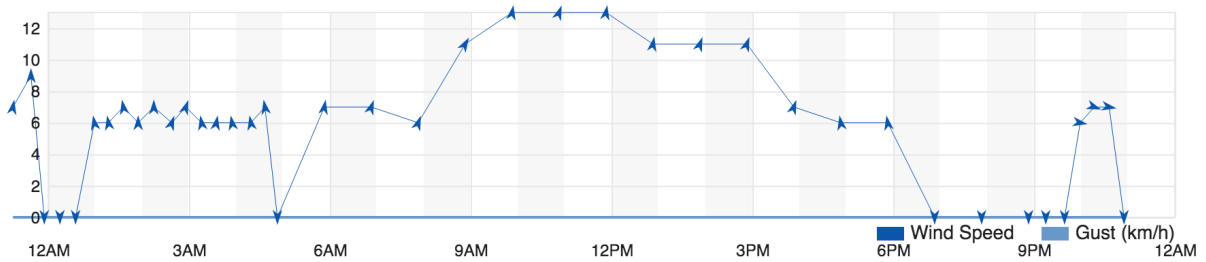


Figure 3.27. Test day wind condition [8]

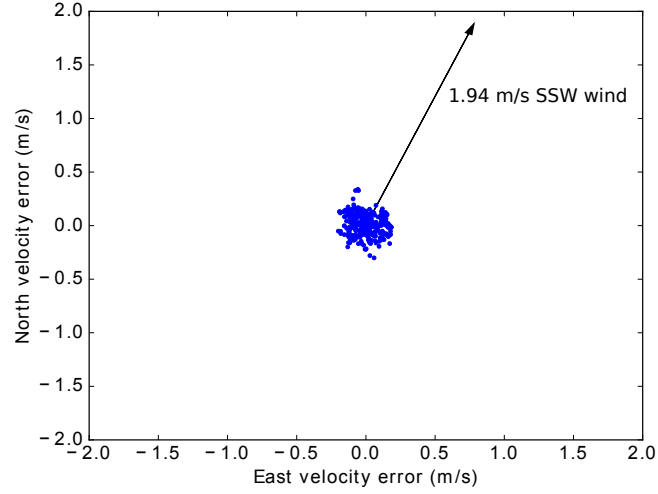


Figure 3.28. Payload horizontal velocity tracking error, with wind shown as vector

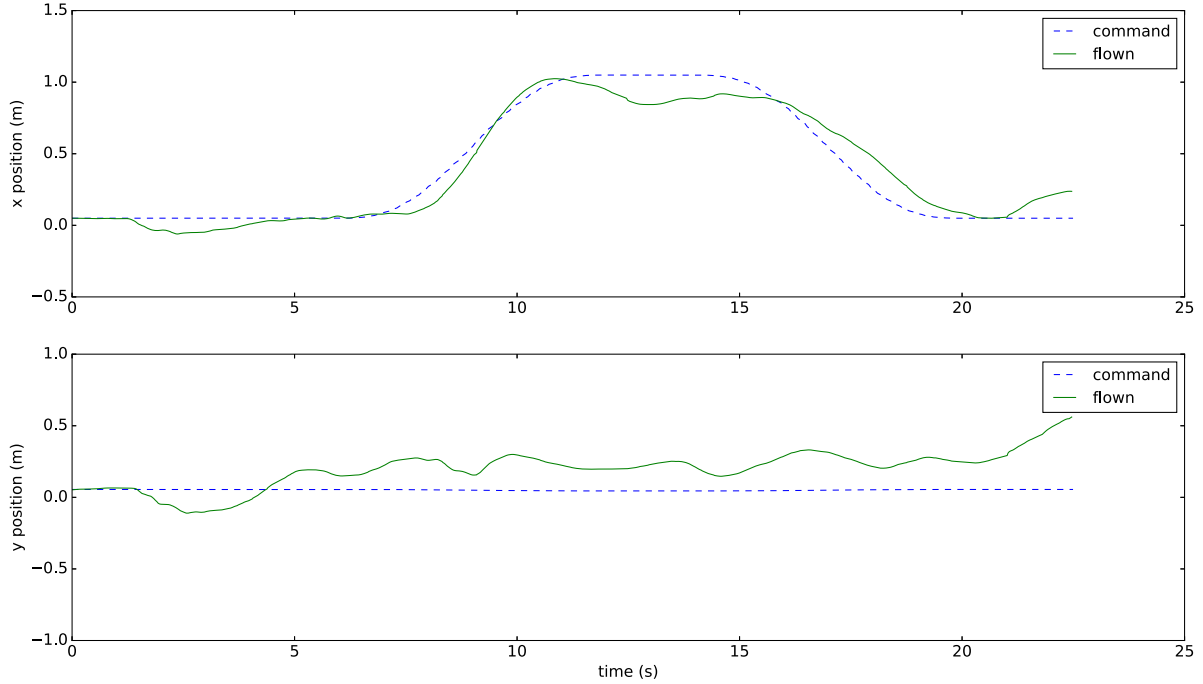


Figure 3.29. Payload horizontal position

architecture where the payload is the leader. Thus rather than treating the payload as a disturbance acting on a rotorcraft formation, the payload is explicitly controlled, either to follow a desired trajectory or via human-in-the-loop control.

The cable force computation is defined as an optimization problem. This optimization problem is shown to be non-convex (although it is nearly convex if cables are constrained

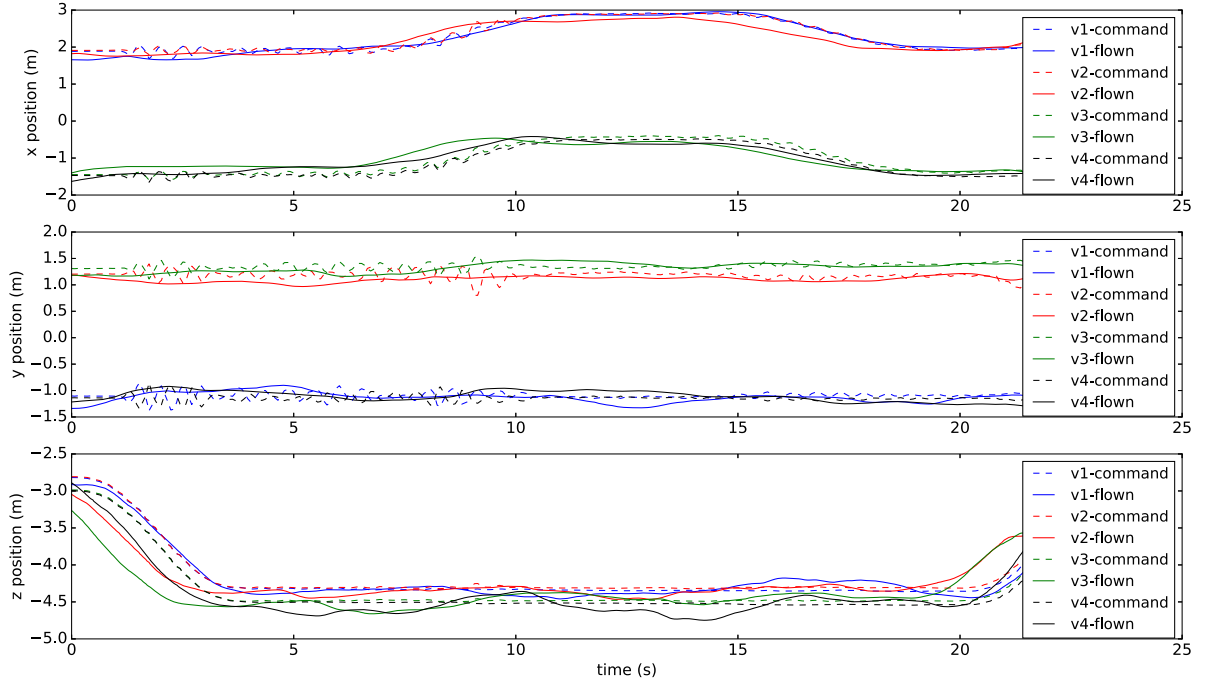


Figure 3.30. Position of the robots

to remain within a small angle of a nominal condition). Additional constraints are given that “convexify” the cable force optimization problem.

Desired rotorcraft states based on payload states and the required cable forces are derived for a general cable. Three special cases (inextensible cable, spring/damper cable model, and rigid formation) are shown to be derivable from the general case.

Controllers based on proportional-integral-derivative feedback control with an acceleration feed forward are implemented for both the payload and rotorcraft. The analysis based on singular perturbation shows the full closed-loop system can track the reference exponentially within some error bound.

A hardware implementation that uses four small multirotors and a payload is described. All computations associated with the coordinated transport problem are hosted on single board computers carried onboard the payload and rotorcraft so that the whole transportation team is self-contained.

Flight tests conducted in an indoor motion capture studio as well as outdoor demonstrate the utility of the approach. Indoor results showing trajectory following, disturbance rejection, human-in-the-loop control of the payload, and formation change are presented. The convex formulation of the cable force optimization problem is shown to have faster convergence of required cable forces and is shown to be more robust to the assumed

initial guess. A disturbance rejection test (where the payload is disturbed by an external impulse) shows quick return to stable hover. Human-in-the-loop control (where the human operator gives speed and heading commands to the payload via a joystick interface) shows good control and workload similar to that of flying a generic multirotor in attitude stabilized mode. Tests demonstrating formation change show that the system operates well even during in-flight changes of cable geometry. Stable payload hover is achieved and the cable force optimization problem is solved in real time onboard the payload.

Results of an outdoor flight using GPS as the main position/velocity sensor showed that hover and lateral translation commands were well-tracked even in the presence of a light breeze (7 km/h).

Chapter 4 |

Slung Load Inertial Property Estimation

This chapter presents inertial properties estimation for an unknown slung load. This is a critical technology for enabling cooperative aerial transportation with little a priori payload information. The load-leading framework of Chapter 3 assumes that payload inertial properties (mass, center of mass location, moments of inertia) are known. Here, a method to estimate these parameters is described. This is challenging because: limited system payload capacity restricts the weight and physical dimension of the sensors can be carried in the context of small aerial vehicles; the complexity and coupling of the system imposes difficulty on system excitation and parameter isolation; the conflict between adequate excitation and ensuring that the system does not exceed actuation capabilities. This chapter presents: (a) an analysis on payload motion and system perception; (b) an indirect method for estimating cable force without any tension load cells; (c) an estimation strategy to estimate different inertial parameters under different payload motion patterns; (d) indoor hardware experiments to validate the developed algorithm; (e) controller compensation tests with estimated parameters involved into the closed-loop system.

In Section 4.1, a general payload motion analysis in response to cable forces provides insight into the excitation and resulting motion required to estimate payload inertial properties. Benefiting from the load-leading platform, the sensors carried by the payload provides real-time payload motion information. To compensate for the lack of a cable tension sensor, an indirect method on the rotorcraft sides to estimate the cable force is described. This is accomplished by analyzing the rotorcraft motion given the knowledge of flight status from the onboard sensors.

A sequence of flight maneuvers is designed in Section 4.2 to make different inertial

properties observable using different payload motion patterns. Payload mass can be estimated in steady hover while center of mass and moments of inertia need payload rotation motion. Three estimation algorithms, including least-squares method, maximum likelihood and Kalman filter are derived for the estimation of various inertial properties with different dynamical characteristics.

In Section 4.3, flight tests in an indoor motion capture studio compare results of inertial properties estimation for these derived estimation methods under various excitation showing the estimator performance. Payload mass estimation occurs in steady hover. Then pre-planned trajectories that excite the payload rotation motion are executed by the system to estimate the slung load center of mass location and the moments of inertia.

Controller compensation tests for the compensated and uncompensated cases are then conducted and compared in Section 4.4 to show the benefit of system performance by incorporating the estimated payload inertial properties. A sine wave path and a figure 8 pattern are flown for different system configurations with increasing system frequency.

Section 4.5 summarizes results of this chapter. The energy efficient cooperative aerial transportation is discussed in Chapter 5 addressing trajectory planning based on load distribution.

4.1 System Motion and Perception

Proper perception must be established before the payload inertia property estimation could be performed. The load-leading platform designed in Chapter 3 provides a convenient platform for payload parameter estimation. The sensors carried by the payload provide real-time information for payload motion on a reference point. This information (payload response) can be used to derive the payload inertia property based on the dynamics given the input (external forces). Payload states with respect to the center of mass can thus be obtained given the states of the reference point and the inertial property.

4.1.1 Slung Load Motion and Sensing

4.1.1.1 Slung Load Motion

For an unknown payload, the body fixed frame \mathcal{F}_L may not be centered at the payload center of mass. It could be the payload geometry center, or any other convenient reference

point on the payload. Here, \mathcal{F}_L is chosen to be fixed at the point where the autopilot is mounted, with the body axes $\{\mathbf{x}_L, \mathbf{y}_L, \mathbf{z}_L\}$ pointing forward, right and down. The dynamics of the multilift slung load has been derived in Chapter 2 (2.1). Recall that the payload dynamics are

$$\mathbf{M}_L \ddot{\mathbf{x}} + \mathbf{C}_L \dot{\mathbf{x}} = {}^e \mathbf{W}_t \quad (4.1)$$

where

$$\mathbf{M}_L = \begin{bmatrix} m_L \mathbf{I}_3 & -m_L [{}^e \mathbf{r}_L]^\times \\ m_L [{}^e \mathbf{r}_L]^\times & {}^e \mathbf{J}_{cm} - m_L [{}^e \mathbf{r}_L]^\times [{}^e \mathbf{r}_L]^\times \end{bmatrix} \quad (4.2)$$

$$\mathbf{C}_L \dot{\mathbf{x}} = \begin{bmatrix} m_L [\boldsymbol{\omega}]^\times [\boldsymbol{\omega}]^\times {}^e \mathbf{r}_L \\ \boldsymbol{\omega} \times ({}^e \mathbf{J}_{cm} - m_L [{}^e \mathbf{r}_L]^\times [{}^e \mathbf{r}_L]^\times) \boldsymbol{\omega} \end{bmatrix} \quad (4.3)$$

$$\mathbf{W}_g = \begin{bmatrix} 0 & 0 & m_L g & m_L r_y g & -m_L r_x g & 0 \end{bmatrix}^T \quad (4.4)$$

$${}^e \mathbf{J}_{cm} = {}^e \mathbf{R}_L {}^L \mathbf{J}_{cm} {}^L \mathbf{R}_e \quad (4.5)$$

For convenience of the derivation of this chapter, denote the total external wrench on the payload about \mathcal{O}_L as ${}^e \mathbf{W}_t = [{}^e \mathbf{F}_p \ {}^e \mathbf{M}_p]$. Notice that ${}^e \mathbf{W}_t$ includes the gravity wrench ${}^e \mathbf{W}_g = [{}^e \mathbf{G}_g \ {}^e \mathbf{M}_g]$ and the wrench generated by cable force ${}^e \mathbf{W}_f = [{}^e \mathbf{f}_f \ {}^e \mathbf{M}_f]$.

It can be seen from (4.2)(4.3) that the payload dynamics relies directly on the relative position between the center of mass and the reference point.

4.1.1.2 Sensing

The autopilot mounted on the payload can provide the real-time linear acceleration and angular rates. The angular acceleration can be obtained by numerically differentiating the angular rates. Here a first-order low pass filter was implemented after directly differentiating the angular rates to obtain angular acceleration. A similar approach was conducted in [25]. Angular acceleration could also be obtained directly by using multiple accelerometers instead of differentiation [68, 69], but that requires additional sensors and computation..

Let us consider two points on the payload: center of mass \mathcal{O}_g and the reference point (body frame origin) \mathcal{O}_L , see Fig. 4.1. Denote the linear acceleration of \mathcal{O}_g as \mathbf{a}_o , the linear acceleration of \mathcal{O}_L as \mathbf{a}_L ($\mathbf{a}_L = {}^e \ddot{\mathbf{p}}$). Also note the angular acceleration $\dot{\boldsymbol{\omega}}$ as $\boldsymbol{\alpha}$.

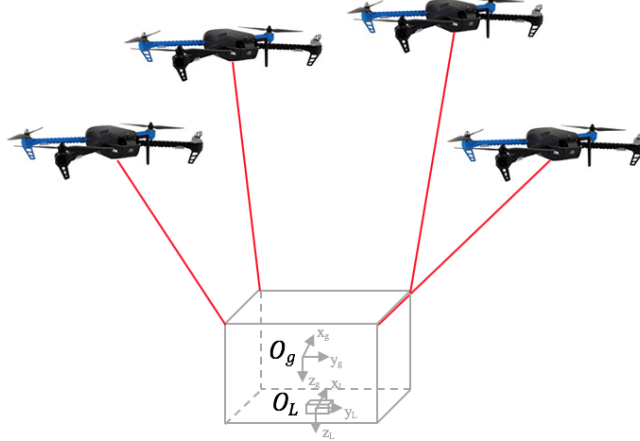


Figure 4.1. Diagram of multilift with electronics attached on payload

Newton's equation tells us

$$\mathbf{a}_L = \mathbf{a}_o - \boldsymbol{\alpha} \times {}^e\mathbf{r}_L - \boldsymbol{\omega} \times \boldsymbol{\omega} \times {}^e\mathbf{r}_L \quad (4.6)$$

where

$$\mathbf{a}_o = \frac{{}^e\mathbf{F}_p}{m_L} \quad (4.7)$$

from Newton's Second law. Therefore, if the total force acting on the payload is known as well as the payload angular rate and angular acceleration, the position ${}^e\mathbf{r}_L$ and the payload mass m_L can be estimated. Since the autopilot onboard the payload can provide the acceleration of the reference point and the payload angular rate as well as angular acceleration, parameter estimation can be implemented. Notice that if $1/m_L$ is treated as unknown instead of m_L , all the unknown parameters appear linearly.

Similarly, Euler equation can be expressed as

$${}^e\mathbf{J}_{cm}\boldsymbol{\alpha} = -\boldsymbol{\omega} \times {}^e\mathbf{J}_{cm}\boldsymbol{\omega} + {}^e\mathbf{M}_p - {}^e\mathbf{r}_L \times {}^e\mathbf{F}_p \quad (4.8)$$

By knowing the total force and moment acting on \mathcal{O}_L and the payload angular acceleration $\boldsymbol{\alpha}$, the moments of inertia matrix about the center of mass principle axes can be estimated.

4.1.2 Cable Force Estimation

From (4.6), knowledge of total force and moment acting on the payload is the key to estimating payload inertial parameters. For the multilift system, the total force and moment acting on the payload comes directly from the cable forces. If each of the cable forces can be computed, the total force and moment acting on the payload can be obtained through payload geometry.

The most straight forward method to obtain cable force is through a tension load cell along each cable. However, adding load cells increases the total weight of the whole system, which reduces payload capacity. It also increases total system cost. In addition, the cable direction must also be obtained. Here, an indirect method that uses rotorcraft dynamics is used to compute cable force.

4.1.2.1 Indirect Method for Cable Force Estimation

Rotorcraft dynamics were derived in Chapter 2 (2.6)(2.7), recall that the dynamics of the i^{th} rotorcraft can be expressed as

$$\begin{aligned} m_i \mathbf{\ddot{r}}_i &= -T_i \mathbf{R}_{V_i} \mathbf{Z}_{V_i} + m_i g \mathbf{Z}_e + {}^e \mathbf{f}_i + {}^e \mathbf{f}_{Aero,i} \\ {}^{V_i} \mathbf{J}_i \boldsymbol{\omega}_i &= {}^{V_i} \boldsymbol{\tau}_i - \boldsymbol{\omega}_i \times {}^{V_i} \mathbf{J}_i \boldsymbol{\omega}_i \end{aligned}$$

During low speed/low wind flight (e.g. indoor flight as discussed in this chapter), $\mathbf{f}_{Aero,i}$ can be neglected. The remaining forces are gravity $\mathbf{G}_{g,i} = m_i g \mathbf{Z}_e$, thrust \mathbf{T}_i and cable force \mathbf{f}_i as shown in Fig. 4.2.

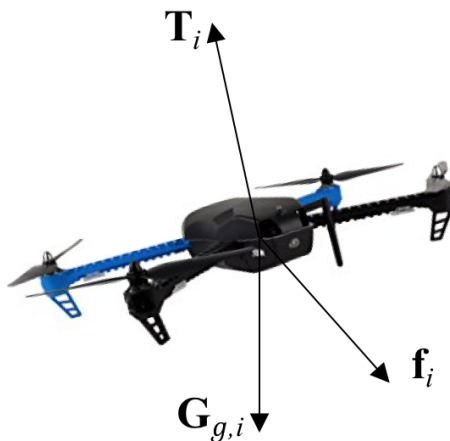


Figure 4.2. Force analysis on one quadcopter

Low speed rotorcraft dynamics can be written as

$$T_i \mathbf{d}_{T_i} + f_i \mathbf{d}_{f_i} + \mathbf{G}_{g,i} = m_i \mathbf{a}_{o_i} \quad (4.9)$$

where f_i is the magnitude of cable tension. $\mathbf{d}_{T_i} = -{}^e\mathbf{R}_{V_i} \mathcal{Z}_{V_i}$ and \mathbf{d}_{f_i} are the directions of thrust and cable force. $\mathbf{a}_{o_i} = {}^e\ddot{\mathbf{r}}_i$ is the acceleration of the center of mass of the rotorcraft.

It is assumed that all cables are under tension and that the cable attachment at the rotorcraft is at the rotorcraft's center of mass. The rotorcraft used in the study have a 0.55m motor to motor diameter [70]. The cables are attached to the center of the bottom of the rotorcraft, approximately 1cm below the geometric center of the vehicle. The rotorcraft mass is assumed to be fixed for the battery powered vehicle.¹

During flight, the rotorcraft acceleration and the orientation can be obtained from the onboard autopilot. ${}^e\mathbf{R}_{V_i}$ and \mathbf{a}_{o_i} can thus be obtained. At the same time, the navigation system can locate the rotorcraft center of mass ${}^e\mathbf{r}_i$ and payload reference point ${}^e\mathbf{p}$. The direction of the cable or the cable force can thus be obtained from the position difference of two cable attachment points. The position of the i^{th} cable attachment on the payload is

$${}^e\mathbf{p}_{att} = {}^e\mathbf{p} + {}^e\mathbf{R}_{V_i} {}^L\mathbf{g}_i \quad (4.10)$$

Hence,

$$\mathbf{d}_{f_i} = \frac{{}^e\mathbf{p}_{att} - {}^e\mathbf{r}_i}{\| {}^e\mathbf{p}_{att} - {}^e\mathbf{r}_i \|}$$

The unknowns in (4.9) are the thrust T_i and cable tension f_i . Rearranging slightly shows that they can be found using least-squares:

$$[\mathbf{d}_{T_i} \quad \mathbf{d}_{f_i}] \begin{bmatrix} T_i \\ f_i \end{bmatrix} = m_i \mathbf{a}_{o_i} - \mathbf{G}_{g,i} \quad (4.11)$$

4.1.2.2 Cable Force Uncertainty Quantification

Quantifying the uncertainty of the estimated cable force would provide help for the payload parameter estimation. There are uncertainties on rotorcraft thrust direction \mathbf{d}_{T_i} due to noise in rotorcraft attitude measurement; on cable force direction \mathbf{d}_{f_i} due to the

¹For larger vehicles when the cable attachment point is not close to the center of mass, a general force balance analysis is needed. Installing tension load cells would also be a straightforward method since the payload capacity of larger vehicles is not as limited. In the case for full-scale fuel burning rotorcraft which have variable internal passengers/cargo, rotorcraft mass is no longer fixed. Cable force measurement would also be needed.

noise from the payload position and orientation and the rotorcraft position measurement; and the uncertainty caused by the accelerometer noise. All of those source of uncertainties will affect the cable force estimation.

To avoid excessive use of subscripts, substitute $\mathbf{d}_{Ti} = \mathbf{a}$, $\mathbf{d}_{fi} = \mathbf{b}$, and $m_i \mathbf{a}_{oi} - \mathbf{G}_{g,i} = \mathbf{y}$ to define a general least-squares problem with T and F as scalar unknowns:

$$\mathbf{a}T + \mathbf{b}F = \mathbf{y} \quad (4.12)$$

where both \mathbf{a} and \mathbf{b} are Gaussian random variables with mean $\boldsymbol{\mu}_a$ and $\boldsymbol{\mu}_b$, covariance matrices Σ_a , Σ_b , i.e. $\mathbf{a} \sim \mathcal{N}(\boldsymbol{\mu}_a, \Sigma_a)$, $\mathbf{b} \sim \mathcal{N}(\boldsymbol{\mu}_b, \Sigma_b)$.

Taking the first order Taylor series expansion of (4.12):

$$(\boldsymbol{\mu}_a + \boldsymbol{\delta}_a)(\hat{T} + \delta T) + (\boldsymbol{\mu}_b + \boldsymbol{\delta}_b)(\hat{F} + \delta F) = \hat{\mathbf{y}} + \delta \mathbf{y} \quad (4.13)$$

where $\hat{\cdot}$ is the nominal value of a variable, $\boldsymbol{\delta}_a \sim \mathcal{N}(\mathbf{0}, \Sigma_a)$, $\boldsymbol{\delta}_b \sim \mathcal{N}(\mathbf{0}, \Sigma_b)$. Removing the higher order terms, (4.13) becomes:

$$(\boldsymbol{\mu}_a \hat{T} + \boldsymbol{\mu}_b \hat{F}) + \boldsymbol{\mu}_a \delta T + \boldsymbol{\mu}_b \delta F + \hat{T} \boldsymbol{\delta}_a + \hat{F} \boldsymbol{\delta}_b = \hat{\mathbf{y}} + \delta \mathbf{y} \quad (4.14)$$

Notice that $\hat{\mathbf{y}} = \hat{\boldsymbol{\mu}}_a \hat{T} + \hat{\boldsymbol{\mu}}_b \hat{F}$. This shows that the expected values of T and F can be solved using least-squares.

The uncertainty in computed thrust and cable tension can now be obtained:

$$\boldsymbol{\mu}_a \delta T + \boldsymbol{\mu}_b \delta F + \hat{T} \boldsymbol{\delta}_a + \hat{F} \boldsymbol{\delta}_b = \delta \mathbf{y} \quad (4.15)$$

Rewriting,

$$[\boldsymbol{\mu}_a \quad \boldsymbol{\mu}_b] \begin{bmatrix} \delta T \\ \delta F \end{bmatrix} = \delta \mathbf{y} - \hat{T} \boldsymbol{\delta}_a - \hat{F} \boldsymbol{\delta}_b = \mathbf{e} \quad (4.16)$$

Here $\mathbf{e} \sim \mathcal{N}(\mathbf{0}, \Sigma_e)$, where

$$\Sigma_e = \Sigma_y + \hat{T} \Sigma_a \hat{T}^T + \hat{F} \Sigma_b \hat{F}^T \quad (4.17)$$

Letting the unknown vector $\mathbf{x}_\mu = [\delta T \quad \delta F]^T$, where $\mathbf{x}_\mu \sim \mathcal{N}(\mathbf{0}, \Sigma_{x_\mu})$. Therefore, the uncertainty of the unknowns estimated by the least-squares method is:

$$\Sigma_{x_\mu} = (\mathbf{C}^T \mathbf{C})^{-1} \mathbf{C}^T \Sigma_e \mathbf{C} (\mathbf{C}^T \mathbf{C})^{-1} \quad (4.18)$$

where $\mathbf{C} = [\boldsymbol{\mu}_a \ \boldsymbol{\mu}_b]$. Note that $\mathbf{y} = m_i \mathbf{a}_{o_i} - \mathbf{G}_{g,i}$ is obtained from an IMU carried on board the rotorcraft and the assumed-known mass of the rotorcraft, hence Σ_y is the sensor noise of the IMU. Furthermore, $\mathbf{a} = \mathbf{d}_{Ti}$ is obtained from the autopilot's estimate of vehicle attitude and $\mathbf{b} = \mathbf{d}_{fi}$ is obtained from the difference in position of the cable attachment on payload and rotorcraft. Hence Σ_a and Σ_b can be obtained from the uncertainty in vehicle orientation and position relative to the payload, respectively.

Examination of the uncertainty shows: (1) the magnitude of the uncertainty in cable force and thrust is dependent on the magnitudes of those forces, hence large forces will lead to large uncertainties; (2) the uncertainty in cable force depends on the measurement noise of the IMU; (3) uncertainty in computed cable force depends on uncertainty in vehicle orientation.

4.2 Estimation of Slung Load Parameters

Three approaches are applied to the problem of payload parameter estimation: (1) linear least-squares, that estimates $\frac{1}{m_L}$, \mathbf{r}_L , $\frac{1}{J_{xx}}$, $\frac{1}{J_{yy}}$, and $\frac{1}{J_{zz}}$; (2) maximum likelihood, to directly address the coefficient uncertainty in the payload mass estimation problem; (3) Kalman filter, which can be implemented either as a linear KF when estimating $\frac{1}{m_L}$, \mathbf{r}_L , $\frac{1}{J_{xx}}$, $\frac{1}{J_{yy}}$, and $\frac{1}{J_{zz}}$ or as a nonlinear filter (here, an Unscented Kalman filter) to directly estimate mass properties that appear as non-linear terms.

4.2.1 Least-squares Method for Parameter Estimation

In (4.6), the unknown parameters appear linearly if $1/m_L$ is treated as unknown instead of m_L . Least-squares method can thus be used for the parameter estimation. The general least-squares problem is given by

$$\tilde{\mathbf{y}}(k) = \mathbf{H}(k)\boldsymbol{\theta} \quad (4.19)$$

$$\tilde{\mathbf{y}}(k) = \mathbf{H}(k)\hat{\boldsymbol{\theta}} + \mathbf{e}(k) \quad (4.20)$$

where k represents the time step, $\boldsymbol{\theta} \in \mathbb{R}^n$ is the parameter vector, $\tilde{\mathbf{y}} \in \mathbb{R}^m$ and \mathbf{H} are the measurements. \mathbf{e} is the residual error. The goal is to find the estimated parameter vector $\hat{\boldsymbol{\theta}}$.

An optimal choice for the unknown parameters that minimize the sum of square of

the residual errors is selected as,

$$\min_{\hat{\theta}} J(k) = \frac{1}{2} \sum_{i=1}^k \lambda^{k-i} \mathbf{e}(k)^T \mathbf{e}(k) = \frac{1}{2} \sum_{i=1}^k (\tilde{\mathbf{y}}(i) - \mathbf{H}(i)\hat{\theta})^T (\tilde{\mathbf{y}}(i) - \mathbf{H}(i)\hat{\theta}) \quad (4.21)$$

based on Gauss's principle of least-squares [71]. Here, λ is a forgetting factor such that $0 < \lambda \leq 1$, which gives more weight to the most recent data. Notice that the cost function is quadratic with the residual error over k time steps and the m equations for each time step. A summary of least-squares estimation is given [71, 72].

4.2.1.1 Batch Case

For the batch least-squares problem with forgetting factor $\lambda = 1$ over k times steps, the estimated solution is

$$\hat{\theta} = \hat{\Phi}^{-1} \hat{\gamma} \quad (4.22)$$

$$\mathbf{P}^{-1} = \sum_{i=1}^k \mathbf{H}(i)^T \mathbf{W} \mathbf{H}(i) \quad (4.23)$$

where

$$\begin{aligned} \hat{\Phi} &= \frac{1}{mk} \sum_{i=i}^k \mathbf{H}(i)^T \mathbf{W} \mathbf{H}(i) \\ \hat{\gamma} &= \frac{1}{mk} \sum_{i=1}^k \mathbf{H}(i)^T \mathbf{W} \tilde{\mathbf{y}}(i) \end{aligned}$$

\mathbf{W} is a weight matrix that accounts for measurement error.

4.2.1.2 Sequential Case

For the recursive least-squares scenario, e.g. the measurements are available sequentially, the estimated solution is

$$\hat{\theta}(k+1) = \hat{\theta}(k) + \mathbf{K}(k+1)(\tilde{\mathbf{y}}(k+1) - \mathbf{H}(k+1)\hat{\theta}(k)) \quad (4.24)$$

where

$$\begin{aligned} \mathbf{K}(k+1) &= \mathbf{P}(k) \mathbf{H}^T(k+1) (\mathbf{H}(k+1) \mathbf{P}(k) \mathbf{H}^T(k+1) + \mathbf{W}^{-1}(k+1))^{-1} \\ \mathbf{P}(k+1) &= (\mathbf{I} - \mathbf{K}(k+1) \mathbf{H}(k+1)) \mathbf{P}(k) \end{aligned}$$

or

$$\mathbf{P}^{-1}(k+1) = \mathbf{P}^{-1}(k) + \mathbf{H}^T(k+1)\mathbf{W}(k+1)\mathbf{H}(k+1)$$

4.2.1.3 Experimental Condition

The system must be properly excited so that the unknown parameters can be estimated [72]. In fact, the system is persistently excited if

$$\lim_{k \rightarrow \infty} \frac{1}{k} \sum_{i=1}^k \mathbf{H}(i)^T \mathbf{H}(i) > 0 \quad (\text{positive definite}) \quad (4.25)$$

This persistent excitation condition guarantees that $\hat{\Phi}$ is invertible in (4.22) and the covariance matrix does not go to infinity in (4.24).

4.2.2 Maximum Likelihood Estimation

The standard least-squares problem (4.19) assumes that there is no uncertainty in the coefficient matrix \mathbf{H} . Although this situation occurs in many general systems, this assumption may not be true for the mass estimation problem discussed in this dissertation. In fact, the coefficients in the payload mass estimation problem are either estimated cable force or payload angular rate and angular acceleration obtained from the sensors (4.6), which must contain estimated or measurement errors. To address the coefficient uncertainty and achieve higher accuracy, a maximum likelihood method is derived for payload mass estimation.

Let us consider the problem of finding optimal value of parameters given the noise in input-output data. In this regard, the problem of fitting a straight line is through noisy data points:

$$\tilde{x}_i = x_i + \nu_1, \quad i = 1, 2, \dots, N \quad (4.26)$$

$$\tilde{y}_i = y_i + \nu_2 \quad (4.27)$$

where, x_i and y_i represent the true coordinates of the a point while \tilde{x}_i and \tilde{y}_i represent the measured data points. ν_1, ν_2 represent data noise which are assumed to be Gaussian random variables with joint density function given as:

$$p(\nu_1, \nu_2) = \mathcal{N} \left(\begin{bmatrix} \nu_1 \\ \nu_2 \end{bmatrix}; \begin{bmatrix} 0 \\ 0 \end{bmatrix}, \begin{bmatrix} \sigma_1^2 & \sigma_{12} \\ \sigma_{21} & \sigma_2^2 \end{bmatrix} \right) \quad (4.28)$$

The problem is to find the best estimates for linear model parameters which explains the given data points:

$$y_i = mx_i + c \quad (4.29)$$

Notice that in this problem, the unknowns are x_i , m and c , the problem differs from the standard least-squares due to the noise in x_i .

The measurement model can be written as

$$y_i = mx_i + c \quad (4.30)$$

$$x_i = \tilde{x}_i - \nu_1 \quad (4.31)$$

$$y_i = \tilde{y}_i - \nu_2 \quad (4.32)$$

Substituting (4.31) and (4.32) into (4.30) leads to the following expression:

$$\tilde{y}_i - m\tilde{x}_i - c = \nu_2 - m\nu_1 \quad (4.33)$$

Define a new noise variable as:

$$\bar{\nu} = \frac{\nu_2 - m\nu_1}{\sqrt{\sigma_2^2 + \sigma_1^2 m^2 - 2m\sigma_{12}}} = \frac{\tilde{y}_i - m\tilde{x}_i - c}{\sqrt{\sigma_2^2 + \sigma_1^2 m^2 - 2m\sigma_{12}}} \quad (4.34)$$

$\bar{\nu}$ is a linear combination of two Gaussian random variables. This new variable is a normalization of (4.33). Hence, it is also a Gaussian random variable with mean and covariance

$$E[\bar{\nu}] = E\left[\frac{\nu_2 - m\nu_1}{\sqrt{\sigma_2^2 + \sigma_1^2 m^2 - 2m\sigma_{12}}}\right] = \frac{E[\nu_2 - mE[\nu_1]]}{\sqrt{\sigma_2^2 + \sigma_1^2 m^2 - 2m\sigma_{12}}} = 0 \quad (4.35)$$

$$E[\bar{\nu}^2] = E\left[\frac{(\nu_2 - m\nu_1)^2}{\sigma_2^2 + \sigma_1^2 m^2 - 2m\sigma_{12}}\right] = 1 \quad (4.36)$$

Notice that the new noise variable is a function of model unknown parameters, leading to a likelihood:

$$p(\bar{\nu}) = \mathcal{N}\left(\bar{\nu} = \frac{\tilde{y}_i - m\tilde{x}_i - c}{\sqrt{\sigma_2^2 + \sigma_1^2 m^2 - 2m\sigma_{12}}}; 0, 1\right) \quad (4.37)$$

Maximization of the log-likelihood leads to the minimization of the following cost function:

$$J = \sum_{i=1}^N \frac{(\tilde{y}_i - m\tilde{x}_i - c)^2}{\sigma_2^2 + \sigma_1^2 m^2 - 2m\sigma_{12}} \quad (4.38)$$

Notice that the cost function J is a function of only two unknowns m and c . The first order necessary condition leads to the following equations to solve for m and c directly from the measurement data.

$$\frac{\partial J}{\partial m} = \sum_{i=1}^N \left(\frac{2(\tilde{y}_i - m\tilde{x}_i - c)(-\tilde{x}_i)}{\sigma_2^2 + \sigma_1^2 m^2 - 2m\sigma_{12}} - \frac{(\tilde{y}_i - m\tilde{x}_i - c)^2(2\sigma_1^2 m - 2\sigma_{12})}{(\sigma_2^2 + \sigma_1^2 m^2 - 2m\sigma_{12})^2} \right) = 0 \quad (4.39)$$

$$\frac{\partial J}{\partial c} = \sum_{i=1}^N (-2(\tilde{y}_i - m\tilde{x}_i - c)) = 0 \quad (4.40)$$

4.2.3 Kalman Filter Method

A Kalman Filter (KF) is a Bayesian filter for a linear system with Gaussian noise and Gaussian initial conditions. It is primarily used for state estimation. These techniques consist of two fundamental steps: a prediction step by a postulated system model and a correction step by measurement update. Kalman filters can also be applied to the problem of parameter estimation by defining the unknown parameters as auxiliary state variables. Consider the payload inertial parameter estimation problem with unknown parameter $\boldsymbol{\theta}$. For a payload with fixed weight and mass distribution, the auxiliary dynamics are

$$\dot{\boldsymbol{\theta}} = \mathbf{0} \quad (4.41)$$

The process model of the extended discrete system can be presented as:

$$\boldsymbol{\theta}_{k+1} = \boldsymbol{\theta}_k + \mathbf{w}_k \quad (4.42)$$

$$\mathbf{y}_k = g(\boldsymbol{\theta}_k) + \boldsymbol{\nu}_k \quad (4.43)$$

where $\mathbf{w}_k = \mathcal{N}(\mathbf{0}, \mathbf{Q}_k)$ and $\boldsymbol{\nu}_k = \mathcal{N}(\mathbf{0}, \mathbf{R}_k)$ are independent Gaussian process and measurement noise, respectively. Here, $\boldsymbol{\theta}$ is the payload inertial property vector; the measurement model is the Newton or Euler equation (4.6)(4.8), where the measurement \mathbf{y} is the acceleration of \mathcal{O}_L or angular acceleration of the payload. $g(\cdot)$ is nonlinear with respect to payload mass and moments of inertia, but is linear with respect to the payload center of mass. A standard KF can be used to estimate the parameters when $g(\cdot)$ is linear. In the case of nonlinear $g(\cdot)$, an Extended Kalman filter (EKF) or

unscented Kalman filter (UKF) [73] can be used.

In the case when the unknown parameter is constant, setting $\mathbf{Q}_k = \mathbf{0}$ reduces the linear KF to the recursive least-squares algorithm. However, setting of \mathbf{Q}_k as an adaptive parameter increases the flexibility of the algorithm when the model parameters are subjected to random fluctuations [68].

4.2.4 Inertial Properties Estimation for Multilift

Beginning with Newton's Law (4.6) and denoting $\mathbf{a}_L = [a_{Lx}, a_{Ly}, a_{Lz}]^T$, $\mathbf{a}_o = \left[\frac{F_x}{m_L}, \frac{F_y}{m_L}, \frac{F_z}{m_L} \right]^T$, $\boldsymbol{\alpha} = [\alpha_x, \alpha_y, \alpha_z]^T$ and $\boldsymbol{\omega} = [\omega_x, \omega_y, \omega_z]^T$, also denoting the total cable force as ${}^e\mathbf{f}_f = [f_x, f_y, f_z]^T = {}^e\mathbf{F}_p - {}^e\mathbf{G}_g$, (4.6) can then be written explicitly as

$$\begin{bmatrix} a_{Lx} \\ a_{Ly} \\ a_{Lz} - g \end{bmatrix} = \begin{bmatrix} f_x & \omega_y^2 + \omega_z^2 & -\omega_x\omega_y + \alpha_z & -\omega_x\omega_z - \alpha_y \\ f_y & -\omega_x\omega_y - \alpha_z & \omega_x^2 + \omega_z^2 & -\omega_y\omega_z + \alpha_x \\ f_z & -\omega_x\omega_z + \alpha_y & -\omega_y\omega_z - \alpha_x & \omega_x^2 + \omega_y^2 \end{bmatrix} \begin{bmatrix} \frac{1}{m_L} \\ r_x \\ r_y \\ r_z \end{bmatrix} \quad (4.44)$$

Two assumptions are made in analyzing the Euler equations (4.8): (1) The payload body axes are close to the principal axes so the non-diagonal terms in the inertia matrix are small. (2) The system is excited about one body axis at a time, so the term $\boldsymbol{\omega} \times {}^e\mathbf{J}_{cm}\boldsymbol{\omega}$ can be neglected. This occurs when the cargo is symmetric with respect to all three body axes, for example, a CONEX cargo container. For a general cargo without symmetry, excitation about one body axis can still estimate the diagonal terms of the inertia matrix. Additional excitation about each body axis would then be needed to estimate the non-diagonal terms of the inertia matrix.

Denoting $\mathbf{J}_{cm} = \text{diag}(J_{xx}, J_{yy}, J_{zz})$, which is a diagonal matrix; the total moment about the reference point as ${}^e\mathbf{M}_p = [M_x, M_y, M_z]$; the total force on the reference point as ${}^e\mathbf{F}_p = [F_x, F_y, F_z]$, (4.8) can thus be written explicitly as

$$\begin{aligned} J_{xx}\alpha_x &= M_x - (r_y F_z - r_z F_y) \\ J_{yy}\alpha_y &= M_y - (r_z F_x - r_x F_z) \\ J_{zz}\alpha_z &= M_z - (r_x F_y - r_y F_x) \end{aligned} \quad (4.45)$$

4.2.4.1 Estimation of Slung Load Mass

When the multilift system is in hover condition, payload angular rate and angular acceleration are nominally zeros. Hence, f_x and f_y are also zeros. If those terms are removed from (4.44), the z -component of the Newton equation during hover becomes:

$$a_{Lz} - g = f_z \frac{1}{m_L} \quad (4.46)$$

As mentioned in Section 4.1.1.2, the problem is linear when $1/m_L$ is treated as unknown. Hence, applying the batch least-squares method for data collected from k time steps yields

$$\hat{m}_L = \frac{\sum_{i=1}^k f_z^2(i)}{\sum_{i=1}^k f_z(i)(a_{Lz}(i) - g)} \quad (4.47)$$

In hover condition, it is clearly that f_z is non-zero since z -component of the total cable force exists to balance payload weight. Therefore, the system satisfies the persistent excitation condition (4.25).

Maximum likelihood estimation described in Section 4.2.2 can be used for payload mass estimation when the estimated cable force uncertainty is taken into account. When f_z and $a_{Lz} - g$ in (4.46) are treated as input-output data with $1/m_L$ as unknown, (4.39) can be written as:

$$\left(\sum_{i=1}^N x_i y_i \sigma_1^2 \right) m^2 + \sum_{i=1}^N (x_i^2 \sigma_2^2 - y_i^2 \sigma_1^2) m - \sum_{i=1}^N x_i y_i \sigma_2^2 = 0 \quad (4.48)$$

where $x_i = f_z$, $y_i = a_{Lz} - g$, $m = 1/m_L$. This is a quadratic equation in m . Payload mass m_L can be obtained from $1/m$.

The Kalman filter method can also be used with the z -component of acceleration $y_k = a_{Lz} - g$ in (4.46) as the measurement. Since the measurement model (4.46) is nonlinear with respect to the payload mass m_L , one can either use a unscented Kalman filter (UKF) to directly estimate m_L or use a KF to estimate $1/m_L$. Here, a UKF is used to directly estimate the payload mass $\theta_k = m_L$ as a comparison to the standard least-squares method. In this case, the uncertainty in cable force is treated as an equivalent accelerometer noise and included in measurement noise $R'_k = R_k + \Sigma_{x_\mu:3}/m_L$, where $:3$ is the 3rd diagonal component of Σ_{x_μ} (4.18). The UKF algorithm is applied to identify the payload mass in the following computational steps [73]:

1. The UKF is initialized as:

$$\hat{\theta}_0^+ = E(\theta_0) \quad (4.49)$$

$$P_0^+ = E[(\theta_0 - \hat{\theta}_0^+)(\theta_0 - \hat{\theta}_0^+)^T] \quad (4.50)$$

2. Time update:

$$\Theta_{k-1}^+ = \begin{bmatrix} \hat{\theta}_{k-1}^+ & \hat{\theta}_{k-1}^+ + \eta\sqrt{P_{k-1}^+} & \hat{\theta}_{k-1}^+ - \eta\sqrt{P_{k-1}^+} \end{bmatrix} \quad (4.51)$$

$$\Theta_k^- = \Theta_{k-1}^+ \quad (4.52)$$

$$\hat{\theta}_{k-1}^- = \Theta_k^- \mathbf{w}_m \quad (4.53)$$

$$P_k^- = [\Theta_{k-1}^- - \hat{\theta}_{k-1}^-] \mathbf{w}_c [\Theta_{k-1}^- - \hat{\theta}_{k-1}^-]^T + Q_{k-1} \quad (4.54)$$

3. Measurement update:

$$\mathbf{Y}_{k-1}^- = g(\Theta_k^-) \quad (4.55)$$

$$\hat{y}_{k-1}^- = \mathbf{Y}_{k-1}^- \mathbf{w}_m \quad (4.56)$$

$$P_{yy} = [\mathbf{Y}_{k-1}^- - \hat{y}_{k-1}^-] \mathbf{w}_c [\mathbf{Y}_{k-1}^- - \hat{y}_{k-1}^-]^T + R'_k \quad (4.57)$$

$$P_{xy} = [\Theta_{k-1}^- - \hat{\theta}_{k-1}^-] \mathbf{w}_c [Y_{k-1}^- - \hat{y}_{k-1}^-]^T \quad (4.58)$$

$$K_k = P_{xy} P_{yy}^{-1} \quad (4.59)$$

$$\theta_k^+ = \theta_k^- + K_k (y_k - \hat{y}_{k-1}^-) \quad (4.60)$$

$$P_k^+ = P_k^- - K_k P_y K_k^T \quad (4.61)$$

where η , \mathbf{w}_m and \mathbf{w}_c are weight coefficients.

4.2.4.2 Estimation of Slung Load Center of Mass

Once the slung load mass is obtained, the payload center of mass can be estimated from (4.6).

When whole multilift system is under pure yaw motion (Fig. 4.3(a)), payload roll and pitch angular rate and angular acceleration are approximately zero. When these terms are eliminated from (4.44), Newton's Law becomes:

$$\begin{bmatrix} a_{Lx} - \frac{f_x}{m_L} \\ a_{Ly} - \frac{f_x}{m_L} \end{bmatrix} = \begin{bmatrix} \omega_z^2 & \alpha_z \\ -\alpha_z & \omega_z^2 \end{bmatrix} \begin{bmatrix} r_x \\ r_y \end{bmatrix} \quad (4.62)$$

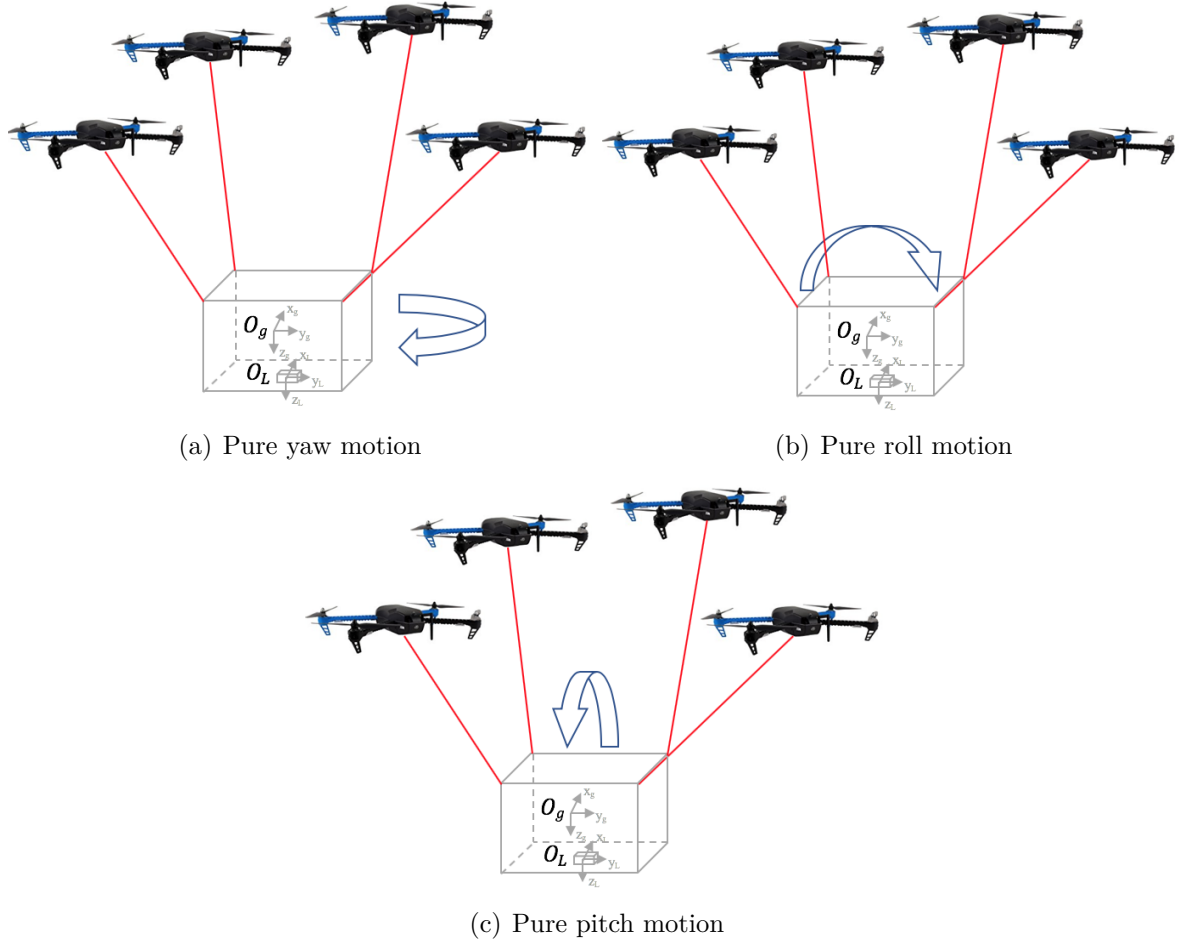


Figure 4.3. Payload excited motion

The methods discussed before can be applied to estimate the unknown parameter vector $[r_x, r_y]^T$. Notice that r_z can not be estimated during this motion. The depth z -dimension of payload center of mass is not observable during pure yaw motion of the payload.

If the multilift system is commanded to be in a pure roll motion (Fig. 4.3(b)), the payload pitch and roll angular rate and angular acceleration are approximately zero. (4.6) thus becomes:

$$\begin{bmatrix} a_{Ly} - \frac{f_y}{m_L} \\ a_{Lz} - g - \frac{f_z}{m_L} \end{bmatrix} = \begin{bmatrix} \omega_x^2 & \alpha_x \\ -\alpha_x & \omega_x^2 \end{bmatrix} \begin{bmatrix} r_y \\ r_z \end{bmatrix} \quad (4.63)$$

The unknown parameter vector is $[r_y, r_z]^T$.

Similarly, if the multilift system is excited to a pure pitch motion (Fig. 4.3(c)),

eliminating the roll and yaw angular rate and angular acceleration in (4.44) yields,

$$\begin{bmatrix} a_{Lx} - \frac{f_x}{m_L} \\ a_{Lz} - g - \frac{f_z}{m_L} \end{bmatrix} = \begin{bmatrix} \omega_y^2 & -\alpha_y \\ \alpha_y & \omega_y^2 \end{bmatrix} \begin{bmatrix} r_x \\ r_z \end{bmatrix} \quad (4.64)$$

The unknown parameter vector $[r_x, r_z]^T$ can now be estimated.

4.2.4.3 Estimation of Slung Load Moments of Inertia

The Euler equation (4.8) can be written as

$$\alpha_x = M_x \frac{1}{J_{xx}} - F_z \frac{r_y}{J_{xx}} + F_y \frac{r_z}{J_{xx}} \quad (4.65)$$

$$\alpha_y = M_y \frac{1}{J_{yy}} + F_z \frac{r_x}{J_{yy}} - F_x \frac{r_z}{J_{yy}} \quad (4.66)$$

$$\alpha_z = M_z \frac{1}{J_{zz}} - F_y \frac{r_x}{J_{zz}} + F_x \frac{r_y}{J_{zz}} \quad (4.67)$$

Equation (4.65) shows that if the system is excited about the roll axis, the linear estimator can be applied using flight data to estimate the unknowns $\boldsymbol{\theta} = [\frac{1}{J_{xx}}, \frac{r_y}{J_{xx}}, \frac{r_z}{J_{xx}}]^T$. An equivalent procedure can be used along for the pitch and yaw axes to estimate J_{yy} , J_{zz} and r_x .

4.3 Hardware Experiment

Indoor flight tests were performed to validate the proposed slung load property estimation strategy. Payload mass estimation occurs in steady hover. Then pre-planned trajectories that excite the payload rotation motion are executed by the system to estimate the slung load center of mass location and moments of inertia.

4.3.1 Experiment Setup

4.3.1.1 Vicon Object Coordinate Frame

The Vicon motion capture system provides position and orientation information for the objects under Vicon environment. Each rotorcraft's body frame origin is placed at its geometric center, which is close to the vehicle center of mass. The payload's body frame origin is placed at \mathcal{O}_L , the location of the autopilot module. Body axes are aligned with

the payload front-right-down directions. The motion capture system thus reports the position and orientation of \mathcal{O}_L and simulates the use of GPS for outdoor deployment.

4.3.1.2 Initialization of Inertial Property Estimates

To estimate the payload inertial properties, corresponding payload motion needs to be excited as discussed in Section 4.2. Initial guesses for the properties are needed for the system to fly and be able to excite the specific motion.

For mass estimation, as long as the rotorcraft have enough total lifting capability considering the payload weight, the system can lift and hover. In this way, payload feedback is not required so that the initial guess for payload mass is not necessary. Hence, the rotorcraft can be commanded to take off and lift to a fixed altitude so that the payload can be carried above the ground and hover. Notice that in this scenario, a quasi-static model with a fixed rotorcraft formation is flown.

Corresponding payload rotation motion needs to be excited to estimate the payload center of mass location and the moments of inertia, as discussed in Section 4.2. An initial guess with zero offset ${}^e\mathbf{r}_L$ is made in (4.1). In this case, the reference point is treated as the center of mass. The initial estimate of payload inertia is computed from the contributions of parts of the payload.

4.3.2 Experiment Implementation

The state machine is the same as one developed in Chapter 3. The system will transit to HOVER then FOLLOW_TRAJ state to track some pre-planned trajectories which can excite specific payload motion for parameter estimation. The flight data recorded in those states will be replayed and pro-processed recursively for payload inertial property estimation.

4.3.3 Estimation of Slung Load Mass During Hover

In this experiment, the system is commanded to hover with the payload at an altitude of 0.6 m for 20 seconds. Note that this places the rotorcraft well out of ground effect. Two groups of flight tests are performed (summarized in Table 4.1): the first directly commands the rotorcraft to prescribed positions placing the payload above the ground at an altitude 0.6 m (denoted feedforward flight (ff)) and then holds hover; the second begins with the system in the TAKEOFF state, then the payload commands the rotorcraft to a desired state in the FOLLOW_TRAJ state, driving the payload to an altitude 0.6 m

Table 4.1. Flight Tests Definition for Mass Estimation

	Payload mass		
Group 1 (feedforward)	$m_1 = 639\text{g}$	$m_2 = 808\text{g}$	$m_3 = 988\text{g}$
Group 2 (feedback)	$m_1 = 639\text{g}$	$m_2 = 808\text{g}$	$m_3 = 988\text{g}$

Table 4.2. Estimated payload mass

Method	Estimated mass (% error)		
	$m_1 = 639\text{ g}$	$m_2 = 808\text{ g}$	$m_3 = 988\text{ g}$
RLS-ff	654.4 g (+2.4%)	809.3 g (+0.2%)	1013.6 g (+2.6%)
MLE-ff	655.9 g (+2.6%)	816.8 g (+1.1%)	1017.8 g (+3.0%)
UKF-ff	655.5 g (+2.6%)	805.0 g (-0.4%)	1013.7 g (+2.6%)
RLS-fb	625.4 g (-2.1%)	806.7 g (-0.2%)	975.3 g (-1.3%)
MLE-fb	623.1 g (-2.5%)	805.7 g (-0.3%)	975.4 g (-1.3%)
UKF-fb	623.2 g (-2.5%)	803.5 g (-0.6%)	972.0 g (-1.6%)

(denoted feedback flight (fb)). For the feedback flights, an initial guess for the payload mass with 20% deviation from the truth is given. For each group of tests, a payload with three different masses is carried (three flights for each group). Then, three methods are used for mass estimation in each flight: recursive least-squares (RLS), maximum likelihood (MLE) and unscented Kalman filter (UKF).

Results of mass estimation are summarized in Table 4.2. Worst-case error was +3.0% of true mass during feedforward flight, and mean error during feedforward flight is 1.9% of true mass. During feedback flight the worst-case error was -2.5%, and mean error was -1.4% of true mass. Hence payload state feedback flight does improve mass estimation. Recall that there is no cable force sensor: cable forces were estimated.

There are some interesting results. Payload mass was consistently over-estimated during feedforward flight and under-estimated during feedback flight. This indicates the likely presence of a bias caused by unmodeled parameters. For example, the mass of cables is assumed to be negligible here, when in fact the total cable mass of 97 g will contribute meaningfully to the total thrust required and hence to the estimated payload mass. As the mass of the payload becomes larger compared to cable mass, this effect should become smaller. In the case of feedback flight, the cable attachment point is assumed to lie at the center of mass of each vehicle, but there is a vertical offset that results in a small difference in actual versus commanded cable angle.

Note also that mass estimation of the 808 g payload is always better than mass estimation for the 639 g payload and the 988 g payload. During flight the 639 g payload was visibly more responsive to buffeting from rotor wakes, resulting in oscillations that

adversely affect cable tension estimates. The 988 g payload was very close to the net maximum lift capacity of the quadrotor team, which also resulted in payload oscillations. To use the approach developed in this paper in estimating payload mass, a rough initial estimate of the payload should be made to assess whether the rotorcraft team is actually able to lift the payload, or the system should include an “error trap” to detect a too-heavy payload.

As expected, the recursive least-squares and the UKF estimators gave very similar results: the UKF implementation assumes constant mass and implemented a very small process noise, and Kalman filters reduce to recursive least-squares if process noise is zero [72].

The maximum likelihood method did not show obvious advantages for payload mass estimation. This could be due to the inaccurate input data (vertical component of the cable force in this case) noise modeling. Since there is no direct sensor measuring cable force, modeling the cable force uncertainty using the difference between the estimated cable force and commanded cable force may not be sufficient to provide accurate uncertainty quantification.

Time histories showing convergence of payload mass estimates for the three different masses using the recursive least-squares method for both feedforward and feedback flight are shown in Fig. 4.4. It is clear that the estimation result from the feedback flight is better than that from the feedforward flight. The estimated error in the feedback cases are always within or close to the $1-\sigma$ standard deviation of the estimated covariance and converge quickly. However, in the feedforward cases, the estimated error converged much more slowly. There was noticeably larger payload oscillation during the feedforward flight test comparing to the feedback case, which caused noisier cable tension estimates and hence poorer estimation results. This also verifies that the system has superior performance by following dynamic feasible trajectory obtained from the hierarchical approach compared to the quasi-static models.

Fig. 4.5 show the four vertical component of the cable force estimates (which directly affects mass estimation) for the payload with mass 639 g from a feedback flight. The lack of a cable tension sensor means that truth data is not available, but one can compare the estimated with the commanded cable tension, see Table. 4.3. It is clear that the commanded f_z from the payload is always within or close to one standard deviation of estimated. It also shows that the estimated standard deviation from the feedforward cases are larger than that from the feedback case, which again reflects the advantage of the feedback method. In the case of feedback flight, the average total commanded

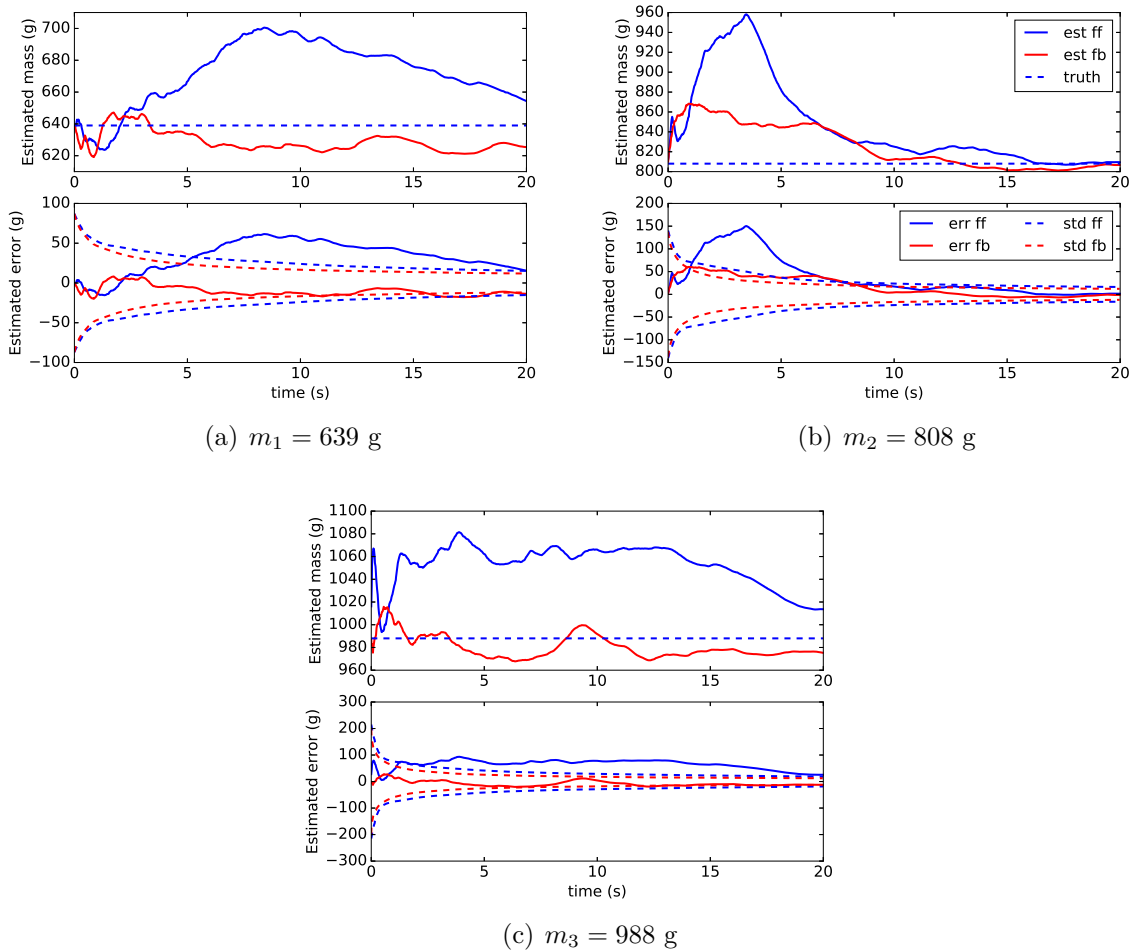


Figure 4.4. Converging curve for different masses (the label “std” in the lower plots denote 1σ bounds)

Table 4.3. Comparison of Commanded and Estimated Vertical Component (f_z) of Cable force

	Average fb	Total Commanded	Average fb	Total Estimated	Average ff	Total Estimated
$m_1 = 639 \text{ g } (mg = 6.27 \text{ N})$	-6.88		-6.10 \pm 0.60	-6.39 \pm 0.78		
$m_2 = 808 \text{ g } (mg = 7.93 \text{ N})$	-8.30		-7.90 \pm 0.64	-7.94 \pm 1.07		
$m_3 = 988 \text{ g } (mg = 9.69 \text{ N})$	-10.42		-9.55 \pm 0.78	-9.91 \pm 1.16		

vertical cable force is higher than the estimated force: the integrator term in the payload trajectory tracking controller is compensating for unmodeled biases in the system.

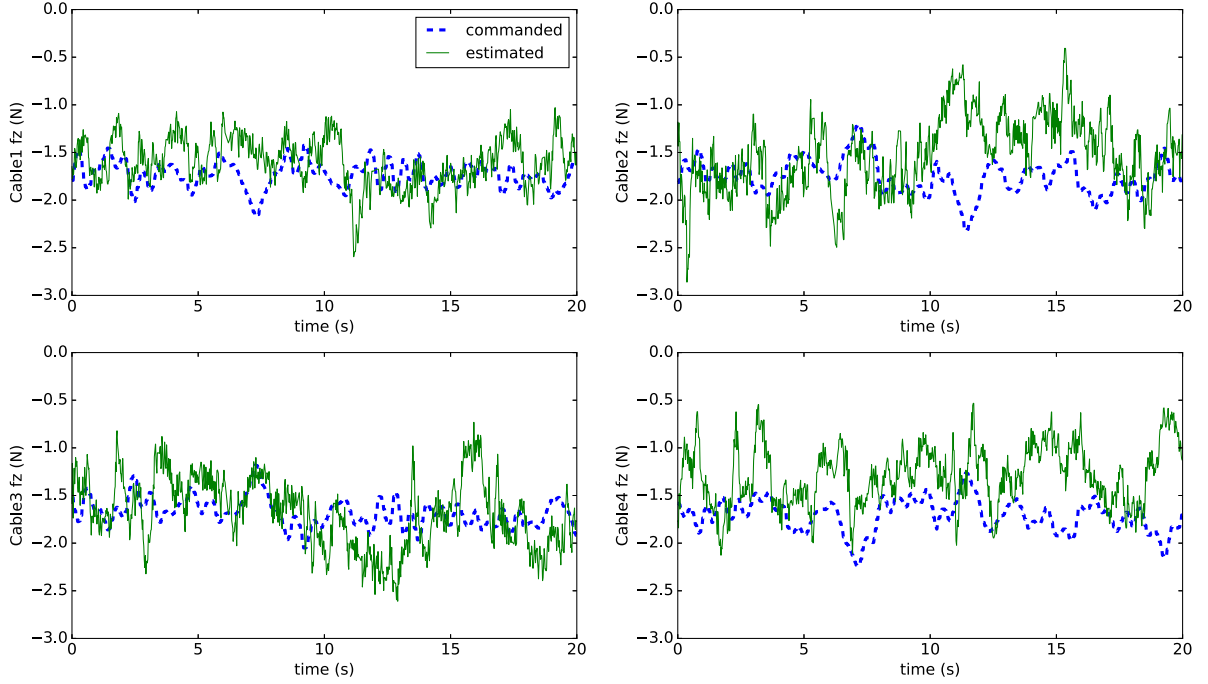


Figure 4.5. Cable force estimate z-component

4.3.4 Estimation of Slung Load Center of Mass (CM)

As discussed in Section 4.2.4, slung load center of mass estimation requires proper system excitation. In this experiment, the system is first commanded to take off position. A pre-planned trajectory is then executed by the system in the FOLLOW_TRAJ state to excite the corresponding rotation motion for each corresponding parameter. The flight data in this state is then used for slung load CM estimation. For the estimator initialization, a zero initial guess for the slung load CM is given (so that the initial guess for CM coincides with the autopilot module). The recursive least-squares and Kalman filter methods are used for estimation.

Three test trajectories were flown: (1) yaw: 90 degree positive yaw motion of the slung load in 10 seconds and then yaw back in another 10 seconds; (2) pitch: -8 degrees pitch motion in 10 seconds and then rotate 10 seconds back; (3) roll: -8 degrees roll motion and then roll back. This design ensures that the system motion is within the actuator limitations. Notice that in the work of [69], the authors formulated a similar problem to estimate the CM of a satellite. The change of attitude was less than 1 degree, and the CM estimation can be completed in 5 seconds. In the case of multilift slung load mass estimation, sufficient excitation of yaw dynamic is not difficult since all the rotorcraft move nearly within a 2D plane. It is more challenging to excite roll and pitch



(a) On the top surface

(b) On the back surface

Figure 4.6. Payload with 200g extra weight attached

sufficiently, since that can cause uneven load distribution among the rotorcraft. However, as long as the pitch or roll dynamics are excited, the angular velocity and acceleration will show up in the Newton equation with a significant difference from that on the other axes so that the parameters of interest can be estimated. In this case the excitation of less than 10 degrees in roll and pitch is sufficient to enable estimation of the center of mass.

Three loading cases were tested to show estimator performance: (1) the multilift system with original (i.e. 808 g) payload; (2) the payload with a 200g extra weight added to the center of the top surface, see Fig. 4.6(a), which causes a theoretical CM change $\Delta Z_{truth} = -3.35$ cm offset along the body z-axis (i.e. the new CM is higher than on the original payload); (3) an extra 200g weight is added to the center of back surface of the payload, which generates a $\Delta X_{truth} = -4.02$ cm offset of CM along the body x-axis, see Fig. 4.6(b). Note that adding 200 g to the payload results in a total mass that is close to the maximum total lift capacity of the the quadrotor team.

By comparing case 1 and case 2 from the pitch and roll tests, Table 4.4 shows the error in estimated change of z -component (ΔZ) of CM. It can be seen ΔZ of CM can be estimated from both tests with the estimated error less than a few millimetres. The recursive least-squares works qualitatively the same as the Kalman filter method. Note the difference in estimated error for the pitch test and the roll test: the cable attachment points are located at the corners of a rectangle that is longer in the payload longitudinal direction, so controllability over the pitch degree of freedom is greater than over the roll degree of freedom.

Fig. 4.7 shows the converging curve of the z -component of the CM estimation for

Table 4.4. Estimated error of ΔZ (cm)

	RLS	KF
pitch test	-0.05	0.10
roll test	0.27	0.39

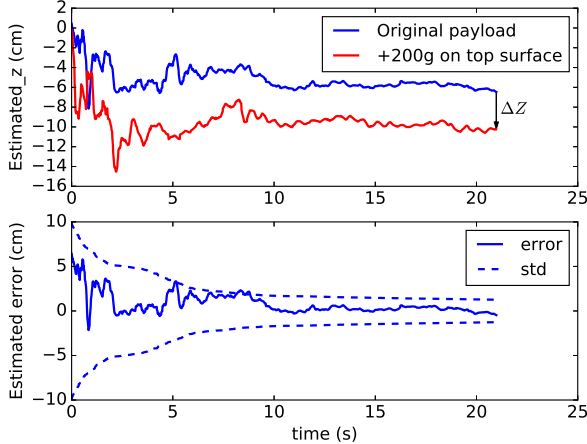


Figure 4.7. Converging curve of z component of CM estimation (the label “std” in the lower plot denotes 1σ bound).

payload with two different weights and the estimated error for the original payload. It is clear that adding an extra weight on the center of top surface of the payload does drive the z -component of CM higher than before. The estimated error converges within 10 seconds.

Fig. 4.8 shows the estimated x , y components of the CM in 2D plane for the two cases (1 and 2) by performing the yaw test. The payload is nearly symmetric with respect to the body x and y axes. The projection of the payload CM on the 2D plane does not change with an extra weight added to the center of the top surface. Notice that the estimated value is close to the truth for both cases. However, the estimated results for the original payload is slightly better than the one with an extra 200g weight added to the top surface. In fact, adding an extra 200g weight to the payload causes the rotorcraft close to the limit of lifting capability, which leads to undesired oscillation and inefficient maneuver during flight.

The error of the estimated change of x -component (ΔX) of CM from the yaw test is shown in Table 4.5. Both the recursive least-squares and the Kalman filter method can estimate the payload ΔX of CM with the estimation error less than a few millimeters. The converging curve of the x -component of the payload CM estimation with different weight and the estimated error for the original payload is shown in Fig. 4.9. Adding an

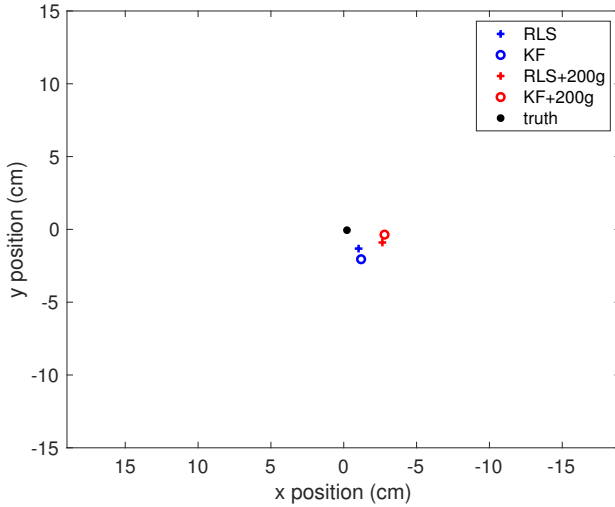


Figure 4.8. x and y component of CM estimation. Axis limits fit the physical dimension of the real payload

Table 4.5. Estimated error of ΔX (cm)

	RLS	KF
yaw test	-0.58	-0.52

extra weight to the payload at the center of back surface clearly drives the CM to the negative direction of payload body x -axis.

4.3.5 Estimation of Slung Load Moments of Inertia

The flight data which excited the payload rotational motion can also be used for payload moments of inertia estimation with the excitation about one payload body axis at a time. The method described in Section 4.2.4.3 was applied for two cases: one with the original multilift slung load, the other with a 200g extra weight added to the payload at the center of top surface. The total external moment on the payload reference point \mathcal{O}_L can be obtained from the estimated cable force and the payload geometry.

Flight results for the roll excitation for the two cases are shown in Fig. 4.10. Notice that larger cable force moments are required for the case with a 200g extra weight on the payload top surface, which can be observed to produce less angular acceleration yielding smaller angular velocity.

Table 4.6 shows the results of payload moments of inertia estimation by applying the least-squares method for all the combination of cases and axes. The estimated uncertainty (1σ bound) of J_{xx} , J_{yy} and J_{zz} for the original payload are 3.17, 6.13 and

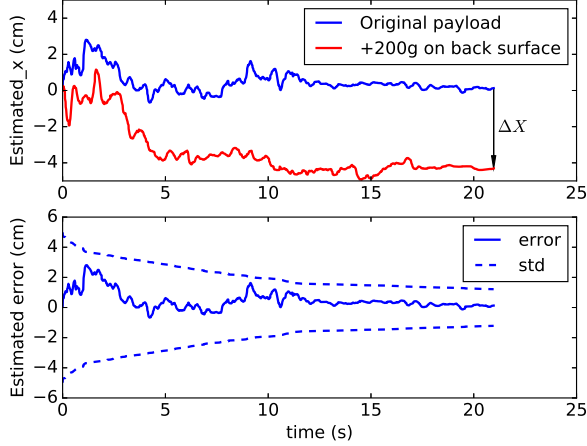


Figure 4.9. Converging curve of x component of CM estimation (the label “std” in the lower plot denotes 1σ bound).

Table 4.6. Payload estimated moments of inertia ($\text{g} \cdot \text{m}^2$)

Case	J_{xx}	J_{yy}	J_{zz}
Original payload	22.8	23.1	32.0
Payload + 200g mass	32.9	33.7	34.2
ΔJ	10.1	10.6	2.2

$2.87 \text{ g} \cdot \text{m}^2$; and $3.72, 5.41$ and $2.25 \text{ g} \cdot \text{m}^2$ when adding extra 200g mass. The difference of uncertainty between y and x axes are due to the non-square payload and thus also non-square multilift formation geometry. Notice that the moments of inertia estimation for different payload weights on different axes behave qualitatively as expected. There is only a slight increase of the moments of inertia about z -axis for the payload since the extra mass is added to the center of the top surface which is nearly coincident with the body z axis. Meanwhile, significant increases in J_{xx} and J_{yy} are observed when adding extra mass to the payload. One can determine the change in J_{xx} and J_{zz} (ΔJ_{xx} , ΔJ_{yy}) based on the knowledge of the CM change and the payload geometry. Applying the parallel axis theorem to determine the change in moment of inertia (including the change in net CM location) gives $\Delta J_{xx} = \Delta J_{yy} = m_L(\Delta Z)^2 + m_e r^2 = 10.6 \text{ g} \cdot \text{m}^2$, where $m_L = 808 \text{ g}$ is the payload mass, $\Delta Z = 0.0335 \text{ m}$ is the change in CM location caused by adding mass, $m_e = 200 \text{ g}$ is the added mass, and $r = 0.22 \text{ m}$ is the distance from the added mass to the new CM location. This is within rounding of the estimated change in J_{yy} and within 5% of the estimated change in J_{xx} (see Table 4.6).

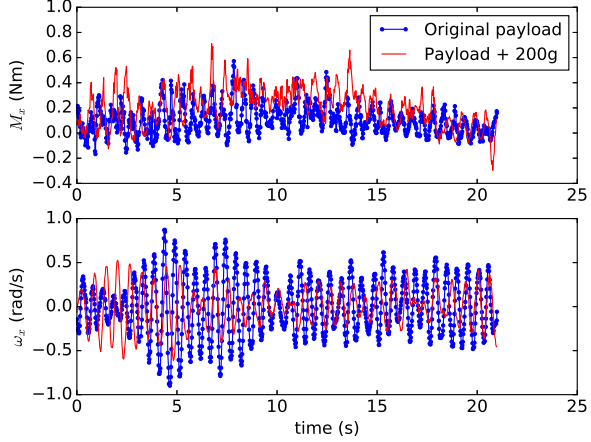


Figure 4.10. Roll moment and angular rate data

4.4 Controller Compensation

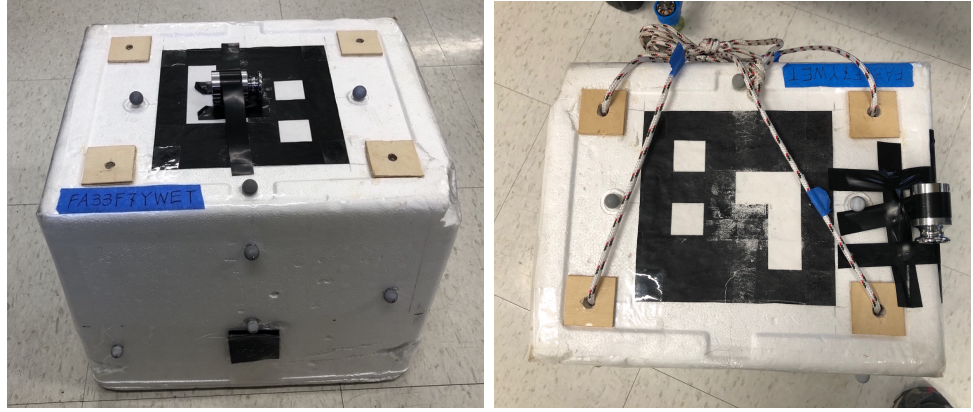
The utility of the payload inertial property estimation is examined by comparing results of payload trajectory following using compensated (i.e. using the estimated payload center of mass offset) and uncompensated (i.e. using the zero offset as if the reference point is the center of mass) controller.

Two loading configurations are tested: one with 200g extra mass attached at the center of the top surface of the payload (so that the mass is greater than nominal and the CM is offset upwards) and the other one with 200g extra mass added to the right-hand edge of the top surface (so the mass is greater than nominal and the CM is offset upwards and in the negative body x direction). This is shown in Fig. 4.11. For each configuration, a group of tests with compensated and uncompensated cases are conducted and compared by implementing the system to track a specific pre-planned trajectory.

4.4.1 Group 1: Single Channel Sinusoidal Movement

In the first group of tests the payload is commanded to move sinusoidally along the inertial y -axis, with frequency increasing smoothly from f_{t_0} to f_{t_T} Hz over T seconds. Such a trajectory is given by

$${}^e\mathbf{p}(t) = \begin{bmatrix} x(t_0) \\ y(t_0) - A_y \sin(2\pi((1 - \alpha_f)f_{t_0} + \alpha_f f_{t_T}))t \\ z(t_0) \end{bmatrix}, \quad 0 \leq t \leq T, \quad (4.68)$$



(a) Test group 1: at the center of the top surface (b) Test group 2: at the middle of right edge of the top surface

Figure 4.11. Payload configuration for controller compensation test

where α_f is defined as

$$\alpha_f = \frac{t}{T} \quad (4.69)$$

This ensures that the frequency of the payload trajectory smoothly changes from f_{t_0} to f_{t_T} Hz in T seconds, as α_f changes from 0 to 1. The desired payload roll/pitch/yaw angles are set to zero. The desired velocity and angular rate can be obtained from the derivatives of the path. Here, the parameters are selected as $f_{t_0} = 1/15$ Hz to $f_{t_T} = 1/5$ Hz in $T = 15$ seconds, the amplitude of the sine wave $A_y = 0.6$ m. This choice ensures that the obtained trajectory is within the sensor and actuator limitations of the experimental system.

Fig. 4.12 shows the payload tracking performance. The system moves along the inertial y -axis with a sinusoidally pace faster and faster as the frequency increases. Due to the payload onboard feedback controller correcting the tracking behavior, which also reduces the system sensitivity to the error [74] and the slower payload responses comparing to the faster rotorcraft dynamics [7], the payload tracking performances are qualitatively the same for both compensated (i.e. using estimated payload inertial properties) and uncompensated (i.e. using nominal payload inertial properties) cases.

Although the *payload* tracking behavior does not show significant difference between the compensated and uncompensated cases, the commanded cable forces in each case do show clear differences (Fig. 4.13). There are clear high-frequency oscillations in commanded cable force in the uncompensated case, and there is a clear difference in *vehicle* position tracking error (Fig. 4.14). As the trajectory frequency (and thus magnitude of commanded payload acceleration) increases, the vehicle tracking error

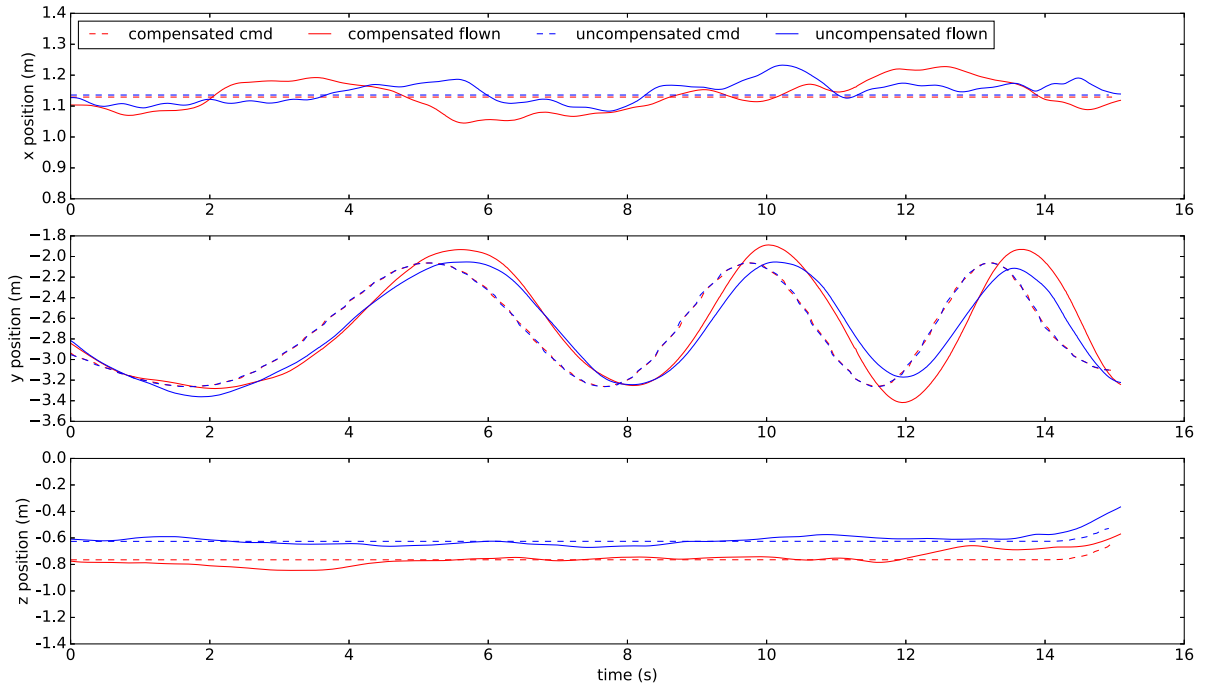


Figure 4.12. Payload trajectories for test group 1 with increasing frequency

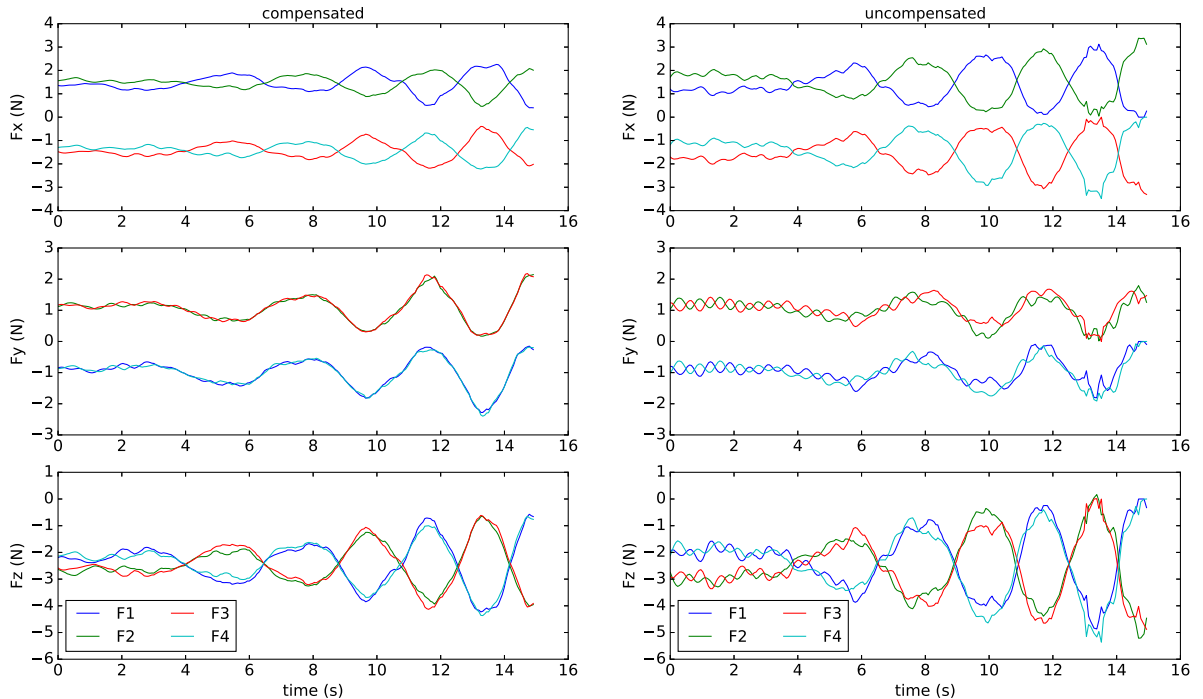


Figure 4.13. Payload command cable force for test group 1 with increasing frequency

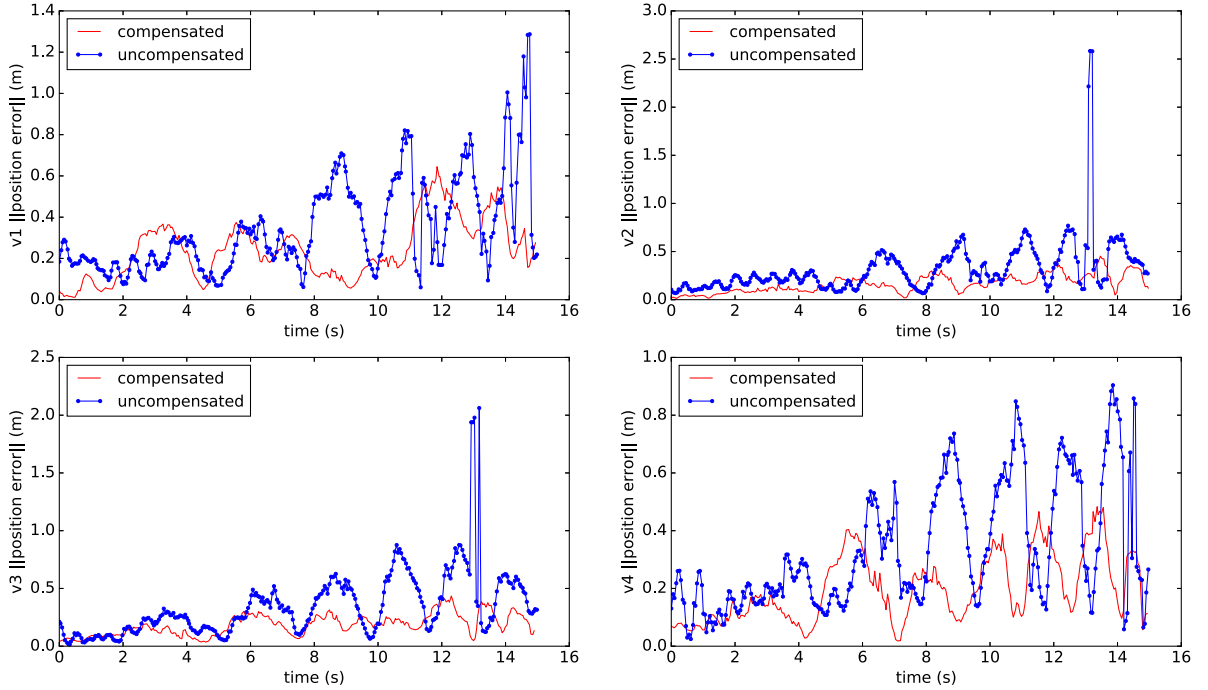


Figure 4.14. Rotorcraft tracking error (in 2-norm) for test group 1 with increasing frequency

increases for both the compensated and uncompensated system, but the uncompensated system has significantly greater tracking error. Vehicle position tracking error in the uncompensated case exceeds 1 meter, which in the system described here is large enough that maintaining vehicle separation becomes problematic. Further, large vehicle position tracking error also leads to significant difference between commanded and flown cable force, reducing overall system stability. In fact, all flight tests of the uncompensated system ended with loss of controlled flight.

4.4.2 Group 2: Double Channel Sinusoidal Movement (“Figure 8” Pattern)

For the second group of flight test, a more challenging trajectory with “figure 8” pattern is designed for the system. Specifically, the trajectory is a superposition of two sine waves along both the y and z -axes with smoothly increasing frequency, given by

$${}^e\mathbf{p}(t) = \begin{bmatrix} x(t_0) \\ y(t_0) - A_y \sin(2\pi((1 - \alpha_f)f_{t_0} + \alpha_f f_{t_T}))t \\ z(t_0) - A_z \sin(2\pi((1 - \alpha_f)2f_{t_0} + \alpha_f 2f_{t_T}))t \end{bmatrix}, \quad 0 \leq t \leq T, \quad (4.70)$$

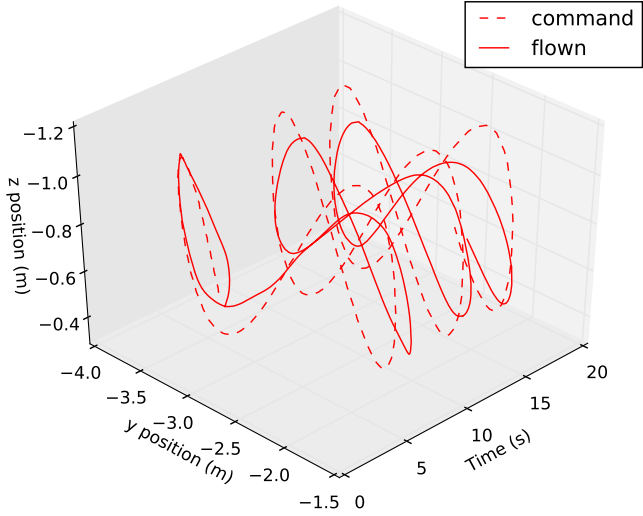


Figure 4.15. Payload trajectories for the compensated case in test group 2 with increasing frequency

Notice that the frequency of the altitude z direction is double that of the lateral y direction so that the resulting trajectory is a “figure 8” pattern. Considering the space size and the actuator limit, the parameters are selected as $f_{t_0} = 1/18$ Hz to $f_{t_T} = 1/6$ Hz in $T = 18$ seconds for the lateral direction. The amplitudes are chosen as $A_y = 0.8$ m, $A_z = 0.4$ m.

The multilift system repeatedly flew a “figure 8” pattern faster and faster as shown in Fig. 4.15. The payload trajectories for both compensated and uncompensated cases in three axes are shown in Fig. 4.16. As before, the payload tracks the commanded position trajectory quite well for both cases. Commanded cable forces are shown in Fig. 4.17. The more complex trajectory excites more payload modes and it is clear that the commanded cable forces have more high frequency content than in the single-channel sinusoid case. Again, the uncompensated case shows high frequency oscillation that is not present in the compensated case, and the rotorcraft tracking error (Fig. 4.18) is lower in the compensated case. As with the single channel case, flights with the uncompensated system ended with loss of controlled flight.

Payload orientation error is shown in Fig. 4.19. The compensated case generally shows smaller magnitude error in payload orientation, and the uncompensated case shows a steady bias in pitch angle induced by the offset center of mass location.

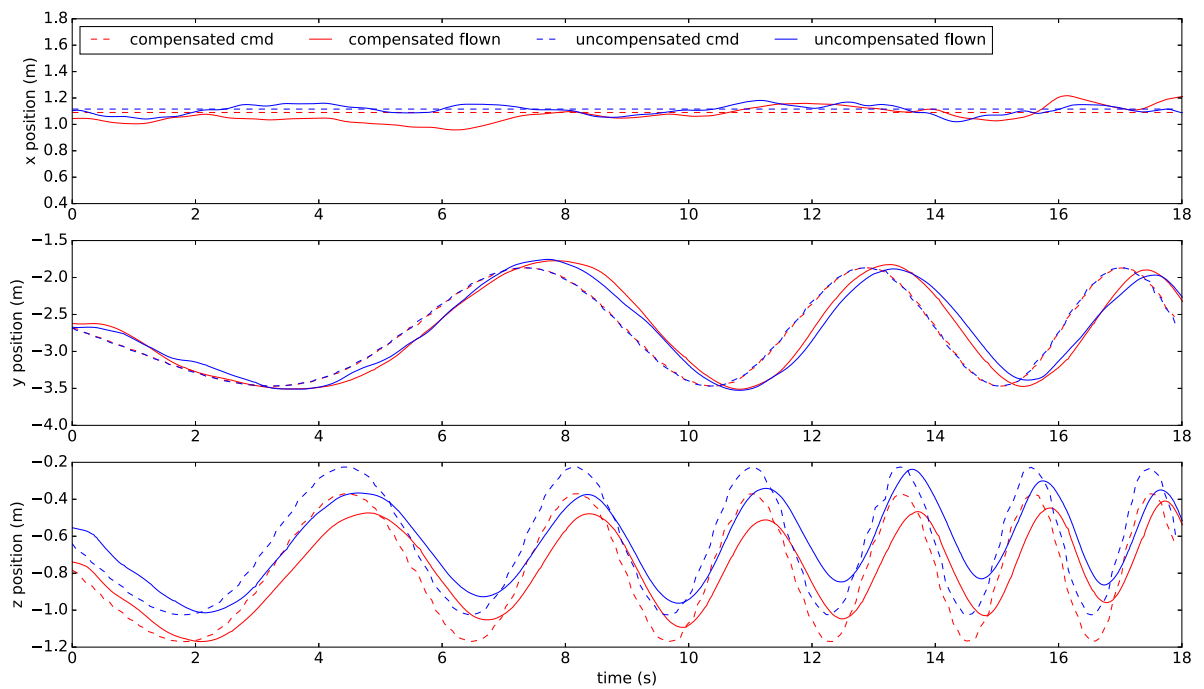


Figure 4.16. Payload tracking behavior for test group 2 with increasing frequency

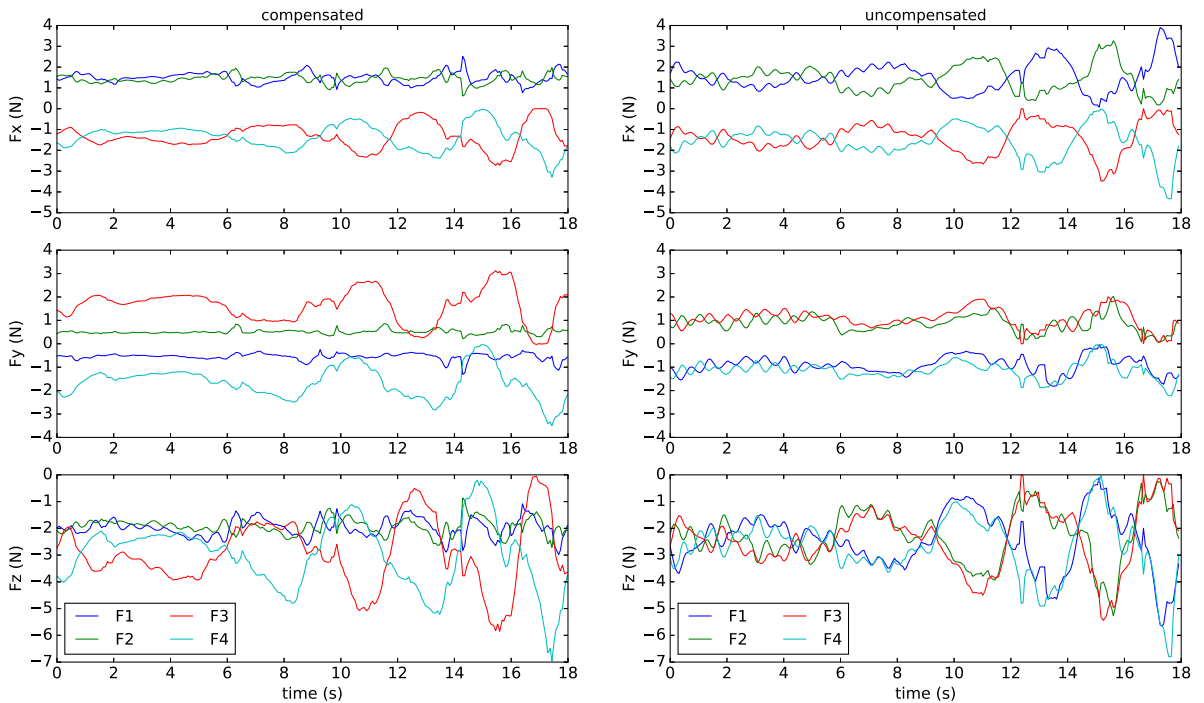


Figure 4.17. Payload command cable force for test group 2 with increasing frequency

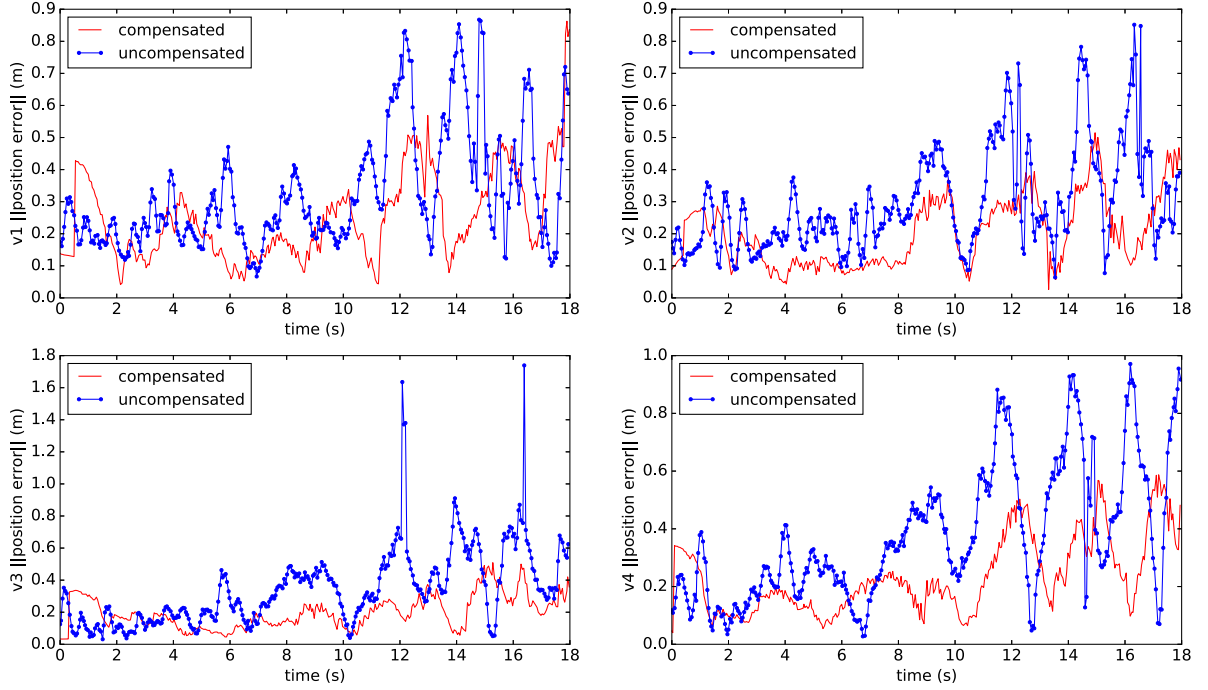


Figure 4.18. Rotorcraft tracking error (in 2-norm) for test group 2 with increasing frequency

4.5 Summary

This chapter proposed a method to estimate the inertial properties for an unknown slung load of multilift to enable transportation with little a priori payload information. The relation between the input (cable forces) and output (payload response) is defined by the slung load motion analysis. Here, cable forces are estimated using an indirect method at the rotorcraft side so that tension load cells are not required. In addition, uncertainty quantification is performed for the cable force computation via Taylor series expansion. An estimation strategy is then designed through the slung load motion analysis so that payload inertial properties (mass, center of mass location, moments of inertia) are observable. Three different estimation algorithms (recursive least-squares, maximum likelihood estimation, and Kalman filter) are introduced and derived for specific parameter estimation problem. Application to multilift inertial property estimation is then detailed based on the derived estimation algorithms.

Flight tests are performed indoors in a Vicon motion capture studio to validate and compare the proposed methods. Payload mass estimation occurs in steady hover. Then pre-planned trajectories that excite the payload rotation motion are executed by the system to estimate the slung load center of mass location and the moments of inertia.

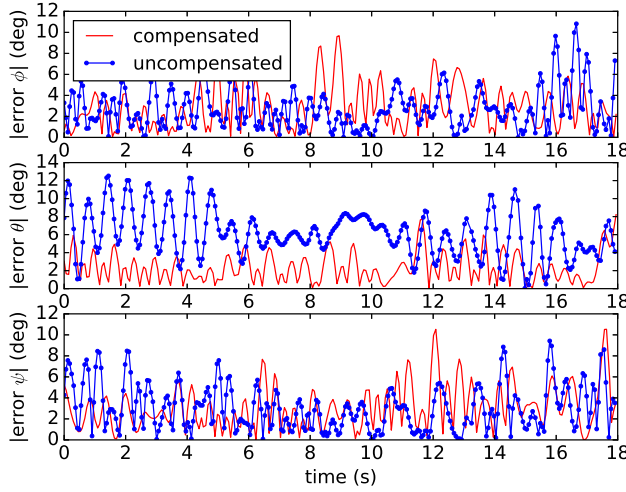


Figure 4.19. Absolute value of the payload Euler angle tracking error for test group 2 with increasing frequency

Results show that even without tension load cells, payload mass can be estimated within 3% of the true mass. Extra mass is added to the payload to verify the payload center of mass and moments of inertia estimation. The estimated change of center of mass is within a few millimeters of truth, with convergence requiring less than ten seconds. The moments of inertia estimate behaves qualitatively as expected.

Controller compensation tests for the compensated and uncompensated cases are then conducted and compared to show the benefit of system performance by incorporating the estimated payload parameters. A sine wave path and a figure 8 pattern are flown for two system configurations with increasing system frequency. Comparison shows that incorporating estimated payload center of mass location into the closed-loop control system (rather than nominal payload center of mass) does not significantly improve payload trajectory tracking performance (although payload orientation tracking is improved), but does significantly improve performance of rotorcraft command following. Cable tensions and rotorcraft motion is significantly smoother when corrected inertial properties are incorporated into the closed-loop system.

Chapter 5 |

Trajectory Planning and Control Based on Load Distribution

This chapter describes a trajectory planning and tracking control method that seeks to evenly distribute cable tension. This has two main purposes: first, in a homogeneous fleet of rotorcraft, even load distribution will ensure that all rotorcraft have similar overhead available for control so as for safety (to avoid losing effectiveness of a single vehicle); second, the power required for near hover low speed flight varies with $(\text{thrust})^{\frac{3}{2}}$, and even load distribution will minimize the total power (and thus total energy) required to complete a mission.

The load-leading control strategy described in Chapter 3 forms the basis of the trajectory planning problem. The problem can thus be simplified from a complex multi-vehicle planning problem to planning for the payload, with cable force acting as the input.

Load distribution based planning is complicated by two main factors. First, as the number of vehicles (i.e. cables) increases, the dimension of the planning problem increases. This leads to a challenge in computing feasible solutions in real time. Second, the nonlinearity in the system leads to challenges in tracking control.

This chapter describes: (a) a formulation of the trajectory planning and tracking problems in optimal control format; (b) analysis of the formulated problems and methodology for solutions; (c) numerical simulation for different arriving time and under external disturbances (i.e. wind gusts); (d) indoor hardware experiment to validate the developed approach; (e) preliminary results and discussion towards reinforcement learning based trajectory planning.

This chapter assumes the payload property is known before planning based on the developed estimation techniques described in Chapter 4. Hence, the payload body frame \mathcal{O}_L is placed at center of mass.

In Section 5.1, the multilift trajectory planning problem is simplified as planning for payload. The trajectory planning is formulated as an optimal control problem that simultaneously plans payload trajectory and cable forces while satisfying path and force constraints and minimizing the difference in cable forces. Then, inspired by the neighboring feedback control approach, the tracking problem is formulated as another optimal control problem with linear quadratic (LQ) format based on small perturbation.

Analysis of the necessary condition for the formulated optimal control problems is presented in Section 5.2. Direct collocation method is then introduced to solve the planning problem. The LQ optimal control problem for tracking is solved by using backward sweep method.

Section 5.3 presents the numerical simulation. Three test cases for planning are considered with different given final time. A 2.5 m/s wind gust is then added to the environment to test the effectiveness of the tracking control by applying the designed LQ feedback controller.

In Section 5.4, flight results from indoor hardware implementation are presented. Two cases are tested and compared to show the advantage of the proposed planning approach on energy efficiency: one with proposed load distribution based planning and the neighboring feedback control approach; the other one with polynomial curve planning method and the hierarchical approach with real-time cable force computation.

Reinforcement learning (RL) based multilift trajectory planning is presented in Section 5.5. Planning based on load distribution using proximal policy optimization is formulated. Preliminary simulation results and discussion are provided to show the effectiveness of the RL framework and the advantages and disadvantages of this approach.

Finally, a summary of this chapter is given in Section 5.6.

5.1 Load Distribution Based Trajectory Planning and Control Problem

The hierarchical load-leading strategy provides a convenient platform for the trajectory planning problem. Given a well-planned trajectory, the payload can compute the command for the rest of the system as team leader. Hence, the trajectory planning

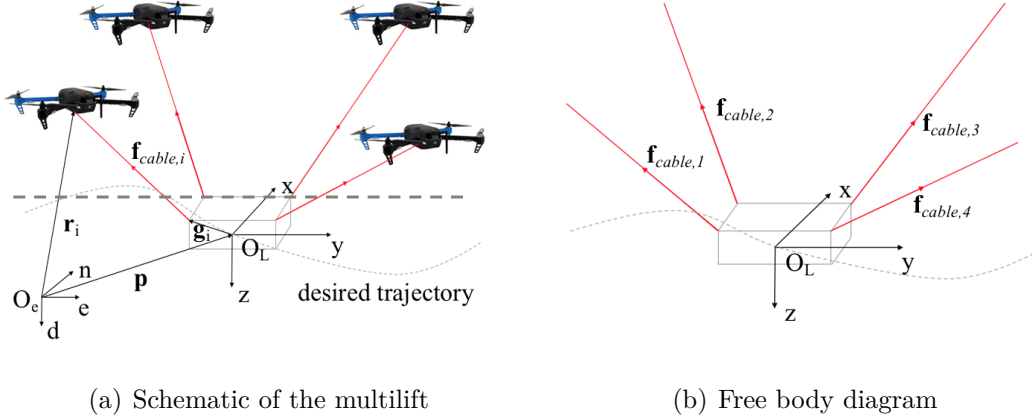


Figure 5.1. Multilift problem and simplification

problem for multilift can be simplified as planning for payload while considering other physical and geometric constraints.

5.1.1 Problem Simplification

The key part of the hierarchical load-leading approach is computing the set of required cable forces. Given the cable forces (i.e. tension and direction), the desired rotorcraft states (i.e. position, velocity and acceleration) can be determined through the direct kinematics relation between payload and rotorcraft. Assuming that the rotorcraft can respond instantly to commands for some bounded set of cable forces, one can treat the system as a rigid body motion with a set of cable forces as inputs, Fig. 5.1(b).

The focus of this chapter is on the payload trajectory generation. The goal is to find a trajectory, including the payload states and input sequence and the corresponding control mechanism to achieve evenly distributed load on each tether when flying from given waypoints A to B in a fixed amount of time while satisfying the payload equation of motion and the input constraints. This essentially combines the trajectory generator, the trajectory following controller, and the cable force computation blocks of Fig. 2.2. To achieve this goal, the problem is split in two parts: (1) Pre-plan a desired trajectory for the payload and cable force while considering the load distribution for the ideal environment. (2) Design a feedback controller for the system to track the desired reference trajectory under disturbance.

Assumption 1: In this study, payload trajectories with small pitch and roll angles are considered since the near hover case was successfully tested in hardware flight [70]. Large

slung load maneuver (greater than 10° pitch and roll) is beyond the scope of this chapter.

Assumption 2: The cables are always in tension when the system stays in the air. Cable force vectors remain in the same quadrant within a fixed sector region $\Delta\beta$ [70] (see Fig.3.1) in the payload body frame so that cables will not cross and ensure vehicle separation. Note that $\Delta\beta$ won't affect the payload controllability as long as the four cables remain with in different quadrants [59]. The cone angle α_i between each cable and the vertical axis of payload body frame is designed to be maintained at a specified value to ensure vehicle separation and payload controllability. In fact, it has been showed that the payload becomes more controllable as the cone angle increases [59]. However, it requires higher cable tension. Notice that here a fixed cable cone angle α is considered since it is the scenario for most of cruise flight.

5.1.2 Trajectory Planning Problem

In order to equalize the load distribution, Berrios designed a cost function to penalize load distribution inequality of the tension difference between two cables for a dual-lift system [17]. A feedback controller was designed based on the difference in the cable tension error. However, increasing the number of rotorcraft beyond two adds complication. It is necessary to find a proper measure to quantify the load distribution. Here, minimizing the tension variance of all the cables is proposed so that the load distribution can be equalized. The control input or the cable force can also be planned at the same time.

Remark 1. For a near hover low speed payload with equal cable cone angles, the cable tension is directly related to the power of rotorcraft. By equalizing the cable tension, the rotorcraft can achieve near-evenly distributed power [16, 17].

Let us consider payload state vector: $\mathbf{x}_s = [{}^e\mathbf{p}^T, \boldsymbol{\Omega}^T, {}^e\dot{\mathbf{p}}^T, \boldsymbol{\omega}^T]^T$, where $\boldsymbol{\omega}$ is payload angular rate in \mathcal{F}_L . Notice that the pose of the payload is described in Chapter 2 by vector $\mathbf{x}_L = [{}^e\mathbf{p}^T, \boldsymbol{\Omega}^T]^T$. The input vector is chosen as $\mathbf{u} = [f_1, \beta_1, f_2, \beta_2, f_3, \beta_3, f_4, \beta_4]^T$, where f_i is the tension magnitude of the i^{th} cable, $i = 1, 2, \dots, 4$. β_i is the angle between the cable force projection on the 2D plane (payload body $x - y$ plane) and the positive direction of payload body x -axis.

Hence, the trajectory planning problem based on load distribution can be formulated as:

$$\begin{aligned} \min_{\mathbf{u}} \quad & J = \Phi(t_f) + \int_{t=t_0}^{t=t_f} L(\mathbf{x}_s, \mathbf{u}) dt \\ \text{subject to} \quad & \mathbf{x}_s(t_0) = \mathbf{x}_0 \end{aligned} \tag{5.1}$$

$$\begin{aligned}
& \mathbf{x}_s(t_f) = \mathbf{x}_{t_f} \\
& 0 \leq f_i \leq f_{max}, \quad \beta_1 \leq \beta_i \leq \beta_2, \quad i = 1, \dots, 4 \\
& |\phi| \leq \phi_{max}, \quad |\theta| \leq \theta_{max} \\
& \dot{\mathbf{x}}_s = f(\mathbf{x}_s, \mathbf{u})
\end{aligned}$$

where $\Phi(t_f) = 0$, $L(\mathbf{x}_s, \mathbf{u}) = \frac{1}{4} \sum_{i=1}^4 (f_i - \frac{1}{4} \sum_{j=1}^4 f_j)^2$ is the variance of the cable tension. $\mathbf{x}_s(t_0)$ and $\mathbf{x}_s(t_f)$ are the waypoints given before flight. f_{max} is the maximum tension cable can sustain. ϕ_{max} and θ_{max} are the payload small attitude limit. $f(\cdot)$ is the payload equation of motion given by:

$$\dot{\mathbf{x}}_L = [{}^e\dot{\mathbf{p}}^T, \dot{\boldsymbol{\Omega}}^T]^T \quad (\text{Kinematics}) \quad (5.2)$$

$$m_L {}^e\ddot{\mathbf{p}} = \sum_{i=1}^4 {}^e\mathbf{R}_L \mathbf{f}_{cable,i} + \mathbf{G}_g \quad (\text{Dynamics: Newton eqn}) \quad (5.3)$$

$$\mathbf{J}_{cm}\dot{\boldsymbol{\omega}} = \sum_{i=1}^4 \mathbf{g}_i \times \mathbf{f}_{cable,i} - \boldsymbol{\omega} \times \mathbf{J}_{cm}\boldsymbol{\omega} \quad (\text{Dynamics: Euler eqn})$$

where $\dot{\boldsymbol{\Omega}} = \mathbf{W}_L \boldsymbol{\omega}$, and

$$\mathbf{W}_L = \begin{bmatrix} 1 & \sin \phi \tan \theta & \cos \phi \tan \theta \\ 0 & \cos \phi & -\sin \phi \\ 0 & \sin \theta / \cos \theta & \cos \phi / \cos \theta \end{bmatrix} \quad (5.4)$$

Recall that \mathbf{g}_i is the geometry vector from the payload \mathcal{O}_L to the i^{th} cable attachment point in frame \mathcal{F}_L . $\mathbf{f}_{cable,i} = [f_i \sin \alpha \cos \beta_i, f_i \sin \alpha \sin \beta_i, -f_i \cos \alpha]^T$ is the i^{th} cable force vector in frame \mathcal{F}_L .

Notice that in (5.2)(5.3), the angular motion is independent of translation motion. However, the translation motion is directly affected by the angular motion. The objective cost of (5.1) (i.e. the variance of cable tension) is in a quadratic form and the system equations of motion are nonlinear.

5.1.3 Tracking Problem

Once the desired payload trajectory is generated, a feedback controller is designed for the system to track the desired reference trajectory.

Here, a small perturbation method linearizing the payload equation of motion about the nominal path is used inspired by the classical neighboring feedback control approach

[75]. Let us consider small perturbation from the desired nominal path. It is expected that such perturbations will give rise to perturbation $\delta\mathbf{x}_s$, $\delta\mathbf{u}$, governed by linearizing the system equation of motion (5.2)(5.3) around the extremal path, $\delta\mathbf{x}_s = \mathbf{x}_s(t) - \mathbf{x}_s^*(t)$, $\delta\mathbf{u} = \mathbf{u}(t) - \mathbf{u}^*(t)$:

$$\begin{aligned}\delta\dot{\mathbf{x}}_s &= f_{\mathbf{x}_s}\delta\mathbf{x}_s + f_{\mathbf{u}}\delta\mathbf{u} \\ \delta\mathbf{x}_s(t_0) &\text{specified}, \quad \delta\mathbf{x}_s(t_f) \text{specified}\end{aligned}\tag{5.5}$$

where $f_{\mathbf{x}_s}$, $f_{\mathbf{u}}$ are the Jacobian of (5.2)(5.3) with respect to the nominal path. The system is supposed to track the desired trajectory, which means the perturbation $\delta\mathbf{x}_s$, $\delta\mathbf{u}$ should be small. The problem is formulated as finding control law of $\delta\mathbf{u}$ to minimize the energy due to perturbation:

$$\begin{aligned}\min_{\delta\mathbf{u}} \quad & \delta^2 J = \frac{1}{2} \int_{t_0}^{t_f} (\delta\mathbf{x}_s^T Q \delta\mathbf{x}_s + \delta\mathbf{u}^T R \delta\mathbf{u}) \\ \text{subject to} \quad & \delta\dot{\mathbf{x}}_s = f_{\mathbf{x}_s}\delta\mathbf{x}_s + f_{\mathbf{u}}\delta\mathbf{u} \\ & \delta\mathbf{x}_s(t_0) \text{specified}, \quad \delta\mathbf{x}_s(t_f) \text{specified}\end{aligned}\tag{5.6}$$

where Q and R are some positive definite matrices.

The overall control required to drive $\mathbf{x}_s(t_0) + \delta\mathbf{x}_s(t_0)$ to a final state would be equal to

$$\mathbf{u}(t) = \mathbf{u}^*(t) + \delta\mathbf{u}^*(t)\tag{5.7}$$

Notice that $\mathbf{u}^*(t)$ is the pre-planned payload nominal input under given cable force constraints. Redundancy for real flight perturbation has already been considered in the constraints to guarantee the overall control $\mathbf{u}(t)$ still be within the system flight ability. In this regard, no designed constraints will be added on $\mathbf{u}(t)$.

5.2 Analysis and Methodology

This section analyses the formulated trajectory planning and tracking problems. Direct collocation method is introduced to solve the trajectory optimization problem. Tracking problem is solved by using the backward sweep method.

5.2.1 Planning

5.2.1.1 Problem Analysis

A necessary condition for solving the optimal control problem is that the control should be chosen so as to optimize the Hamiltonian [76]. A Hamiltonian is a function used to solve an optimal control problem for a dynamical system. The Hamiltonian function of (5.1) can be defined as [77],

$$H(\mathbf{x}_s, \mathbf{u}) = L(\mathbf{x}_s, \mathbf{u}) + \boldsymbol{\lambda}^T f(\mathbf{x}_s, \mathbf{u})$$

where $\boldsymbol{\lambda}$ defines the co-states. The first order necessary conditions for optimal trajectory with no active constraints are then given by $\dot{\mathbf{x}}_s = H_{\lambda}$, $\dot{\boldsymbol{\lambda}} = -H_{\mathbf{x}_s}$ and $H_{\mathbf{u}} = 0$, where the subscript means the gradient.

Remark 2. Appendix. B.1 describes the necessary conditions in detail. From these equations, it can be inferred that there is trivial solution for co-state vector, $\boldsymbol{\lambda}$ when the cable tensions are equal, i.e., $\frac{1}{4} \sum_{i=1}^4 (f_i - \frac{1}{4} \sum_{j=1}^4 f_j)^2 = 0$. In fact, for ideal case when all the cable tension are equal,

$$L_{u_i} = \frac{3}{8} f_i - \frac{1}{8} \sum_{j \neq i} f_j = 0, i, j = 1, 3, 5, 7$$

$H_{\mathbf{u}}$ can be written as a linear combination of the co-states: $H_{\mathbf{u}} = \mathbf{E} \tilde{\boldsymbol{\lambda}}$, where $\tilde{\boldsymbol{\lambda}} = [\lambda_7, \dots, \lambda_{12}]^T$. It's easy to show that \mathbf{E} has rank 6 under the setup in this problem. Hence, $\tilde{\boldsymbol{\lambda}} = 0$ for $H_u = 0$. Furthermore, (B.6) and (B.10) corresponding to $\dot{\boldsymbol{\lambda}} = -H_x$ leads to $\lambda_k = 0, k = 1, 2, 3$ when $\tilde{\lambda} = 0$. Similarly, (B.7), (B.11)-(B.13) lead to $\lambda_4 = \lambda_5 = \lambda_6 = 0$.

Note that zero co-state implies $H_{\mathbf{u}}, H_{\mathbf{uu}}$ and higher order derivatives are all zeros. There is a singularity. Physically, it implies that payload dynamics do not affect the solution. Intuitively, this means that one can always find an equal tension solution, as long as the system is near hover (i.e. acceleration is small and external forces such as drag are small). For fixed cone angle, equal cable tension implies five unknowns of input (tension and four sector angles), and payload dynamics includes six equations. Hence, there is a least-squares solution for a specified acceleration. However, for large acceleration or large external force (aerodynamic drag), cable angle constraints will become active, and that may make an equal tension solution impossible.

5.2.1.2 Collocation

A variety of methods have been developed to solve this nonlinear trajectory optimization problems [78, 79]. Here, the direct collocation method is used, converting the trajectory optimization problem into a nonlinear programming problem [80].

According to this method, the time is first discretized into N uniformly distributed subintervals (for the fixed final time case). Then, an initial guess of states and input for each one of the $N + 1$ collocation points $\bar{\mathbf{x}}_s(t_k)$, $\bar{\mathbf{u}}(t_k)$, $k = 0, 1, \dots, N$ is given. In each interval, since $\dot{\bar{\mathbf{x}}}_s(t_k)$ is also known through the system dynamics, a cubic interpolation for states while linear interpolation for inputs can be performed. Denote $\tau = \frac{t-t_k}{h}$, where $h = t_k - t_{k-1}$.

$$\begin{aligned} x_i^k(\tau) &= a_i^k + b_i^k\tau + c_i^k\tau^2 + d_i^k\tau^3 \\ \dot{x}_i^k(\tau) &= \frac{b_i^k}{h} + 2\frac{c_i^k\tau}{h} + 3\frac{d_i^k\tau^2}{h} \\ u_i(\tau) &= \bar{\mathbf{u}}_i(t_k) + (\bar{\mathbf{u}}_i(t_{k+1}) - \bar{\mathbf{u}}_i(t_k))\tau \end{aligned}$$

where the subscripts i, j denote the i th states and j th input. $x_i^k(0) = \bar{\mathbf{x}}_{s,i}(t_k)$, $x_i^k(1) = \bar{\mathbf{x}}_{s,i}(t_{k+1})$, $\dot{x}_i^k(0) = f_i(\bar{\mathbf{x}}_s(t_k), \bar{\mathbf{u}}(t_k))$, $\dot{x}_i^k(1) = f_i(\bar{\mathbf{x}}_s(t_{k+1}), \bar{\mathbf{u}}(t_{k+1}))$. The mid point of each interval can then be evaluated easily as well as the error:

$$\begin{aligned} x_i^k(1/2) &= \frac{1}{2}(\bar{\mathbf{x}}_{s,i}(t_k) + \bar{\mathbf{x}}_{s,i}(t_{k+1})) \\ &\quad + \frac{h}{8}[f_i(\bar{\mathbf{x}}_s(t_k), \bar{\mathbf{u}}(t_k)) - f_i(\bar{\mathbf{x}}_s(t_{k+1}), \bar{\mathbf{u}}(t_{k+1}))] \\ \dot{x}_i^k(1/2) &= -\frac{3}{2h}(\bar{\mathbf{x}}_{s,i}(t_k) - \bar{\mathbf{x}}_{s,i}(t_{k+1})) \\ &\quad - \frac{1}{4}[f_i(\bar{\mathbf{x}}_s(t_k), \bar{\mathbf{u}}(t_k)) + f_i(\bar{\mathbf{x}}_s(t_{k+1}), \bar{\mathbf{u}}(t_{k+1}))] \\ u_i^k(1/2) &= \frac{\bar{\mathbf{u}}_i(t_k) + \bar{\mathbf{u}}_i(t_{k+1})}{2} \end{aligned}$$

By evaluating the error:

$$e_i^k = \dot{x}_i^k(1/2) - f_i(\bar{\mathbf{x}}_s(t_{k+\frac{h}{2}}), \bar{\mathbf{u}}(t_{k+\frac{h}{2}}))$$

The original optimal control problem thus is transcribed as a nonlinear programming

problem

$$\min_{\mathbf{u}} \quad J = \Phi(\mathbf{x}_s(t_N)) + \frac{1}{2} \sum_{k=0}^N [L(\bar{\mathbf{x}}_s(t_k), \bar{\mathbf{u}}(t_k), t_k) + L(\bar{\mathbf{x}}_s(t_{k+1}), \bar{\mathbf{u}}(t_{k+1}), t_{k+1})] h \quad (5.8)$$

$$\text{subject to } e_i^k = 0, \quad k = 0, 1, 2, \dots, N \quad (5.9)$$

5.2.2 Tracking

Problem (5.6) is a linear quadratic problem. An analytic solution can be obtained by using Bryson's backward sweep method [75].

$$\begin{aligned} \delta \mathbf{u}(t) = & -(K - R^{-1} B^T V P^{-1} V^T) \delta \mathbf{x}_s(t) \\ & - R^{-1} B^T V P^{-1} \delta \mathbf{x}_s(t_f) \end{aligned} \quad (5.10)$$

where

$$A(t) = f_{\mathbf{x}_s}, \quad B(t) = f_{\mathbf{u}} \quad (5.11)$$

$$\begin{aligned} -\dot{S} &= A^T S + S A - S B R^{-1} B^T S + Q \\ K &= R^{-1} B^T S \\ -\dot{V} &= (A - BK)^T V \\ \dot{P} &= V^T B R^{-1} B^T V \end{aligned} \quad (5.12)$$

$S(t_f) = 0$ is given, $V(t_f) = I$, $P(t_f) = 0$. Given the final time states $S(t_f) = 0$, the whole sequence $S(t)$ can be solved by backwards integration. $V(t)$ can be solved in the same way. Notice that the feedback control term $\delta \mathbf{u}$ only relies on the state error, which means there is no need to put on cable tension sensors along the cables.

5.3 Simulation

In this section, numerical simulation results are presented. Three test cases are considered for planning: one with the given final time $t_f = 5.0$ sec based on the flight tests described in [70], the other two with $t_f = 2.8, 2.3$ sec by reducing the arriving time to stress the system. As for the tracking, the system is simulated by applying the designed neighboring feedback controller (5.11) under the wind gust environment to show the effectiveness of

the developed feedback controller.

5.3.1 Setup

5.3.1.1 Multilift Parameter

The parameters used for multilift are the same as those developed in load-leading hardware platform desried in Chapter 3, see Table.3.1 and Table.3.2 of the parameters for payload and cables as well as the cable attachment geometry.

5.3.1.2 Setup for Trajectory Planning

For the trajectory planning problem, the system is scheduled flying from waypoint A to B . Without loss of generality, pick A as the origin with zero velocity and payload level. B is a waypoint with prescribed position ${}^e\mathbf{p}_B = [1.5, 1.8, -0.9]^T$ and zero velocity and payload level.

The nonlinear programming solver “fmincon” in MatLab is used to solve the formulated problem (5.8). The “sqp” algorithm (sequence quadratic programming) is selected. $Np = 31$ collocation points are used for discretization considering the solver convergence speed and the accuracy after trials.

The polynomial curve method described in Chapter 3 is used for generating an initial guess of payload states \mathbf{x}_s . The trajectory is generated from a 3rd order polynomials as the linear and angular acceleration with zero boundary conditions. The payload linear and angular velocity and position are then generated by higher order polynomials which satisfy waypoint boundary conditions. The total force and moment acting on the payload can then be obtained from the corresponding acceleration. Cable force as the payload input \mathbf{u} is then initialized with least-norm solution to satisfy the net forces and moments and null space solution to satisfy cable tension magnitude and geometry constraints.

5.3.1.3 Tracking Controller Parameter

The parameters for the tracking controller are designed as $Q = 1.0 \times \mathbf{I}_{12}$, $R = 3.0 \times \mathbf{I}_8$. Sweep method is then implemented to compute the controller gain (5.11). $\delta\mathbf{x}_s(t_0)$ is selected as a Gaussian random variable with zero mean and 6cm position standard deviation based on the hardware flight test [70]. $\delta\mathbf{x}_s(t_f)$ is generated as a zero vector.

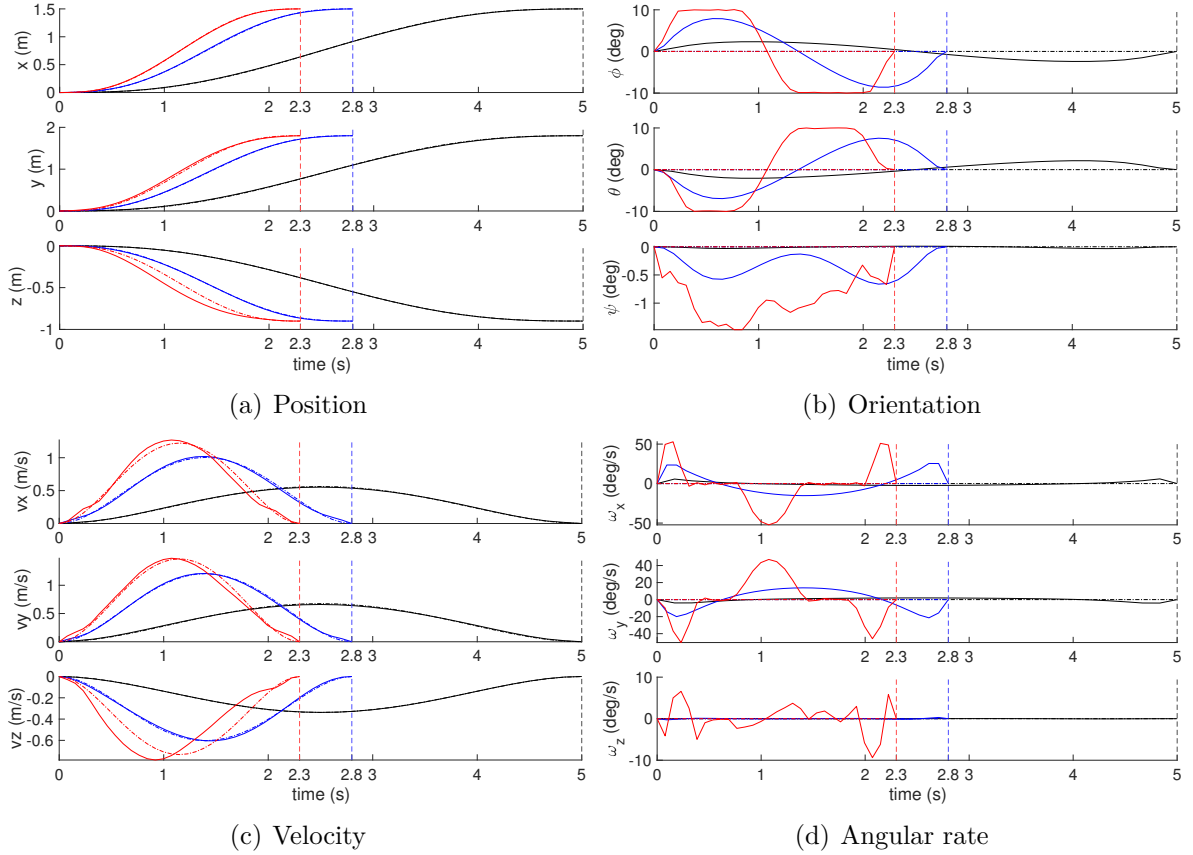


Figure 5.2. Payload state for $t_f = 5.0$ (black), 2.8 (blue), 2.3 (red) sec, initial guess (dashed) and optimal solution (solid)

5.3.1.4 Wind Gust

Wind gusts is added as an external disturbance when the system is simulated during flight tracking the reference trajectory. This gust acts upon the payload as an aerodynamic drag force [81, 82]:

$$D = \frac{1}{2} \rho v_a^2 S C_d \quad (5.13)$$

where $\rho = 1.225\text{kg/m}^3$ is the air density, \mathbf{v}_a is payload airspeed, S is the reference area of payload, C_d is the drag coefficient. A mild wind gusts \mathbf{w} modeled using a normal distribution with zero mean and standard deviation 2.5m/s is considered. Also, notice that the inertial velocity of payload $\mathbf{v} = \mathbf{v}_a + \mathbf{w}$.

5.3.2 Planning Results and Discussion

Fig. 5.2 shows the payload states of all three cases. It can be seen the nonlinear solver can find the minimum which satisfies all the constraints. The payload is able to be driven

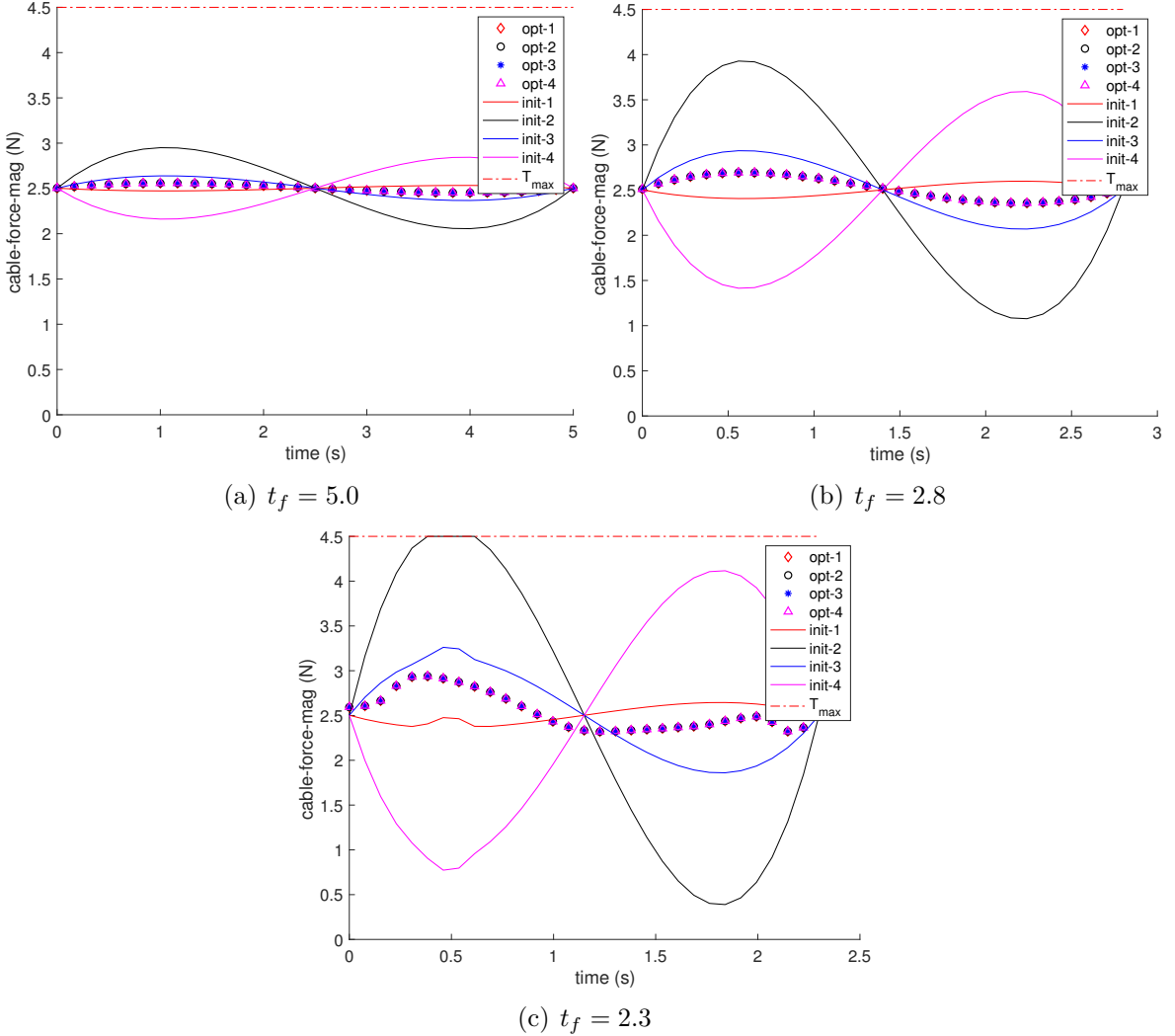


Figure 5.3. Cable tension

to the destination for all cases.

Note that the position and velocity histories of the polynomial trajectory and the optimal (i.e. load-distributed) solution are very close. Orientation and angular rate, however, differ significantly. The reason for this lies in the mechanism of payload motion under load-distributed control: translation occurs via changes in payload orientation (similar to translation control of a multi-rotor).

The initial and optimized cable tension as well as the sector angle of the four cables are compared in Fig. 5.3 and Fig. 5.4. Note that the cable tensions: the optimal load distribution controller results in very nearly equal cable tensions throughout the payload trajectory.

From Fig. 5.2, 5.3(b) and 5.4(b) one can observe by reducing the arriving time, all

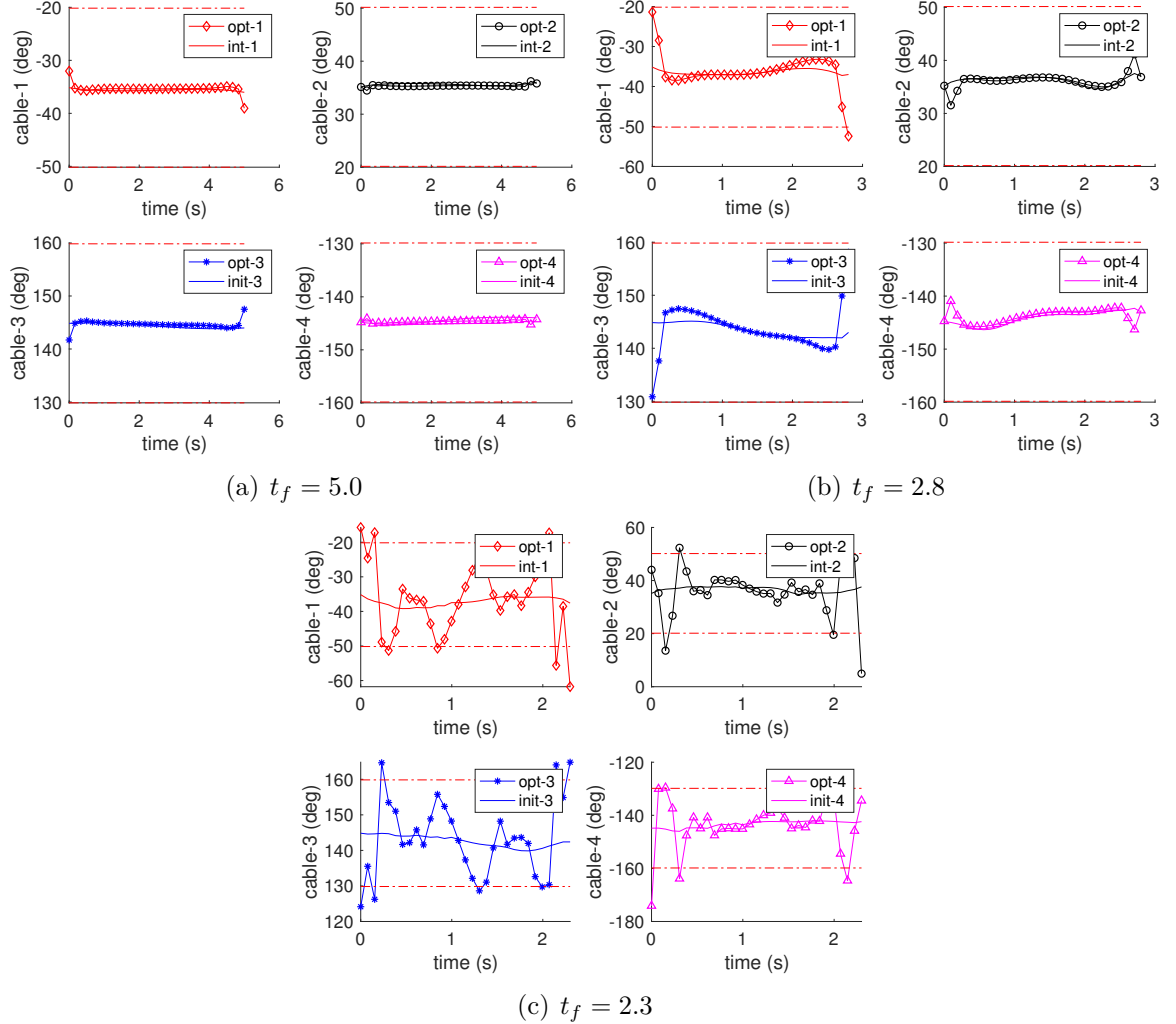


Figure 5.4. Cable sector angle

the cable tension increase but still with a evenly distributed load. The payload ended with a larger rotation maneuver and a more aggressive change of sector angle in order to achieve the goal in a shorter time by bigger acceleration. If reducing the arriving time even further, see the case when $t_f = 2.3$ sec, Fig. 5.2(b), 5.3(c) and 5.4(c), in order to achieve the goal while maintain small attitude, the system can only accelerate by changing the sector angle, resulting in hitting the bound fluctuatedly, which (depending on the payload contents) may not be ideal. Therefore, one can say this mission cannot be achieved by small maneuver.

Remark 3. In general, the solution obtained from the direct method is only a numerical local minimum. However, in the problem discussed above, the direct collocation method can find the optimal solution (i.e. equal cable tension) for near hover situation (small

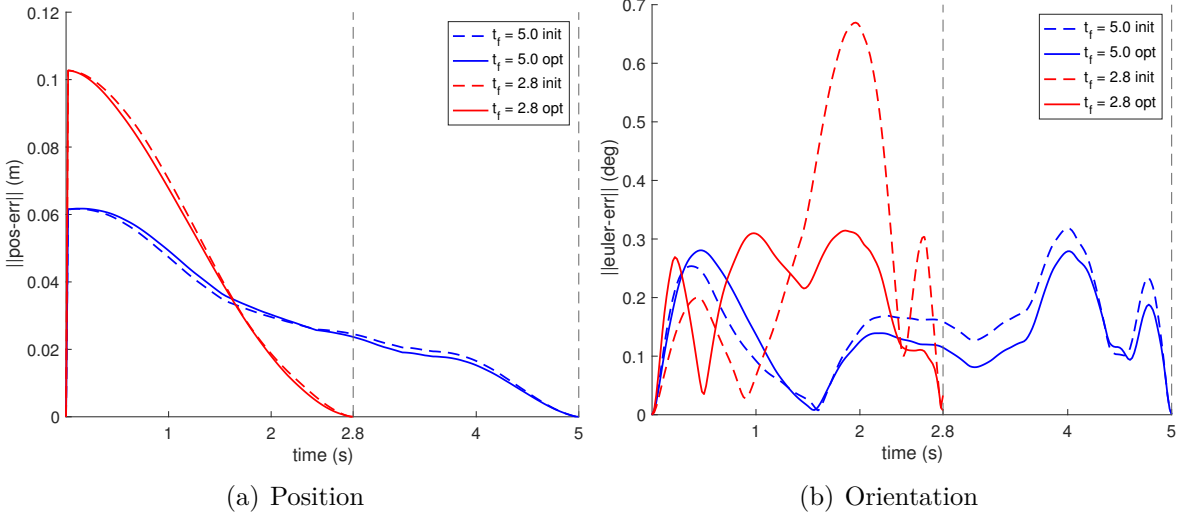


Figure 5.5. Tracking error (in 2-norm) of payload states under wind gust

Table 5.1. Maximum cable tension tracking error

Case	$t_f = 5.0$ (N)	$t_f = 2.8$ (N)
Initial trajectory	0.0821	0.1012
Optimized trajectory	0.0596	0.0893

maneuver).

5.3.3 Tracking Results Under Wind Gust

Fig. 5.5 shows the tracking error when $t_f = 5.0, 2.8$ sec for both initial polynomial trajectory and optimal load-distributed trajectory. The system encounters disturbance during the flight under the wind gust environment. The feedback controller is able to correct the system and drive the slung load to the desired trajectory.

As for the control input, Fig. 5.6 show the input tracking error for optimal trajectory tracking. None of input saturate during the flight simulation. However, the case when $t_f = 2.8$ clearly shows bigger tracking error due to the bigger maneuver. Table. 5.1 shows the maximum cable tension tracking error for both the initial and optimal trajectory tracking. The initial trajectory tracking ends with bigger cable tension tracking error, which is harmful for the real hardware flight since the overload due to the uneven distributed tension could cause motor and power failure for the vehicle with the highest cable tension.

Table. 5.2 shows the load distribution cost, or the total cable tension variance of four groups of trajectory: initial guess, optimized trajectory and flight simulation under

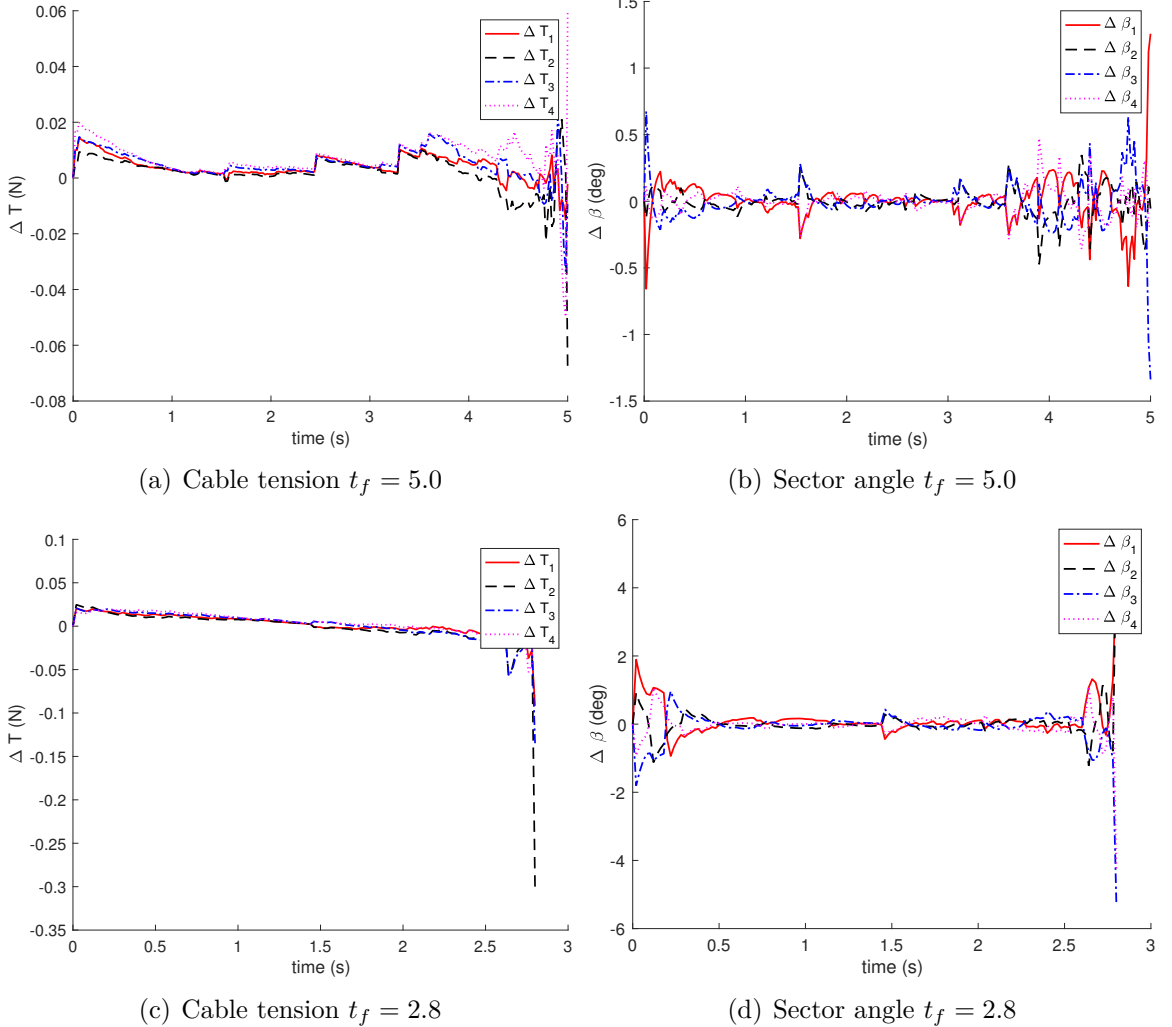


Figure 5.6. Input tracking error

wind gust for two cases. Compared with the initial guess (i.e. the polynomial-derived trajectory), even with external disturbances (e.g. wind gusts) cable forces of the optimized trajectory are more evenly distributed. In fact, the cable load cost is still an order of magnitude lower than the initial guess, even with wind gusts acting upon the payload.

5.4 Hardware Experiment

In this section, hardware tests in an indoor motion capture studio are performed to validate the proposed trajectory planning and control approaches. Two cases are tested and compared: one with proposed load distribution based planning and the neighboring feedback control approach; the other one with polynomial curve planning method and

Table 5.2. Cost of load distribution

Case	cost	
	$t_f = 5.0$	$t_f = 2.8$
Initial guess	13.8729	78.9977
Optimized trajectory	2.3731e - 9	2.6821e - 09
Initial trajectory tracking	14.0180	79.2331
Optimal trajectory tracking	0.0075	0.0337

the hierarchical approach with real-time cable force computation.

5.4.1 Experiment Setup

The system is scheduled to lift off the ground for 0.5m after take off in the FOL_LOW_TRAJ state, denote this point as start point A with ${}^e\mathbf{p}_A = [x_0, y_0, z_0]^T$; then fly to waypoint B with ${}^e\mathbf{p}_B = [x_0 + 1.5, y_0 + 1.8, z_0 - 0.9]^T$ in 5.0 sec; hold for 0.5 sec and then fly back to A in 5.0 sec; finally descend to touchdown and land. This design ensures the system can be better fit in and use the available Vicon capture volume. Meanwhile, the system movement in all direction can be excited within the limitations of sensors and actuators.

The control parameters designed in simulation provides a start for real hardware flight. The final control parameters used for the flight tests are the results after tweaking based on the Bryson's rule [75]. The basic idea of this technique is to normalize the contribution that the state outputs and the control term may have on the quadratic cost function. The anticipated maximum values or deviation of the individual outputs and controls is usually used to accomplish this normalization, i.e.

$$q_{ii} = \frac{1}{\max(x_{ii})^2}, \quad i = 1, 2, \dots, 12 \quad (5.14)$$

$$r_{jj} = \frac{1}{\max(u_{jj})^2}, \quad j = 1, 2, \dots, 8 \quad (5.15)$$

The final parameters used in real hardware implementation are given in Appendix.B.2.

Two cases are tested and compared: (1) the load distribution based planning and the neighboring feedback control approach proposed in this chapter. (2) polynomial curve fitting method and the hierarchical approach with real-time cable force computation.

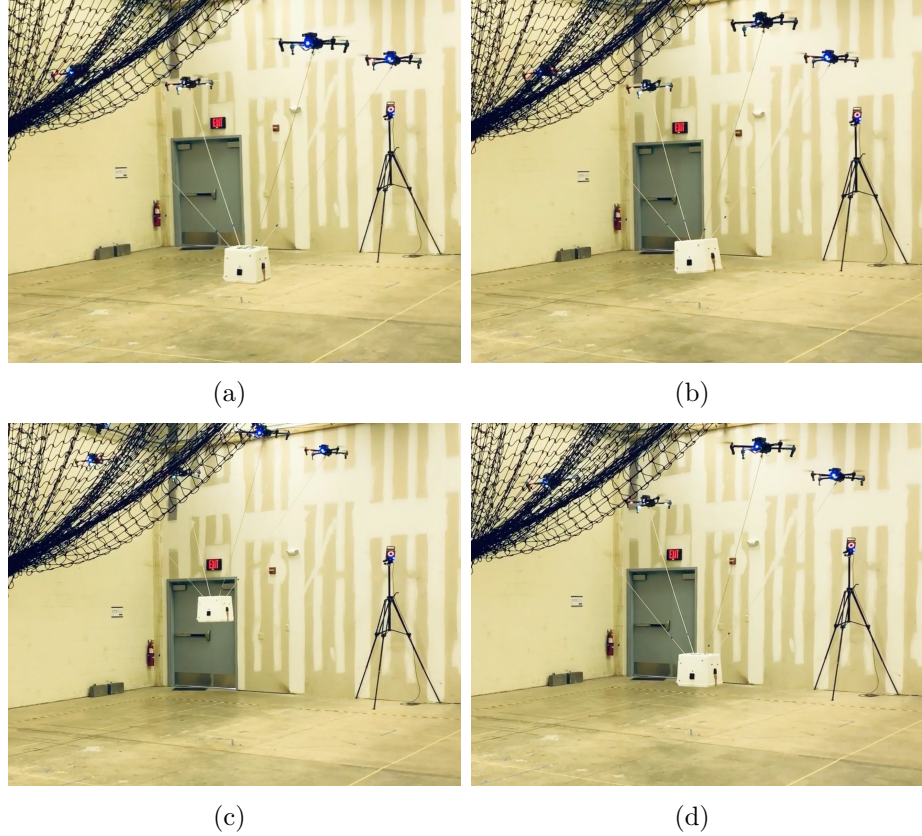


Figure 5.7. Sequence of images showing system behavior using the load distribution based trajectory planning and control

5.4.2 Results and Discussion

Fig. 5.7 depicts a sequence of images from the flight test. The system lifts the payload above the ground for 0.5m at point A, Fig. 5.7(a); on the way of flying to waypoint B, Fig. 5.7(b); arrives waypoint B, Fig. 5.7(c); flies back to waypoint A.

Payload tracking performance is shown in Fig. 5.8. It can be seen that in both cases, the payload can be transported to the desired waypoints successfully under the payload leading approach.

However, the cable tension and sector angle comparison presented in Fig. 5.9 and Fig. 5.10 show that the cable tension ends with larger variance in case 2. Planning based on load distribution clearly reduced the cable tension variance by conducting proper feedback control. The cable sector angles are shown in Fig. 5.10. All cables remain in the valid quadrant with respect to the payload during flight within several degrees variation.

Fig. 5.11 show the four rotorcraft tracking performance. In both cases, the rotorcraft behaving as the actuators can effectively execute the payload command and track the

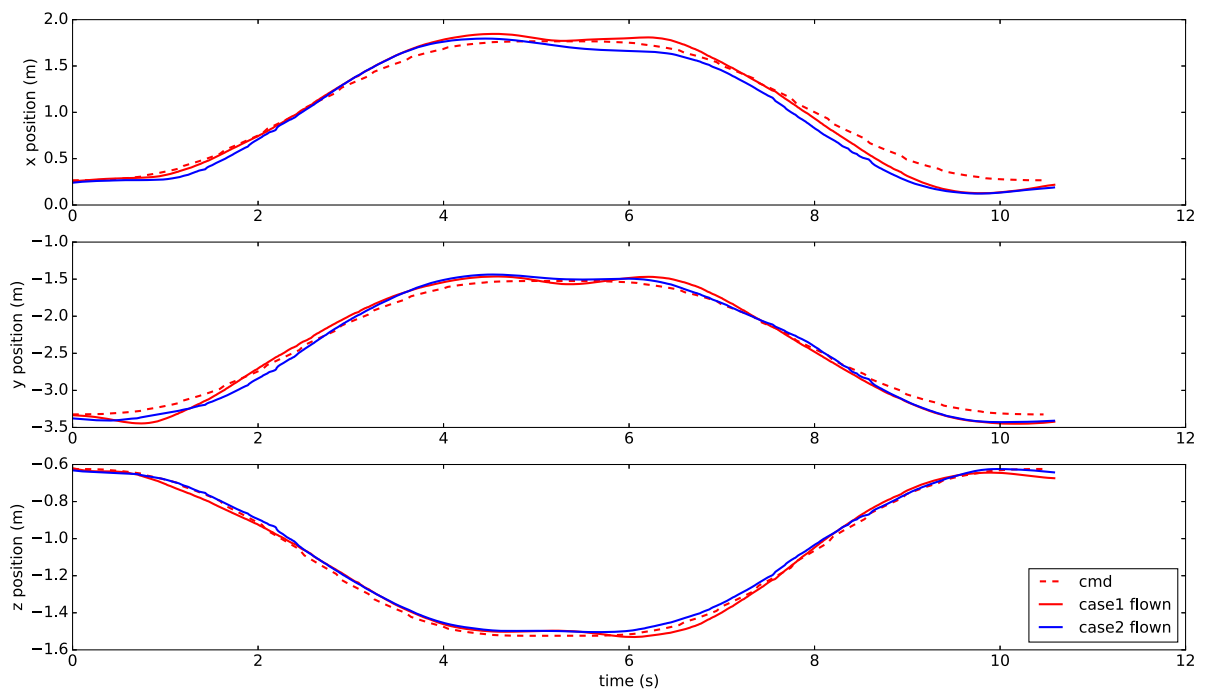


Figure 5.8. Payload tracking performance

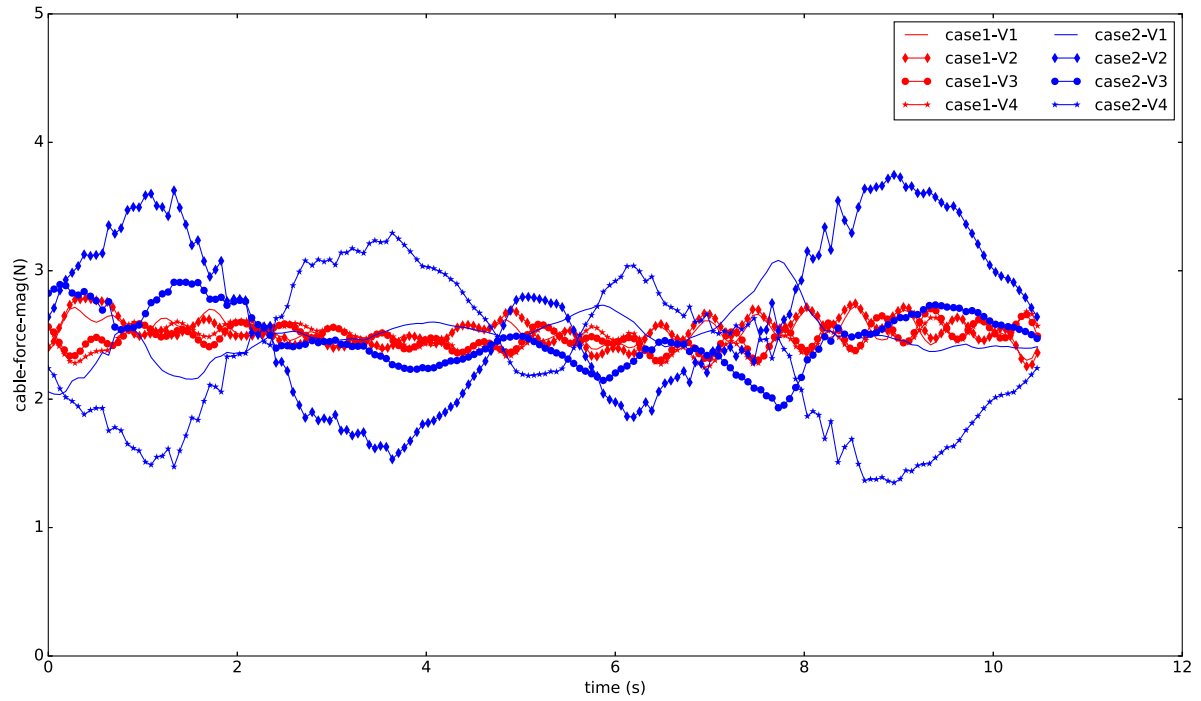


Figure 5.9. Cable tension

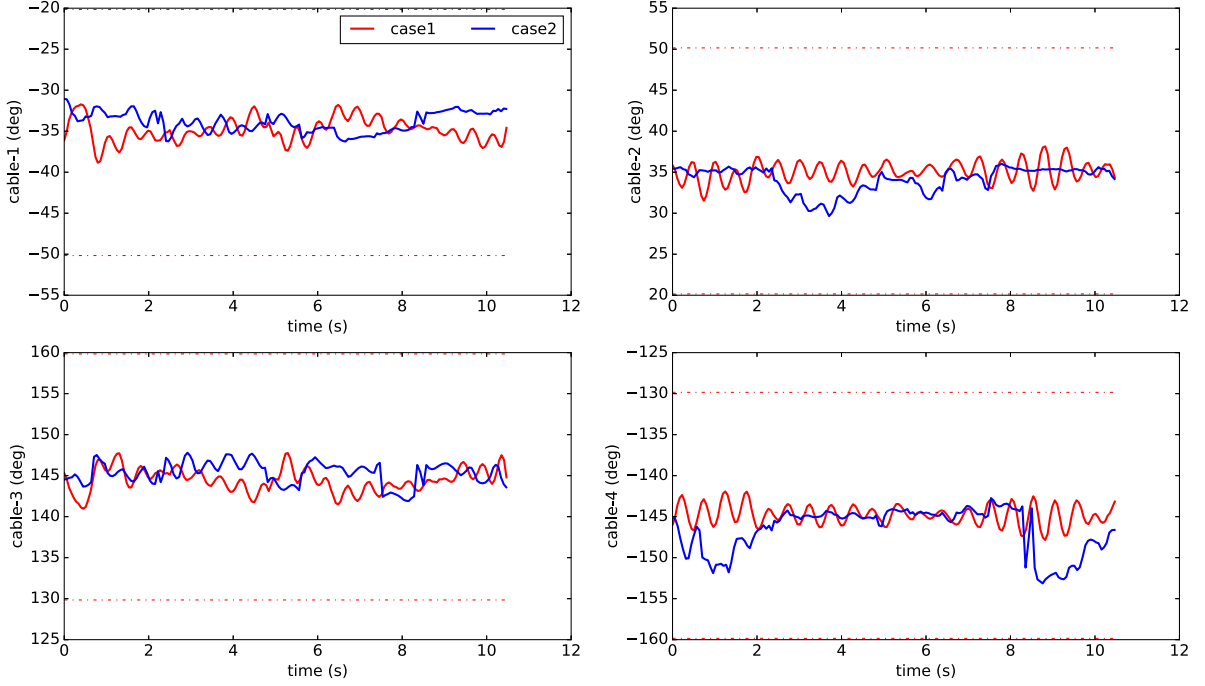


Figure 5.10. Cable sector angle

Table 5.3. Comparison of energy consumption performance

Quantity	Case 1	Case 2
Average cable tension variance (N^2)	0.0076	0.2092
Average individual robot power (W)	189.14	191.44
Average total power (W)	756.7	765.8
Average power std (W)	6.011	7.642

commanded position.

Particularly, it is worth to notice that due to the less variant cable tension performance, case 1 shows a superior power consumption performance. In fact, Fig. 5.12(a) and Fig. 5.12(b) show the time history of the total power consumption and the standard deviation (std) of the power consumption of the four rotorcraft. Table. 5.3 provides a comparison of specific quantities of the energy consumption performance. One can clearly observe that planning based on load distribution followed by the neighboring feedback control approach clearly reduces the total power of the four robots. The multilift system achieves a more near-equal power consumption among the robots comparing to the case without planning based on load distribution.

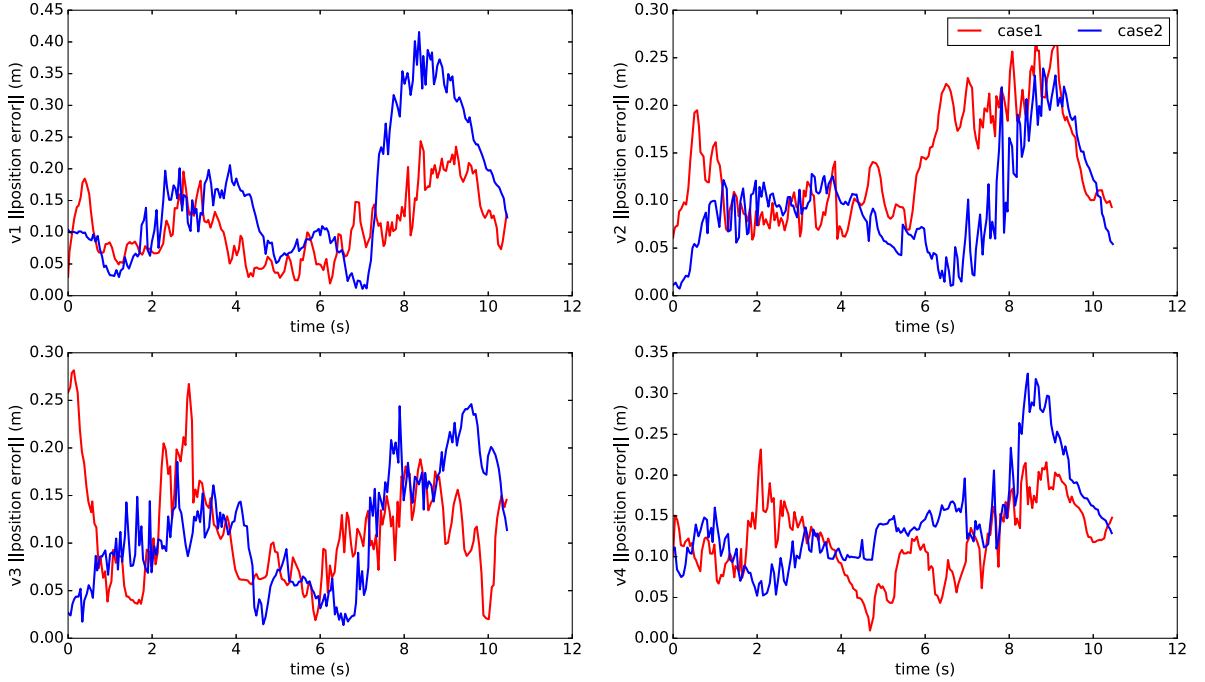
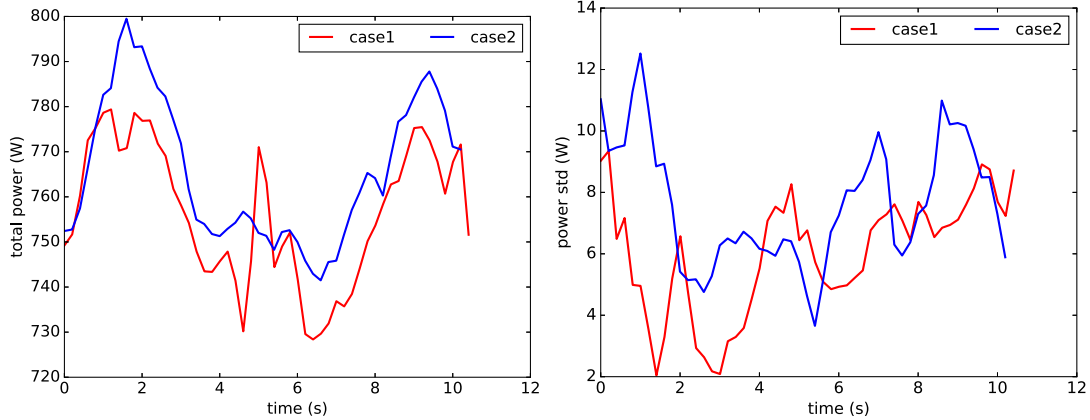


Figure 5.11. Robots tracking performance



(a) Total power consumption of the four robots (b) Standard deviation of the robots' power consumption

Figure 5.12. Energy consumption performance of the rotorcraft

5.5 Towards Reinforcement Learning Based Trajectory Planning

Optimal control theory provides a way for developing a framework for load-leading multilift trajectory planning and control based on load distribution. However, due to the system complexity, accurate modeling the multilift and the environment, including the

aerial robots system, cable performance, aerodynamics is challenging. Recent model free reinforcement learning (RL) opens another possibility for multilift planning and control problem. On one hand, RL does not require any human knowledge of pre-set rules. Instead, in RL, an agent is trained to take an optimized action within an environment by maximizing some notion of cumulative reward [83]. This model-free nature of RL is appealing to the multi-robot cooperation problem because of the complexity in model-based approach. On the other hand, the flexibility and robustness of the well-trained RL framework enables the versatile operation of the multi-robot system in stochastic and complex environment, which satisfies the adaptive requirement from various application.

RL has demonstrated great potential in achieving optimal policies for complex robotic problems, such as aerobatic helicopter [84], bio-inspired inverted landing [85], imitating the diverse and agile locomotion skills of animals [86], where a rather accurate model is required for traditional controller design [87–90]. Unlike supervised learning where labeled data is available, RL agent learns and obtains data during the process of interacting with the environment by smartly transforming the received reward. There are in general two classes of RL (1) value-based: knowing the value first and then find the policy based on the value function, such as deep Q-network (DQN), where the target network provides a temporal labeled data. This works well for many problem with discrete actions spaces; (2) policy based: directly train for the policy without accurately knowing the value (this is essential for the problem with continuous action space), such as the actor critic method, where the policy and value networks partially overlap to obtain the policy while providing some understanding on how good the actions were [91]. Among the recent developed RL algorithms, proximal policy optimization (PPO) performs a balance between ease of implementation, sample complexity, and ease of tuning. It computes an update at each step that minimizes the cost function while ensuring the deviation from the previous policy is relatively small [92].

In this section, trajectory planning based on load distribution using RL framework is investigated. Inherited from the hierarchical load-leading strategy, the planning problem can be simplified as planning for payload while considering other physical and geometric constraints. An application of the PPO algorithm on a slung load with the goal of achieving waypoint navigation while minimizing the cable tension variance is presented. Benefiting from the load-leading concept, the RL agent, which is the payload, directly learns the cable forces. The constraints are considered in the design of reward function and the termination criteria for each data episode. Results show that RL based planning can successfully plan the trajectory for multilift between waypoints while considering

the load distribution. Comparing with the optimal control based planning, RL based planning results shows robust open-loop performance.

This study has several contributions. First, it develops a model-free RL based framework for multilift trajectory planning, which provides a different perspective of planning other than optimal control. Second, it shows that the feasible trajectory with equal cable tension is not unique given the initial and final waypoints. Third, the advantages and disadvantages of RL based approach when applying to the planning problem is discussed.

5.5.1 Multilift Learning Problem

The goal is to plan trajectory for payload waypoint navigation while minimizing the cable tension variance. The system is scheduled flying from waypoint A to B in a fixed amount of time t_{goal} .

In the implementation, the state space is still the 12-dimensional payload state vector: $\mathbf{x}_s = [{}^e\mathbf{p}^T, \boldsymbol{\Omega}^T, {}^e\dot{\mathbf{p}}^T, \boldsymbol{\omega}^T]^T$, or the position, orientation, velocity and angular rate.

The action space is the cable forces acting on the payload. Instead of using the original full input vector $\mathbf{u} = [f_1, \beta_1, f_2, \beta_2, f_3, \beta_3, f_4, \beta_4]^T$, the action space is selected as $\mathbf{u} = [f_c, \beta_1, \beta_2, \beta_3, \beta_4]^T$, where f_c is the equal cable tension acting on the payload. This design leverages the conclusion made from the optimal control based planning approach: one can always find an equal tension solution as long as the system is in small maneuver. It automatically generates the trajectory with minimum cable tension variance if there is a feasible solution while reducing the dimension of action space, which is usually the key factor affecting the total learning time.

The reward function penalizes the distance from the goal states while shaping the velocity. The velocity shaping avoids the situation that the agent achieves the goal rapidly then keeps static. To reduce the numerical instability, the distance penalty and velocity shaping are normalized. The agent is rewarded when it reaches the goal within reasonable amount of time or penalized when it violates the feasible physics or exceeds the maximum time. In either of those situation, the episode terminates and restarts a new one. Here, feasible physics represents the reasonable orientation and payload

acceleration. The overall reward function is designed as:

$$r(\mathbf{x}_s) = \begin{cases} \left[1 - \left(\frac{\|{}^e\mathbf{p} - {}^e\mathbf{p}_{goal}\|}{\|{}^e\mathbf{p}_0 - {}^e\mathbf{p}_{goal}\|}\right)^{\sigma_1}\right] \left[1 - \left(\frac{\min(\|{}^e\dot{\mathbf{p}}, v_{max}\|)}{v_{max}}\right)^{\sigma_2}\right] & \|\mathbf{x}_s - \mathbf{x}_{s,goal}\| < \epsilon_1 \text{ and } |t - t_{goal}| < \epsilon_2 \\ a_1 & \|\boldsymbol{\Omega}\| > \epsilon_3 \text{ or } \|{}^e\ddot{\mathbf{p}}\| > acc_{max} \\ -a_2 & t > t_{max} \\ -a_3 \end{cases} \quad (5.16)$$

To obtain the state transition function samples, a simplified model of the free payload without cable attachment (*reduced system*) is used for simulation, which is the same as the simplification in optimal control approach (Section 5.1.1). The simulator returns the next system state \mathbf{x}_s , when an action \mathbf{u} is applied. Equations (5.2) and (5.3) describes the payload motion.

5.5.2 PPO Algorithm

As mentioned before, PPO has become popular in RL because of its ease of use and good performance. As a policy based method, it is suitable to be used for the multilift payload with continuous action space. PPO is a derivatives of the classic actor critic methods such as A2C and A3C. It creates an improvement by changing the formula used to estimate policy gradients. Instead of computing the gradient of logarithm probability of the action taken, PPO algorithm designs a different objective: the ratio between the new and the old policy scaled by the advantages.

Specifically, the objective function of the classical A2C is [83]

$$J_\theta = E_t[\log \pi_\theta(\mathbf{u}_t | \mathbf{x}_{s,t}) A_t] \quad (5.17)$$

where $\pi(\cdot)$ is the policy with parameter $\boldsymbol{\theta}$, $\mathbf{x}_{s,t}$, \mathbf{u}_t are the state and action at time t , $A_t = Q(\mathbf{x}_{s,t}, \mathbf{u}_t) - V(\mathbf{x}_{s,t})$ is the estimated advantage (the difference between Q function and value function) at time t . $E_t[\cdot]$ represents the empirical expectation over timesteps.

The new objective proposed by PPO algorithm is:

$$J(\boldsymbol{\theta}) = E_t \left[\frac{\pi_\theta(\mathbf{u}_t | \mathbf{x}_{s,t})}{\pi_{old}(\mathbf{u}_t | \mathbf{x}_{s,t})} A_t \right] \quad (5.18)$$

inspired by the importance sampling idea. Clipped objective gradient is used to limit the update. Denote the ratio $r_t(\boldsymbol{\theta}) = \frac{\pi_\theta(\mathbf{u}_t | \mathbf{x}_{s,t})}{\pi_{old}(\mathbf{u}_t | \mathbf{x}_{s,t})}$, the clipped objective function can be

written as:

$$J(\boldsymbol{\theta})^{clip} = E_t[\min(r_t(\boldsymbol{\theta})A_t, \text{clip}(r_t(\boldsymbol{\theta}), 1 - \epsilon, 1 + \epsilon)A_t)] \quad (5.19)$$

The ratio is limited between the old and new policy in the interval $[1 - \epsilon, 1 + \epsilon]$. By varying ϵ , the size of the update can be limited. This objective function implements a way to do a Trust Region update [93]. It is compatible with Stochastic Gradient Descent, and simplifies the algorithm by removing the KL penalty and need to make adaptive updates [91].

A more general estimation is used in PPO for the advantage function :

$$A_t = \sigma_t + (\gamma\lambda)\sigma_{t+1} + (\gamma\lambda)^2\sigma_{t+2} + \dots + (\gamma\lambda)^{T-t+1}\sigma_{T-1} \quad (5.20)$$

where where γ is the discount factor balancing the current and future rewards. $\sigma_t = r_t + \gamma V(\mathbf{x}_{s,t+1}) - V(\mathbf{x}_{s,t})$. While $\lambda = 1$, as in the classical A2C method, is a special case.

The overall goal of the learning is to optimize the policy parameter (actor network) such that the expected reward for each episode, or the objective function $J(\boldsymbol{\theta})$ is maximized while adjusting the critic network (evaluates the action). The $\boldsymbol{\theta}$ is updated as:

$$\boldsymbol{\theta} \leftarrow \boldsymbol{\theta} + \alpha_\theta \nabla_{\boldsymbol{\theta}} J(\boldsymbol{\theta}) \quad (5.21)$$

where α_θ is the learning rate, $\nabla_{\boldsymbol{\theta}} J(\boldsymbol{\theta})$ is the policy gradient.

5.5.3 Application of PPO to Multilift Trajectory Planning

At each episode, the payload starts at the A with initial state \mathbf{x}_0 . Then moves towards the goal under the current policy until arrives the goal or stops due to other termination criteria (infeasible physics or maximum time). After a long sequence of samples is obtained from the environment, the advantage and reference value function are estimated for the whole sequence before several epochs of training are performed. The parameters for the actor and critic nets are updated during each epoch based on the gradient of the designed objective function.

The well-trained actor network induces a policy π for generating the payload trajectory. Given a state \mathbf{x}_s , policy $\pi(\mathbf{x}_s)$ returns an action \mathbf{u} . The resulting action moves the system to the next state based on the system dynamics to achieve the highest reward. The algorithm starts with the initial state. Then it generates an action according to policy π . The action transits the system to next state. This process repeats until the goal is reached or stops due to other termination criteria. The state and action sequence is the

Table 5.4. Parameters for Multilift Learning

Parameter	Value	Parameter	Value
γ	0.99	λ	0.95
Learning rate actor	1e-5	Learning rate critic	1e-4
Hidden size actor	256	Hidden size critic	256
PPO ϵ	0.2	PPO batch size	64
σ_1	0.6	σ_2	1.0
ϵ_1	0.2 m	ϵ_2	0.05 s
ϵ_3	15 deg	v_{max}	2.0 m/s
acc_{max}	0.3 m/s ²	t_{max}	5.0 s
t_{goal}	5.0 s	a_1	50
a_2	50	a_3	5

planned trajectory for multilift payload.

5.5.4 Simulation

5.5.4.1 Setup

The parameters used for multilift are the same as those used in optimal control based planning approach, including the parameters for payload and cables as well as the cable attachment geometry (Fig. 3.1).

The parameters implemented for RL based multilift trajectory planning is summarized in Table. 5.4.

For numerical stability, the action space is normalized to -1 and 1 for the actor network and transformed back to physical space for simulation.

Without loss of generality, pick A as the origin with zero velocity and payload level. B is a waypoint with prescribed position ${}^e\mathbf{p}_B = [1.5, 1.8, 2.0]^T$ and zero velocity and payload level. Two cases are investigated: one with only distance as the reward function, the other one with velocity shaping involved.

5.5.4.2 Preliminary Results and Discussion

Fig. 5.13 shows the planned payload states with only distance as the reward function. Trajectory from the optimal control based approach is also shown as a comparison. The corresponding control inputs are shown in Fig. 5.14 and Fig. 5.15. It can be seen that comparing to the planned results from the optimal control based approach, the RL based approach can also find feasible solution with equal cable tension, bounded sector

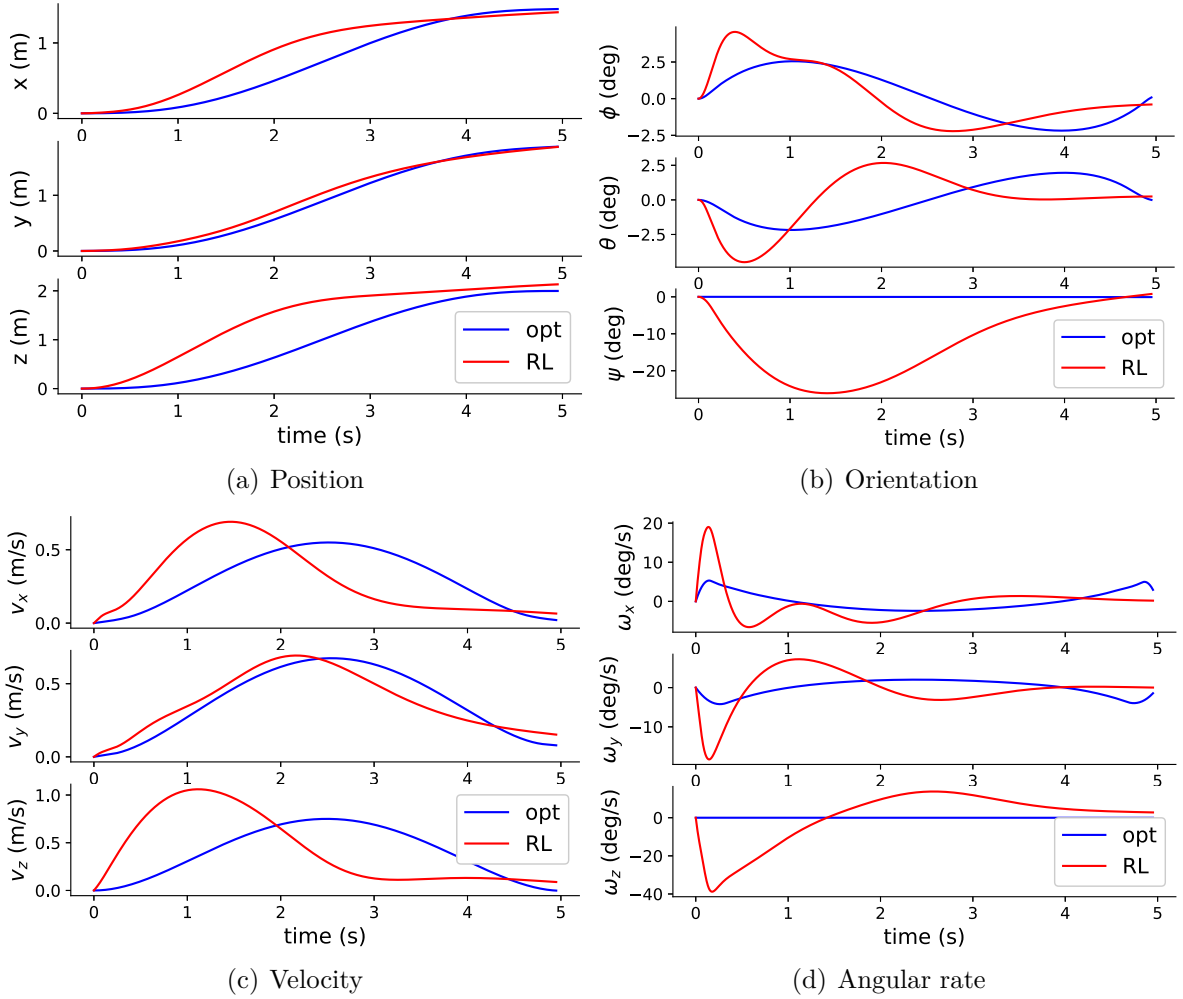


Figure 5.13. Payload States with only distance in reward function

angles. The planned trajectory arrives at the goal position in the end. However, by only penalizing distance in the reward function, the agent tries to arrive the goal rapidly and then keeps static, which ends with a large acceleration and rotation maneuver at the beginning phase. This can be observed from Fig. 5.13(c), Fig. 5.13(d) and Fig. 5.15. The large maneuver is not ideal for real implementation since it would over load the motors of the aerial vehicles.

When getting velocity shaping involved into the reward function, the trajectory becomes less aggressive, see Fig. 5.16. This is obvious when comparing Fig. 5.13(c) with Fig. 5.16(c), where the maximum velocity shows a clear decrease. Although rotation maneuver is still large at the beginning phase, the magnitude has been reduced significantly, see the orientation and angular rate. More parameter turning on the reward function and termination criteria design could improve this. At the same time, the

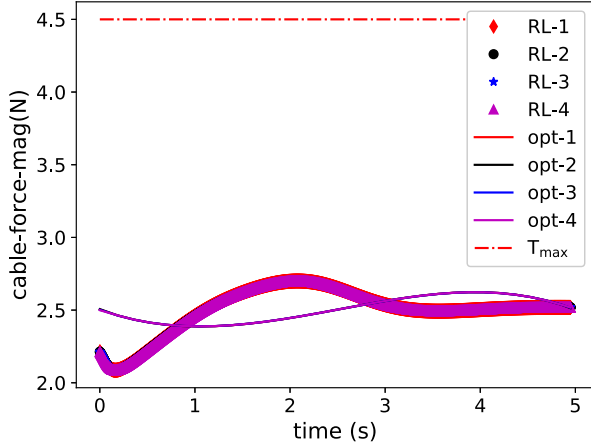


Figure 5.14. Cable tension with only distance in reward function

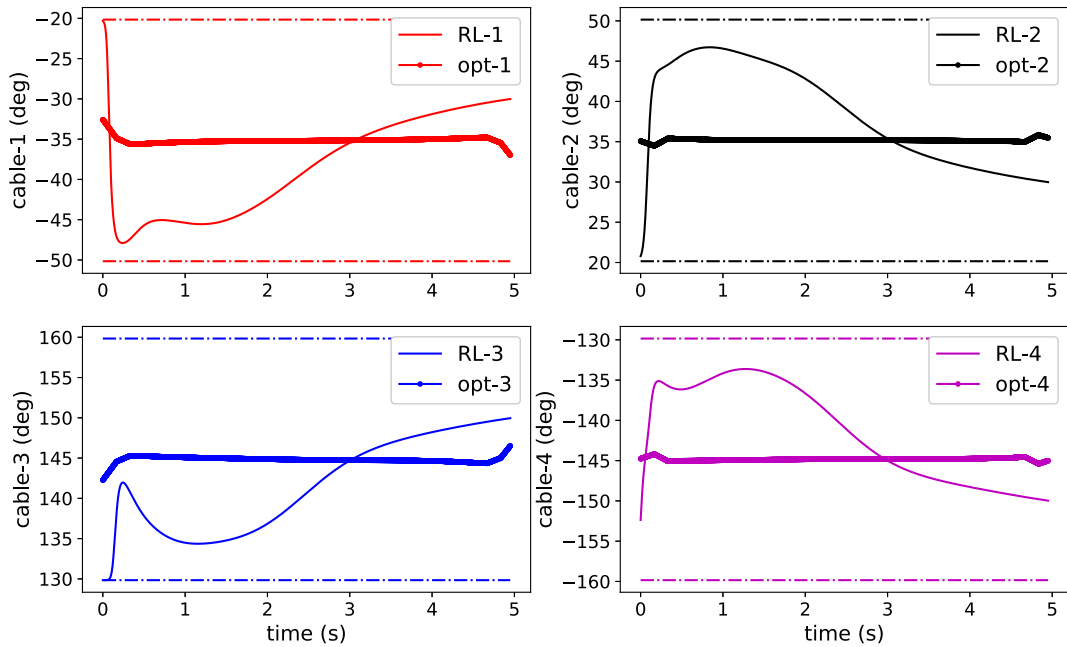


Figure 5.15. Sector angle comparison with only distance in reward function

cable tension planning shows a good match with the results from optimal control based approach.

The planned trajectory is generated based on the given initial waypoint. Then the well-trained policy (actor network) returns an action in RL frame while in the optimal control based approach, the action comes from the pre-planned sequence. The action transits the system to next states. This process repeats until the goal is reached or stops due to other termination criteria. Here, a payload motion model with numerical integration is implemented to simulate this process.

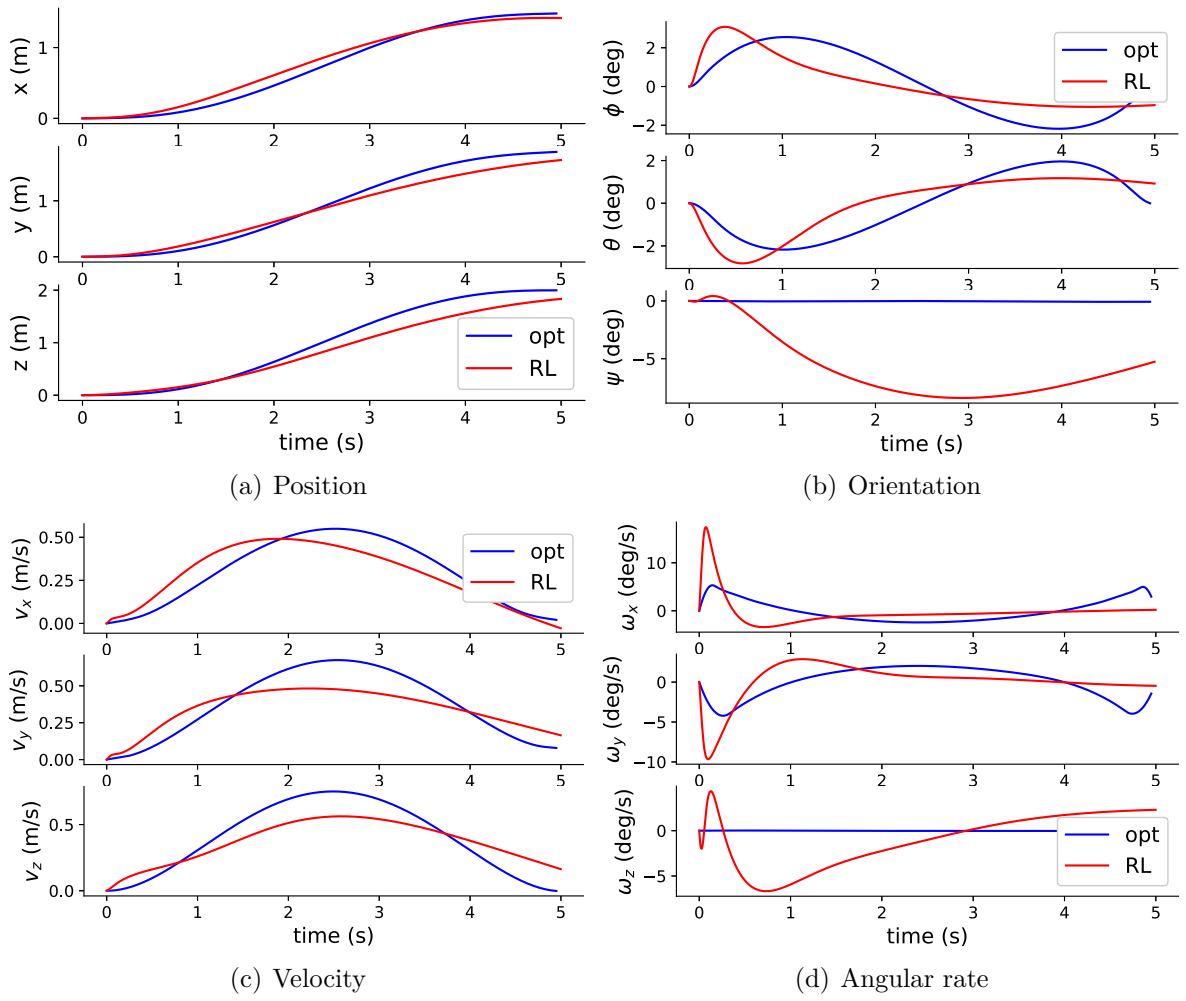


Figure 5.16. Payload States with velocity shaping involved into the reward function

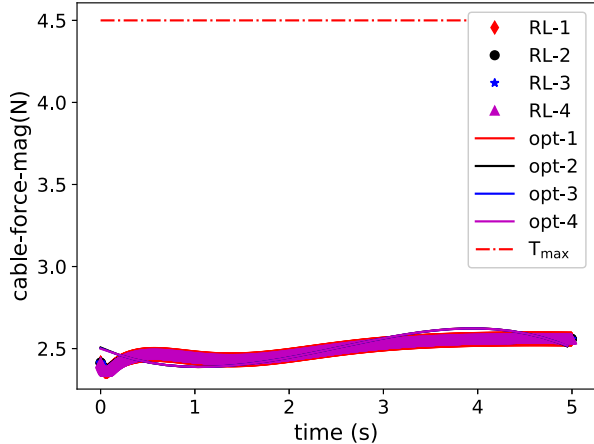


Figure 5.17. Cable tension comparison with velocity shaping involved into the reward function

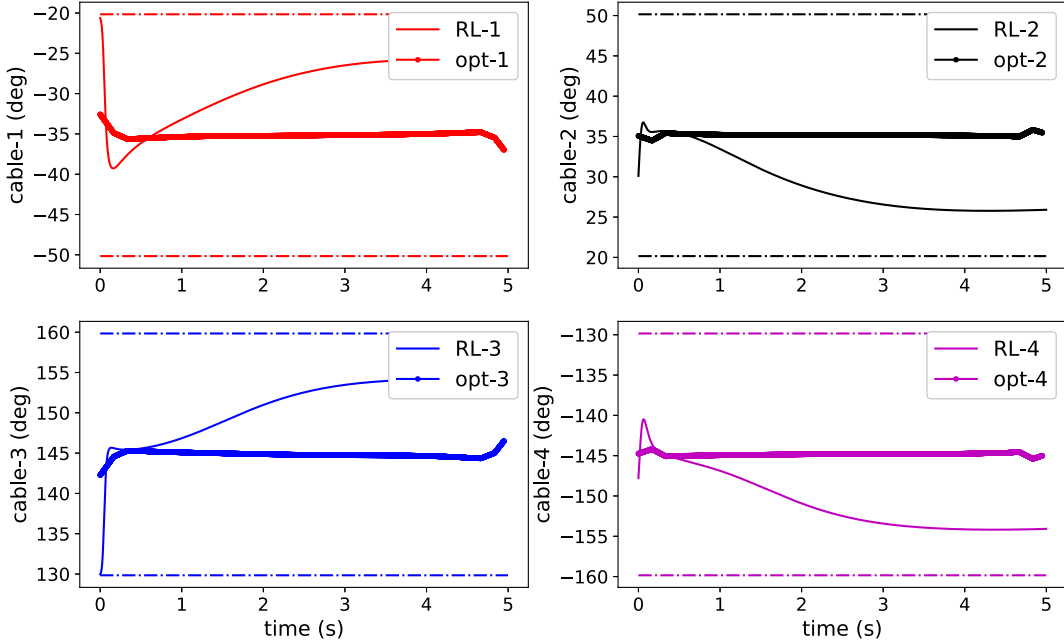


Figure 5.18. Sector angle comparison with velocity shaping involved into the reward function

Notice that the integration time stamp plays a key role for the simulation performance. In the two cases presented above, the integration time stamp is selected as $\Delta t = 0.001s$ to make the numerical integration error negligible so that the planning performance can be focused on. By doing this, it is assumed that some feedback techniques will be implemented during real tracking application, such as the neighboring feedback control developed in Section 5.2.2. However, if the integration time stamp is increased to $\Delta t = 0.02s$, which is 50 Hz (a common frequency for control), the simulation of the trajectories from optimal control based approach shows significantly deteriorate performance, see Fig. 5.19. In fact, without feedback control, the open-loop performance diverges quickly at about 2s, see Fig. 5.19(a). Meanwhile, the action generated from the RL policy network can still drives the payload to the goal without any feedback involved. This shows the superior performance of the well-trained RL policy network, which is more robust to the numerical integration error.

However, there is no free lunch. RL based approach needs a long time to train the network (> 8 hours, Fig. 5.20 shows the learning curve for the case with only distance in the reward function), while the optimal control approach requires much shorter time (< 0.5 hour). In addition, tuning the parameters in the RL approach, especially the reward function and termination criteria design is challenging and time consuming, which limits the RL based approach to be applied to more broad scenarios that needs real-time

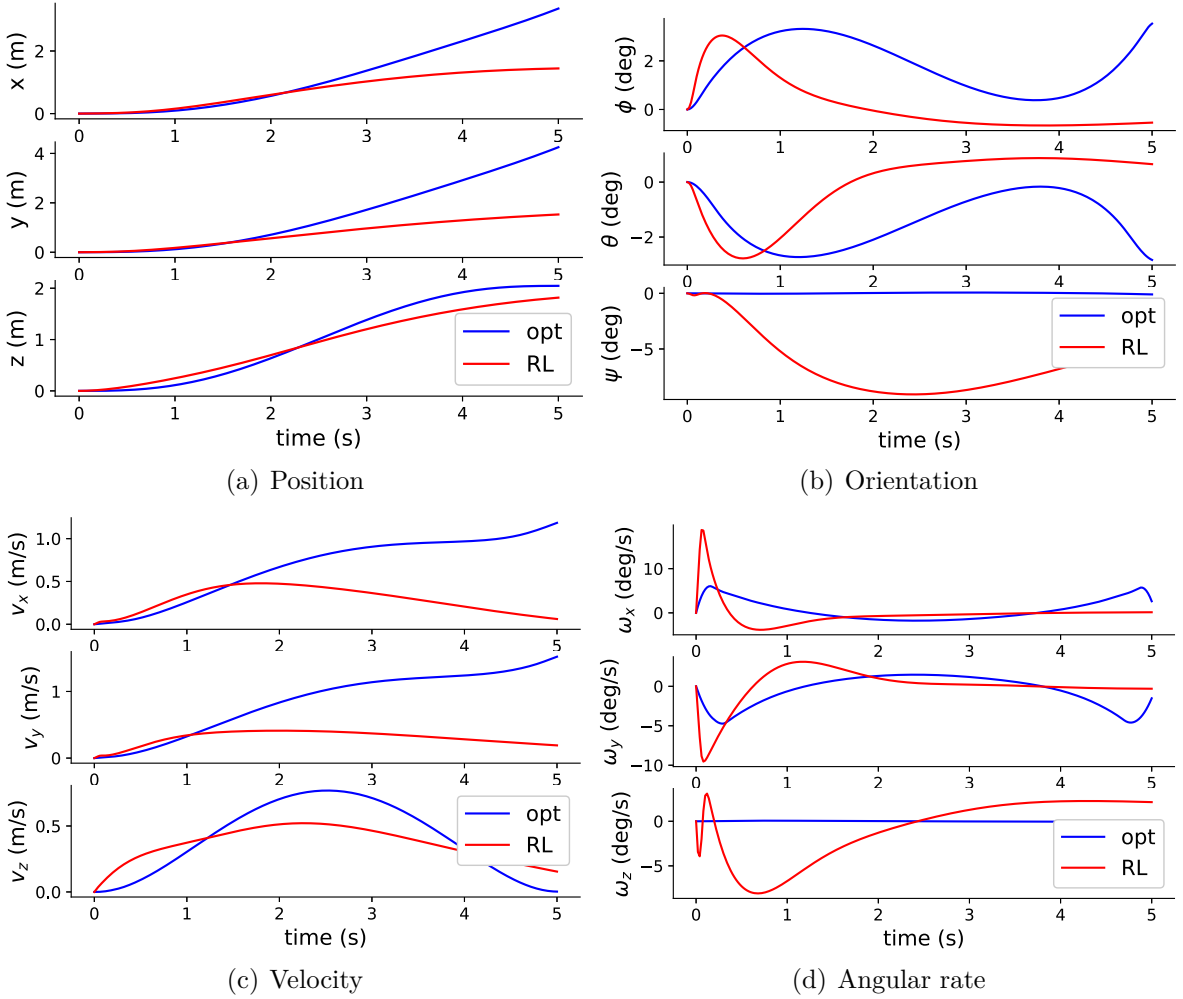


Figure 5.19. Payload States with velocity shaping $\Delta t = 0.02s$

planning.

It is worth to note that RL provide a model free method for multilift trajectory planning. It also shows that the feasible trajectory with minimum cable tension variance is not unique when given the fixed initial and final waypoints. For offline planning, it shows robust performance for open-loop simulation, thanks to the well-trained policy network which can model complex nonlinear behavior. More effort on the parameter tuning, reward function and termination criteria design is needed to well train the RL agent. This characteristic determines that it is not suitable for the scenarios that need real-time planning.

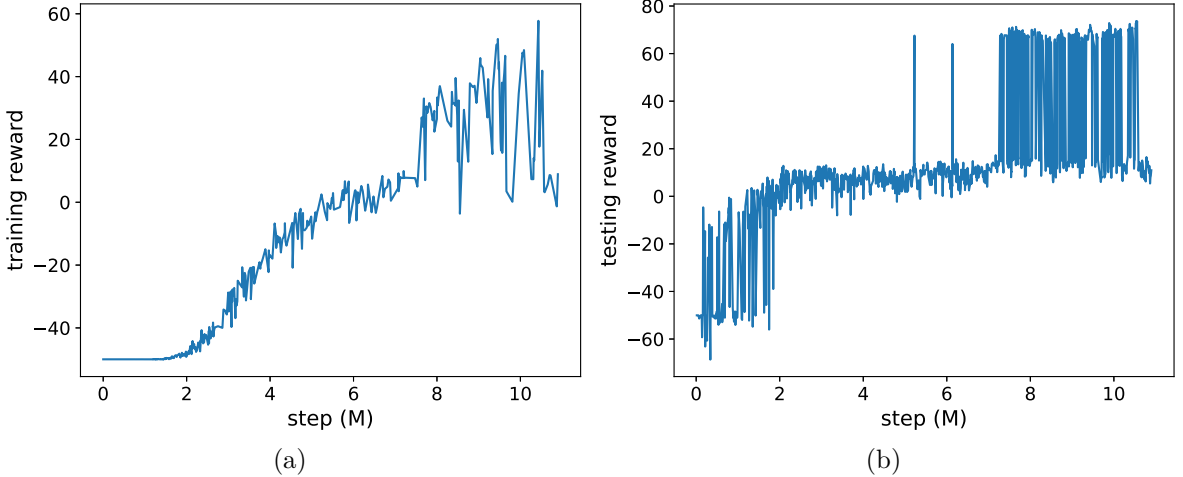


Figure 5.20. Multilift learning for trajectory planning based on load distribution

5.6 Summary

This chapter described in detail a load distribution based trajectory planning and control strategy for multilift system to achieve energy efficiency. It proposed a method that simultaneously plans payload trajectory and cable forces while satisfying path and force constraints and minimizing the difference in cable forces. The planning and tracking are both formulated as optimal control problems. The necessary condition analysis shows that as long as the system is near hover at low speed, there always exists an equal tension solution. Direct collocation method is used to solve the formulated planning problem. Then, a neighboring feedback law is designed to equalize the cable tension load distribution for the real flight. Here, small perturbation is performed to linearize the system with respect to the nominal path. An LQR controller is then designed for the system to track the reference trajectory.

Both numerical simulation and hardware flight experiments are performed to validate the proposed approach. Three test cases for planning are considered in simulation: with the given final time $t_f = 5.0, 2.8, 2.3$ sec. A 2.5 m/s wind gust is added to the environment to test the effectiveness of the tracking control by applying the designed feedback controller. Simulation results show that by reducing the arriving time, all cable tension increases but still with an evenly distributed load. The payload ended with a larger rotation maneuver and a more aggressive change of sector angle in order to achieve the goal in a shorter time by bigger acceleration. The system has a good performance even in the wind gust environment. The cable tension ended with more evenly distributed load comparing with the case without planning based on the load distribution.

Flight results from hardware implementation performed in a Vicon motion capture studio are presented. The final parameters used for the real flight tests are tweaked based on the Bryson's rule. Two cases are tested and compared: one with proposed load distribution based planning and neighboring feedback control approach; the other one with polynomial curve planning method and the hierarchical approach with real-time cable force computation. Results show that payload can be transported to desired waypoints in both cases. However, system has superior performance on the energy consumption in the case with planning based on load distribution. The rotorcraft ended with less variant cable tension, less total power and near-equal energy consumption.

Formulation towards reinforcement learning based multilift trajectory planning is presented. RL provides a model free method for multilift trajectory planning. Proximal policy optimization is used to formulate the planning problem based on load distribution. Preliminary simulation results show that the planned trajectory becomes less aggressive at the beginning phase when getting velocity shaping involved into the reward function. It also shows that the feasible trajectory with minimum cable tension variance is not unique. RL framework has robust open-loop performance. However, more effort on the parameter tuning, reward function and termination criteria design is needed to well train the RL agent. This characteristic determines it is not suitable for the scenarios that need real-time planning.

Chapter 6 | Conclusion

Cooperative slung load aerial transportation is challenging for multi robot autonomous system. Significant advances in coordination, sensing, perception, estimation, control and planning must be realized before the multilift system can be deployed. This dissertation is especially concerned with developing a self-contained multilift that can adapt to unknown payload properties and is able to achieve energy efficiency.

The research was motivated in part by the economical efficiency of using multiple aerial robots to carry a single large and heavy payload that occur only infrequently. The focus was on enabling three tasks: maintain coordinated controlled flight (*coordinated control*); obtain the knowledge of the payload so that the system can adapt to the unknown payload properties (*estimation*); schedule the path to reach the destination while considering the power consumption (*planning*). The system complexity and the coupling between the payload and aerial robots complicate these tasks.

The complexity inherent to the multilift suggests that unexpected and undesired payload motion will be hazards to the aerial vehicles if only flying a formation without considering the external slung load. The complex coupling produces not only the high nonlinearity of the system, but also imposes different modeling and control requirements for the slung load and the aerial robots.

Without the knowledge of payload properties or states, there is no guarantee that the system is able to feasibly transport the payload, especially in the unknown environment like in scenarios such as search and rescue when slung load properties may be unknown as prior. However, payload inertial properties are important for achieving good transportation performance since they are directly related to the payload dynamics. Specialized equipment may be required for the scenario when the payload is large or very heavy. A payload inertial property estimation technique can enable transportation with little a priori payload information.

Energy efficient multilift is appealing for the transportation mission that requires longer flight time. However, the power limitation of the individual aerial vehicle limits the global cooperative transportation performance. In the case of a homogeneous fleet of rotorcraft carrying a payload, it is intuitively appealing to operate the vehicles at near-equal load so that all vehicles operate at near-equal energy consumption. The ability to plan trajectory while considering energy consumption can make the transportation energy efficient.

The solution of the multilift problem has three main foci: develop a comprehensive coordinated control strategy for the multilift system to minimize the coupling of the payload and aerial vehicles while accounting for the payload dynamics; develop a payload inertial property estimation approach for enabling transportation with little a priori payload information; develop a trajectory planning method that considers power consumption.

The coordinated control strategy decomposes the complex multi agent problem into several sub-tasks so that each of them can be solved in a hierarchical manner. This is the core ingredient that determines the solutions of other parts of the system. The combination of the system complexity and the difficulty of coordinated control results in a multilift problem that cannot reliably be solved using the standard techniques for single robot. To address this difficulty, a hierarchical load-leading strategy was implemented and shown to be scalable, able to bring a human into the loop. The implementation at each level does not have a significant effect on other parts of the control architecture.

A key component of the strategy is computation of cable forces to enable desired payload behavior. This is shown to be a non-convex optimization problem, and a method to “convexify” cable force computation is introduced and implemented. Desired rotorcraft states for a given payload state is then derived. Three special cases are shown to be derivable from the general case. A stability analysis based on singular perturbation shows that the closed-loop system can track the reference exponentially within an error bound.

The estimation technology is critical for enabling transportation with little a priori payload information. The designed estimator fuses the payload input and response to determine the inertial properties. The load-leading platform provides convenience for estimation. The sensors carried by the payload gives real-time information for payload motion with respect to a reference point. This information is then used to derive the payload inertia property. Limited payload capacity restricts the weight and physical dimension of the sensors can be carried. This dissertation addresses this issue by creating an indirect method on the aerial robots side to estimate the cable force without

introducing any cable tension load cells.

The complexity and coupling of the system imposes difficulty on system excitation and parameter isolation. This dissertation designs a sequence of flight test to make different inertial properties observable using different payload motion patterns. Payload mass can be estimated in steady hover while center of mass and moments of inertia need payload rotation motion. Three estimation algorithms, including least-squares method, maximum likelihood and Kalman filter are derived and implemented to estimate payload inertial properties.

To achieve near equal load distribution among the aerial vehicles for energy efficiency, addition strategy is needed to optimally plan trajectory for the system. However, as the number of aerial vehicles increases, the dimension of the planning problem increases significantly, leading to challenge of finding feasible solutions. Thanks to the developed hierarchical load-leading strategy, the multilift trajectory planning problem is simplified as planning for payload while considering other physical and geometric constraints.

The trajectory planning is formulated as an optimal control problem that simultaneously plans payload trajectory and cable forces while satisfying path and force constraints and minimizing the difference in cable forces. Then, a feedback control law for tracking in the neighbor of the optimal trajectory is developed to equalize the cable tension load distribution.

Formulation towards reinforcement learning based multilift trajectory planning is presented. RL provides a model free method for multilift trajectory planning. Proximal polity optimization is used to formulate the planning problem based on load distribution.

This dissertation designs a hardware platform that uses four small multirotors and a payload to implement all of the developed approaches. All computations associated with the coordinated transport problem are hosted on single board computers carried onboard the payload and rotorcraft so that the whole transportation team is self-contained.

Indoor results demonstrated the effectiveness of the hierarchical load-leading approach by showing trajectory following, impulse disturbance rejection, human-in-the-loop control of the payload, and formation change. The convex formulation of the cable force optimization problem has faster convergence rate and is more robust to the initial guess. The system can quickly return to stable hover under external impulse disturbance. Good control and workload similar to that of flying a generic multirotor in attitude stabilized mode was shown in the human-in-the-loop test. The system operates well even during in-flight changes of cable geometry. Stable payload hover is achieved and the cable force optimization problem with changing constraints is solved in real time onboard the

payload.

Results of an outdoor flight using GPS as the main position/velocity sensor showed that hover and lateral translation commands were well-tracked even in the presence of a light breeze (7 km/h).

The proposed slung load inertial property estimation approach has been validated indoor. Results show that even without tension load cells, payload mass can be estimated within 3% of the true mass. Extra mass is added to the payload to verify the payload center of mass and moments of inertia estimation. The estimated center of mass is within a few millimeters of truth, with convergence requiring less than ten seconds. The moments of inertia estimation behaves qualitatively as expected.

Controller compensation tests shows that incorporating estimated payload center of mass location into the closed-loop control system does not significantly improve payload trajectory tracking performance, but does significantly improve performance of rotorcraft command following. Cable tensions and rotorcraft motion is significantly smoother when corrected inertial properties are incorporated into the closed-loop system.

Regarding the load distribution based trajectory planning and control, simulation/hardware results showed that the system has a good performance even in the wind gust environment. The system has a superior performance on the energy consumption in the case with planning based on load distribution. The rotorcraft ended with less variant cable tension, less total power and near-equal energy consumption comparing to the case without planning based on load distribution.

Under the RL framework, preliminary simulation results showed that the planned trajectory becomes less aggressive at the beginning phase when getting velocity shaping involved into the reward function. It also shows that the feasible trajectory with minimum cable tension variance is not unique. RL framework has robust open-loop performance. However, more effort on the parameter tuning, reward function and termination criteria design is needed to well train the RL agent.

6.1 Summary of Contributions

- **A Comprehensive Hierarchical Load-leading Control Strategy**

This dissertation developed a hierarchical load-leading control strategy for the multilift system. The strategy employs a load-leading approach, where the payload pose control, cable force computation, and aerial vehicle kinematics commanding are achieved in a hierarchical manner. This dissertation extends the state of art by

showing the cable force optimization problem is non-convex, and the constraints that make the problem convex are introduced and compared. A general derivation of desired rotorcraft states based on kinematics of the multilift problem is presented. This general case is then constrained to present results for the special cases of rigid connector, a spring/damper cable, and a rigid rotorcraft formation.

- **Estimator Design for Slung Load Inertial Properties**

A method for estimation of payload inertial properties without the need for cable tension sensors was introduced. An indirect method on the aerial vehicle side is used to estimate the cable force. An analysis on payload motion in response to cable forces provides insight into the excitation and resulting motion required to estimate inertial properties. Three estimation methods: recursive least-squares, maximum likelihood, and Kalman filter are derived and implemented for the estimation of various inertial properties with different dynamics characteristics.

This study provides guidance on the design of estimation strategy for the complex system and motivates the experiment design for validation and system identification.

- **Trajectory Planning and Control Approach Based on Load Distribution**

This dissertation introduced a trajectory planning approach that simultaneously pre-plans the slung load trajectory and cable forces while satisfying path and force constraints and minimizing the variance in cable tension. The load distribution based planning problem is formulated as an optimal control problem which is solved by the direct collocation method. Then, a feedback control law for tracking in the neighbor of the optimal trajectory is designed to equalize the cable tension load distribution during flight.

The methodology and tools developed for the multilift planning and control based on load distribution can be extended to other general multi-robot system to decrease the power consumption and extend the flight range and endurance. Therefore, It has the potential for saving costs in real cooperative mission.

- **Hardware Testbeds for Both Indoor and Outdoor Performance Verification**

This dissertation designed hardware testbeds for both indoor and outdoor flight testing. Flight demonstrations are presented for all three contributions addressed above. This implementation uses small single board computers carried onboard the

payload and the rotorcraft to host all algorithms. Flight demonstrations conducted in an indoor motion capture studio are presented to show trajectory following, human-in-the-loop control of the payload, rejection of an impulse disturbance, and formation changes. An outdoor flight demonstration using RTK GPS shows payload control and trajectory following in the presence of light winds.

The estimation strategy has been validated in an indoor motion capture studio. The inertial properties, including payload mass, center of mass and moments of inertia are well estimated. Furthermore, trajectory tracking tests comparing uncompensated (i.e. nominal) center of mass and compensated (estimated) center of mass shows the benefit of system performance. Incorporating the estimated payload parameters into the compensated controller significantly improves the tracking performance for the aerial robots.

Indoor flight tests also shows that the load distribution based approach has a superior performance on the energy consumption over the conventional unequalized approach. The aerial robots ended up with less variance in cable tension, less total power and near-equal energy consumption.

6.2 Recommendations for Future Work

Research problems tend to generate more questions than answers, and this dissertation was no exception. The complex multilift problem still has several facets that require additional work.

6.2.1 Different Cone Angles for Each Cable

The cone angle and sector angles in the cable force computation and load distribution based trajectory planning problem play a vital role for computing desired rotorcraft command. This dissertation showed the effectiveness of multilift by fixing the cone angles for each cables (most of the flight cases) or changing cone angles at the same speed (formation change with cable internal motion). Allowing different cone angles for each cable attachment may produce more flexibility. It can bring the vehicle characteristic into account when performing the optimization, leading to a more general optimization problem with more constraints. Additional analysis and algorithm are needed to solve for the optimization problem.

6.2.2 General Cable Model

This dissertation developed all the algorithms based on the assumption that the cables are always in tension when flying in the air. While this is valid for most of the scenarios, the cable cannot be in tension when some of the vehicles behave abnormally or lose power. It is also hard to guarantee that the cables are always in tension when performing the state transition, such as TAKE_OFF to FOLLOW_TRAJ or FOLLOW_TRAJ to LANDING when the payload is close to ground. Furthermore, the state of cable: in tension or lost tension (slack cable) may switch between each other rapidly and it cannot be treated as continuous transitions.

The multilift with cable tension states considered is a hybrid system. If the tension in any of the cables goes to zero, or if tension in any of the slack cables is reestablished, then the system dynamics switches, making this a hybrid system. [19] proposed a method by assuming that at most one cable tension can either drop to zero or one slack cable can get its tension reestablished to a nonzero value at any given moment. It also assumes that this happens sequentially. However, how to rigorously analyze the hybrid multilift is still an open research.

6.2.3 General Dynamics Model

For low speed and steady situation, aerodynamic forces acting on payload, cables and rotorcraft is neglected. Payload inertial parameter estimation can be performed in low speed situation before the transportation starts. However, regarding the energy efficiency, while the rotorcraft power consumption is mainly affected by the cable tension for the low speed flight with small maneuver, the aerodynamic forces will dominate the energy consumption for a long distance transport with more complex operational condition.

For the system operating in more complex condition, a general dynamic model with aerodynamic forces considered would increase the control accuracy. Additional sensors, like pitot tubes or high fidelity aerodynamics models are needed. As for trajectory planning, besides equalizing cable tension distribution for both safety and energy efficiency in the low speed scenario, a more general optimal control problem needs to be formulated to take the parasite power (induced by the drag forces) into account so that energy efficiency can be optimized in the complex environment.

6.2.4 Complex Environment with Obstacles

The ultimate goal of multilift is to transport payload in general flight condition. When flying in urban environment or clustered forest, obstacles such as architectures, trees are the main challenge. This dissertation focuses largely on coordinated control, parameter estimation and planning between waypoints without obstacles. Additional technology and algorithms on obstacle detection and avoidance are needed to perform multilift in complex environment.

Based on the developed hierarchical load-leading strategy, the perception required for obstacle avoidance can be setup in two ways: one is to deploy all the sensors (such as camera, LIDAR) and algorithms on payload and treat the possible maximum system volume bound as a constraint to avoid obstacles (this well executes the load-leading concept); the other way is to deploy auxiliary sensors on both the payload and the aerial vehicles. The information measured by both payload and vehicles helps make decisions on vehicles action to avoid obstacles.

Significant advances in sensing, perception, estimation and data fusion, control, trajectory planning are required before multilift obstacle avoidance can be performed. As computer vision, LIDAR, AI, and processing power improves, it may be possible to gather information about the relative states between payload and the aerial vehicles, the real-time environment states, etc. Incorporating these information into the multilift coordination and guidance would permit more reliable decision-making, coordinated control, further reducing the transportation costs, and allowing the system to avoid unfavorable regions.

6.2.5 Reinforcement Learning and Distributed System

Multilift as a multi robot cooperation problem can be combined with the recent advancement of artificial intelligence (AI), e.g. reinforcement learning (RL). The dissertation discusses the preliminary development towards RL based trajectory planning for multilift. Thanks to the hierarchical load-leading strategy, the multilift planning problem can be simplified as planning for the payload. Proximal policy optimization was implemented for the single agent planning problem.

The multilift can also be enriched by extending the strategy to decentralized mode. This would reduce the coupling and dependence of each robots to improve the system robustness. Thanks to the RL algorithms, such as deep deterministic policy gradient (DDPG) [94], the agents will be trained in a centralized leader-follower mode, and

subsequently be deployed in a decentralized mode.

6.2.6 Other Domains

The developed multiift can be applied in other domain, such as underwater environment. In scenario such as underwater salvage, the payload can be large and heavy, which is similar to multilift application. Issues will arise in the use of additional information that may become available due to the underwater environment.

Autonomous underwater vehicles (AUVs) do not have access to GPS signals. Navigation systems such as arrays of acoustic transducers, inertial measurements aided by multi-beam sonar, and vision based navigation can be used. However, each of them has additional issues such as the high weight and cost for acoustics transducers, the priori environment knowledge requirement for the sonar based inertial measurements and the light condition for vision. Proper sensor combination needs to be investigated before the underwater salvage can be performed.

For the underwater environment, the fluid drag cannot be ignored. Accurate models for payload, cable, and vehicles need to be established for analyzing the system dynamics and the corresponding control techniques.

6.2.7 System Redundancy

Cooperative transportation using multiple aerial vehicles increases the lifting capability of the system. It can also provides system redundancy. If any of individual aerial vehicle loses effectiveness during flight, the rest of the vehicles that are still in operation should be able to take over.

Two issues arise before successful system redundancy can be achieved. One is the physically attachment. The vehicle that lost effectiveness should be able to release the cable attachment on payload so that the rest of the system can still operate without interference. A servo release mechanism triggered by the system exception detection unit may serve this function. The other issue is the control allocation. Any releasing of the aerial vehicles would results in different vehicle geometric formation. The hierarchical load-leading strategy developed in this dissertation can be used to solve the changing formation problem. The distributed system discussed in Section 6.2.5 can also be applied due to the independence of each agent. Addition control allocation algorithm needs to be investigated for the physical transition.

Appendix A |

Stability Proof

A.1 Proof of Prop. 1

For the reduced system, the closed-loop accelerations of the payload can be computed directly as :

$$\begin{aligned} \mathbf{M}_L \ddot{\mathbf{x}} + \mathbf{C}_L \dot{\mathbf{x}} &= {}^e \mathbf{W}_g + {}^e \mathbf{W}_f \\ &= {}^e \mathbf{W}_g + {}^e \mathbf{R}_L \mathbf{G} {}^L \mathbf{f}_{cable} \end{aligned} \quad (\text{A.1})$$

$$= {}^e \mathbf{W}_g + {}^e \mathbf{R}_L \mathbf{G} (\mathbf{G}^T (\mathbf{G} \mathbf{G}^T)^{-1} {}^L \mathbf{W}_{f,d} + \tilde{\mathbf{G}} c) \quad (\text{A.2})$$

$$\begin{aligned} &= {}^e \mathbf{W}_g + {}^e \mathbf{W}_{f,d} \\ &= {}^e \mathbf{W}_g + \mathbf{M}_L \ddot{\mathbf{y}} + \mathbf{C}_L \dot{\mathbf{x}} - {}^e \mathbf{W}_g \end{aligned} \quad (\text{A.3})$$

$$\mathbf{M}_L \ddot{\mathbf{x}} = \mathbf{M}_L (\ddot{\mathbf{x}}_d + \mathbf{K}_p \mathbf{e} + \mathbf{K}_i \int_0^t \mathbf{e} d\tau + \mathbf{K}_d \mathbf{e}_v) \quad (\text{A.4})$$

Thus, the error dynamics of the payload's pose for the reduced system is

$$\ddot{\mathbf{e}}_p^r = -\mathbf{k}_{pp} \mathbf{e}_p^r - \mathbf{k}_{pi} \int_0^t \mathbf{e}_p^r d\tau - \mathbf{k}_{pd} \mathbf{e}_{\dot{p}}^r \quad (\text{A.5})$$

$$\ddot{\mathbf{e}}_\Omega^r = -\mathbf{k}_{\Omega p} \mathbf{e}_\Omega^r - \mathbf{k}_{\Omega i} \int_0^t \mathbf{e}_\Omega^r d\tau - \mathbf{k}_{\Omega d} \mathbf{e}_\omega^r \quad (\text{A.6})$$

where the superscript r denotes the error for reduced system. $\mathbf{k}_{pp}, \mathbf{k}_{\Omega p}$ are the block matrices of \mathbf{K}_p so as $\mathbf{k}_{pi}, \mathbf{k}_{\Omega i}$ from \mathbf{K}_i and $\mathbf{k}_{pd}, \mathbf{k}_{\Omega d}$ from \mathbf{K}_d . Thus, the errors of the payload's translational and rotational motion are decoupled from each other. Hence, each of them can be treated as an independent subsystem. Suitable gains exist for the reduced system such that almost global exponential stability is guaranteed (see for example [95] [96]).

A.2 Proof of Prop. 2

Rearranging the terms in the payload dynamics under full system model:

$$\ddot{\mathbf{x}} = \mathbf{M}_L^{-1}(-\mathbf{c}_L \dot{\mathbf{x}} + {}^e\mathbf{W}_g + \mathbf{M}_L^{-1}({}^e(\mathbf{G}\delta\mathbf{f}_{cable}) + {}^e\mathbf{W}_{f,d})) \quad (\text{A.7})$$

$$= \mathbf{M}_L^{-1}(-\mathbf{c}_L \dot{\mathbf{x}} + {}^e\mathbf{W}_g + \mathbf{M}_L^{-1}({}^e(\mathbf{G}\delta\mathbf{f}_{cable}) + (\mathbf{M}_L \ddot{\mathbf{y}} + \mathbf{c}_L \dot{\mathbf{x}} - {}^e\mathbf{W}_g))) \quad (\text{A.8})$$

where $\delta\mathbf{f}_{cable} = [\delta^L\mathbf{f}_{cable,1} \ \delta^L\mathbf{f}_{cable,2} \ \dots \ \delta^L\mathbf{f}_{cable,n}]^T$. Next, rewriting the equation in terms of the errors from the full system

$$\begin{bmatrix} \ddot{\mathbf{e}}_p \\ \ddot{\mathbf{e}}_\Omega \end{bmatrix} = \begin{bmatrix} \ddot{\mathbf{e}}_p^r \\ \ddot{\mathbf{e}}_\Omega^r \end{bmatrix} + \mathbf{M}_L^{-1} {}^e(\mathbf{G}\delta\mathbf{f}_{cable}) \quad (\text{A.9})$$

Moreover, the faster dynamics of the rotorcraft can be rewritten as

$$\epsilon \begin{bmatrix} \dot{\tilde{e}}_{x_{i3}} \\ \dot{\tilde{\mathbf{e}}}_{\Omega_i} \\ \dot{\mathbf{e}}_{\omega_i} \end{bmatrix} = \begin{bmatrix} -k_{i,p}\tilde{e}_{x_{i3}} - k_{i,i} \int_0^t \tilde{e}_{x_{i3}} d\tau - k_{i,d}\dot{\tilde{e}}_{x_{i3}} \\ \mathbf{e}_{\omega_i} \\ -(k_d + \mathbf{C}_i \mathbf{J}_i^{-1} \boldsymbol{\omega}_i \times \mathbf{J}_i \boldsymbol{\omega}_i - \dot{\mathbf{C}}_i \mathbf{C}_i^{-1}) \mathbf{e}_{\omega_i} - k_p \tilde{\mathbf{e}}_{\Omega_i} \end{bmatrix} \quad (\text{A.10})$$

where $\tilde{e}_{x_{i3}} = e_{x_{i3}}/\epsilon$, $\tilde{\mathbf{e}}_{\Omega_i} = \mathbf{e}_{\Omega_i}/\epsilon$ are the new error functions. For properly selected gain parameters, the rotorcraft's thrust and orientation will be tracked exponentially. Next, treating ϵ as the perturbation parameter of the error dynamics, when $\epsilon \rightarrow 0$, $\delta\mathbf{f}_{cable} \rightarrow 0$. Notice that the dynamical feasible trajectory ${}^e\mathbf{r}_{i,d}$, ${}^e\dot{\mathbf{r}}_{i,d}$, ${}^e\ddot{\mathbf{r}}_{i,d}$ comes from the payload and cable kinematics, which takes the internal motion into account. As long as the rotorcraft can track these reference, $\delta\mathbf{f}_{cable} \rightarrow 0$. In this case, the error of the full system becomes the error of the reduced system, thus it decay exponentially by Prop 1. Although ϵ can never become exactly zeros in real physical system, singular perturbation indicates that for sufficiently small ϵ , the exponential stability of the reduced system can still be preserved for the full system under certain conditions [64, Thm. 11.4]. In fact: (1) zero is an isolated equilibrium for both the faster and the reduced system; (2) the origin of the error dynamics for the reduced system is exponentially stable under properly selected gain parameters; (3) all the partial derivatives up to the second order are bounded according to the boundedness of states since all the expressions involved in the dynamics are smooth so that their partial derivatives are continuous; (4) the faster rotorcraft dynamics are exponentially stable. Thus, there exists an $\bar{\epsilon}$ such that when $\epsilon < \bar{\epsilon}$, the error for the full system would tend to zero exponentially.

Appendix B | Necessary Condition and Controller Parameters

B.1 Necessary Condition of the Planning Problem

The necessary conditions on $H_{\mathbf{u}} = 0$ leads to the following system of equation:

$$H_{\mathbf{u}} = L_{\mathbf{u}} + f_{\mathbf{u}}^T \boldsymbol{\lambda} = 0 \quad (\text{B.1})$$

where $\boldsymbol{\lambda}$ is the co-states, $L = \frac{1}{4} \sum_{i=1}^4 (f_i - \frac{1}{4} \sum_{j=1}^4 f_j)^2$, which is the cable tension variance at each time. The necessary conditions on $H_{\mathbf{u}} = 0$ leads to the following system of equation:

$$H_{\mathbf{u}} = L_{\mathbf{u}} + f_{\mathbf{u}}^T \boldsymbol{\lambda} \quad (\text{B.2})$$

where

$$L_{u_k} = \begin{cases} \frac{3}{8}f_i - \frac{1}{8} \sum_{j \neq i} f_j, & k = 2i-1, i, j = 1, 2, 3, 4 \\ 0, & k = 2i \end{cases}$$

$$f_{\mathbf{u}} = \begin{bmatrix} \mathbf{0}_{6 \times 8} \\ \cdots \\ \mathbf{E}_{6 \times 8} \end{bmatrix} \quad (\text{B.3})$$

where the $2i - 1$ th column of \mathbf{E} :

$$\mathbf{e}_{2i-1} = \begin{bmatrix} \frac{R_{11} \sin \alpha \cos \beta_i + R_{12} \sin \alpha \sin \beta_i - R_{13} \cos \alpha}{m_L} \\ \frac{R_{21} \sin \alpha \cos \beta_i + R_{22} \sin \alpha \sin \beta_i - R_{23} \cos \alpha}{m_L} \\ \frac{R_{31} \sin \alpha \cos \beta_i + R_{32} \sin \alpha \sin \beta_i - R_{33} \cos \alpha}{m_L} \\ \frac{-g_{1y} \cos \alpha - g_{1z} \sin \alpha \sin \beta_i}{J_{xx}} \\ \frac{g_{1z} \sin \alpha \cos \beta_i + g_{1x} \cos \alpha}{J_{yy}} \\ \frac{g_{1x} \sin \alpha \sin \beta_i - g_{1y} \sin \alpha \cos \beta}{J_{zz}} \end{bmatrix} \quad (\text{B.4})$$

the $2i$ th column of \mathbf{E} :

$$\mathbf{e}_{2i} = \begin{bmatrix} \frac{-R_{11} f_i \sin \alpha \sin \beta_i + R_{12} f_i \sin \alpha \cos \beta_i}{m_L} \\ \frac{-R_{12} f_i \sin \alpha \sin \beta_i + R_{22} f_i \sin \alpha \cos \beta_i}{m_L} \\ \frac{-R_{31} f_i \sin \alpha \sin \beta_i + R_{32} f_i \sin \alpha \cos \beta_i}{m_L} \\ \frac{-g_{1z} f_i \sin \alpha \cos \beta_i}{J_{xx}} \\ \frac{-g_{1z} f_i \sin \alpha \sin \beta_i}{J_{yy}} \\ \frac{g_{1x} f_i \sin \alpha \cos \beta_i + g_{1y} f_i \sin \alpha \sin \beta_i}{J_{zz}} \end{bmatrix} \quad (\text{B.5})$$

where R_{ij} is the component of the rotation matrix from frame \mathcal{F}_L to frame \mathcal{F}_e . \mathbf{g}_i is the cable attachment geometry vector of the i^{th} cable.

The necessary conditions on $\dot{\lambda} = -H_{\mathbf{x}_s}$ gives

$$\dot{\lambda}_1 = 0 \quad (\text{B.6})$$

$$\dot{\lambda}_2 = 0$$

$$\dot{\lambda}_3 = 0$$

$$\begin{aligned} -\dot{\lambda}_4 &= \lambda_4(\omega_y \cos \phi \tan \theta - \omega_z \sin \phi \tan \theta) \\ &+ \lambda_5(-\omega_y \sin \phi - \omega_z \cos \phi) + \lambda_6 \left(\omega_y \frac{\cos \phi}{\cos \theta} - \omega_z \frac{\sin \phi}{\cos \theta} \right) \\ &+ \frac{\lambda_7}{m_L} [(\sin \phi \sin \psi + \cos \phi \sin \theta \cos \psi) F_{Ty} + (\cos \phi \sin \psi - \sin \phi \sin \theta \cos \psi) F_{Tz}] \\ &+ \frac{\lambda_8}{m_L} [-\sin \phi \cos \psi + \cos \phi \sin \theta \sin \psi) F_{Ty} - (\cos \phi \cos \psi + \sin \phi \sin \theta \sin \psi) F_{Tz}] \\ &+ \frac{\lambda_9}{m_L} [\cos \phi \cos \theta F_{Ty} - \sin \phi \cos \theta F_{Tz}] \end{aligned} \quad (\text{B.7})$$

$$\begin{aligned}
-\dot{\lambda}_5 &= \lambda_4 \left(\omega_y \frac{\sin \phi}{\cos^2 \theta} + \omega_z \frac{\cos \phi}{\cos^2 \theta} \right) + \lambda_6 \left(\omega_y \frac{\sin \phi}{\cos^2 \theta} \sin \theta + \omega_z \frac{\cos \phi}{\cos^2 \theta} \sin \theta \right) \\
&\quad + \frac{\lambda_7}{m_L} (-\sin \theta \cos \psi F_{Tx} + \sin \phi \cos \theta \cos \psi F_{Ty} + \cos \phi \cos \theta \cos \psi F_{Tz}) \\
&\quad + \frac{\lambda_8}{m_L} [-\sin \theta \sin \psi F_{Tx} + \sin \phi \cos \theta \cos \psi F_{Ty} + \cos \phi \cos \theta \cos \psi F_{Tz}] \\
&\quad + \frac{\lambda_9}{m_L} [-\cos \theta F_{Tx} - \sin \phi \sin \theta F_{Ty} - \cos \phi \sin \theta F_{Tz}]
\end{aligned} \tag{B.8}$$

$$\begin{aligned}
-\dot{\lambda}_6 &= \frac{\lambda_7}{m_L} [-\cos \psi F_{Tx} - (\cos \phi \cos \psi + \sin \phi \sin \theta \sin \psi) F_{Ty} \\
&\quad + (\sin \phi \cos \psi - \cos \phi \sin \theta \sin \psi) F_{Tz}] \\
&\quad + \frac{\lambda_8}{m_L} [\cos \theta \cos \psi F_{Tx} + (-\cos \phi \sin \psi + \sin \phi \sin \theta \cos \psi) F_{Ty} \\
&\quad + (\sin \phi \sin \psi + \cos \phi \sin \theta \cos \psi) F_{Tz}]
\end{aligned} \tag{B.9}$$

where F_{Ti} is the component of the total cable force acting on the payload CG in body frame.

$$\dot{\lambda}_7 = -\lambda_1 \tag{B.10}$$

$$\dot{\lambda}_8 = -\lambda_2$$

$$\dot{\lambda}_9 = -\lambda_3$$

$$-\dot{\lambda}_{10} = \lambda_4 + \lambda_{11} \frac{J_{zz} - J_{xx}}{J_{yy}} \omega_z + \lambda_{12} \frac{J_{xx} - J_{yy}}{J_{zz}} \omega_y \tag{B.11}$$

$$\begin{aligned}
-\dot{\lambda}_{11} &= \lambda_4 (\sin \phi + \tan \theta) + \lambda_5 \cos \phi + \lambda_6 \frac{\sin \phi}{\cos \theta} \\
&\quad + \lambda_{10} \frac{J_{yy} - J_{zz}}{J_{xx}} \omega_z + \lambda_{12} \frac{J_{xx} - J_{yy}}{J_{zz}} \omega_x
\end{aligned} \tag{B.12}$$

$$\begin{aligned}
-\dot{\lambda}_{12} &= \lambda_4 \cos \phi \tan \theta - \lambda_5 \sin \phi + \lambda_6 \frac{\cos \phi}{\cos \theta} \\
&\quad + \lambda_{10} \frac{J_{yy} - J_{zz}}{J_{xx}} \omega_y + \lambda_{11} \frac{J_{zz} - J_{xx}}{J_{yy}} \omega_x
\end{aligned} \tag{B.13}$$

B.2 Controller Parameters for Hardware Implementation

Based on [66] [70], the maximum desired state deviation from the nominal state can be selected as:

$$dx = dy = dz = 0.14\text{m} \quad (\text{B.14})$$

$$d\phi = d\theta = d\psi = 5\text{deg} \quad (\text{B.15})$$

$$dv_x = dv_y = dv_z = 0.15\text{m/s} \quad (\text{B.16})$$

$$d\omega_x = d\omega_y = d\omega_z = 20\text{deg/s} \quad (\text{B.17})$$

Similarly, the maximum allowable input deviation from the nominal input are chosen as:

$$df_i = 0.07\text{N}, \quad i = 1, 2, \dots, 4 \quad (\text{B.18})$$

$$d\beta_i = 0.5\text{deg} \quad (\text{B.19})$$

The matrices Q and R can then be designed based on the Bryson's rule:

$$q_{ii} = \frac{1}{\max(x_{ii})^2}, \quad i = 1, 2, \dots, 12 \quad (\text{B.20})$$

$$r_{jj} = \frac{1}{\max(u_{jj})^2}, \quad j = 1, 2, \dots, 8 \quad (\text{B.21})$$

which are

$$Q = \text{diag}[51.02, 51.02, 51.02, 131.31, 131.31, 131.31, \dots] \quad (\text{B.22})$$

$$44.44, 44.44, 44, 44, 8.21, 8.21, 8.21] \quad (\text{B.23})$$

$$R = \text{diag}[204.08, 13131.23, 204.08, 13131.23, \dots] \quad (\text{B.24})$$

$$204.08, 13131.23, 204.08, 13131.23] \quad (\text{B.25})$$

where “diag ·” is the function to generate a diagonal matrix use the given vector.

Bibliography

- [1] CURTISS, H. and F. WARBURTON (1985) “Stability and control of the twin lift helicopter system,” *Journal of the American Helicopter Society*, **30**(2), pp. 14–23.
- [2] CICOLANI, L. S. and G. E. EHLERS (2002) “Modeling and simulation of a helicopter slung load stabilization device,” in *58th Annual Forum of the American Helicopter Society*, AHS, Montreal, Canadas.
- [3] (2016), “The world’s largest helicopter can lift an airliner with remarkable ease,” <https://www.businessinsider.com/russia-mi-26-helicopter-11ft-biggest-2016-8>, accessed: 2020-05-17.
- [4] CARTER, E. S. (1982) “Implication of heavy lift helicopter size effect trends and multilift options for filling the need,” in *European Rotorcraft Forum, 8 th*, Aix-en-Provence, France.
- [5] BERNARD, M. and K. KONDAK (2009) “Generic slung load transportation system using small size helicopters,” in *Robotics and Automation, 2009. ICRA ’09. IEEE International Conference on*, IEEE, Kobe, Japan, pp. 3258–3264.
- [6] KLAUSEN, K., C. MEISSEN, T. I. FOSSEN, M. ARCAK, and T. A. JOHANSEN (2020) “Cooperative Control for Multirotors Transporting an Unknown Suspended Load Under Environmental Disturbances,” *IEEE Transactions on Control Systems Technology*, **28**(2), pp. 653–660.
- [7] ENCIU, J., J. F. HORN, and J. W. LANGELAAN (2017) “Formation Control of a Rotorcraft Multilift System,” *Journal of the American Helicopter Society*, **62**(4), pp. 1–14.
- [8] (2020), “State College, PA Weather History, UNIVERSITY PARK AIRPORT STATION,” <https://www.wunderground.com/history/daily/us/pa/state-college/KUNV/date/2019-10-29>.
- [9] JACKSON, P. (1984) “Super Puma,” *Air International*, **26**(1), pp. 7–12, 33–35.
- [10] HUTTO, A. (1976) “Flight-Test Report on the Heavy-Lift Helicopter Flight-Control System,” *Journal of the American Helicopter Society*, **21**(1), pp. 32–40.

- [11] MCGONAGLE, J. G. (2001) “The design, test, and development challenges of converting the K-MAX helicopter to a heavy lift rotary wing UAV,” in *AHS International Annual Forum, 57 th*, Washington, DC.
- [12] MURRAY, R. M. (1996) “Trajectory generation for a towed cable system using differential flatness,” in *IFAC Proceedings Volumes*, vol. 29, Elsevier, pp. 2792–2797.
- [13] SMIRNOV, G. (1990) “Multiple-power-path nonplanetary main gearbox of the Mi-26 heavy-lift transport helicopter,” *Vertiflite*, **36**, pp. 20–23.
- [14] JONES, T., T. JOHNSON, D. SHEMWELL, and C. SHREVES (2012) “Photogrammetric technique for center of gravity determination,” in *53rd AIAA/ASME/ASCE/AHS/ASC Structures, Structural Dynamics and Materials Conference*, AIAA, Honolulu, Hawaii, p. 1882.
- [15] GORBAN, A. N., L. I. POKIDYSHEVA, E. V. SMIRNOVA, and T. A. TYUKINA (2011) “Law of the minimum paradoxes,” *Bulletin of mathematical biology*, **73**(9), pp. 2013–2044.
- [16] ENCIU, J. and J. F. HORN (2017) “Flight Performance Optimization of a Multilift Rotorcraft Formation,” *Journal of Aircraft*, **54**(4), pp. 1521–1538.
- [17] BERRIOS, M., M. TAKAHASHI, M. WHALLEY, G. SCHULEIN, L. CICOLANI, and J. POWELL (2018) “Load Distribution Control and Swing Angle Feedback for an Autonomous Dual Lift System with Flight Test Results,” in *74th Annual Forum of the American Helicopter Society*, AHS, Phoenix, AZ.
- [18] MICHAEL, N., J. FINK, and V. KUMAR (2011) “Cooperative manipulation and transportation with aerial robots,” *Autonomous Robots*, **30**(1), pp. 73–86.
- [19] SREENATH, K. and V. KUMAR (2013) “Dynamics, control and planning for cooperative manipulation of payloads suspended by cables from multiple quadrotor robots,” in *Robotics: Science and Systems 2013*, Berlin, Germany.
- [20] MASONE, C., H. H. BÜLTHOFF, and P. STEGAGNO (2016) “Cooperative transportation of a payload using quadrotors: A reconfigurable cable-driven parallel robot,” in *Intelligent Robots and Systems (IROS), 2016 IEEE/RSJ International Conference on*, IEEE, New York, NY, pp. 1623–1630.
- [21] LEE, T. (2018) “Geometric control of quadrotor UAVs transporting a cable-suspended rigid body,” *IEEE Transactions on Control Systems Technology*, **26**(1), pp. 255–264.
- [22] LI, Z., J. F. HORN, and J. W. LANGELAAN (2014) “Coordinated Transport of a Slung Load by a Team of Autonomous Rotorcraft,” in *AIAA Guidance, Navigation, and Control Conference*, AIAA, National Harbor, MD.

- [23] STEVENS, H. D., M. E. S., R. S.M., and R. CANNON (1994) “Object-Based Task-Level Control: A Hierarchical Control Architecture for Remote Operation of Space Robots,” in *Proceedings of the AIAA/NASA Conference on Intelligent Robotics in Field, Factory, Service, and Space*, 1994-1209, AIAA, Houston, TX.
- [24] DAI, S., T. LEE, and D. S. BERNSTEIN (2014) “Adaptive control of a quadrotor UAV transporting a cable-suspended load with unknown mass,” in *53rd IEEE Conference on Decision and Control*, IEEE, Los Angeles, CA, USA, pp. 6149–6154.
- [25] MELLINGER, D., Q. LINDSEY, M. SHOMIN, and V. KUMAR (2011) “Design, modeling, estimation and control for aerial grasping and manipulation,” in *Intelligent Robots and Systems (IROS), 2011 IEEE/RSJ International Conference on*, IEEE, San Francisco, CA, USA, pp. 2668–2673.
- [26] STUCKEY, R. A. (2001) *Mathematical modelling of helicopter slung-load systems*, Tech. Rep. DSTO-TR-1257, Defence Science and Technology Organization, Victoria, Australia.
URL <http://www.dtic.mil/get-tr-doc/pdf?AD=ADA401423>
- [27] FAILLE, D. and A. VAN DER WEIDEN (1995) “Robust regulation of a flying crane,” in *Control Applications, 1995., Proceedings of the 4th IEEE Conference on*, IEEE, Albany, NY, pp. 494–499.
- [28] THEODORE, C. R., M. B. TISCHLER, and J. D. COLBOURNE (2004) “Rapid frequency-domain modeling methods for unmanned aerial vehicle flight control applications,” *Journal of Aircraft*, **41**(4).
- [29] BISGAARD, M. (2008) *Modeling, estimation, and control of helicopter slung load system*, Ph.D. thesis, Department of Control Engineering, Aalborg University.
- [30] STUMP, E. and V. KUMAR (2006) “Workspaces of cable-actuated parallel manipulators,” *Journal of Mechanical Design*, **128**(1), pp. 159–167.
- [31] HUNT, K. H. (1978) *Kinematic geometry of mechanisms*, vol. 7, Oxford University Press, USA.
- [32] PHILLIPS, J. (2007) *Freedom in machinery*, vol. 1, Cambridge University Press.
- [33] MITTAL, M., J. PRASAD, and D. P. SCHRAGE (1992) “Comparison of stability and control characteristics of two twin-lift helicopter configurations,” *Nonlinear Dynamics*, **3**(3), pp. 199–223.
- [34] OH, S.-R., J.-C. RYU, and S. K. AGRAWAL (2006) “Dynamics and control of a helicopter carrying a payload using a cable-suspended robot,” *Journal of Mechanical Design*, **128**(5), pp. 1113–1121.
- [35] MITTAL, M., J. PRASAD, and D. P. SCHRAGE (1991) “Nonlinear adaptive control of a twin lift helicopter system,” *IEEE Control Systems*, **11**(3), pp. 39–45.

- [36] BERNARD, M. and K. KONDAK (2009) “Generic slung load transportation system using small size helicopters,” in *IEEE Conference on Robotics and Automation*, IEEE, Kobe, Japan.
- [37] SONG, Y., J. F. HORN, Z. LI, and J. W. LANGEALAAN (2013) “Modeling, Simulation, and Non-Linear Control of a Rotorcraft Multi-Lift System,” in *Annual Forum Proceedings, 69th American Helicopter Society International Annual Forum*, vol. 4, AHS International Alexandria, VA, pp. 2695–2714.
- [38] BISGAARD, M., A. LA COUR-HARBO, and J. BENDTSEN (2007) “Full state estimation for helicopter slung load system,” in *AIAA Guidance, Navigation and Control Conference and Exhibit*, Hilton Head, SC, p. 6762.
- [39] BISGAARD, M., A. LA COUR-HARBO, E. N. JOHNSON, and J. D. BENDTSEN (2007) “Vision aided state estimator for helicopter slung load system,” *IFAC Proceedings Volumes*, **40**(7), pp. 425–430.
- [40] REDDI, Y. and E. BOJE (2014) “System Identification for Low-cost Small-scale Helicopters,” *IFAC Proceedings Volumes*, **47**(3), pp. 8831–8836.
- [41] LEE, H. and H. J. KIM (2017) “Estimation, control, and planning for autonomous aerial transportation,” *IEEE Transactions on Industrial Electronics*, **64**(4), pp. 3369–3379.
- [42] CORAH, M. and N. MICHAEL (2017) “Active estimation of mass properties for safe cooperative lifting,” in *2017 IEEE International Conference on Robotics and Automation (ICRA)*, IEEE, Singapore, Singapore, pp. 4582–4587.
- [43] MITTAL, M. and J. PRASAD (1993) “Three-dimensional modeling and control of a twin-lift helicopter system,” *Journal of Guidance, Control and Dynamics*, **16**(1), pp. 86–95.
- [44] FINK, J., N. MICHAEL, S. KIM, and V. KUMAR (2011) “Planning and control for cooperative manipulation and transportation with aerial robots,” *The International Journal of Robotics Research*, **30**(3), pp. 324–334.
- [45] GENG, J. and J. W. LANGEALAAN (2020) “Mass and Center of Mass Location Estimation for a Multi-lift Slung Load,” in *AIAA Scitech 2020 Forum*, Orlando, FL, p. 2067.
- [46] TAKAHASHI, M., M. WHALLEY, S. G.J., and B. M.G. (2018) “A System for Autonomous Rotorcraft Dual-Lift Flight Research,” in *74th Annual Forum of the American Helicopter Society*, AHS, Phoenix, AZ.
- [47] LAMAURY, J. and M. GOUTTEFARDE (2013) “Control of a large redundantly actuated cable-suspended parallel robot,” in *Robotics and Automation (ICRA), 2013 IEEE International Conference on*, IEEE, Karlsruhe, Germany, pp. 4659–4664.

- [48] BRUCKMANN, T. and A. POTT (2012) *Cable-driven parallel robots*, vol. 12, Springer.
- [49] (2016), “Cable-driven parallel robots – Motion simulation i,” <https://www.youtube.com/watch?v=9KMptw7ZgVI>, accessed: 2020-05-17.
- [50] (2017), “CableEndy juggler – cable-driven parallel robot (B&R Automation),” <https://www.youtube.com/watch?v=7HNAL8ZKdyM>, accessed: 2020-05-17.
- [51] NGUYEN, D. Q. and M. GOUTTEFARDE (2014) “Study of reconfigurable suspended cable-driven parallel robots for airplane maintenance,” in *Intelligent Robots and Systems (IROS 2014), 2014 IEEE/RSJ International Conference on*, IEEE, Chicago, IL, USA, pp. 1682–1689.
- [52] GAGLIARDINI, L., S. CARO, M. GOUTTEFARDE, P. WENGER, and A. GIRIN (2015) “A reconfigurable cable-driven parallel robot for sandblasting and painting of large structures,” in *Cable-Driven Parallel Robots*, Springer, pp. 275–291.
- [53] MERLET, J.-P. (2014) “Checking the cable configuration of cable-driven parallel robots on a trajectory,” in *Robotics and Automation (ICRA), 2014 IEEE International Conference on*, IEEE, Hong Kong, China, pp. 1586–1591.
- [54] LAMAURY, J., M. GOUTTEFARDE, A. CHEMORI, and P.-E. HERVÉ (2013) “Dual-space adaptive control of redundantly actuated cable-driven parallel robots,” in *Intelligent Robots and Systems (IROS), 2013 IEEE/RSJ International Conference on*, IEEE, Tokyo, Japan, pp. 4879–4886.
- [55] BOSSCHER, P. and I. EBERT-UPHOFF (2004) “Wrench-based analysis of cable-driven robots,” in *Robotics and Automation, 2004. Proceedings. ICRA’04. 2004 IEEE International Conference on*, vol. 5, IEEE, New Orleans, LA, USA, pp. 4950–4955.
- [56] MIKELSONS, L., T. BRUCKMANN, M. HILLER, and D. SCHRAMM (2008) “A real-time capable force calculation algorithm for redundant tendon-based parallel manipulators,” in *Robotics and Automation, 2008. ICRA 2008. IEEE International Conference on*, IEEE, Pasadena, CA, USA, pp. 3869–3874.
- [57] MEEK, T., G. CHESLEY, ET AL. (1970) “Twin helicopter lift system study and feasibility demonstration,” *Sikorsky Engineering Report*, **64323**.
- [58] MAZA, I., K. KONDAK, M. BERNARD, and A. OLLERO (2009) “Multi-UAV cooperation and control for load transportation and deployment,” in *Selected papers from the 2nd International Symposium on UAVs, Reno, Nevada, USA June 8–10, 2009*, Springer, pp. 417–449.
- [59] LI, Z. (2014) *Coordinated Transport of a Slung Load by a Team of Autonomous Rotorcraft*, Ms thesis, Department of Aerospace Engineering, The Pennsylvania State University.

- [60] BOYD, S. and L. VANDENBERGHE (2004) *Convex optimization*, Cambridge university press.
- [61] LEE, D., A. FRANCHI, H. I. SON, C. HA, H. H. BÜLTHOFF, and P. R. GIORDANO (2013) “Semiautonomous haptic teleoperation control architecture of multiple unmanned aerial vehicles,” *IEEE/ASME Transactions on Mechatronics*, **18**(4), pp. 1334–1345.
- [62] MELLINGER, D. and V. KUMAR (2011) “Minimum snap trajectory generation and control for quadrotors,” in *2011 IEEE International Conference on Robotics and Automation*, IEEE, Shanghai, China, pp. 2520–2525.
- [63] LEE, T., M. LEOK, and N. H. MCCLAMROCH (2010) “Geometric tracking control of a quadrotor UAV on SE (3),” in *49th IEEE conference on decision and control (CDC)*, IEEE, Atlanta, GA, USA, pp. 5420–5425.
- [64] KHALIL, H. K. and J. W. GRIZZLE (2002) *Nonlinear systems*, vol. 3, Prentice hall Upper Saddle River, NJ.
- [65] WU, G. and K. SREENATH (2014) “Geometric control of multiple quadrotors transporting a rigid-body load,” in *53rd IEEE Conference on Decision and Control*, IEEE, Los Angeles, CA, USA, pp. 6141–6148.
- [66] GENG, J. and J. W. LANGELAAN (2019) “Implementation and demonstration of coordinated transport of a slung load by a team of rotorcraft,” in *AIAA SciTech 2019 Forum*, 2019-0913, AIAA, San Diego, CA.
- [67] QUIGLEY, M., K. CONLEY, B. GERKEY, J. FAUST, T. FOOTE, J. LEIBS, R. WHEELER, and A. Y. NG (2009) “ROS: an open-source Robot Operating System,” in *Proceedings of Open-Source Software Workshops ICRA*, vol. 3, Kobe, p. 5.
- [68] MANSHADI, A. and F. SAGHAFI (2018) “In-Flight Estimation of Time-Varying Aircraft Center of Gravity Position Based on Kinematics Approach,” *Journal of Aircraft*, **55**(5), pp. 2037–2049.
- [69] HE, H., Z. JUN, and L. YINGYING (2015) “A new method for online identification of the center of mass of spacecraft using multiple accelerometers,” *Proceedings of the Institution of Mechanical Engineers, Part G: Journal of Aerospace Engineering*, **229**(1), pp. 110–118.
- [70] GENG, J. and J. W. LANGELAAN (2020) “Cooperative Transport of a Slung Load Using Load-Leading Control,” *Journal of Guidance, Control, and Dynamics*, **43**(7), pp. 1313–1331.
- [71] CRASSIDIS, J. L. and J. L. JUNKINS (2004) *Optimal estimation of dynamic systems*, Chapman and Hall/CRC.

- [72] ÅSTRÖM, K. J. and B. WITTENMARK (2013) *Adaptive control*, Courier Corporation.
- [73] SIMON, D. (2006) *Optimal state estimation: Kalman, H infinity, and nonlinear approaches*, John Wiley & Sons.
- [74] FRANKLIN, G. F., J. D. POWELL, A. EMAMI-NAEINI, and J. D. POWELL (1994) *Feedback control of dynamic systems*, vol. 3, Addison-Wesley Reading, MA.
- [75] BRYSON, A. E. (2018) *Applied optimal control: optimization, estimation and control*, Routledge.
- [76] KIRK, D. E. (2004) *Optimal control theory: an introduction*, Courier Corporation.
- [77] LEWIS, F. L., D. VRABIE, and V. L. SYRMON (2012) *Optimal control*, John Wiley & Sons.
- [78] BETTS, J. T. (1998) “Survey of numerical methods for trajectory optimization,” *Journal of guidance, control, and dynamics*, **21**(2), pp. 193–207.
- [79] ADURTHI, N., P. SINGLA, and M. MAJJI (2016) “Sparse Approximation-Based Collocation Scheme for Nonlinear Optimal Feedback Control Design,” *Journal of Guidance, Control, and Dynamics*, **40**(2), pp. 248–264.
- [80] KELLY, M. (2017) “An introduction to trajectory optimization: how to do your own direct collocation,” *SIAM Review*, **59**(4), pp. 849–904.
- [81] ANDERSON JR, J. D. (2010) *Fundamentals of aerodynamics*, Tata McGraw-Hill Education.
- [82] HOERNER, S. F. (1965) “Fluid-dynamic drag,” *Hoerner Fluid Dynamics*.
- [83] SUTTON, R. S. and A. G. BARTO (2018) *Reinforcement learning: An introduction*, MIT press.
- [84] ABBEEL, P., A. COATES, M. QUIGLEY, and A. Y. NG (2007) “An application of reinforcement learning to aerobic helicopter flight,” in *Advances in neural information processing systems*, pp. 1–8.
- [85] LIU, P., J. GENG, Y. LI, Y. CAO, Y. C. BAYIZ, J. W. LANGELAAN, and B. CHENG (2020) “Bio-inspired Inverted Landing Strategy in a Small Aerial Robot Using Policy Gradient,” in *Intelligent Robots and Systems (IROS), 2020 IEEE/RSJ International Conference on*, IEEE, Las Vegas, NV, p. Accepted.
- [86] PENG, X. B., E. COUMANS, T. ZHANG, T.-W. LEE, J. TAN, and S. LEVINE (2020) “Learning Agile Robotic Locomotion Skills by Imitating Animals,” in *Robotics: Science and Systems 2020*, Virtual.
- [87] HORN, J. F. (2019) “Non-linear dynamic inversion control design for rotorcraft,” *Aerospace*, **6**(3), p. 38.

- [88] GRAULE, M., P. CHIRARATTANANON, S. FULLER, N. JAFFERIS, K. MA, M. SPENKO, R. KORNBLUH, and R. WOOD (2016) “Perching and takeoff of a robotic insect on overhangs using switchable electrostatic adhesion,” *Science*, **352**(6288), pp. 978–982.
- [89] JIANG, H., M. T. POPE, E. W. HAWKES, D. L. CHRISTENSEN, M. A. ESTRADA, A. PARLIER, R. TRAN, and M. R. CUTKOSKY (2014) “Modeling the dynamics of perching with opposed-grip mechanisms,” in *2014 IEEE International Conference on Robotics and Automation (ICRA)*, IEEE, pp. 3102–3108.
- [90] RAIBERT, M. H. (1984) “Hopping in legged systems—modeling and simulation for the two-dimensional one-legged case,” *IEEE Transactions on Systems, Man, and Cybernetics*, (3), pp. 451–463.
- [91] LAPAN, M. (2018) *Deep Reinforcement Learning Hands-On: Apply modern RL methods, with deep Q-networks, value iteration, policy gradients, TRPO, AlphaGo Zero and more*, Packt Publishing Ltd.
- [92] SCHULMAN, J., F. WOLSKI, P. DHARIWAL, A. RADFORD, and O. KLIMOV (2017) “Proximal policy optimization algorithms,” *arXiv preprint arXiv:1707.06347*.
- [93] SCHULMAN, J., S. LEVINE, P. ABBEEL, M. JORDAN, and P. MORITZ (2015) “Trust region policy optimization,” in *International conference on machine learning*, pp. 1889–1897.
- [94] SILVER, D., G. LEVER, N. HEES, T. DEGRIS, D. WIERSTRA, and M. RIEDMILLER (2014) “Deterministic policy gradient algorithms,” in *Proceedings of the 31st International Conference on Machine Learning- Volume 32*, Beijing, China, pp. I–387.
- [95] BULLO, F. and A. D. LEWIS (2019) *Geometric control of mechanical systems: modeling, analysis, and design for simple mechanical control systems*, vol. 49, Springer.
- [96] LEE, T., M. LEOK, and N. H. MCCCLAMROCH (2011) “Stable manifolds of saddle equilibria for pendulum dynamics on S^2 and $SO(3)$,” in *2011 50th IEEE Conference on Decision and Control and European Control Conference*, IEEE, Orlando, FL, USA, pp. 3915–3921.

Vita

Junyi Geng

Education

Ph.D. Aerospace Engineering with Minor in Electrical Engineering, Pennsylvania State University, 2020

M.S. Aerospace Engineering, Pennsylvania State University, 2016

B.S. Aerospace Engineering, Nanjing University of Aeronautics and Astronautics, 2013

Publications

- [1] **Geng, J.**, and J. W. Langelaan (2020) “Cooperative Transport of a Slung Load Using Load-leading Control,” *Journal of Guidance, Control, and Dynamics* 43(7), pp. 1313-1331.
- [2] **Geng, J.**, and J. W. Langelaan (2020) “Estimation of Inertial Properties for a Multilift Slung Load”, *Journal of Guidance, Control, and Dynamics*. (accepted).
- [3] Li, Y., M. Tofighi, **J. Geng**, V. Monga, and Y. C. Eldar (2020) “Efficient and Interpretable Deep Blind Image Deblurring Via Algorithm Unrolling,” *IEEE Transactions on Computational Imaging* 6, pp. 666-681.
- [4] Liu, P., **J. Geng**, Y. Li, Y. Cao, Y. E. Bayiz, J. W. Langelaan, and B. Cheng (2020) “Bio-inspired Inverted Landing Strategy in a Small Aerial Robot Using Policy Gradient,” in *Intelligent Robots and Systems (IROS), 2020 IEEE/RSJ International Conference on*, IEEE, Las Vegas, NV. (accepted)
- [5] **Geng, J.**, P. Singla, and J. W. Langelaan (2021) “Trajectory Planning and Control for a Multi-lift System Based on Load Distribution”, in *AIAA Scitech 2021 Forum*, Nashville, Ten. (accepted)
- [6] **Geng, J.** and J. W. Langelaan (2020) “Mass and Center of Mass Location Estimation for a Multi-lift Slung Load,” in *AIAA Scitech 2020 Forum*, Orlando, FL, p. 2067.
- [7] **Geng, J.** and J. W. Langelaan (2019) “Implementation and Demonstration of Coordinated Transport of a Slung Load by a Team of Rotorcraft,” in *AIAA SciTech 2019 Forum*, 2019-0913, AIAA, San Diego, CA.
- [8] **Geng, J.** and J. W. Langelaan (2017), “A Quasi Polar Local Occupancy Grid Approach for Vision-based Obstacle Avoidance,” in *AIAA Guidance, Navigation, and Control Conference*, AIAA, Grapevine, TX, p. 1907.